



**HAL**  
open science

## 3D resolved distortion measurements by Bragg diffraction imaging: application to ice crystals

Rafael Kluender

► **To cite this version:**

Rafael Kluender. 3D resolved distortion measurements by Bragg diffraction imaging: application to ice crystals. Other [cond-mat.other]. Université de Grenoble, 2011. English. NNT : 2011GRENY041 . tel-00635598

**HAL Id: tel-00635598**

**<https://theses.hal.science/tel-00635598>**

Submitted on 25 Oct 2011

**HAL** is a multi-disciplinary open access archive for the deposit and dissemination of scientific research documents, whether they are published or not. The documents may come from teaching and research institutions in France or abroad, or from public or private research centers.

L'archive ouverte pluridisciplinaire **HAL**, est destinée au dépôt et à la diffusion de documents scientifiques de niveau recherche, publiés ou non, émanant des établissements d'enseignement et de recherche français ou étrangers, des laboratoires publics ou privés.

## THÈSE

Pour obtenir le grade de

## DOCTEUR DE L'UNIVERSITÉ DE GRENOBLE

Spécialité : **Physique des matières condensées & rayonnement**

Arrêté ministériel : 7 août 2006

Présentée par

« **Rafael Thomas KLUENDER** »

Thèse dirigée par « **José BARUCHEL** » et  
codirigée par « **Armelle PHILIP** »

préparée au sein des **Laboratoires ESRF et LGGE**  
dans l'**École Doctorale de Physique**

# Mésures de distortions en trois dimensions par imagerie en diffraction Bragg : application aux cristaux de glace

Thèse soutenue publiquement le « **29 septembre 2011** »,  
devant le jury composé de :

**Dr. José BARUCHEL**

Chef du groupe imagerie – ESRF, Directeur de thèse

**Dr. Pierre BASTIE**

Chercheur - ILL, Président du jury

**Dr. Bernard CAPELLE**

Directeur de l'IMPMC, Rapporteur

**Dr. Samuel FOREST**

Chercheur au Centre des Matériaux – Mines Paris, Examineur

**Dr. Wolfgang Ludwig**

Chercheur à l'INSA, Rapporteur

**Dr. Jacques Meyssonier**

Chercheur au LGGE, Invité

**Dr. Armelle Philip**

Chercheur au LGGE, Codirecteur de thèse





Ich widme diese Arbeit meiner Oma,  
die am Dienstag, den 26. Juli 2011 verstorben ist.

# Acknowledgements

The experimental work presented in the manuscript was carried out at the ESRF and the LGGE. I want to thank these institutes for financing my PhD project.

I would like to pronounce the deepest gratitude for my direct supervisors, José Baruchel at the ESRF and Armelle Philip at the LGGE, for accepting my PhD candidature and for their support during the three years of the project. At this point I want to mention the importance of Jacques Meyssonier from the LGGE as well, who followed the progress of the project with great passion.

I had the occasion to participate on some experimental work on quartz crystals with Pierre Bastie from the ILL. It was a great honour for me having M. Bastie as the president of the defence jury.

Profuse thanks go to Bernard Capelle, head of the Institut de minéralogie et de physique des milieux condensés and to Wolfgang Ludwig from the Institut national des sciences appliquées - Lyon for their acting as referee and for accepting their invitation to be a member of the jury.

A special thanks goes to Samuel Forest from the Centre des matériaux - Mines Paristech for being an important member of the jury and for the discussions about the deformation process during the defence.

A thank you goes to the workgroup of the BM05 that helped me to prepare the experiments in particular our technician Jean-Yves Massonnat who retired during in the meantime of my PhD. Here a special thanks, once again, to Armelle and Jacques who participated in every beamtime and at any time of the day or night.

Very important was the support of my family in Germany and Poland. My friends in Grenoble and every else were a great help, too.

Last but not least I thank google for providing sketchup + layout. A major part of the figures in my Phd report are drawn by using those outstanding programs.

# Abstract

**Abstract:** The viscoplastic deformation of ice is strongly anisotropic. The preferred glide system is on the basal plane. In a polycrystal each grain exhibits its own deformation direction. As a result the deformation of polycrystalline ice is associated with strain incompatibilities, especially at the grain boundaries and the triple junction. The deformation process was experimentally investigated by measuring crystal lattice distortions of single- and polycrystalline, artificially grown ice crystals. The experiments were benefiting from a synchrotron X-ray beam. A new experimental method, based on Bragg diffraction imaging (X-ray topography) methods, as white beam X-ray diffraction topography, rocking curve imaging, section- and pinhole X-ray topography was used. Angular misorientations, full-width-half-maxima and integrated Bragg diffracted intensities have been measured along the three spatial dimensions of the sample and with a spatial resolution of around  $50 \mu\text{m} \times 50 \mu\text{m} \times 50 \mu\text{m}$ . Data analysis algorithms were written in order to extract quantitative results from the data and to calculate all nine components of the curvature tensor, as well as the entire lattice distortion in the sample. The results give an insight into the early stages of plastic deformation of ice, i.e. the polygonisation of a grain was observed.

**Keywords:** hexagonal ice, viscoplastic deformation, crystalline anisotropy, dislocation density, geometrically necessary dislocations, curvature tensor, lattice distortions, X-ray imaging, 3D imaging, Bragg diffraction, X-ray topography, Rocking curve imaging, Section topography, Pinhole topography.

**Résumé:** La déformation visco-plastique de la glace est fortement anisotrope, le plan de glissement préféré étant la plan de base. Le fait que dans un polycrystal chaque grain possède sa propre direction de déformation produit des incompatibilités et un champ de contrainte complexe. La déformation a été étudiée expérimentalement en mesurant la distortion des plans cristallins de mono- et polycristaux de glace artificielle. Les expériences ont été réalisées à l'aide d'un faisceau synchrotron. Une nouvelle procédure expérimental, basée sur les méthodes de l'imagerie en diffraction de Bragg, comme lumière blanche, imagerie sur la courbe de diffraction et topographie laminaire et ponctuelle, a été développée. Les désorientations angulaires, les largeurs à mi-hauteur et les intensités intégrées ont été mesurées dans les trois dimensions spatiales de l'échantillon et avec une résolution de  $50 \times 50 \times 50 \mu\text{m}^3$ . Les algorithmes d'analyse de données ont été écrits pour extraire des données des résultats quantitatifs, et pour calculer les neuf composantes du tenseur de courbure ainsi que la distortion entière des plans cristallins. Les résultats ont permis d'observer les premières étapes de la déformation de la glace. Par exemple la polygonisation d'un grain a été observée.

**Mots clés:** glace  $I_h$ , déformation viscoplastique, anisotropie cristalline, densité des dislocations, dislocations géométriquement nécessaires, tenseur de courbure, distortions des plans cristallins, imagerie en rayons X, imagerie en 3D, diffraction de Bragg, topographie en rayons X, rocking curve imaging, topographie en sections, topographie en points.

# Contents

<b>Introduction</b>	<b>1</b>
<b>1 Structure and deformation of ice</b>	<b>4</b>
1.1 Ice crystal structure . . . . .	4
1.2 Dislocations . . . . .	5
1.3 Viscoplastic deformation . . . . .	8
1.4 Crystalline misorientations . . . . .	9
1.5 Lattice distortions and dislocation density . . . . .	11
<b>2 X-ray physics</b>	<b>14</b>
2.1 X-ray generation . . . . .	14
2.1.1 X-ray tube radiation . . . . .	14
2.1.2 Synchrotron radiation . . . . .	15
2.2 X-ray diffraction topography . . . . .	17
2.2.1 Elements of dynamical diffraction theory . . . . .	18
2.2.2 Contrast mechanisms . . . . .	21
2.2.3 Bragg diffraction in ice . . . . .	22
2.3 X-ray diffraction topographic methods . . . . .	23
2.3.1 White beam diffraction topography (WBT) . . . . .	23
2.3.2 Rocking curve imaging (RCI) . . . . .	24
2.3.3 Section X-ray diffraction topography . . . . .	25
2.3.4 Pinhole X-ray diffraction topography . . . . .	26
<b>3 Experimental procedures</b>	<b>28</b>
3.1 Conventions for coordinate system . . . . .	28
3.2 The BM05 beamline at the ESRF . . . . .	29
3.3 Sample and sample environment . . . . .	31
3.3.1 Crystal growth and crystal manufacturing . . . . .	31
3.3.2 Sample . . . . .	34
3.3.3 Sample environment . . . . .	34
3.4 Experiment . . . . .	35
3.4.1 Orienting the crystal . . . . .	35
3.4.2 Step scanning the crystal . . . . .	37
3.4.3 Multi-pinhole X-ray diffraction topography . . . . .	38
3.4.4 Deforming the crystal . . . . .	41
3.4.5 Data usage . . . . .	42
<b>4 Data analysis</b>	<b>43</b>
4.1 Recorded raw data . . . . .	43
4.2 Step scanning data analysis . . . . .	43
4.2.1 Local rocking curve analysis . . . . .	44

4.2.2	Calculating misorientation	46
4.3	Multi pinhole data analysis	47
4.3.1	Rod image analysis	47
4.3.2	Calculating misorientation	49
4.4	Volume composition	49
4.4.1	Composing step scanning maps to a crystal volume	50
4.4.2	Composing pinhole vectors to a crystal volume	50
4.4.3	Axis scaling in 3D crystal volume matrix	52
4.5	Calculating curvature tensor	53
<b>5</b>	<b>Results</b>	<b>54</b>
5.1	Initial deformation state	55
5.2	Intermediate deformation state	60
5.2.1	Basal Bragg diffraction	60
5.2.2	Prismatic Bragg diffraction	62
5.3	Final deformation state	64
5.3.1	Basal Bragg diffraction	65
5.3.2	Prismatic Bragg diffraction	67
5.4	Curvature tensor components	70
5.5	Chapter conclusion	71
<b>6</b>	<b>Discussion</b>	<b>72</b>
6.1	Dislocation visibility	72
6.2	Crystal deformation	74
6.3	Final deformation state characteristics	75
6.4	3D versus 2D	77
6.5	Sample stability	78
6.6	Curvature tensor components	79
	<b>Conclusion</b>	<b>81</b>
	<b>A Dispersive effects</b>	<b>83</b>
	<b>B Lateral deviations of the Bragg diffracted beam</b>	<b>88</b>
	<b>C Permuting rotations</b>	<b>92</b>
	<b>D Curvature tensor calculations</b>	<b>93</b>
	<b>E Figures in large format</b>	<b>94</b>
	<b>References</b>	<b>120</b>

# Introduction

The polar ice sheets on the poles and the glaciers in mountains represent the major part of fresh water on our planet. They exhibit a huge impact on the earth climate. According to recent studies, the global warming will be mostly pronounced on the pole regions, where the strongest temperature rises are prognosticated [ipp 01]. The consequences of this global warming are important and controversial. In the context of changes the planet earth will face, the material ice and its mechanical properties gets more and more attention of the scientific community.

On the other hand, big effort is made to access the local strain of crystalline materials by experiments, for instance metal alloys, in order to understand mechanical processes like strain hardening or fatigue cracks. The mechanical properties of a solid strongly depend on its crystallite quality and therefore the early stages of deformation, from a high quality crystalline structure on, must be understood. In crystal lattice distortion measurements, the use of Bragg diffraction methods at synchrotron sources [King 08, Robach 11] plays an important role.

Ice is an important material to be studied in this context: it is not only important for environmental topics, but it also displays a very strong anisotropy, and a very weak absorption for X-rays. The plastic deformation of hexagonal ice is indeed strongly anisotropic: the main deformation mechanism is the dislocation glide of  $\vec{b} = 1/3\langle 11\bar{2}0 \rangle$  dislocations on the basal (0001)-plane [Glen 54]. The preference for one slip system implies strain incompatibilities when single crystals confined in their deformation directions or polycrystals are deformed. The resulting strain field is complicated and inconsistent with grain size independent plasticity theory: polycrystals do exhibit a dependence of yield stress on grain size. In order to understand the mechanical behaviour and the evolution of crystalline material a grain size dependent plasticity theory is needed. It could be compared with numerical simulations of the deformation process and in this way contribute to the development of a more general plasticity theory.

A lot of scientific work was devoted to the mechanical deformation of ice. According to Hondoh [Hondoh 00] the stress parallel to the basal glide planes that is necessary to induce dislocation movement of an entire  $\vec{b} = 1/3\langle 11\bar{2}0 \rangle$  dislocation is so high that the crystal would crack. The dislocation glide therefore requires a thermal activation and as a result viscoplastic deformation of ice is only possible at high temperatures, close to the melting point. Beside the preferred slip mode, further ones are needed to allow each grain in a polycrystal to accommodate a general distortion and to meet the shape changes imposed by its neighbours. Therefore attention was also paid to dislocations that do not glide on the basal planes [Liu 92, Jones 70, Higashi 88, Shearwood 89].

The wish to understand the behaviour of ice is also motivated by similar deformation properties in other materials, for instance metals exhibiting a hexagonal crystal structure. Here ice at a temperature not too far from its melting point may be considered as a model material for hot metals. The advantage is that “hot ice” is easier to create and to study than a hot metal exhibiting a hexagonal crystal structure as calcium (melting point at  $T = 842^\circ\text{C}$ ) or titanium (melting point at  $T = 1668^\circ\text{C}$ ).

The elastic scattering of X-rays on the crystal lattice of a solid is widely used to investigate crystals. Bragg diffraction allows to determine the structure and characterise the defects in a crystal. X-ray Bragg diffraction topography was first used in the 20th century, greatly contributed to the characterisation of crystals grown for the semiconductors industry, and was the origin of many newer methods that were partially boosted by the use of synchrotron generated intense beams. Whereas registering a topograph by using a laboratory X-ray generator may take hours, the task is generally accomplished in a few seconds when using a synchrotron. This allows studying many processes in-situ. The diffraction topographic work performed on the deformation of samples containing more than one single crystal grain is of major interest for the present work. A pioneering, and very important work, was performed by Milena Polcarova and co-workers to study the plastic deformation of Fe-Si high quality bicrystals [Polcarova 98] (and references therein), which included the study of the complex slip transfer across the grain boundary [Polcarova 06]. On the other hand, synchrotron radiation has also been used to follow the dislocation movement and/or generation on ice samples: some examples are the works of Ahmad and Whitworth (1988) [Ahmad 88], or Liu, Baker and Dudley (1993) [Liu 92]. The use of synchrotron radiation makes, in addition, rocking curve imaging possible, where hundreds or even thousands of images are recorded. A further example is surely the diffraction contrast tomography procedure [King 08], a method also related to Bragg diffraction topography. It allows to measure the shapes and orientation of the grains in polycrystalline samples, composed of up to hundreds of grains, and resolves lattice distortions down to a few miliradians. This very sophisticated method (as well as other ones developed over the last years [Robach 11]) is not actually suited for the studies we are concerned with on the very early stages of deformation, where the lattice distortions only amount a few tens of microradians: these studies require a high spatial and angular resolution.

The present project is the logical continuation of the pioneering work that was accomplished by Laura Capolo in her thesis [Capolo 07] (supervised by the Armelle Philip and Jacques Meyssonier). The work consisted of the characterisation the initial states of distortion in three grain ice crystals that were stepwise mechanically deformed. The experiments were strongly based on white beam topography, which exhibits the advantage of providing several Bragg diffraction spots of all three grains at the same time. This allowed accessing the entire lattice distortions of a grain as well as the simultaneous observation of several grains, and provided an ensemble of qualitative features associated with the initial states of ice deformation. But the obligation to use of films as detector led to limitations concerning the quantification of the Bragg diffracted intensity, and the precision of the curvature tensor components that can be derived.

The present work wishes to progress on several aspects. The crystal growth procedure is optimised to provide high quality ice crystals. This crystalline quality of the samples also allows increasing the crystal thickness in order to reduce the surface effects observed before. The method used in the present work aims extracting quantitative results from the data. This method was not available, and has to be developed. It is based on rocking curve imaging, where a monochromatic beam is used and the crystal is stepwise turned around a well defined spatial orientation. This only allows recording one Bragg diffraction spot at once, but both the spatial and the angular resolutions are substantially increased. Further on the method combines rocking curve imaging with section topography, to be able to measure the lattice distortion in all three spatial dimensions (3D), which is an important improvement since the plastic deformation of a crystal is a three dimensional problem.

We give, in chapter I (Chap. 1), some elements on structure and deformation of ice we think could be needed by the reader for the understanding of the obtained results. chapter II (Chap. 2) is devoted to the description of the experimental probe we used, i.e. synchrotron

radiation X-ray beams, and of the techniques we combine (section and pinhole topography, rocking curve imaging) to have access to the wished results on the initial deformation states of ice. The main experimental procedures are described on chapter III (Chap. 3). It includes the very important sample growth process that allows having, as initial samples, very high quality crystals (or three-grain-crystals, which is the simplest case of a polycrystal). As the X-ray technique implemented is not standard, it has to be commissioned. The experimental commissioning, as well as the data analysis procedures, are presented in chapter IV (Chap. 4) and on the appendixes (A to D). In particular, the dispersion corrections, compulsory for very weakly deformed crystals, is not available in the literature for the transmission case we are concerned with, and is calculated (App. B).

The commissioning of the experimental procedures proved to be more time consuming than foreseen at the beginning of this work. The first series of experimental results, recorded with incomplete procedures, were difficult to exploit. We therefore choose to present in chapter V (Chap. 5) only the results obtained in march 2011, with the optimised procedure. These results display, besides the wished curvature tensor components, a series of original aspects, in particular because we have access to virtual slices inside the crystal: these aspects are discussed in chapter VI (Chap. 4).

Finally, at the level of the conclusion, we discuss the capabilities and limitations of this new technique, and the scientific perspectives it opens.

# Structure and deformation of ice

The mechanical properties of crystals are controlled by the presence, movement and creation of dislocations (an introduction can be found in the book of Weertman & Weertman [Weertman 70]). They allow viscoplastic deformation of ice crystals under applied stresses. Dislocation movement in ice crystals is very easy within the basal planes and rather difficult in directions perpendicular to these planes [Glen 54]. The anisotropic behaviour of ice leads to complicated strain fields and a hardly predictable deformation process, especially for polycrystals. A part of the dislocation density is associated with lattice distortions by analytical equations. A way to study the deformation process therefore consists on measuring lattice curvatures (see Chap. 1.5).

## 1.1 Ice crystal structure

Depending on the environmental pressure and temperature water crystallises in different ice structures. There are 14 different allotropes known. Under normal pressure on Earth of  $10^5$  Pa the crystallising temperature of water defines the zero point of the Celsius temperature scale,  $T = 0^\circ\text{C}$ . The oxygen atoms in that kind of ice crystal are arranged in a hexagonal lattice [Petrenko 99], shown in Fig. 1.1. The lattice parameters are  $a = 4.52 \text{ \AA}$

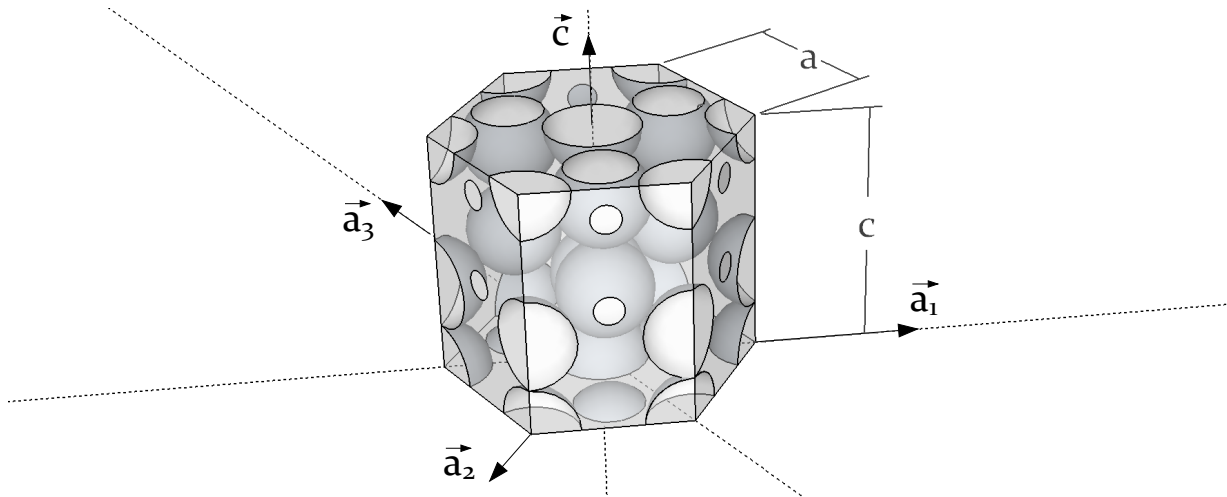
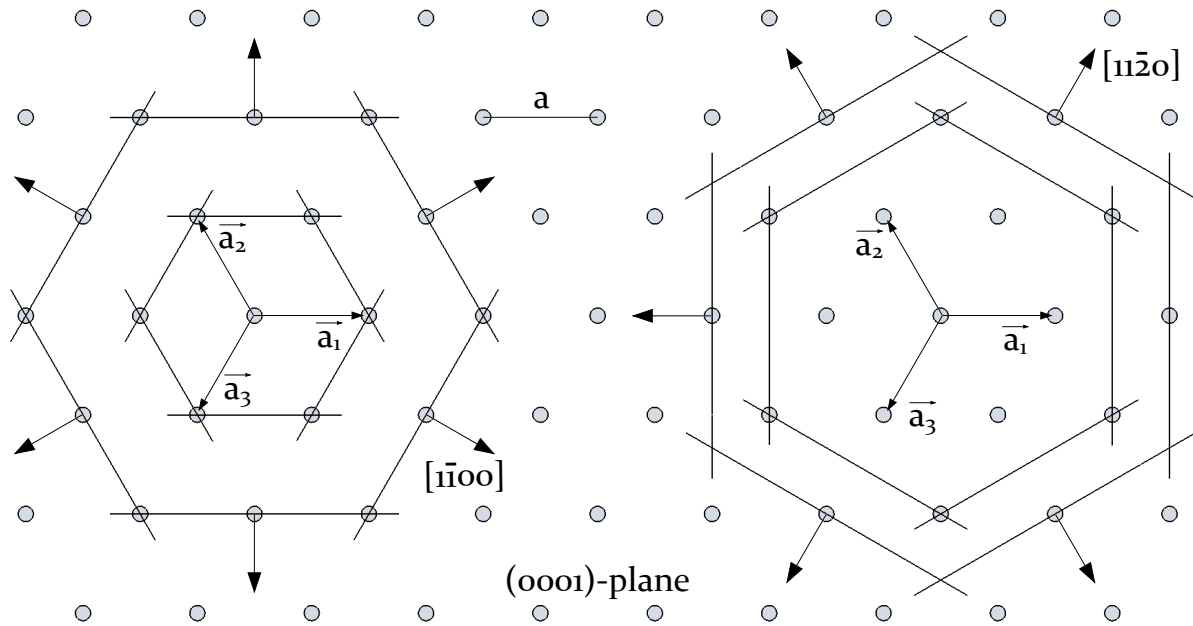


Figure 1.1: Non primitive ice unit cell; oxygen atoms are represented as spheres.

and  $c = 7.36 \text{ \AA}$ , the ratio  $c/a = 1.63$ , found to be practically constant for temperatures above 120 K [Röttger 94], is very close to the value of “ideally close-packed” structures:  $c/a = \sqrt{8/3}$ . In the following, the described ice phase will simply be called “ice”. The lattice planes perpendicular to the  $\vec{c}$ -axis are called “basal” lattice planes, the ones parallel

to  $\vec{c}$  “prismatic” and any other lattice planes are called “pyramidal”. The volume of the unit cell shown in Fig. 1.1 is  $1.5\sqrt{3}a^2c$ . It contains three lattice points. The volume of a primitive unit cell therefore is  $V_{\text{primitive}} = (1/2)\sqrt{3}a^2c$ .

Lattice points in hexagonal structures are often expressed by a linear combination of four basis vectors  $\vec{a}_1$ ,  $\vec{a}_2$ ,  $\vec{a}_3$  and  $\vec{c}$ , where  $\vec{a}_3 := -\vec{a}_1 - \vec{a}_2$  (Fig. 1.1). Despite an overdetermined basis the four axis notation is illustrative: lattice plane families with the same symmetries are described by the same indices for the first three components. An example is shown in Fig. 1.2. The notation of the first order prismatic planes,  $\{11\bar{2}0\}$ , reveals their geometrical equivalence, whereas in a three axis notation it would be:  $(110)$ ,  $(1\bar{2}0)$  and  $(\bar{2}10)$ .



**Figure 1.2:** Basal lattice plane in the hexagonal structure; LHS: 1st order prismatic planes, RHS: 2nd order.

By declaring a lattice point in the centre of a conventional oxygen atom the following positions for the atoms in a primitive unit cell are deduced:

$$\vec{r}_1 = \begin{pmatrix} 0 \\ 0 \\ 0 \end{pmatrix} \quad \vec{r}_2 = \begin{pmatrix} -1/3 \\ 1/3 \\ 2/16 \end{pmatrix} \quad \vec{r}_3 = \begin{pmatrix} -1/3 \\ 1/3 \\ 8/16 \end{pmatrix} \quad \vec{r}_4 = \begin{pmatrix} 0 \\ 0 \\ 10/16 \end{pmatrix} \quad (1.1)$$

The positions are expressed in the basis vectors  $\{\vec{a}_1, \vec{a}_2, \vec{c}\}$ . Taking into account the symmetries of the atomic basis and of the lattice structure the space group of ice can be determined as  $P6_3/mmc$  [Fletcher 70].

**Light polarisation:** Ice is optically uniaxial, a property that is used to determine the orientation of the  $\vec{c}$ -axis. The orientation of the  $\vec{a}$ -axis has no influence on the light polarisation.

## 1.2 Dislocations

Dislocations are linear imperfections (defects) in the crystal lattice. There are two basic geometries to be distinguished: *edge-* and *screw dislocation*. In an edge dislocation (Fig. 1.3)

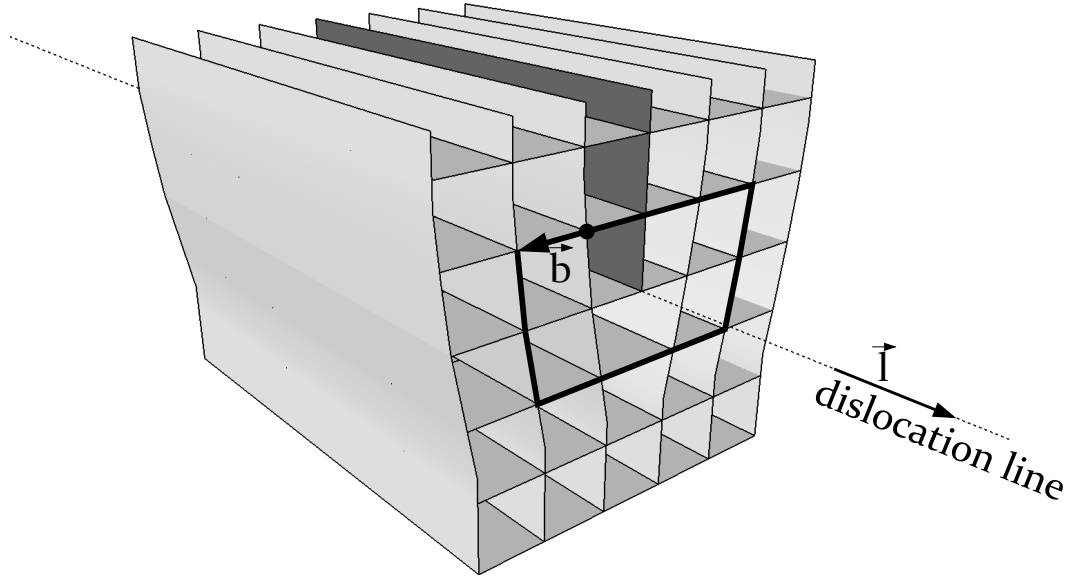


**Figure 1.3:** Edge dislocation in an primitive cubic lattice, including the Burgers circuit [Weertman 70] and the Burgers vector  $\vec{b}$ .

the arrangement of atoms may be described by an additional lattice half plane into the crystal. A screw dislocation (Fig. 1.4) may be created if a crystal is cut and the lattice planes are shifted along the direction of the cut plane and parallel to the dislocation line. The resulting lattice has the spiral form of a screw. Dislocations are characterised by their dislocation line  $\vec{l}$  and their Burgers vector  $\vec{b}$ . Pure edge dislocations have a Burgers vector perpendicular to the dislocation line,  $\vec{b} \perp \vec{l}$ , whereas for screw dislocations the two vectors are parallel,  $\vec{b} \parallel \vec{l}$ . Any dislocation where the relative orientation of  $\vec{b}$  and  $\vec{l}$  is different are called *mixed dislocations* and may be regarded as a superposition of edge- and screw dislocations. The atoms around a dislocation are displaced from the positions of a perfect lattice. The displacement vector field  $\vec{u}(\vec{r}) = (u_1, u_2, u_3)$  is associated with a strain tensor,

$$e_{ij}(\vec{r}) = \frac{1}{2} [u_{i,j}(\vec{r}) + u_{j,i}(\vec{r})] \quad i, j = 1, 2, 3. \quad (1.2)$$

Strain in a solid is associated to a *stress*  $\sigma$  that corresponds for instance to a force applied on a surface. The force, as well as the orientation of the surface, may have three independent components, resulting in nine stress components  $\sigma_{ij}$ . In linear elasticity theory a stress component  $\sigma_{ij}$  in an isotropic solid is linearly correlated to strain  $e_{ij}$  by

$$\sigma_{ij} = 2Ge_{ij} + \lambda e_{ii} \cdot \delta_{ij} \quad i, j = 1, 2, 3 \quad (1.3)$$

where  $\lambda$  and  $G$  are material constants.  $G$  is also known as the *shear modulus*. Another common elastic constant, the *Poisson ratio*  $\nu$  may be expressed as  $\nu = \lambda / (2(\lambda + G))$ .

The presence of a dislocation does not necessarily change the orientation of a lattice plane. An example is shown in Fig. 1.4, where dislocations show no effect on the basal lattice planes. The displacement of the atoms is parallel to the basal planes and their orientation remains unchanged. The misorientation angle  $\alpha(\vec{r}_1, \vec{r}_2)$  expressed by the displacement vectors  $\vec{u}_1, \vec{u}_2$  is

$$\alpha(\vec{r}_1, \vec{r}_2) = - \frac{\vec{n}(\vec{r}_2) \cdot \vec{u}(\vec{r}_2) - \vec{n}(\vec{r}_1) \cdot \vec{u}(\vec{r}_1)}{|\vec{r}_2 - \vec{r}_1|} \quad (1.4)$$

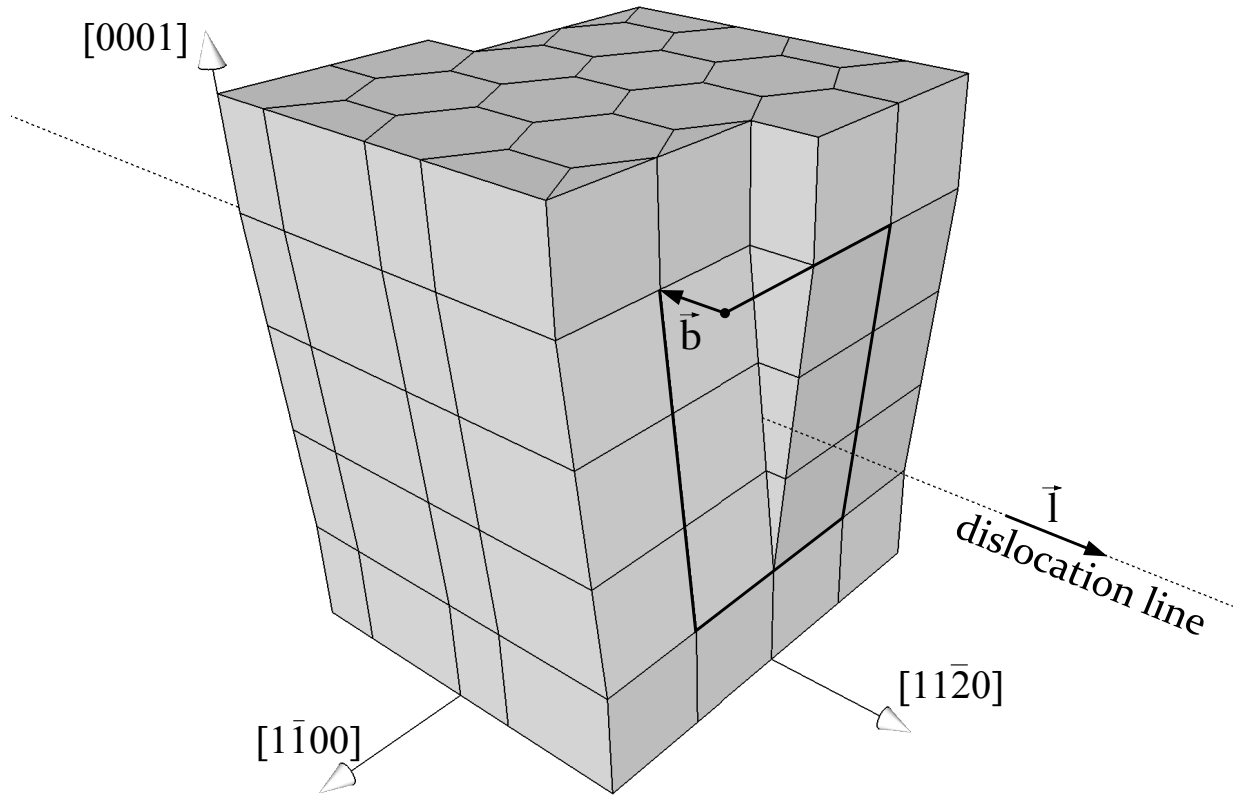


**Figure 1.4:**  $\vec{b} = 1/3\langle 11\bar{2}0 \rangle$  - screw dislocation in the hexagonal lattice; its glide in the basal plane is the major slip system in ice.

where  $\vec{n}$  is the lattice plane normal vector in  $\vec{r}_1$  and  $\vec{r}_2$ . If the atoms are displaced perpendicularly to lattice plane normal vector,  $\vec{n}(\vec{r}) \cdot \vec{u}(\vec{r})$  becomes zero and there will be no lattice plane misorientation.

**Energy of a dislocation:** The lattice distortion due to the presence of a dislocation represents an additive amount of energy that may be calculated for an edge- and for a screw dislocation [Hull 84, Weertman 70]:

$$\begin{aligned} E_{\text{el}}(\text{edge}) &= \frac{Gb^2}{4\pi(1-\nu)} \ln \frac{R}{r_0} \\ E_{\text{el}}(\text{screw}) &= \frac{Gb^2}{4\pi} \ln \frac{R}{r_0} \end{aligned} \quad (1.5)$$

where  $b = |\vec{b}|$  is the norm of the Burgers vector.  $R$  is the radius of a cylindrically formed region around the dislocation. Beyond  $R$  the lattice is regarded as undistorted or the crystal boarder is reached. The radius  $r_0$  describes the boundary between the external, elastically deformed region and the inner core of the dislocation. The values of  $R$  and  $r_0$  are generally unknown. Possible values are the crystal size for  $R$  and  $5b$  for  $r_0$ .

The elastic strain field of a mixed dislocation is the superposition of an edge and a screw component allowing to simply sum up the energy contributions [Hull 84, Weertman 70]:

$$E_{\text{el}}(\text{mixed}) = \frac{Gb^2(1-\nu \cos^2 \theta)}{4\pi(1-\nu)} \ln \frac{R}{r_0} \quad (1.6)$$

where  $\theta$  is the angle between the Burgers vector and the dislocation line.

**Dislocation movement** The movement of dislocations is the major plastic deformation mechanism in crystalline solids [Hull 84]. It occurs inside a crystalline solid when an external stress is applied. Basically two different dislocation motions are possible: *dislocation glide* and *dislocation climb*. In the following the principles of glide are briefly explained. The glide of many dislocations at once is called *slip* and is a major manifestation of plastic deformation in a crystal. The plane on which the dislocations glide is called *slip plane* and normally is a lattice plane with high atomic density [Hull 84]. The slip plane is restricted to planes that contain the dislocation line  $\vec{l}$  and the Burgers vector  $\vec{b}$ . This implies a unique slip plane for the edge component of dislocations, whereas several slip planes for the screw component are possible. The slip plane of a screw dislocation can therefore change during its glide.

A *slip system* consists of the Burgers vector of the dislocation and the slip plane:  $[\vec{b}; (hkil)]$ . To induce a dislocation slip the resolved shear stress must exceed the value of the *Peierls barrier* [Hull 84]:

$$\tau_p \sim \frac{2G}{1-\nu} \exp \left[ \frac{-2\pi d}{b} \right] \quad (1.7)$$

where  $d$  is the lattice spacing distance of the planes perpendicular to the motion direction of the dislocation.

### 1.3 Viscoplastic deformation

As the dislocation energy (Eq. 1.6) is proportional to  $|\vec{b}|^2$ , the dislocations to be mostly found in ice are screw dislocations described by  $\vec{b}_0 = 1/3\langle 11\bar{2}0 \rangle$  [Petrenko 99]. This is also the reason why this dislocation was chosen as an example for a screw dislocation in Fig. 1.4. The dislocation energy  $E_0$  is obtained by putting  $\vec{b}_0$  in Eq. 1.6:

$$E_0 = \frac{Ga^2}{4\pi} \ln \left[ \frac{R}{r_0} \right] \quad (1.8)$$

A value  $G = 3600$  MPa [Sinha 89] and the estimations for  $R$  and  $r_0$  mentioned above lead to  $E_0 \approx 10$  J/m.

Due to the ice lattice geometry the screw dislocations  $\vec{b} = 1/3\langle 11\bar{2}0 \rangle$  will most easily glide on the basal planes. It is known since 1954 [Glen 54] that dislocation slip on the basal plane is by far the main deformation mechanism in ice. Hondoh's experiments [Hondoh 92] show that the basal dislocations in ice glide at very low stress values, according to Duval et al. below 0,01 MPa [Duval 91].

According to Hondoh [Hondoh 00] the Peierls barrier for that slip system is nevertheless  $\tau_p \approx 0,01G = 35$  MPa. An ice crystal loaded by such a stress will instantly crack without deformation, this leading to the conclusion that additional thermal activation is needed to reduce the Peierls barrier. Ice therefore only deforms at high temperatures, close to the water melting point where it behaves similarly to some metals with hexagonal lattice structure at high temperature, such as Ti and Ci [Hull 84].

In polycrystalline ice the amount of slip modes is not sufficient to accommodate a general distortion implying every grain to be able to plastically deform and meet the shape changes imposed by its neighbours. This requires five independent slip systems [Hull 84]. As a result the deformation of ice is strongly anisotropic and deformed polycrystals exhibit complicated strain fields at the grain boundaries and grain triple junctions. The plastic deformation will depend on the relative crystalline orientation of the grains.

## 1.4 Crystalline misorientations

It was already mentioned, that external stress applied on a crystal is associated with an additive amount of elastic strain energy. This energy is generally higher than the energy of a dislocation, this being the reason why an external stress that exceeds certain values creates dislocations inside the crystal. They allow to reduce the elastic energy. The arrangement of

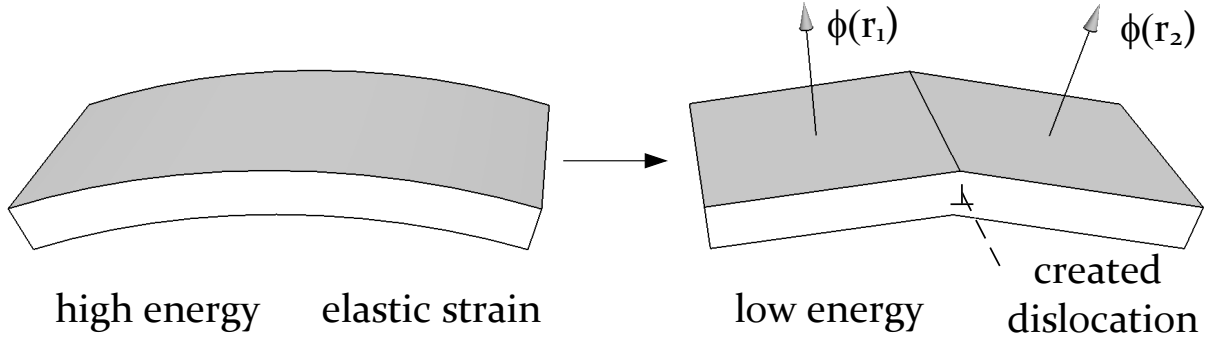


**Figure 1.5:** Creation of a dislocation due to elastic strain; the size of the shown crystal is many orders of magnitude bigger than the length of the Burgers vector.

dislocations in subgrain boundaries may induce variations in the *crystalline orientation*  $\phi$  (Fig. 1.5).

**Crystalline orientation:** A crystalline orientation  $\phi(\vec{r})$  may be described by three linearly independent crystalline directions. For ice those directions could be three basis vectors:

$$\phi(\vec{r}) = \{\vec{a}_1(\vec{r}); \vec{a}_2(\vec{r}); \vec{c}(\vec{r})\} \quad (1.9)$$

The lattice distortions that occur in the early stages of plastic deformation of ice crystals exhibit a long range that is many times larger than the Burgers vector  $\vec{b}$  of an isolated dislocation. We can therefore assume the unit cell geometry to be preserved in the whole crystal and deduce the basis vector  $\vec{a}_2$  by rotating  $\vec{a}_1$  by  $120^\circ$  around  $\vec{c}$ . A crystalline orientation in ice is therefore unambiguously determined by:

$$\phi(\vec{r}) = \{\vec{a}_1(\vec{r}); \vec{c}(\vec{r})\} \quad (1.10)$$

A difference in the crystalline orientation between two regions  $\vec{r}_1, \vec{r}_2$  is called *crystalline misorientation*. It may be described as a 3D rotation  $R_\alpha^{\vec{q}}$  by an angle  $\alpha(\vec{r}_1, \vec{r}_2)$  around an axis  $\vec{q}(\vec{r}_1, \vec{r}_2)$  (Fig. 1.6):

$$\left[ R_\alpha^{\vec{q}} \right] \phi(\vec{r}_1) = \phi(\vec{r}_2) \quad (1.11)$$

It is an important aspect that a misorientation is relative and compares the orientations of two different regions of the crystal. In practice a reference lattice orientation  $\phi_{\text{ref.}}$  is chosen and the misorientation of any region  $\vec{r}$  is totally described by the rotation:

$$\left[ \mathcal{R}_\alpha^{\vec{q}}(\vec{r}) \right] \phi_{\text{ref.}} = \phi(\vec{r}) \quad (1.12)$$

$\phi(\vec{r})$  depends on the chosen reference orientation  $\phi_{\text{ref.}}$ , but the relative misorientation between two orientations as it is expressed by Eq. 1.11, is independent from the chosen reference.

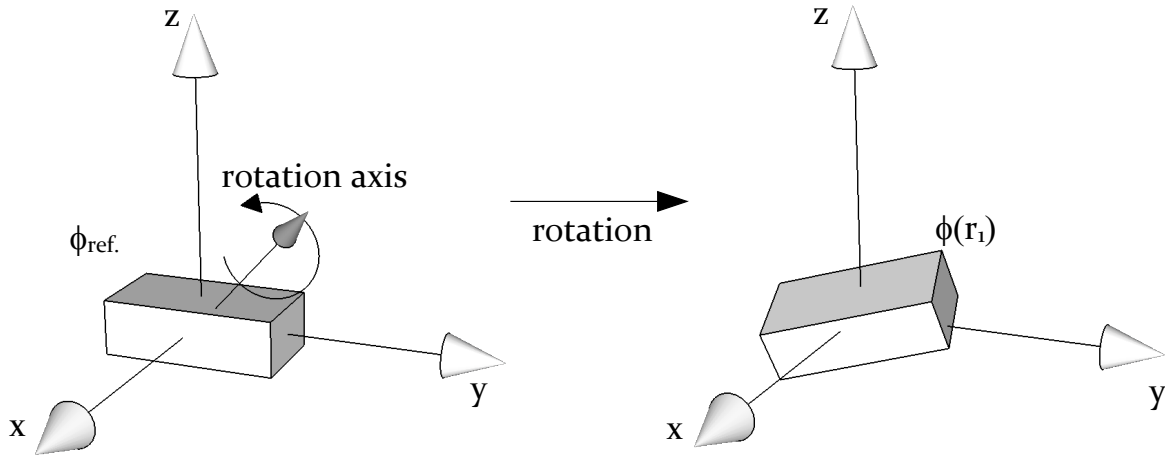


**Figure 1.6:** Crystalline misorientation described by a single rotation in 3D.

**Decomposing misorientation** Any crystalline orientation  $\phi(\vec{r})$  may be obtained by one single rotation  $\mathcal{R}_{\alpha}^{\vec{q}}(\vec{r})$  (Eq. 1.12). The direction of the rotation axis  $\vec{q}$  changes depending on the misorientation. This is an issue because experimental procedures only measure misorientations around a well defined axis. For example rocking curve imaging only measures misorientations around the rocking axis (Chap. 2.3.2). In order to match to an experimental method, it may be useful to decompose  $\mathcal{R}_{\alpha}^{\vec{q}}(\vec{r})$  in several rotation components. Each of these components is associated with a misorientation around an axis that is experimentally measured. A possible decomposition, which applies in particular when the angles are small, could be into rotations around the axis of the coordinate system (Fig. 1.7):

$$\mathcal{R}_{\alpha}^{\vec{q}} \approx \mathcal{R}_{\alpha_z}^{\vec{z}} \mathcal{R}_{\alpha_y}^{\vec{y}} \mathcal{R}_{\alpha_x}^{\vec{x}} \quad (1.13)$$

Although a decomposition may be necessary for experimental reasons it introduces a math-

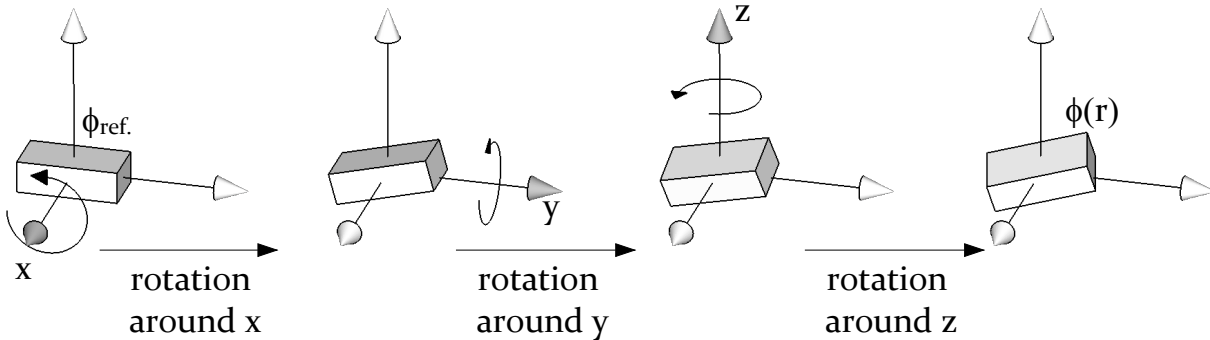


**Figure 1.7:** Decomposition of a misorientation in three rotations along the axis of the coordinate system (Eq. 1.13); the decomposed misorientation is the one presented in Fig. 1.6.

ematical problem: rotations in a 3D space are not commutative:

$$\mathcal{R}_{\alpha_1}^{\vec{q}_1} \mathcal{R}_{\alpha_2}^{\vec{q}_2} \neq \mathcal{R}_{\alpha_2}^{\vec{q}_2} \mathcal{R}_{\alpha_1}^{\vec{q}_1} \quad (1.14)$$

Logically the crystalline orientations that are obtained by applying the decomposed rotations on the reference will depend on their order. However infinitesimal rotations in 3D space are commutative [Stephani 95]. Calculations (Chap. C) show that the errors that occur

due to a permutation of the rotation components are negligible for the misorientations that we measure.

After decomposing the single rotation that represents a crystalline misorientation into rotations around the axis of the coordinate system, we obtain three angular misorientation components  $\alpha_x$ ,  $\alpha_y$  and  $\alpha_z$ . They are shown in Fig. 1.8.

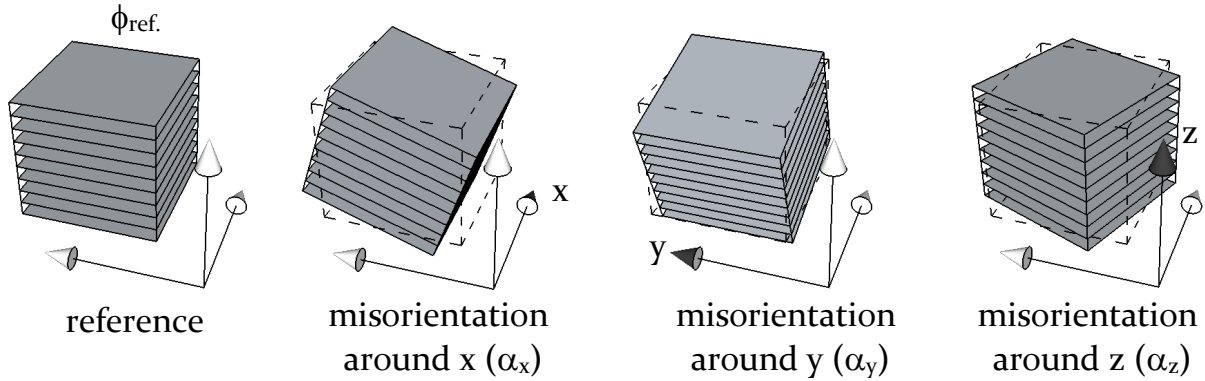


**Figure 1.8:** A reference orientation and the three misorientation components introduced in Eq. 1.13.

**Curvature tensor** As already mentioned the absolute misorientation in a point  $\vec{r}$  depends on the chosen reference orientation (Eq. 1.12), whereas the relative misorientation between two points  $\vec{r}_1$  and  $\vec{r}_2$  does not. This is why relative misorientations are the best experimental way to access the physical properties of a crystal. If for example a crystal is differently oriented in space and the reference orientation remains unchanged, then the absolute misorientations change although the crystal properties do not. A possibility to describe relative misorientations in a crystal is given by Eq. 1.11. They may also be described by the *Riemann curvature tensor*  $K$ . The curvature tensor  $K_{ij}(\vec{r})$  is calculated on the rotation vector field [Kobayashi 96]:

$$K_{ij}(\vec{r}) = \frac{\partial \theta_i}{\partial r_j} = \theta_{i,j} \quad i, j = 1, 2, 3 \quad (1.15)$$

The rotation vector  $\vec{\theta}$  describes a rotation in an equivalent way as the rotation matrix. Its direction is parallel to the rotation axis and its length is the rotation angle. Calculations in Chap. D derive a mathematical relation between a general rotation matrix and the rotation vector.

As in the experiment only misorientation angles around the three axis of the coordinate system are measured, we need a mathematical correlation of those angles to the components of the curvature tensor. The calculations for “small” misorientations are presented in the Chapters C and D. The obtained result is:

$$K_{ij}(\vec{r}) = \alpha_{i,j} \quad i, j = 1, 2, 3 \quad (1.16)$$

The formula will be necessary to derive the curvature tensor components out of relative misorientations.

## 1.5 Lattice distortions and dislocation density

The idea of dislocations that change the crystalline orientation (Fig. 1.5) of a solid may be extended to a mathematical relationship that correlates the curvature tensor with the amount

of dislocations [Nye 53].

**Dislocation density tensor:** In the same way as for a single dislocation an *effective Burgers vector*  $\vec{B}$  can be defined when the Burgers circuit encloses several dislocations. The effective

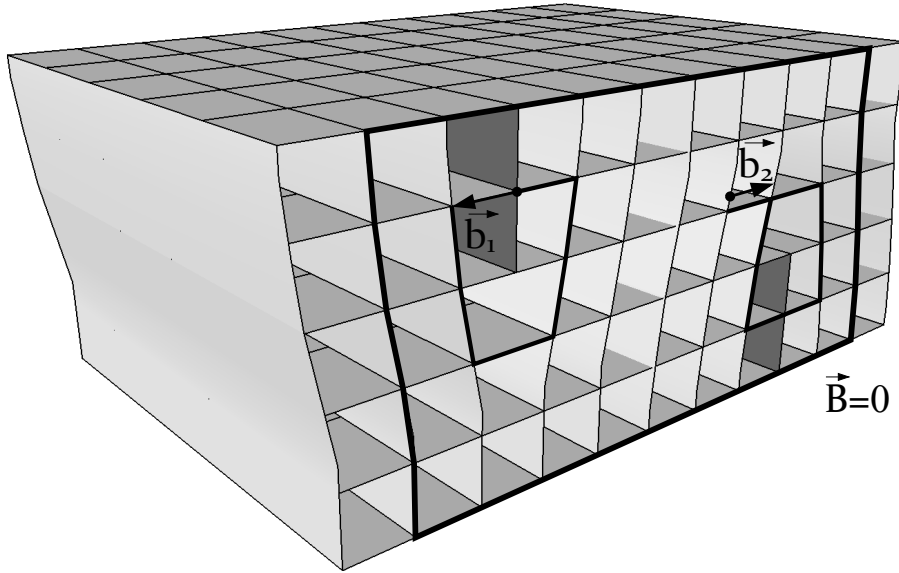


**Figure 1.9:** Effective Burgers vector for two sign-opposed edge dislocations.

ive Burgers vector may be zero although there are dislocations whose Burgers vector go through the Burgers circuit (Fig. 1.9). When deducing a formula for  $\vec{B}$  we suppose the effect of a dislocation to be homogeneous over the area enclosed by the Burgers circuit. This is mathematically expressed by a diverging dislocation number  $n \rightarrow \infty$  and a Burgers vector  $|\vec{b}| \rightarrow 0$  [Hull 84, Nye 53]. The effective Burgers vector is then defined as:

$$B_i(\vec{r}) = \int_A \alpha_{ij}(\vec{r}) n_j dr \quad i, j = 1, 2, 3 \quad (1.17)$$

where  $n_j$  are the components of the normal vector of the surface enclosed by the Burgers circuit.  $\alpha_{ij}(\vec{r})$  is Nye's dislocation density tensor, a full description of the geometrically necessary dislocation density (see the following paragraph). The components  $\alpha_{ii}$  represent the screw components of the dislocations along the directions of the coordinate system, whereas the other six describe the edge components.

**Geometrically necessary dislocations** The distortion associated to two dislocations may be cancelled out if the lattice bending is in the opposite sense (Fig. 1.9). Under the conditions that the effect of a dislocation is averaged over the volume, the lattice distortion in crystal-lite shown in Fig. 1.10 would be zero. Such dislocations are called *statistical dislocations*. Their presence cannot be revealed by lattice distortion measurements. The dislocations that are needed to accommodate the lattice curvature are called *geometrically necessary* [Nye 53, Ashby 70]. A relationship between lattice distortions and the density of geometrically necessary dislocations is proposed by Nye (Fig. 1.11). A cross section area  $A$  of an initially undistorted crystal (Fig. 1.11) with the dimensions  $A = h \cdot L$  is curved into a curvature Radius  $R$  due to the presence of  $n$  geometrically necessary dislocations. They exhibit the same geometry and are described by the same Burgers vector  $\vec{b}$ . The opening angle  $\theta$  of

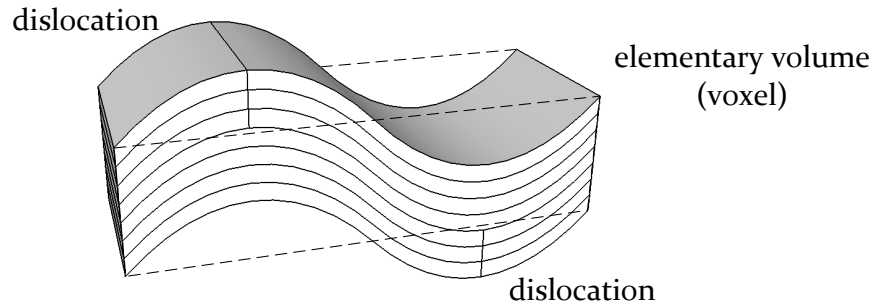


**Figure 1.10:** Statistical dislocations: the lattice curvature is cancelled out and no overall lattice distortion occurs.

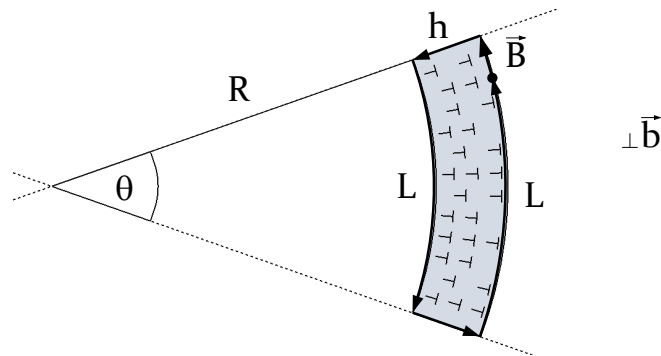


**Figure 1.11:** Lattice curvature due to geometrically necessary dislocations; a geometrically necessary dislocation density may be correlated to the curvature Radius  $R$ .

the curvature can be calculated by  $\theta = L/R$  or by  $\theta = (L + B)/(R + h)$  what gives:  $B = \theta h$ . We define  $\rho$  as the amount  $n$  of the geometrically necessary dislocations divided by the area of the Burgers circuit:

$$\rho = \frac{n}{A} = \frac{B}{b} \frac{1}{hL} = \frac{\theta}{bL} = \frac{1}{Rb} \quad (1.18)$$

The equation associates the density of geometrically necessary dislocations with the lattice curvature. An approach that respects the 3D geometry of the crystal and different dislocation types, as well as direction correlates the dislocation density tensor and the curvature tensor [Kröner 55, Pantleon 08]:

$$\alpha_{ij} = K_{ji} + \delta_{ij}K_{mm} \quad (1.19)$$

The equation allows to calculate all components of Nye's tensor in crystal out of the curvature tensor.

## CHAPTER 2

# X-ray physics

The following chapter describes the basics about the physics of X-rays, that are necessary to understand our experimental procedure.

## 2.1 X-ray generation

There are basically two types of man-made apparatus dedicated to X-ray generation: the X-ray tube and the Synchrotron. They will be briefly described.

### 2.1.1 X-ray tube radiation

The first X-rays, discovered by Wilhelm C. Röntgen in 1899, were generated by a X-ray tube. Its assembly (Fig.2.1) consists of a high voltage source that generates an electric field in a vacuum tube. That field is strong enough to free electrons from the cathode and accelerate them towards the anode where they collide and emit X-rays. The applied voltage is typically in the range of 10 to 100 kV and the electron current may reach 500 mA. The spectrum of a X-ray tube is composed of two parts: the Bremsstrahlung and the characteristic spectrum.

**The Bremsstrahlung** is generated when the electrons collide on the anode and drastically get slowed down due to interaction with atoms. The electron deceleration (negative acceleration) results in an emitted electro-magnetic field and is the origin of the Bremsstrahlung. Its characteristics depend on the voltage  $U$  between cathode and anode and the amount of electrons that collide on the anode. The maximal photon energy, the so called cut-off energy of the Bremsstrahlung, is achieved when the entire kinetic energy  $E_{\text{kin}}$  of one electron is transformed in one X-ray photon. The minimal wavelength  $\lambda_{\text{min}}$  therefore can be calculated by  $E_{\text{kin}} = E_{\text{ph}} \Leftrightarrow Ue = hv \Leftrightarrow \lambda_{\text{min}} = h \cdot c / Ue$ . Here,  $h$  is the Planck-constant,  $c$  the speed of light in the vacuum and  $e$  the elementary charge of an electron. Towards longer wavelengths the spectrum of the Bremsstrahlung is continuous and approximately constant in intensity.

**The characteristic spectrum** consists of sharp peaks at a given wavelength  $\lambda$ , where it is orders of magnitude more intense than the Bremsstrahlung. It is generated when electrons, that impinge on the anode, have enough kinetic energy to ionise bounded electrons in the anode material. This process creates vacancies in the atomic electron configuration that are refilled by electrons from the outer shells. Their energy loss is transformed into a X-ray photon that contributes to the characteristic spectrum. The wavelength positions of the X-ray peaks are characteristic for the anode material because the electron binding energy is specific for each element.

The generation of X-rays in a X-ray tube has drawbacks and limitations. The emitted electromagnetic field has the shape of a dipole field that is approximately isotropic in space. Logically there is no collimation of the emitted X-rays and the achieved intensities at the

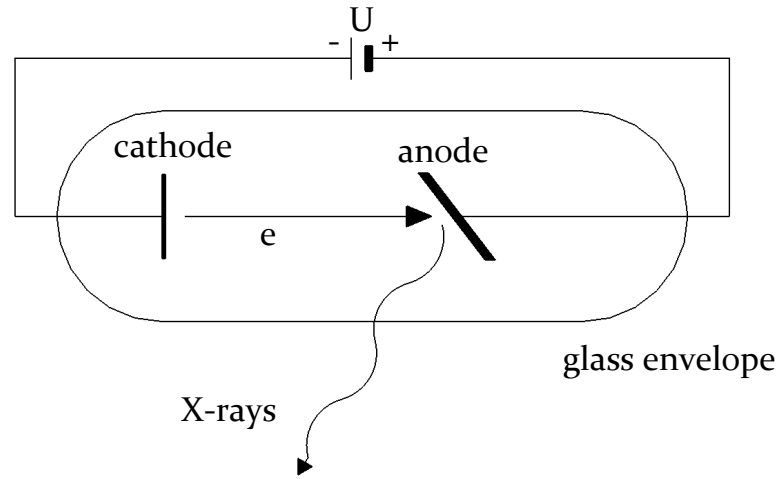


Figure 2.1: Schematic diagram of a X-ray tube

sample position are rather low. Although the intensity is proportional to the electron current there are technical limitations to evacuate the heat on the anode that also increases with a higher current. Almost 99% of the electron energy is transformed into heat.

### 2.1.2 Synchrotron radiation

X-rays generation by a synchrotron is based on the same physical effect as the generation of the Bremsstrahlung by a X-ray tube: acceleration of charged particles provokes the emission of an electromagnetic field. The main difference lies in the electron speed. X-ray tubes accelerate electrons up to 100 keV whereas in a synchrotron, dedicated to generate X-rays (3rd generation X-ray sources), they are accelerated up to several GeV. An accelerated charge emits a dipole field if seen from the moving frame of the charge. For slowly moving electrons ( $v \ll c$ ), e.g. in a X-ray tube, the emitted field has the same shape when seen from the laboratory frame. However when relativistic effects become stronger, the radiation observed from the laboratory frame is confined in a narrow cone as is shown in Fig.2.2. According to Jackson [Jackson 98], the light emitted into a solid angle  $\theta'$  in the moving frame of the electrons is observed in the laboratory frame in a solid angle  $\theta$ . They are correlated by

$$\tan \theta = \frac{\sin \theta'}{\gamma(\beta + \cos \theta')} \quad (2.1)$$

where  $\beta = v/c$  and  $\gamma$  is the inverse Lorentz root,  $\sqrt{1 - v^2/c^2}$ . For relativistic electrons  $\beta \approx 1$  the radiation emitted in  $\theta' = 90^\circ$  is confined in the laboratory frame into

$$\theta = \frac{1}{\gamma} \quad (2.2)$$

the typical opening angle of synchrotron radiation. Therefore the faster the electrons are, the smaller the opening angle of the radiation will be, what makes out of a synchrotron a much stronger X-ray source than a tube, even if the electron current may be smaller.

At the ESRF the electrons get accelerated in two steps up to  $E_{\text{kin}} = 6 \text{ GeV}$ . After the acceleration process they get injected into a storage ring, where their energy is only maintained but not longer increased. The storage ring consists of several straight and circular sections that form a symmetric polygon. In every circular section an electromagnet, the so called bending magnet, generates a homogeneous magnetic field  $\vec{B}$  with field lines vertical to the

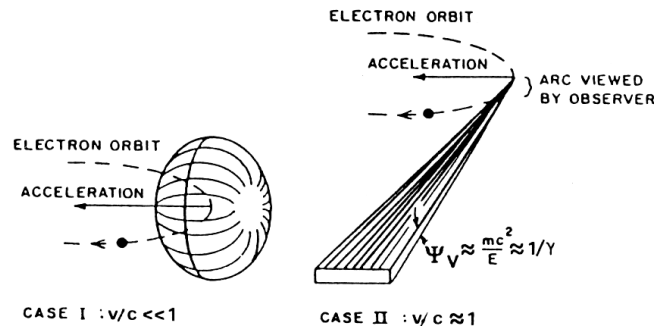


**Figure 2.2:** Radiation of a non-relativistic and relativistic particle [Winick 81].

moving direction of the electrons. When the electrons traverse  $\vec{B}$  at a velocity  $\vec{v}$ , they are deviated into a circular motion by the Lorentz force  $\vec{F}_L = e\vec{v} \times \vec{B}$ . From the physical point of view a circular motion corresponds to a permanent acceleration perpendicular to the moving direction that will cause the electrons to emit an electromagnetic field. The spectrum emitted by a bending magnet source is continuous and covers the range from the far infrared to the hard X-ray region, which is the reason why it is called "white beam". According to Als-Nielsen [Als-Nielsen 01] the maximum in intensity is obtained for a characteristic photon energy

$$E_{char} = \hbar \frac{3}{2} \gamma \omega_0 \quad (2.3)$$

where  $\omega_0$  is the electron circular frequency inside the storage ring. Eq. 2.3 results in  $E_{char} = 20,6$  keV for electrons at 6 GeV and a magnetic field of  $B = 0,85$  T, the parameters at the ESRF. The electrons emit X-rays all their way through the magnetic field as shown in Fig.2.3. Therefore the source as it is seen by the sample (virtual source) has a higher angular divergence along the horizontal direction.

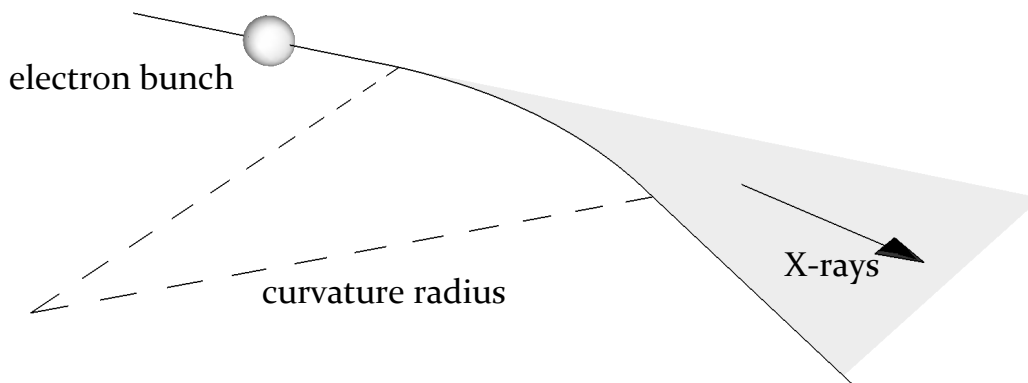


**Figure 2.3:** Electron bunch trajectory through a circular section of the storage ring and the emitted X-rays.

Beside the bending magnets the so called insertion devices (IDs) can be positioned in the straight sections of the storage ring. A 3rd generation synchrotron source actually is designed for IDs that generate a more powerful beam than a BM does. In the IDs the electrons traverse an array of magnetic fields with alternating polarity, generated by permanent magnets. Since they oscillate in the horizontal plane, their trajectory can be considered as a series of arcs, turning to the right and left Fig. 2.4. In each arc they emit X-rays that superpose and generate a more intense beam. There are basically two types of IDs: wigglers and undulators. In a wiggler the magnetic fields are larger and the electrons go through

wider arcs. The wiggler can be considered as a serial connection of bending magnets. The emitted X-rays will have the same spectrum as if they were emitted by a bending magnet, but a  $N \times$  higher intensity, where  $N$  is the number of arcs the electrons go through. In an undulator electrons go through a higher amount of oscillations but with a smaller amplitude. Undulators provide higher beam intensities but only for defined energies. Their spectrum is no longer continuous but composed of a broader peak around a fundamental frequency, followed by peaks at higher harmonics. Since ID sources were not used in our experiments, they are only briefly presented in this work.

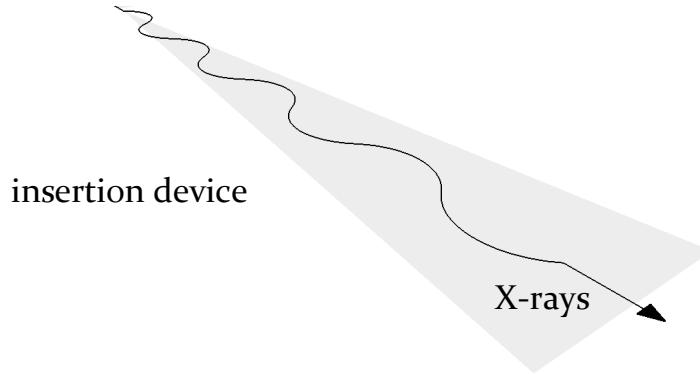


**Figure 2.4:** Electron bunch trajectory through an ID in a straight section of the storage ring and the emitted X-rays.

## 2.2 X-ray diffraction topography

X-ray diffraction topography is an imaging technique based on elastic X-ray scattering on crystalline material (Bragg diffraction). A X-ray beam with a wavelength  $\lambda$  that is impinging on a crystal is “Bragg diffracted” by an angle  $2\theta_B$ , if the following equation (the Bragg equation) is fulfilled:

$$\lambda = 2d_{hkl} \sin \theta_B \quad (2.4)$$

Here  $d_{hkl}$  is the inverse of the length of the diffraction vector  $\vec{h}_{hkl}$  in the reciprocal space. In other words, the beam is diffracted when the angle opened by the incoming beam and the crystal lattice planes (typically called  $\omega$ ) fulfils the Bragg equation,  $\omega = \theta_B$ . The Bragg equation is the scalar expression of the Laue equation that can be written as

$$\vec{k}_0 - \vec{k}_h = \vec{h}_{hkl}, \quad (2.5)$$

where  $\vec{k}_0$  and  $\vec{k}_h$  are the incident and the Bragg diffracted wave vectors. These two vectors form a mathematical basis of the *diffraction plane*. The diffraction vector  $\vec{h}_{hkl}$ , a linear combination of  $\vec{k}_0$  and  $\vec{k}_h$ , lies in the diffraction plane as well.

Beside X-ray diffraction topography, a series of techniques to determine crystal structures are based on Bragg diffraction. They gather information from the angular position and the intensity of the Bragg diffracted beam. X-ray diffraction topography additionally takes into account the contrast inside a single Bragg diffraction spot and visualises imperfections in the crystalline structure. In contrast to radiographic methods that image the directly transmitted beam, X-ray diffraction topography uses the parts of the beam that are Bragg diffracted by the sample.

For platelet shaped samples a distinction between two experimental geometries has been established: the Bragg geometry, where the diffracted beam exits the crystal on the same surface as the direct beam enters and the Laue geometry, where the diffracted beam exits the crystal on the opposite surface. Fig. 2.5 shows the two geometries. In the case of nearly perfect crystals the Bragg geometry is sensitive to a defined sample depth equal the extinction length (Chap. 2.2.1). The Laue geometry reveals the whole thickness of the sample. The

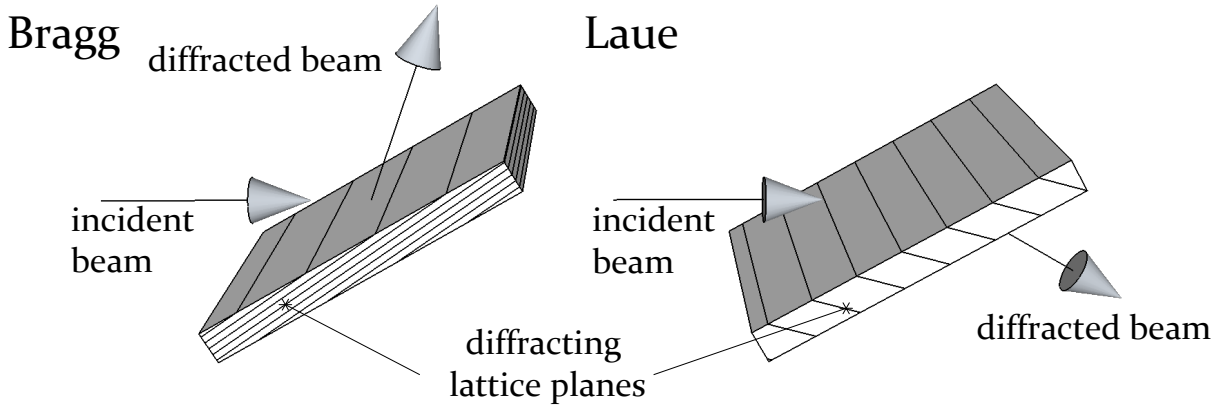


**Figure 2.5:** The two possible experimental geometries in X-ray diffraction topography: Bragg case (left) and Laue case (right)

diffracted beam is recorded on a X-ray sensitive film or by a digital camera. The obtained results are Bragg diffracted 2D images of the crystal. The lattice defects in the crystal produce long range fields that deform the lattice structure and lead to variations in the diffracted intensity or the propagation direction of the diffracted beam. Consequently intensity inhomogeneities in a Bragg diffraction image (contrasts) appear and allow conclusions about the crystalline quality. Basically three different contrast mechanisms are distinguished: contrast, orientation contrast and extinction contrast, where the last one is related to the dynamical diffraction theory (Chap. 2.2.1).

### 2.2.1 Elements of dynamical diffraction theory

In Chap. 2.2 X-ray Bragg diffraction was only introduced through Bragg's law based on geometrical considerations. No re-diffraction of an already diffracted wave has been taken into account (kinematical approximation) [Authier 01]. This neglects any interaction of the incident beam with the Bragg diffracted one. For thin crystals or crystals with low crystalline quality where the coherence of the beam rapidly decreases in the crystal, the kinematical theory, see for instance into the book of the HERCULES courses [Baruchel 93], sufficiently describes the spatial distribution of the Bragg diffracted intensity. Yet there are no predictions about the shape of a Bragg peak and its width: the Bragg equation only gives the angular position of the maximally diffracted intensity. Many further observations can only be explained by multiple X-ray scattering inside the crystal and differences in the refractive index  $n$  between the crystal material and its environment. The so called "dynamical diffraction theory" takes these aspects into account by resolving the Maxwell equations for a periodic structure. The approximations in the dynamical theory, still necessary to analytically resolve the equations, are weaker than those in the kinematical theory. The concept of a wavefield propagating inside the crystal is introduced. Contrarily to the kinematical approximation, in the dynamical diffraction theory the system energy is conserved. The domain of dynamical diffraction theory is too vast to be described in detail in this work. The interested reader

may have a look into [Authier 01, Batterman 64, Härtwig 01]. In the following part some dynamical effects that are of interest for the present thesis will be described.

**Darwin width:** The width of the Bragg diffraction peak may be quantified with the help of the dynamical diffraction theory. The reflectivity curve in the symmetric Bragg case (Fig. 2.5) has the shape of a “top hat”, where the entire intensity of the incident beam is Bragg diffracted if the crystal is thick enough and no absorption is taken into account. The

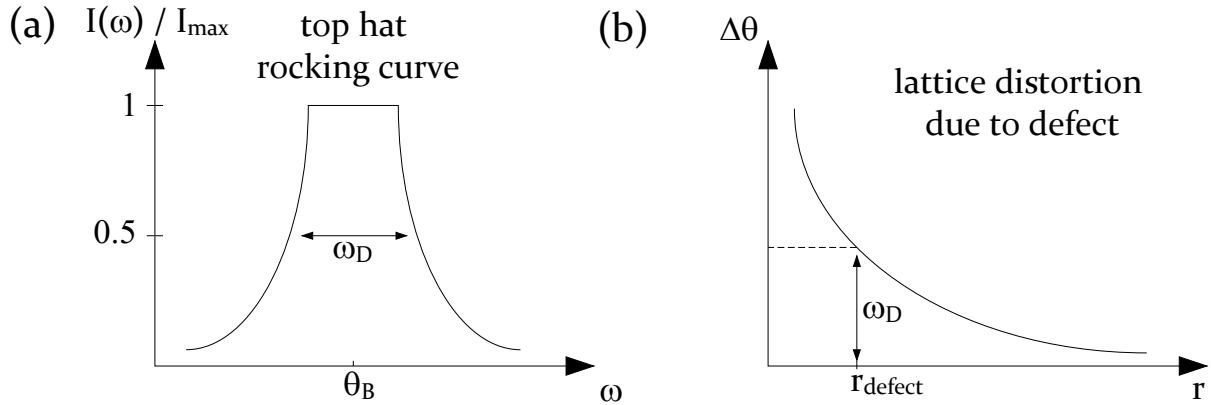


**Figure 2.6:** (a) shape of the reflectivity curve in the symmetric Bragg case; (b) correlation between the lattice plane distortion induced by a defect and its image size.

Darwin width  $\omega_D$  is the FWHM of the reflectivity curve (Fig. 2.6a) and calculated by

$$\omega_D = \frac{2\lambda^2 |F_{hkl}| r_0 P}{\pi V_c \sin 2\theta_B} \quad (2.6)$$

where  $V_c$  is the volume of the unit cell of the crystal structure,  $\lambda$  the wavelength,  $|F_{hkl}|$  the absolute value of the structure factor (Eq. 2.8),  $P$  is the polarisation factor and  $r_0$  the classical electron radius,  $r_0 = 2.81 \cdot 10^{-15}$  m. Eq. 2.6 also applies to the symmetric Laue case, where it provides the intrinsic width of the Bragg diffraction rocking curve. Due to the dependency on the structure factor, there is a general tendency of the rocking curves to become narrower, the higher the order  $h + k + l$  of the diffraction.

**Borrmann triangle:** Fig. 2.7 shows a further phenomenon that can be explained with dynamical diffraction effects. When the size of the incident beam is reduced along one direction down to a few micrometres (section beam), intensity modulations in the Bragg diffraction image may appear under the condition that the crystal exhibits a high crystalline quality. As before the incoming wave is diffracted multiple times inside the crystal, resulting in interfering wavefields (Fig. 2.8). For an incident beam with a spherical wavefront, the wavefields spread out in the so called Borrmann triangle (Fig. 2.7), leading to intensity modulations on the detector. Those intensity modulations attest a high crystalline quality. Lattice distortions perturb the periodicity of the crystal and modify the interference image on the detector, as seen in Fig. 2.8, where the basal Bragg diffraction image of a ice single crystal is shown. The incident beam is composed of six 50  $\mu\text{m}$  thick sections. Each section generates its own Bragg diffraction image. The crystal exhibits lower quality on the surfaces and on the edges, where the intensity modulation disappears. Crystal defects as seen for instance in the right part of the fourth section, perturb the interference.

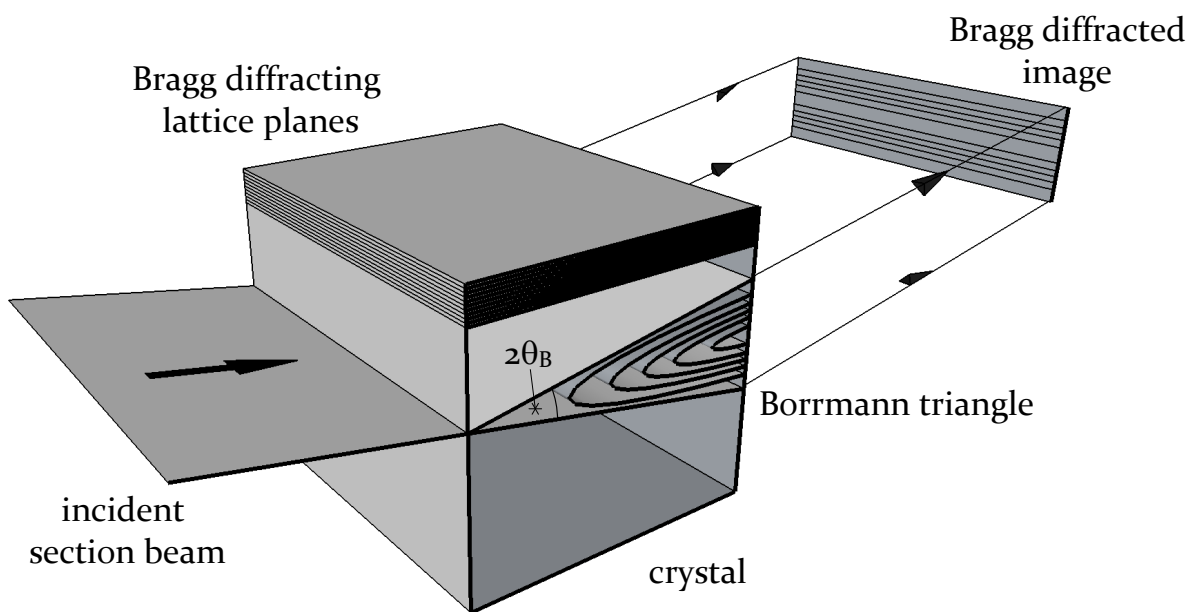


**Figure 2.7:** The formation of the Borrmann triangle in the crystal and the contrast on the detector.

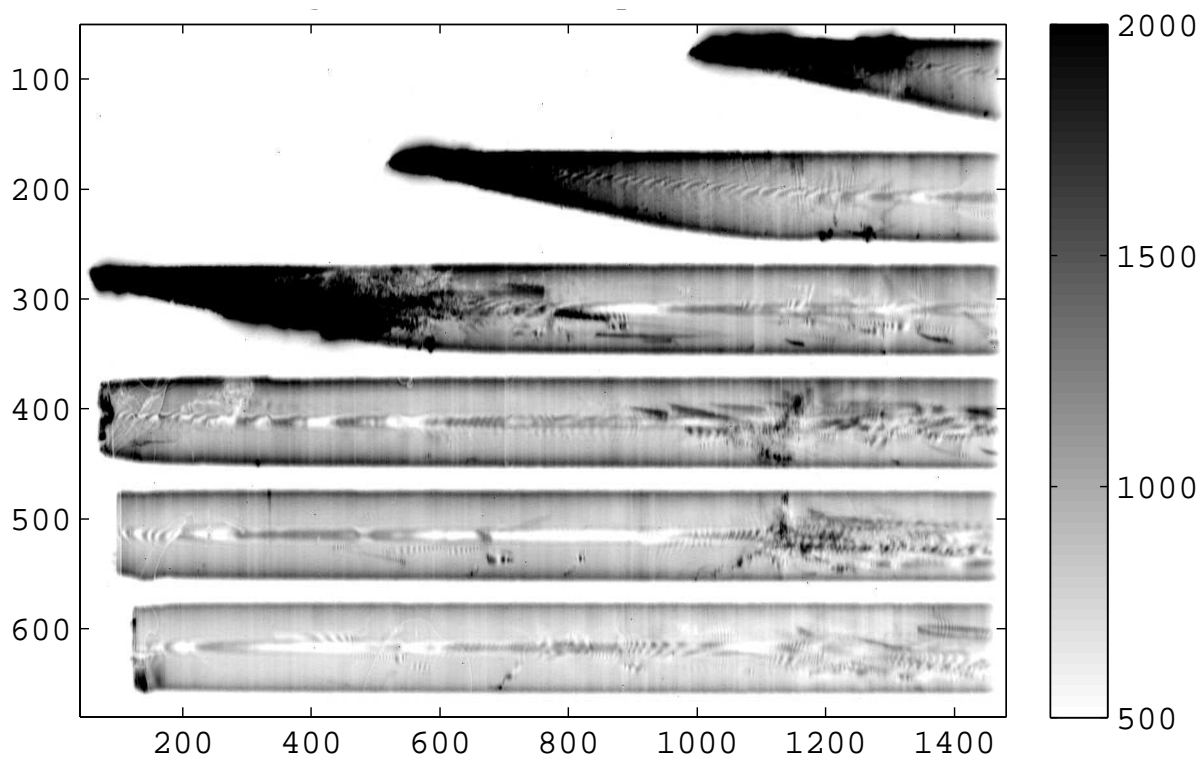


**Figure 2.8:** Borrmann triangle in a basal Bragg diffraction of a 4 mm thick ice single crystal; illuminated with a  $50\ \mu\text{m}$  thick monochromatic beam -  $E_{\text{ph}} = 18\ \text{keV}$ ; axis scaling in pixels - pixelsize  $10\ \mu\text{m}$

**Equal thickness fringes** The formation of the so called *Pendellösung*- or *equal thickness fringes* can be explained by dynamical diffraction effects inside the crystal matrix [Authier 01]. Pendellösung fringes arise from an interaction of two coupled wavefields, that interchange their energy, similar to a coupled pendulum. As result the energy is bouncing inside the crystal with the frequency of the Pendellösung length  $\Lambda_0$ . The length for the symmetrical Laue case (Fig. 2.5) is calculated by

$$\Lambda_0 = \frac{\pi V_c \cos \theta_B}{\lambda |F_{hkl}| r_0} \quad (2.7)$$

Equal thickness fringes are sensitive to crystal distortions. Their modification is one of the first indications for imperfections in the crystal and their presence attest a generally high crystal quality [Kato 66, Hart 66, Ando 66].

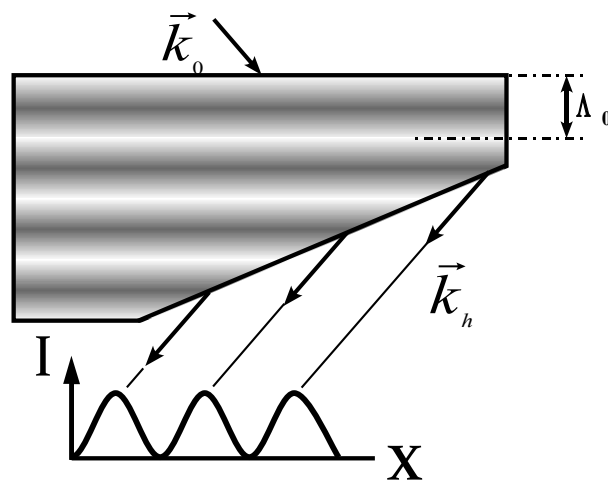


Figure 2.9: Energy bouncing inside a wedge shaped crystal.

## 2.2.2 Contrast mechanisms

**Structure factor contrast** The intensity of a Laue spot ( $hkl$ ) depends on its structure factor  $F_{hkl}$  defined by

$$F_{hkl} = \sum_{i=1}^n f_i \cdot \exp \left[ j \vec{r}_i \cdot \vec{h}_{hkl} \right], \quad (2.8)$$

where  $f_i$  is the scattering power of the atom situated in  $r_i$  of the unit cell and  $\vec{h}$  is the diffraction vector (Eq. 2.5). The scattering power  $f_i$  of an atom depends on the electron distribution in its electron shells and the scattering direction. The atomic scattering values for X-ray scattering are tabulated in the international tables for crystallography [Hahn 95]. The diffracted intensity is proportional to  $|F_{hkl}|^2$  if the kinematical diffraction theory applies. Differences in modulus of  $F_{hkl}$  (twin crystals) can therefore be imaged. In addition when using a spatially coherent beam the phase of  $F_{hkl}$  is accessible as well and phase shifts induced for instance by ferroelectric domains can be measured [Rejmánková-Pernot 98].

**Orientation contrast** The orientation contrast is described on Fig. 2.10, that shows differently oriented regions. These misorientations directly change the angle between the lattice planes and the incoming beam wave vector (Bragg angle  $\theta_B$  in Eq. (2.4)). If the incoming beam spectrum  $\lambda \pm \Delta\lambda$  is broad enough, then differently oriented regions will diffract at

the same time (Fig. 2.10(a)). However the propagation direction of the diffracted beams will be different so that they can overlap or spread out on the detector plane what results in a visible contrast. Alternatively the beam spectrum can be too narrow so that the Bragg equation (Eq. 2.4) is not fulfilled for some regions (Fig. 2.10(b)). Such a crystallite does not diffract X-rays and an intensity loss on the detector is registered. The first *polychromatic* case applies in particular to white beam X-ray diffraction topography (Chap. 2.3.1), the second *monochromatic* case appears in rocking curve imaging (Chap. 2.3.2).

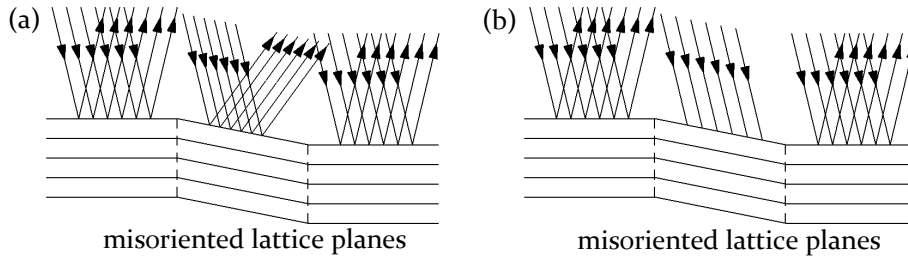


**Figure 2.10:** Orientation contrast: (a) wavelength acceptance of the crystal is bigger (a) or smaller (b) than beam spectrum.

**Dynamical diffraction contrast** Under special conditions different types of image may occur that are explained by the perturbation of the standing wave in the crystal. First of all the so called **direct image** of a defect that occurs in crystals exhibiting low absorption to X-rays (low absorption case). The Darwin width is often in the range of a few arcseconds. The incident beam exhibits a wavelength range  $\Delta\lambda$  and a divergence angle due to dispersive effects (Chap. A), what allows to orient the crystal in an angular interval  $\Delta\omega$  in order to Bragg diffract the incident beam. That interval is up to a hundred times bigger than the Darwin width [Baruchel 93]. We say that the angular acceptance of the crystal is smaller than what is offered by the incident beam. Therefore many components of the incident beam are transmitted through the crystal without being diffracted. Now the presence of a defect in the crystal is associated with a distortion field in the surrounding region. That region is in Bragg position for wavelength components that do not participate to the diffraction in the perfect crystal. As a result an additional amount of Bragg diffracted intensity is obtained. The size of the direct image depends on the Darwin width and on the distortion field associated to the defect (Fig. 2.6b) [Miltat 75].

A different image formation appears when the material's absorption is not negligible. The X-rays get absorbed in the crystal with the exception of the wavefields that form a standing wave (Fig. 2.9) within the crystal. The effect is known as *anomalous absorption* or *Borrmann effect*. When absorption is very strong ( $\mu t > 10$ ) the anomalous transmission generates the major part of the transmitted beam. Now a defect in the crystal disturbs the periodicity of the atoms and displaces the anchor points of the standing wave. The Borrmann effect is in this case suppressed. That **dynamical image** is characterised by defects exhibiting a lower intensity than the perfect crystal matrix. In general both, the direct image and the dynamical one coexist.

### 2.2.3 Bragg diffraction in ice

In most of our experiments a monochromatic beam,  $E = 18 \text{ keV}$  was used to perform basal 0002 and 1st order prismatic ( $1\bar{1}00$ ) Bragg diffraction. The Bragg angles are  $\theta_B(0002) = 5.38^\circ$

for the basal and  $\theta_B((1\bar{1}00)) = 5.06^\circ$  for the 1st order prismatic planes. From atomic form factors  $f_{O^{2-}}$  for an  $O^{2-}$  ion [Hahn 95] and the crystal repeating unit of ice (Eq. 1.1) we obtain the modulus values of the structure factor  $\|F_{hkl}\|$  for the two Bragg reflections 0002 and  $1\bar{1}00$  that we mostly used (Tab. 2.1). For the discussion of our results, the Darwin width  $\omega_D$  and the Pendell'osung length  $\Lambda_0$  of the concerning Bragg diffraction images are useful, and are presented Tab. 2.1.

hkil	$\ F_{hkl}\ /f_{O^{2-}}$	$\ F_{hkl}\ $	$\omega_D$ [arcsec.]	$\Lambda_0$ [ $\mu\text{m}$ ]
0001	0	0	-	-
0002	2.82	21.5	1.53''	98 $\mu\text{m}$
$1\bar{1}00$	3.06	22.6	1.74''	93 $\mu\text{m}$

**Table 2.1:** Bragg diffraction properties of some lattice planes in ice,  $f_{O^{2-}}$  is the scattering factor of the oxygen ion.

## 2.3 X-ray diffraction topographic methods

There is a bunch of experimental methods in X-ray diffraction topography. They are characterised by the type of beam they use (poly- or monochromatic, extended or confined), the type of detector (films, analogue and digital cameras) and the orientation of the crystal (fixed or variable). They achieve different spatial and angular resolutions and are more or less time-consuming. The following part describes the methods that found their application in our experiments.

### 2.3.1 White beam diffraction topography (WBT)

WBT uses a large part of the beam spectrum, so that every part of strongly distorted lattice planes (Fig. 2.10) and even different lattice plane families diffract at the same time and at any orientation of the sample. The detector has a large sensitive area (typically a X-ray film of 18 cm  $\times$  13 cm) and registers many Laue spots at once. Each of them corresponds to a diffraction vector  $\vec{h}$  and contains unique information about the imperfections in each illuminated grain of the sample. Crystal deformations that are not visible in a certain Laue spot due to Eq. 1.4 can be revealed in a different one. Therefore WBT theoretically allows to image the entire crystal deformation with only one exposition.

Contrast in a Laue spot can be generated by angular lattice plane misorientations  $\alpha$  (Eq. 1.12). A lattice plane that is misoriented by  $\alpha$  is associated with a slight change of the direction of the diffraction vector and Bragg diffracts the beam in a slightly different direction (Eq. 2.5). As a result contrast on the detector appears. Therefore WBT is sensitive to lattice misorientations  $\alpha$ . The angular resolution of the lattice distortion measurements is limited by the spatial resolution of the detector (film grain size) and its dynamic range. In practice  $\alpha/\phi \sim 10^{-3} - 10^{-6}$  are achieved.

To record as many Laue spots as possible the detector must have a large sensitive area of several square centimetres and a good resolution of at least ten micrometres. Nowadays only films fulfil these requirements. However the use of films is very time consuming because they need to be changed after each exposition. In addition the following data analysis may be a difficult task, too: the grey tone on a film depends on the film developing process (temperature and concentration of the developer liquid). Therefore, if a correlation between the grey tone on a film and the beam intensity is needed, or if two different expositions

are compared, an accurate film processing is crucial. In practice the use of films often only allows a qualitative data analysis.

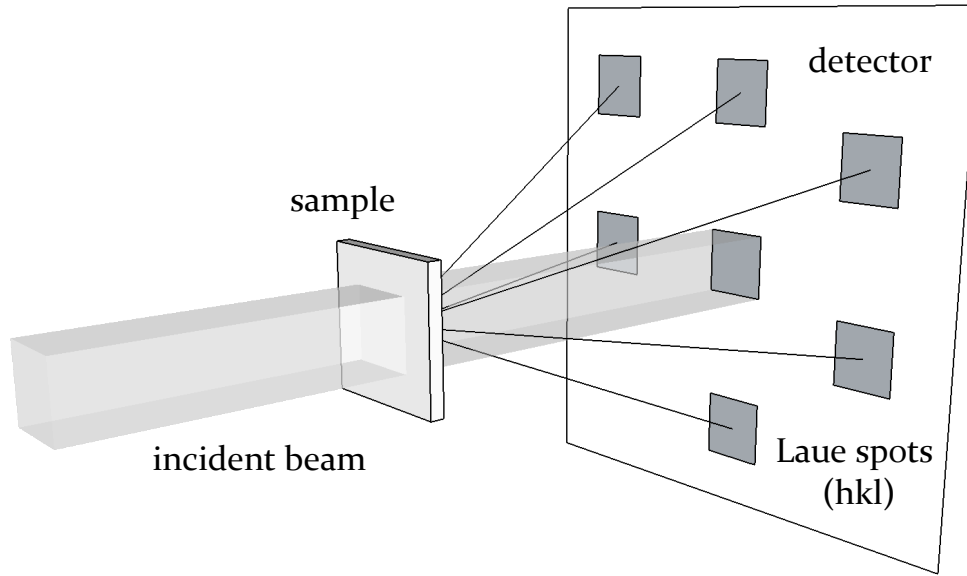


**Figure 2.11:** White beam diffraction topography; several “Laue spots” appear on the detector, each contains unique information about the crystalline defects in the sample.

### 2.3.2 Rocking curve imaging (RCI)

In rocking curve imaging a monochromatic and spatially extended beam of several millimetres is used. The beam is typically generated by a crystal monochromator. Due to the narrow wavelength spectrum  $\Delta\lambda/\lambda = 10^{-4}$  and negligible lattice spacing variations  $d \approx \text{const.}$  (this is the case for our samples), the possible Bragg-angles are restricted to values  $\Delta\theta_B/\tan\theta_B \approx \Delta\lambda/\lambda$ . Unlike in WBT the beam only gets diffracted for a defined spatial orientation of the crystal: the angle  $\omega$ , opened by the incoming beam and the diffracting lattice planes has to lie in a tiny angular interval around the Bragg angle  $\theta_B$  for the chosen wavelength  $\lambda$ ,

$$\omega \in [\theta_B(\lambda) \pm \Delta\theta]. \quad (2.9)$$

Regions of the crystal where Eq. (2.9) is not fulfilled, do not diffract and pure orientation contrast (Chap. 2.2.2) occurs.

In RCI the sample is stepwise rocked by an angle  $\Delta\omega$  around a reference value  $\omega_0$ . The rocking axis is perpendicular to the incoming beam and to the diffraction vector  $\vec{h}$  (Fig. 2.12). The value of  $\omega$  for every region in the crystal changes at each step and the rocking angle  $\Delta\omega$  is chosen big enough to make every region fulfil Eq. (2.9) somewhere in the interval  $[\omega \pm 0, 5\Delta\omega]$ . At each step the Bragg diffracted beam is registered on a 2D detector, typically a digital camera. The final data is composed of an RCI image stack  $I(y, z, \omega)$ , where each image corresponds to an orientation  $\omega$  and each pixel  $(y, z)$  to a region of the crystal volume. In each pixel  $(y, z)$  of the camera a local rocking curve is registered. By analysing all local rocking curves and comparing their mutual angular displacement, quantitative values for the local misorientations  $\alpha(y, z)$  of every crystal region are obtained. The resolution of misorientations in RCI depend on the chosen stepsize and the energy resolution of the monochromator that defines the angular width of the rocking curve. Smaller stepsizes require more images to be taken and present higher demands on the mechanical stability of the experiment. In our experiments stepsizes between  $1/200^\circ$  and  $1/10000^\circ$  were chosen and  $\Delta\omega$  was

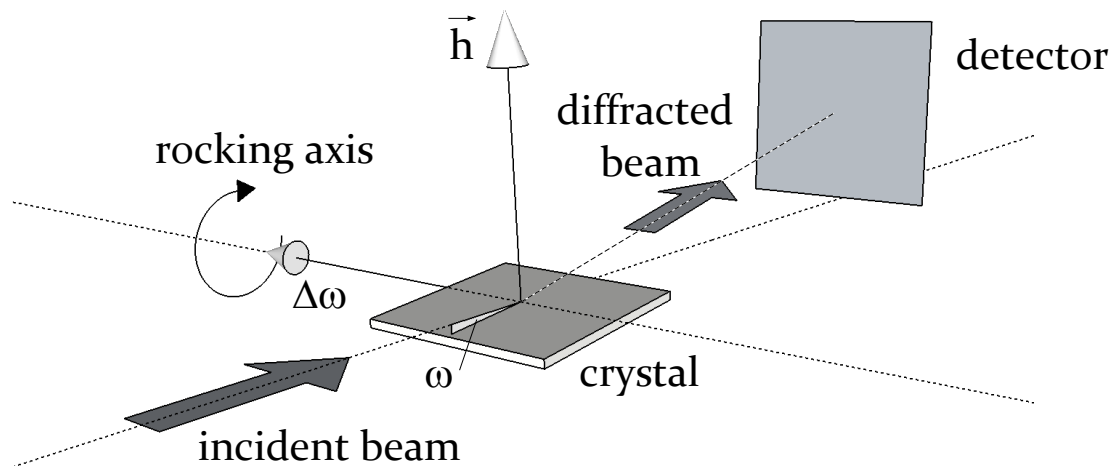


Figure 2.12: Rocking curve imaging experiment in Bragg geometry;  $\vec{h}$ : diffraction vector.

divided in 100 to 300 steps. The spatial resolution (size of a region) mainly depends on the pixel size on the detector. Up to now RCI was mostly used in Bragg geometry. The technique was mainly developed at the ESRF. The method allowed to work on a range of material science topics [Lübbert 00, Hoszowska 01, Lübbert 05, Mikulik 06, Calamiotou 07, Mikulik 08].

### 2.3.3 Section X-ray diffraction topography

In X-ray diffraction topography a 3D sample is imaged on a 2D detector. All points lying on a line that is threading through the sample are projected on a single point on the detector surface (Fig. 2.13). If neglecting the wave propagation inside the Borrmann triangle (Fig. 2.7), the region where the information is coming from corresponds to a line threading through the entire crystal, a more precise localisation along the thickness being impossible. In addition, the bulk contribution to the image is superposed by the diffraction of the crystal surfaces. A crystal surface often exhibits a lower crystalline quality and diffract, in the low absorption case we are concerned with, at higher intensities. Several attempts were made to

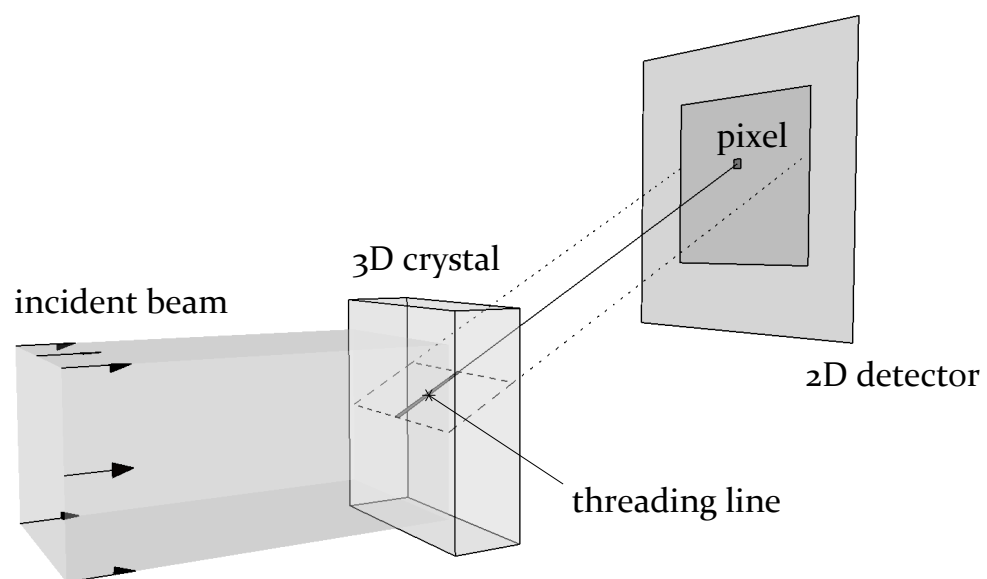


Figure 2.13: Projection of a 3D sample on a 2D detector surface in X-ray diffraction topography

override the 2D characteristics of X-ray diffraction topography. Rather recent development is the combination with tomography [Ludwig 01, Kawado 04, Kawado 05], where series of images are recorded while the sample is rotated around the Bragg diffraction vector. Furthermore slits can be used in order to confine the illuminated volume of the sample to a section. This section X-ray diffraction topography [Lang 57, Andersen 74] is a straightforward way to access detailed volume information [Kawado 79, Kvardakov 07, Allen 11]. In general a slit with a size between  $10\ \mu\text{m}$  –  $100\ \mu\text{m}$  is located in front of the sample to limit the direct beam in one direction (Fig. 2.14). Consequently only a section of the crystal, as thick as the slit, is illuminated. Within the same approximation as mentioned above we can suppose that only the illuminated section of the crystal generates the Bragg diffracted beam. The image on the detector corresponds to the shape of the illuminated crystal volume and its thickness corresponds to the thickness of the crystal. The borders of the section image on the detector correspond to the crystal surface. A geometrical sketch of a section diffraction topography experiment is shown in Fig. 2.14.

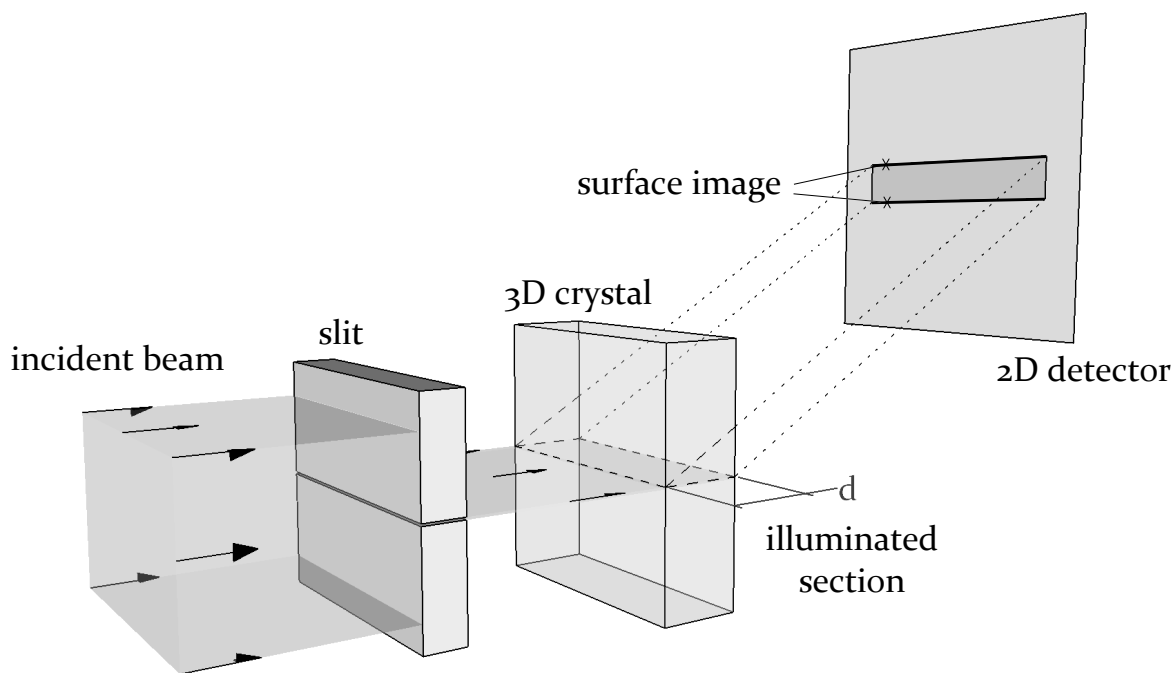
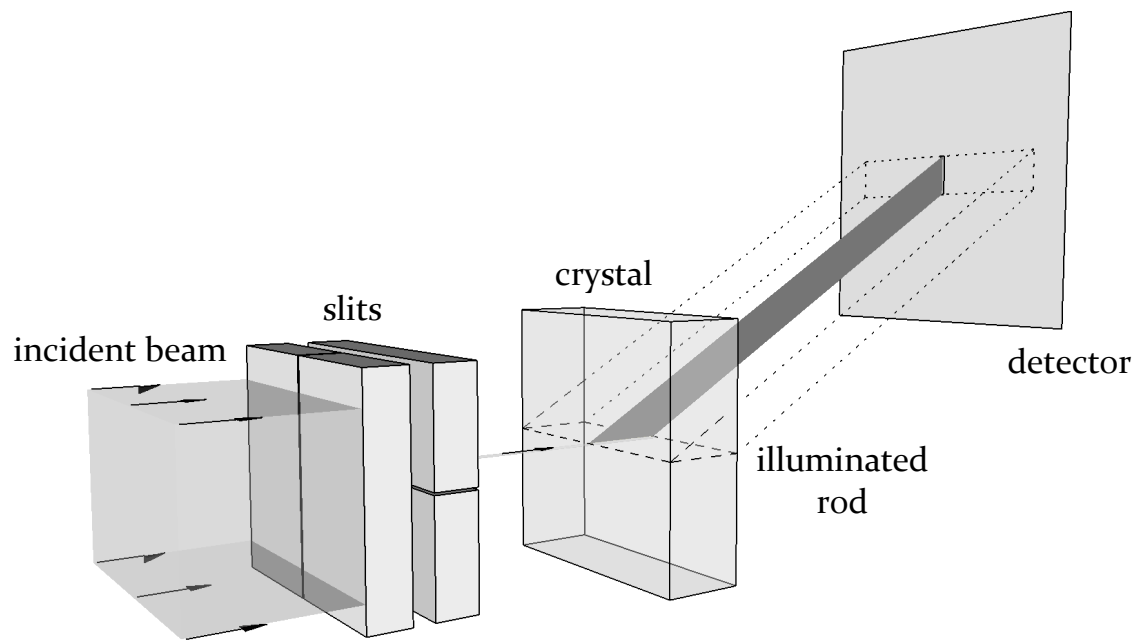


Figure 2.14: Section X-ray diffraction topography

By step scanning the sample 3D rendering of the sample becomes possible [Kajiwara 07]. Rather similar ideas are behind very recently developed techniques like “3D diffraction microscopy” [Poulsen 04]. The method was widely used with a white beam. In the frame of this work we attempt to combine section X-ray diffraction topography with RCI.

### 2.3.4 Pinhole X-ray diffraction topography

In pinhole diffraction topography the beam is limited along two directions and usually has a size between  $10\ \mu\text{m} \times 10\ \mu\text{m}$  –  $100\ \mu\text{m} \times 100\ \mu\text{m}$ . This can be achieved by two thin slits that are perpendicularly set to each other and then located into the beam in front of the sample. The size of the beam corresponds to the smaller size of the two slits (Fig. 2.15). The image on the detector plane has the shape of a line and corresponds to the illuminated volume in the crystal. Pinhole diffraction topography allows to measure possible lateral deviations of the diffracted beam. Such deviations occur for misorientations around the axis described by



**Figure 2.15:** Pinhole X-ray diffraction topography

the direct beam wave vector  $\vec{k}_0$ . Pinhole diffraction topography has therefore been used in the frame of this work to measure angular misorientations around the axis defined by the incident beam wave vector (Fig. 1.8).

## Experimental procedures

We study the initial states of deformation in ice, starting from a large crystal (several mm thick and cm wide) that exhibits a high crystalline quality. The pre-existing methods to measure lattice distortions did not match with the demands concerning the spatial resolution. Therefore a new experimental procedure was needed in order to measure the complete angular misorientation in the entire sample volume and with a sufficient spatial and angular resolution. Our procedures were continuously developed until, at the very end of the thesis, they have shown to be able to measure what was initially expected. The following chapter describes their state of the art as they were applied in our last experiment.

### 3.1 Conventions for coordinate system

This paragraph introduces our default coordinate system. Two axis designations are predefined: the incident X-ray beam defines the x-axis that is positive with the propagation of the beam; the z-axis shows upwards. The y-axis is derived by the right-hand rule (and shows towards the BM05-hutch entrance door, see Chap. 3.2). The sign of rotations respects the mathematical sense and can be derived by the right hand rule: positive rotation is counter-clockwise. These guidelines allow to define the whole coordinate system. An illustration is shown in fig. (3.1). Please note that contrary to other chapters of the thesis manuscript, in this chapter the beam always is coming from the right hand side of the figures. This helps the experimentalist to orient himself because when entering into the experimental hutch at BM05 the beam propagation direction is from the right to the left.

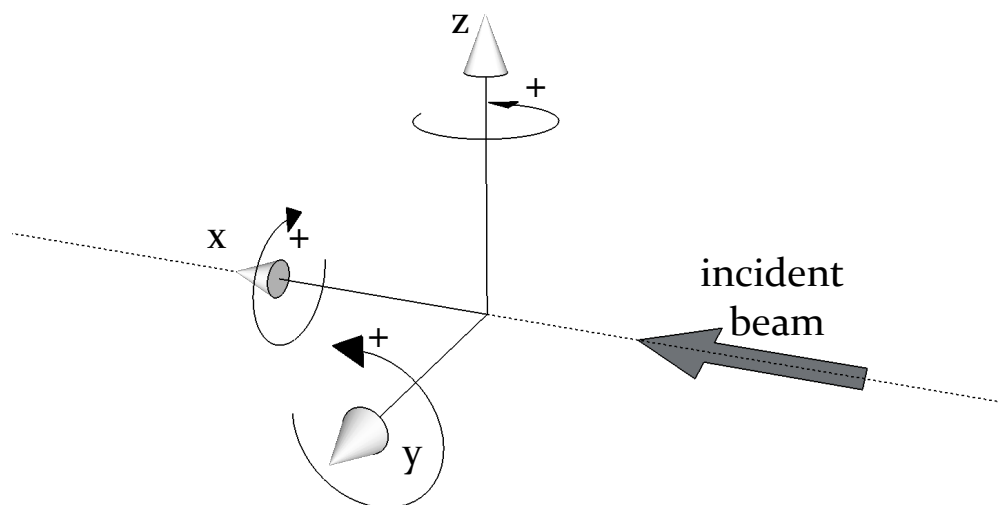


**Figure 3.1:** Preassigned laboratory coordinate system for our experiments

### 3.2 The BM05 beamline at the ESRF

All experiments were performed at the beamline BM05 at the ESRF that is schematically presented in Fig. (3.2). In the following the elements passed by the beam from the source to the detector will be described. The beam is generated by a bending magnet situated in the storage ring. The X-rays are tangentially emitted to the circular arc described by the electron trajectory. The front end is situated at 23 m from the source and separates the beamline instruments from the storage ring. The storage ring is under high vacuum,  $p = 10^{-10}$  bar, whereas the first part of the beamline is under a slowly flowing He-atmosphere. These two sections are separated by a first beryllium window.

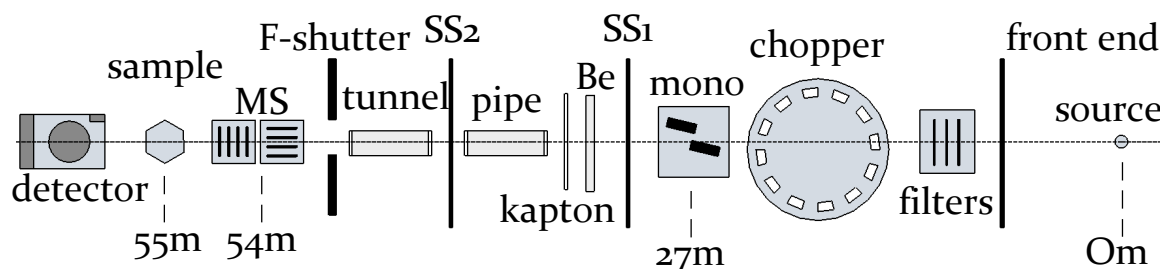


**Figure 3.2:** Schematic presentation of the beamline BM05. Abbreviations: mono - Si monochromator, SS1 - safety shutter 1, Be - Beryllium Window (0,5mm), SS2 - safety shutter 2, F-shutter - fast shutter, MS - multi section device.

- Filter device:** Right after the front end a filter device allows to put three different filters into the beam at the same time. Currently there are copper, nickel and aluminium filters available. As thickness the user can choose 0,5 mm; 1 mm and 2 mm. Filters reduce the beam intensity and modify the beam spectrum. Filtering the beam part with lower energies is a way to reduce the heat load on other elements on the beamline as well as on the sample.
- Chopper:** After the filter device the X-rays pass the chopper. The chopper reduces the beam intensity without modifying the spectrum of the beam. This is a convenient way to adapt the beam intensity and reduce the heat load of the sample to an acceptable value. It consists of two absorbing disks made of tungsten. Each of them is thick enough to absorb the entire beam. The disks have circularly arranged holes that let the beam go through. By shifting the disks against each other the size of the holes seen by the beam can be reduced. The two disks rotate in the same direction and with the same frequency, so that the beam alternately goes through a hole or gets absorbed by the disk material. The chopper acts like a switch that periodically switches the beam on and off. Averaged over a period of time longer than the temporal repetition of the holes, the beam intensity is reduced. Depending on the hole size, values between 0% and 50% of the origin beam intensity can be chosen. 100% can be achieved by stopping the chopper.
- Si Monochromator:** The beam then hits on a silicon-111 crystal monochromator. It consists of two nearly perfect silicon crystals with a well polished 111 Surface. Depending on the experiment the monochromator selects a defined energy  $E$  of the white beam with a resolution of  $\Delta E/E = 10^{-4}$ , corresponding to the Darwin width of the silicon 111-reflection. The monochromator system has a so called "fixed exit". That means that the height of the monochromatic beam does not depend on the chosen

photon energy. The heat load, especially on the first crystal can be considerable and makes cooling compulsory. The crystal is water-cooled. The dimensions of the two monochromator crystals are the limiting factor for the horizontal size of the monochromatic incident beam. The vertical size is associated to the angular divergence of the incoming white beam.

- **Beryllium window:** The beryllium window is needed as a separator between the He atmosphere that protects the Si monochromator and the air in the experimental hutch. In addition a kapton window prevents direct contact to the beryllium window.
- **Pipe and tunnel** In the following a pipe and a tunnel are installed in the beam. Both are filled with helium gas that reduces absorption. Otherwise the intensity loss due to absorption in air, especially of lower energies, would be considerable. The pipe and the tunnel have kapton windows mounted on their ends as well.
- **Fast shutter:** The fast shutter allows short exposure times down to 1/100s.
- **Multi section device:** The multi section device has two sets of slits. Each set has slits that are spaced 1 mm from each other. One is horizontally and one vertically aligned. They allow section- (Chap. 2.3.3) and pinhole diffraction topography (Chap. 2.3.4). The device can be displaced transversally to the beam so that different regions of the sample can be investigated. There were two different versions of multislits in use. The first one is a 2 mm thick tungsten plate with 14 slits of 100  $\mu\text{m}$  slit size. By inclining the plate, smaller slit sizes are possible. These multislits form a multisection beam at every photon energy provided by BM05, however they introduce disturbing phase shifts due to a poor finish of the slit edges. For the last experiment 20  $\mu\text{m}$  thick gold multislits deposited on a double-side polished 200  $\mu\text{m}$  thick Si plate were used. Inside the slits there are 10  $\mu\text{m}$  thick gold wires situated, in order to mechanically stabilise the gold deposition. The use of the gold slits is restricted to lower photon energies where the gold layer is absorbing enough and the slit size is fixed to 50  $\mu\text{m}$ . Yet they provide a higher quality.
- **Sample:** The sample is mounted on a diffractometer tower that provides several translation and rotation motions. They allow to orient the sample. A sketch of the diffractometer is shown in Fig. 3.3. The sample itself as well as its environment are explained in detail in Chap. 3.3.
- **Detector:** Depending on the experiment the detector can be an X-ray film, an analogue white beam camera (Laue camera) or a digital camera. The Laue camera has a poor spatial resolution and a poor dynamic range, but it provides a live image and a large field of view of 20 cm  $\times$  20 cm. Two different digital cameras have been used in our experiments: the *pco.2000* and the *Fast Readout Low Noise camera* (FReLoN). The FReLoN is a specialised ESRF in-house development [Labiche 96]. In terms of image quality the FReLoN is far superior to the *pco.2000*. Yet it is heavier, must not be inclined and requires a stable mounting. Different optical devices are available for the cameras. Once again the optics that can be mounted on the FReLoN provide sharper images and exhibit a larger aperture than those for the *pco.2000* what allows shorter exposure times. The most suited for our experiments provide a pixel size of 10  $\mu\text{m}$   $\times$  10  $\mu\text{m}$  at the *pco.2000* and 8  $\mu\text{m}$   $\times$  8  $\mu\text{m}$  at the FReLoN. Since both cameras use a 2048  $\times$  2048 pixel CCD sensor, the field of view is 2 cm  $\times$  2 cm and 1,6 cm  $\times$  1,6 cm respectively.

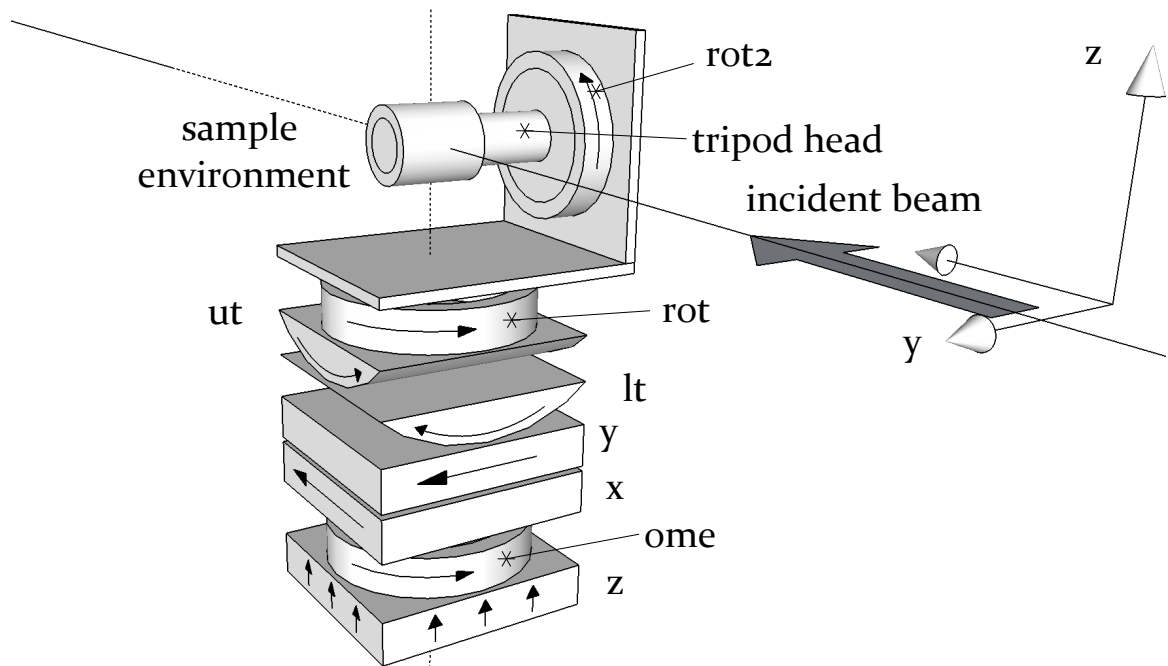


**Figure 3.3:** The diffractometer tower including its motorisation and the motor names in *spe* [spe]. The arrows indicate the positive motion direction.

## 3.3 Sample and sample environment

### 3.3.1 Crystal growth and crystal manufacturing

In order to have reproducible experimental conditions the crystals must exhibit a high crystalline quality in the beginning of the experiment. Initial crystal defects influence the deformation process (Chap. 1.3) and make every individual sample evolving differently. This makes it harder to predict their evolution by simulations. The demand on crystalline quality is rarely fulfilled by natural ice crystals, we therefore use artificially grown ones. Their crystalline quality, crystalline orientation and the geometrical arrangement of the inner grains can easily be adapted to our experimental demands.

**Crystal growth:** the samples are cut out of a polycrystalline ice block that is grown in a  $25\text{ cm} \times 30\text{ cm} \times 25\text{ cm}$  box (Fig. 3.4). The procedure was developed during Laura Capolo's PhD project [Capolo 07]. The walls of the box are made of a heat isolating plastic, whereas the bottom is made of conductive steel. The isolating capacities of the walls are additionally improved by Styrofoam panels that surround the box. The box is put on a cooled, temperature regulated metal table and filled with deionised water. These conditions guarantee a stable temperature gradient between the bottom of the box that is cooled beyond the water melting point,  $T_{\text{bottom}} < 0^\circ\text{C}$ , and the environment at  $T = 0^\circ\text{C}$ . The temperature of the table is regulated to a value that allows water freezing at the bottom of the box and the formation of an ice block. Yet the temperature must not be too low, otherwise the crystal growth would be too fast and the crystalline quality too low. Crystal growth rates below 10 mm per day lead to satisfying results. The temperature is constant over the surface of the bottom on the block what allows independent freezing at different places of the bottom and therefore different crystalline orientations. However, as the growth rate is different for different crystalline orientations, some grains grow faster and overlay the slowly growing ones, leading to bigger grains at the upper layers of the block. The material to grow the block is taken from

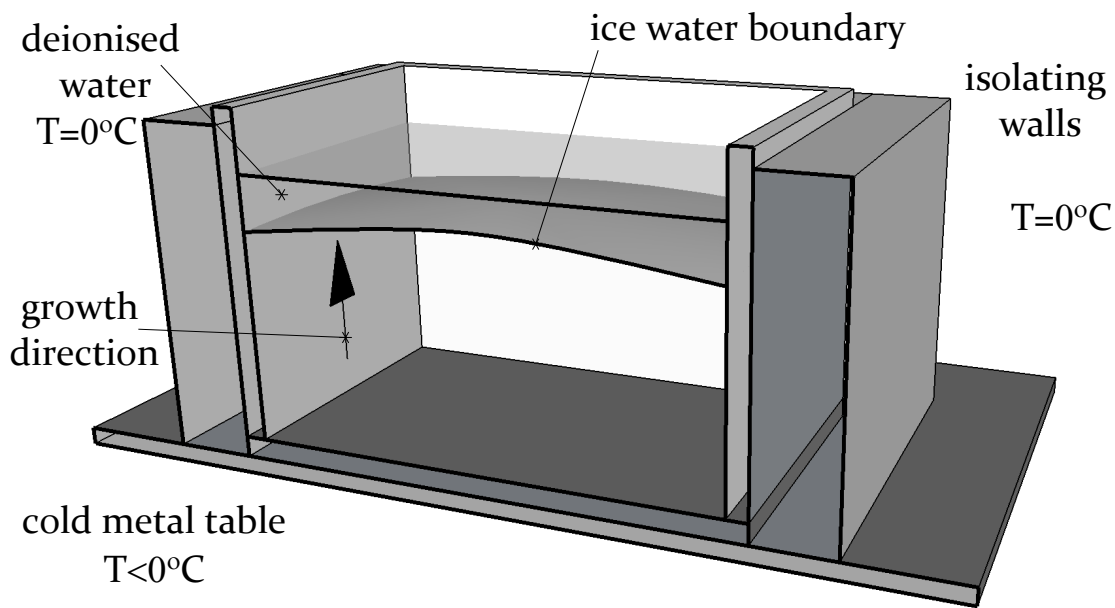


**Figure 3.4:** Section cut through the box for the crystal growth, indicating the box, the crystal block on the bottom and the deionised water.

the deionised water. As the block grows, the water quantity diminishes and the concentration of its impurities grows. Logically the probability to include them into the ice structure is getting higher as well. The water is therefore exchanged every day. Here the old water is evacuated first and then replaced by fresh one at  $5^{\circ}\text{C}$  what remelts the uppermost layer of the ice block. By this possible structure damages that may occur during the water exchange are melted away before the normal crystal growth continues. As ice is a temperature isolating material the temperature of the cooling table must be diminished during the growth process to maintain a constant growth velocity. Typically, when the growth rate falls below  $5\text{ mm per day}$ , the temperature is diminished by  $1^{\circ}\text{C}$ . After one month of crystal growth the block is ready to be mechanically processed into our experimental samples.

**Mechanical processing:** The side surfaces as well as the bottom surface of the polycrystalline ice block have the shape of the walls of the box, whereas the upper surface has a dome shaped form due to temperature inhomogeneities between the ice and the environment (Fig. 3.5). In a first step the dome shaped ice cap of the block is cut away by a manual saw. The cap is then put in a cross polariser device that visualises the crystal grains at the uppermost layer of the block and allows to draw a grain map of the block as is shown in Fig. 3.6. A first selection of the grains that could be used in the experiment is taken. Crystal grains that exhibit regular grain boundaries are supposed to have the highest crystalline quality [Capolo 07]. The ice cap is then cut into quadratic pieces that are glued on glass plates. Their thickness is then reduced to a few tenths of a millimetre by a “microtome” plane tool and the orientation of the  $\vec{c}$ -axis of the grains is measured with the help of a cross polariser device. Here the glass plates are put between two crossed polarisers and then rotated in space until the  $\vec{c}$ -axis is parallel to the polarising direction of the first polariser. The direction of the  $\vec{c}$ -axis of the grains and the shape of their grain boundaries are the criteria for selecting them for the experiment. The motion limits of the diffractometer tower (Fig. 3.3) limit the choice of the  $\vec{c}$ -axis directions to those where the angle between the  $\vec{c}$ -axis and the sample surface is below  $20^{\circ}$ . Once the regions for the samples are chosen, the block is cut into pieces and processed to samples by an industrial milling machine.

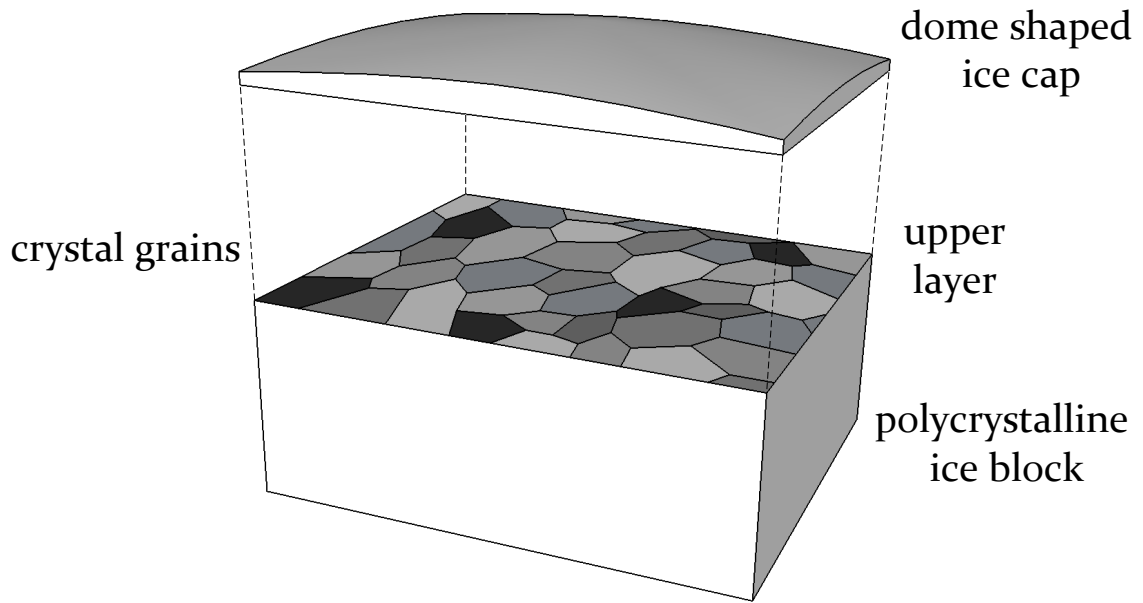


Figure 3.5: Shape of a polycrystalline ice block

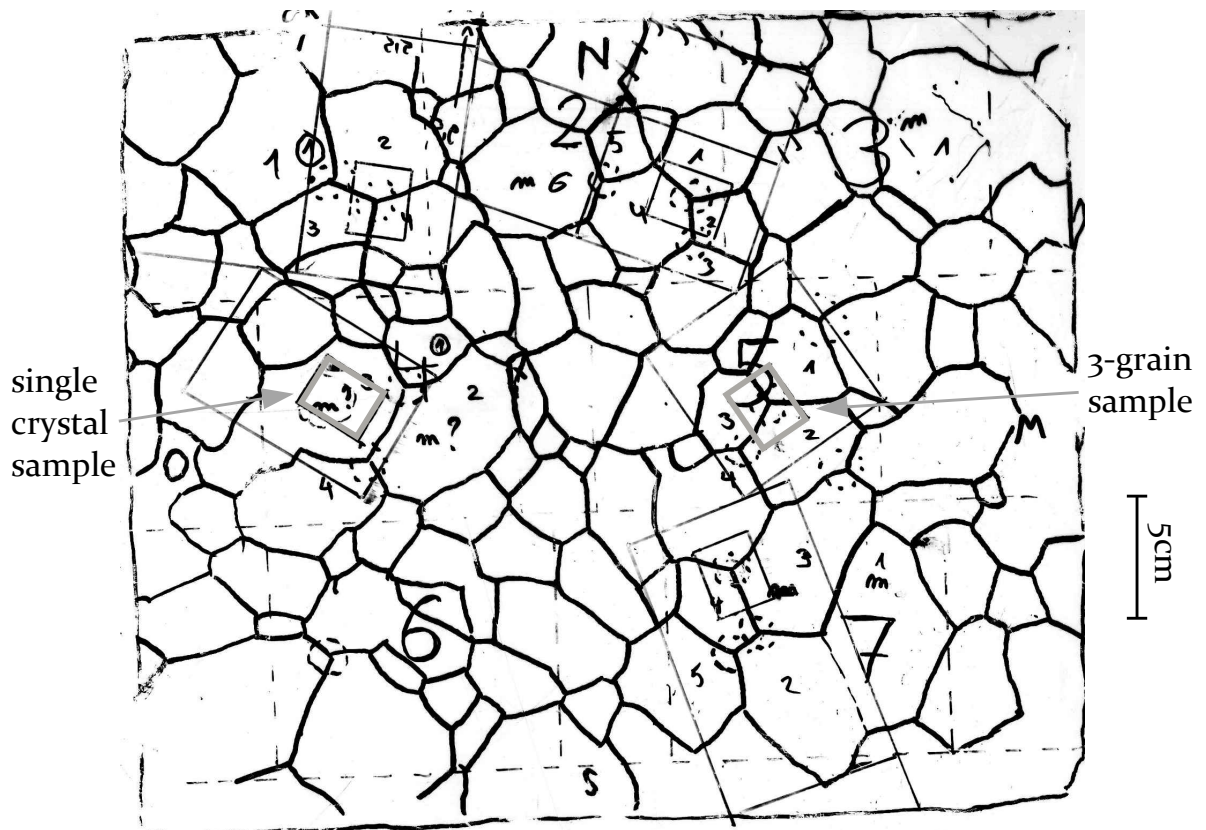
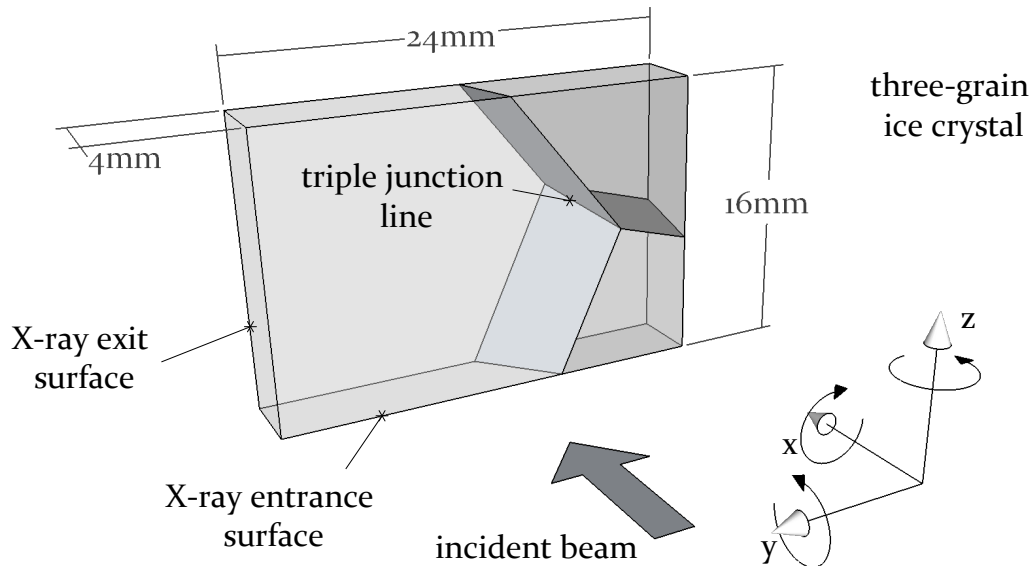


Figure 3.6: Grain map of our 2nd polycrystalline ice block (Block II)

### 3.3.2 Sample

The samples are platelet shaped and processed to the dimensions 24 mm × 16 mm × 4 mm. The chosen sample size allows to study wide range strain fields and is adapted to the field of view of the camera. The sample thickness must be big enough to avoid a buckling of the sample during its loading. Thicker samples also reduce the influence of surface imperfections on the bulk deformation. On the other hand the sample must be thin enough to prevent the superposition of Bragg diffracted images in section X-ray diffraction topography (Chap. 2.3.3). A crystal thickness of 4 mm is here a good compromise. The crystal may contain



**Figure 3.7:** Shape and dimensions of a three-grain ice sample.

only one major crystalline orientation and is then called single crystal. Alternatively crystals with three major orientations were studied in our experiments. These crystals, called three-grain crystals and exemplary shown in Fig. 3.7, contain all attributes of a polycrystal: grain boundaries and a grain triple junction. On the other hand since their polycrystalline behaviour is the simplest among all multiple grain crystals, the experimental observations supposed to remain comprehensible.

**Nomenclature:** Each sample gets an individual code assigned, to distinguish it from the others. The code is composed by:

Block number (Latin) - Glass plate number - Grains numbers - Depth in the block

For example the sample in the last experiment, called “II-5-123-3” was cut out of the second block that was grown and from the fifth glass plate (Fig. 3.6). Here the grains 1,2 and 3 are used. And it was the third sample along the depth of the block.

### 3.3.3 Sample environment

Our samples require a sophisticated sample environment to avoid thermomechanical stress and melting. First of all, the temperature must be maintained at  $T = (-10 \pm 2)^\circ\text{C}$  to avoid crystalline deformations that arise with temperature inhomogeneities and temperature fluctuations. A further problem is the sublimation of ice. Although it is rather slow the long

duration of our experiment of six days requires precautions. Further demands on the sample environment are a low X-ray absorption, low weight to not exceed the maximal charge of the diffractometer tower and a large motion range in order to obtain many different orientations in space.

We have designed a sample environment for our experimental work that takes all these aspects into account. It was progressively improved over the time of the project and is schematically shown in Fig. 3.8 as it was during our last experiment in March 2011. The

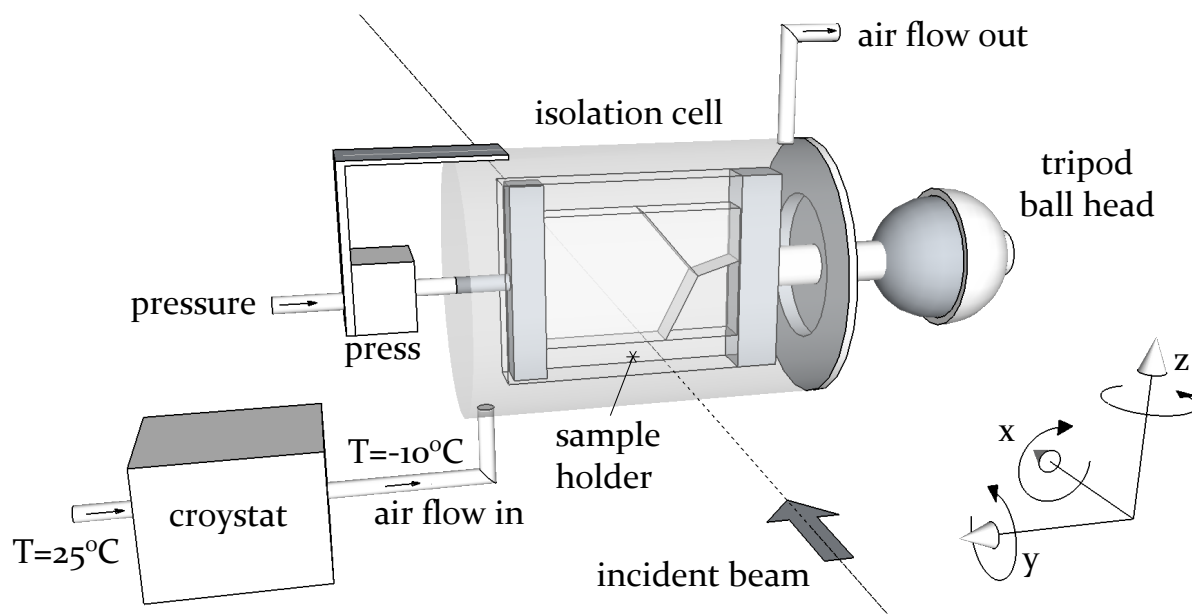


Figure 3.8: Sample environment with a 3-grain crystal mounted.

sample holder is basically made of *Plexiglass*<sup>®</sup>. It keeps the sample in a fixed position, avoids its sublimation and allows to mechanically load the sample along its biggest dimension. The load is created by a pneumatic press that uses the pressurised air provided in the experimental hutch. The side walls of the sample holder exhibit low X-ray absorption. In the last experiment the sample holder was additionally filled with silicone grease to further reduce sublimation of the sample. The sample holder is set up in an isolation cell, basically constituted of a cylindrically formed double plastic wall. That cell is cooled by a constant air flow coming from a commercial cryostat. The cryostat uses the same air supply as the press. The isolation cell including the sample is mounted on a hydrostatic ball head for a photography tripod, model *Manfrotto 468MG*. The ball head allows to align a crystallographic axis in the sample with the rotation axis of the motors on the diffractometer tower.

## 3.4 Experiment

### 3.4.1 Orienting the crystal

The first part of the experiment is carried out with a white beam. It serves as a preliminary verification of the sample's crystalline quality and is the occasion to orient the crystalline axis in space for the following part. For this, the crystalline orientations of the crystal must be determined.

The global orientation of the  $\vec{c}$  axis is measured before the experiment with a cross polariser device (Chap. 3.3.1), whereas the orientation of the  $\vec{a}$  axis can be determined using WBT (Chap. 2.3.1). To avoid irreversible changes in the crystalline structure due to the heat

load of the white beam, the intensity must be reduced (Chap. 3.2). We filter the beam with 3 mm aluminium and reduce the beam intensity to 5% of its initial value by using the chopper. In the beginning of the experiment white beam topographs are registered on films with the aim to identify the basal and one 1st order prismatic (Fig. 1.2) Bragg diffracted images. The data from these images will be used to measure the angular misorientation components (Fig. 1.8). Although the angular misorientation can be revealed by studying other Bragg diffracted images, the basal and a first order prismatic one are preferred for several reasons. They exhibit a comparably high diffracted intensity due to their structure factor (Tab. 2.1). Further on the choice of these two Bragg diffraction images respects the anisotropic properties of ice (Chap. 1.2). Once the basal and the prismatic Bragg diffracted image are identified

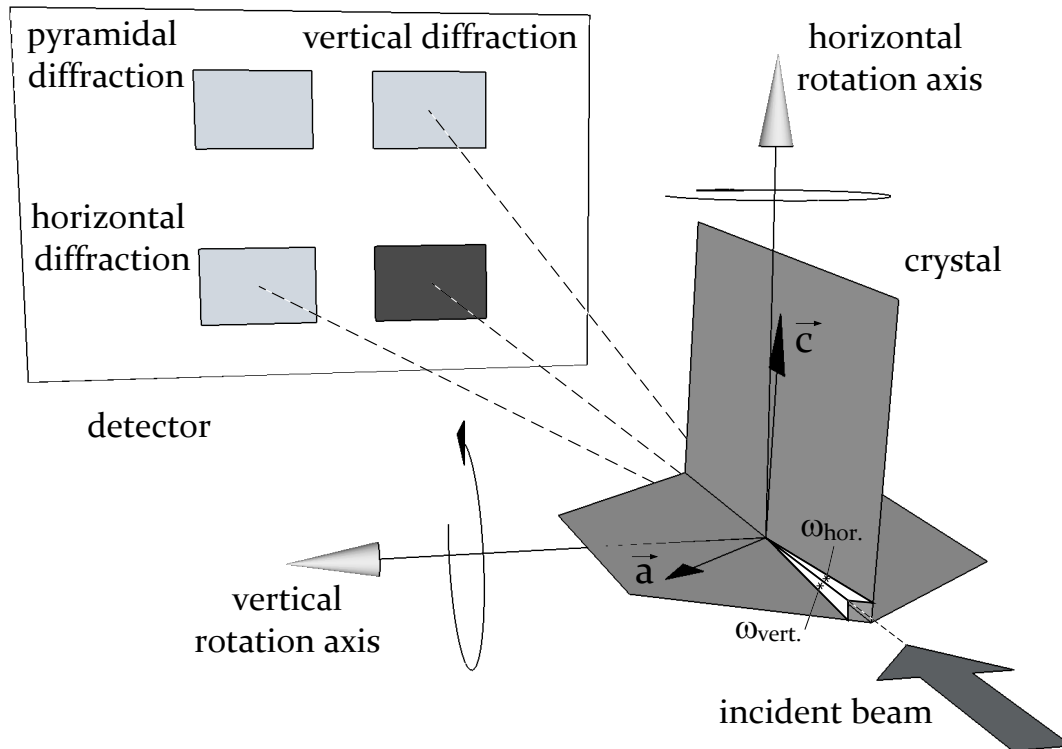


**Figure 3.9:** Crystal orientation for scanning experiment. The basal Bragg diffracted image is vertically diffracted and the prismatic one horizontally. The inverse constellation is possible and equivalent.

on the detector, the crystal is oriented in a way that one of them is vertically upwards of the direct beam image and the other one horizontally on the left of it. For a better understanding, the desired arrangement of the spots on the detector is shown in Fig. 3.9. The basal spot may be vertically and the prismatic one horizontally diffracted or vice versa. Both orientations may be used to deduce the crystalline orientation. The choice mainly depends on the orientation of  $\vec{a}$  and  $\vec{c}$  of the crystal and the motion limits of the motors on the diffractometer tower (Fig. 3.3). The crystal is oriented so that the angles  $\omega_{\text{vert,hor}}$  opened by the direct beam and the diffracting lattice plane families Fig. 3.9 correspond to the Bragg angle at the chosen work energy (typically  $E = 18 \text{ keV}$ ):

$$\omega_{\text{vert,hor}} = \theta_B(E, d_{ihkl}). \quad (3.1)$$

By adjusting  $\omega_{\text{vert,hor}}$  the Bragg diffracted images are easier found when using a monochromatic beam in the following part.

### 3.4.2 Step scanning the crystal

The following step consists of recording a bunch of rocking curves using RCI and requires a monochromatic beam. Therefore the Si-monochromator is driven into the beam, the chopper is turned off and the filters are reduced to 0,5 mm aluminium. With a proper crystal pre-alignment in the first part of the experiment, only slight crystal rotations of less than  $1^\circ$  are necessary to find a crystal orientation where the vertically and the horizontally diffracted Bragg images appear at the same time. Typically a Bragg image diffracted by a pyramidal lattice plane family pops up as well. Together with the direct beam image those four spots form a nearly perfect square on the detector. The orientation of the crystal and the arrangement of the images on the detector is shown in Fig. 3.9, an experimental example can be found in Fig. 3.10.

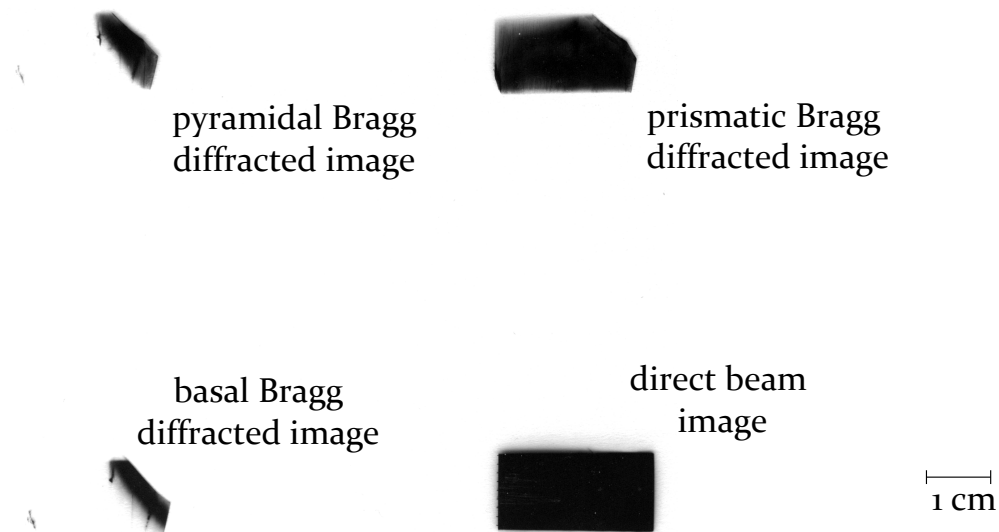


**Figure 3.10:** Image recorded on film; crystal: II\_5\_123\_3 - state 3 - grain 3; orientation: multiple diffraction case; monochromatic beam 18 keV;

The crystal is now aligned in the so called *multiple diffraction* case where the direct beam intensity is distributed on several Bragg diffracted images. Under these circumstances the intensity repartition on each Bragg diffraction image strongly depends on the crystal orientation: any rotation motion of the diffractometer tower changes the orientation of every diffracting lattice plane family and logically modifies  $\omega$ . The multiple diffraction case describes a well defined crystal orientation, we therefore use it as the reference orientation  $\phi_{\text{ref}}$ . (Eq. 1.12). On the other side the intensity repartition on the three Bragg diffracted images is hardly predictable. If rocking curves were recorded in this constellation, the data analysis would be very complicated. Therefore the crystal is slightly disoriented so that only one Bragg diffraction image remains. It is then observed by the digital camera.

As described in Chap. 2.3.2, angular misorientations and dispersive effects (Chap. A) prevent that all illuminated parts of the crystal diffract at the same time and make the recording a rocking curve necessary. The crystal is rotated by the motors *rot* or *ome* for the horizontally Bragg diffracted image and by *rot2* or *ut* for the vertically one (Fig. 3.3). First of all, we determine the motor position of the maximally Bragg diffracted intensity (Bragg peak position) and the two extreme positions around the Bragg peak where no region of the crystal is diffracting any more. The two extreme positions define the angular interval  $[\omega - \Delta\omega/2; \omega + \Delta\omega/2]$  of the rocking curve. The angular stepsize that we choose for the rocking curve depends on its angular width  $\Delta\omega$ . The broader the curve, the bigger

the stepsize, so that the amount of images per rocking curve is around 60 to 300. In our experiments we have chosen values for the stepsize from  $(1/10000)^\circ$  to  $(1/200)^\circ$ .

Standard X-ray diffraction topography (Chap. 2.2) produces 2D projection images of 3D crystals. The method only resolves the origin of the Bragg diffracted beam to a line that is threading through the crystal thickness (Fig. 2.13). We use section diffraction topography (Chap. 2.3.3) in order to determine the depth in the sample where the Bragg diffracted beam is coming from. Before registering the rocking curve, the multisection device (Chap. 3.2) is placed in front of the crystal. It generates an incident beam that is composed of several  $50\ \mu\text{m}$  thick sections, displaced by 1 mm. The sections are horizontally aligned when the vertically Bragg diffracted image is observed and vice versa. The rocking curve is recorded in the angular interval that was determined before. In this way RCI is combined with section diffraction topography and extends the capabilities of Bragg diffraction topography to 3D spatial resolution.

The multisection device covers a big part of the beam so that only a few  $50\ \mu\text{m}$ -thick sections of the crystal, spaced by 1 mm, are illuminated (Fig. 4.3, Fig. 4.4). To study the remaining parts as well, the multisections need to be displaced and further rocking curves need to be registered. Multisections with parameters as ours must be displaced 20 times by  $50\ \mu\text{m}$  to scan through the entire illuminated area of the crystal. In practice we record at least 21 rocking curves to have a superposition of the last one with the first.

In addition, after every rocking curve the multisection device is driven out of the beam and a quick “total” rocking curve with fewer angular steps and a shorter exposure time per image is recorded. This step might be necessary in order to calibrate the angular position of the Bragg peak with the motor position. A discrepancy may occur during the experiment due to backlash of the rotation motor, mechanical relaxations in the sample environment or slight sample motions. The entire step scanning process (Fig. 3.11) of 21 rocking curves

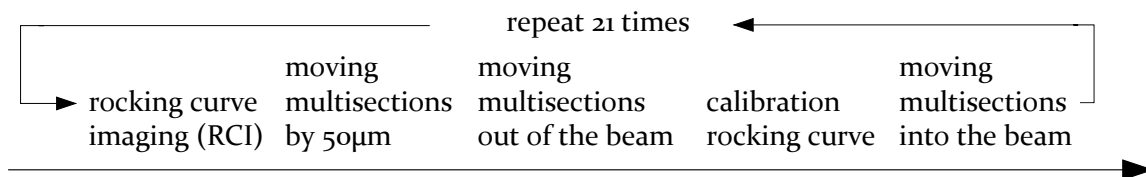


Figure 3.11: Step scanning procedure.

including the calibration rocking curves is automatically controlled by *spec* [*spe*] macros and requires no human intervention. An entire scan of a Bragg diffracted image using this method takes up to twelve hours, depending on the direct beam intensity, the chosen stepsize and the exposition time for each image.

The step scanning procedure is repeated for the second Bragg diffracted image in the same way except that the experimental geometry (rocking axis and orientation of multisections) is turned by  $90^\circ$  around the direct beam. The RCI-scans of the two Bragg diffracted images provide quantitative 3D maps for angular misorientations around the  $y$ - (vertical X-ray diffraction) and the  $z$ -axis (horizontal X-ray diffraction) (Fig. 1.8).

### 3.4.3 Multi-pinhole X-ray diffraction topography

Step scanning the crystal provides angular misorientation components around the  $y$ - and the  $z$ -axis (Fig. 1.8). For geometrical reasons only these two components modify  $\omega$  considerably, whereas the misorientation component around the  $x$ -axis diminishes  $\omega$  but only by a factor

$\cos \alpha_x$ :

$$\omega(\alpha_x) = \omega_0 \cdot \cos \alpha_x \quad (3.2)$$

The derivation is presented in Chap. (B). Here  $\alpha_x$  is the misorientation angle around the x-axis (Eq. 1.13) and  $\omega_0$  the angle between the incident beam and the Bragg diffracting lattice planes as it would occur without misorientation. Our crystals exhibit misorientations  $\alpha_x \leq 0, 1^\circ \Leftrightarrow \cos \alpha_x \approx 1$ . The influence of  $\alpha_x$  is too weak to be measured by RCI with the rocking axis aligned parallel to the y- or the z-axis.

To increase the sensibility to  $\alpha_x$  the crystal could either be turned around the y-axis to repeat a step scanning procedure on the horizontally Bragg diffracted image, or around the z-axis to then repeat the procedure on the vertically diffracted spot. The sample rotation would imply a permutation of the x- and the z-components (or x- and y) and make the step scanning procedure as sensitive to the x-components as it was to the other ones before.

For geometric reasons these solutions turn out to be too difficult in our case. When our sample is turned by  $90^\circ$  around the z-axis, its thickness becomes 24 mm and if the rotation was around the y-axis, the thickness would be 16 mm, Fig. 3.7. Both values exceed the technical limitations of section X-ray diffraction topography where the crystal thickness is projected on the detector surface and would exceed the field of view of our cameras. Too big crystal thickness also leads to superposition of several section images on the detector and restricts to the use of a single section. That would increase the scan time, in our case at least by a factor of 10. Last but not least mechanical limitations do not allow to turn the sample environment (Fig. 3.8).

We therefore use an approach to access the x-component of the misorientation, without rotating the sample by  $90^\circ$ . An angular misorientation around the incident beam wave vector  $\vec{k}_0$  (the x-axis in our case) is associated with a reciprocal lattice vector  $\vec{h}_{hkl}$  that is not perpendicular to the rocking axis but inclined by  $\alpha_x$  (Fig. 3.12). The incident beam wave

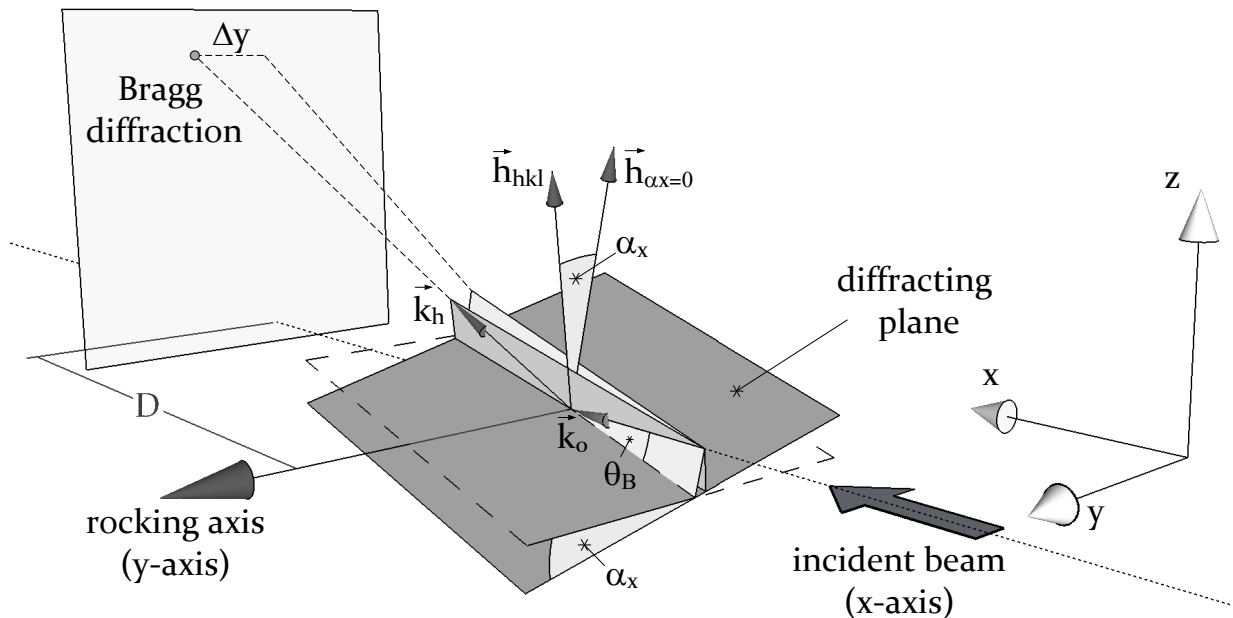


**Figure 3.12:** Lateral deflection of the Bragg diffracted beam due to an angular misorientation around the x-axis. The scene shows a vertically Bragg diffracted beam.

vector remains perpendicular to that axis. Therefore the diffracted beam wave vector  $\vec{k}_h$ , deduced from Eq. 2.5 as  $\vec{k}_0 = \vec{h}_{hkl} - \vec{k}_h$  neither is perpendicular to the rocking axis. As a result

there is a lateral deflection of the diffracted X-ray beam, out of the reference diffraction plane as it is defined (Chap. 2.2).

By measuring the lateral deflection of the Bragg diffracted beam on the detector, one can conclude on the angular misorientation around the  $x$ -axis. Beside the angular misorientation the deflection of the Bragg diffracted beam on the detector plane also depends on the Bragg angle  $\theta_B$  and the distance  $D$ , between the crystal and the detector. A formula that correlates the parameters has been derived by using pure geometric relations (Chap. B):

$$\Delta y = -2D \frac{\sin \theta_B}{\cos 2\theta_B} \cdot \alpha_x, \quad (3.3)$$

where  $\Delta y$  is the lateral deflection on the detector plane. Measuring the angular misorientation around the  $x$ -axis can therefore be reduced to measurements of the lateral deflection of the Bragg diffracted beam on the detector plane.

In section X-ray diffraction topography an entire section in the crystal contributes to the image (Fig. 2.14). Regions in that section exhibiting a misorientation around the  $x$ -axis laterally deflect the Bragg diffracted beam that they emit. The Bragg diffracted beams of those regions might cross or superpose on the detector plane. Under these circumstances a pixel on the detector can hardly be associated to a given region in the illuminated section of the crystal and the Bragg diffracted beams of each region cannot be distinguished. Therefore the lateral deflection  $\Delta y$  cannot be measured. Attempts to solve that problem numerically and project back every Bragg diffracted beam in each pixel of the detector, have been reported [Mikulik 08, Huber 09]. We measure  $\Delta y$  by using pinhole X-ray diffraction topography (Chap. 2.3.4). By crossing our two multisection sets, we generate  $50 \mu\text{m} \times 50 \mu\text{m}$  pinhole beams that are spaced by 1 mm along the  $y$ - and along the  $z$ -axis. A pinhole beam only illuminates a single rod of the crystal. The regions around that rod are not illuminated and do not contribute to the image on the detector and lateral deflections  $\Delta y$  of the beam are revealed.

As it was mentioned the angular misorientation around the  $x$ -axis has almost no influence on  $\omega$  (Eq. 3.2) so recording a stepwise rocking curve is not necessary. We therefore record a continuous rocking curve where the camera is permanently exposed while the crystal is rocked by  $\Delta\omega$  around  $\omega$ . As a result we obtain an integrated rocking curve image. It consists of several rods, where the length of the rods is the projection of the crystal depth. Each rod corresponds to a defined volume ( $50 \mu\text{m} \times 50 \mu\text{m} \times$  threading thickness) in the crystal. The shape of the rod on the detector may be deformed according to the value of  $\alpha_x$ . The lateral deflection of the Bragg diffracted beam is proportional to the distance  $D$  between the crystal and the camera (Eq. 3.3). Therefore we increase  $D$  as much as possible, typically to  $D = 1,5 \text{ m}$ .

Recording an entire rocking curve in only one image requires a longer exposition time because the crystal must be rocked by  $\Delta\omega$  during the exposition. As mentioned in Chap. 2.3.2, a region in the crystal only Bragg diffracts X-rays for a well defined orientation of the crystal given by Eq. (2.9). Logically when rocking the crystal by  $\Delta\omega$ , a region is not Bragg diffracting most of the acquisition time and the detector remains unexposed at the concerning part. On the other side a sufficient illumination of the detector is necessary to get a decent signal to noise ratio. The acquisition time per exposure therefore has to be longer than in stepwise rocking curve imaging.

Unfortunately longer exposition times heat up the sensor in a digital camera and raise the noise level. A further problem arises due to the slightly different light sensitivity of each pixel on the sensor. These variations lead to the so called "hot pixels" that constantly exhibit a higher count rate, especially at longer exposure times. The acquisition time of digital cameras therefore is technically limited. We work around that limitation by using shorter

exposure times, typically up to 15 s, but taking several images of the same scene, sometimes up to 20. The single exposures are summed up afterwards and we obtain integrated images with a better signal to noise ratio. We additionally take “darkfield” images where the camera is exposed while there is no incident beam. A darkfield reveals the hot pixels of the sensor. By subtracting the darkfield image from an integrated image, the hot pixels are removed.

As in step scanning (Chap. 3.4.2) the multi-pinhole method only investigates a small part of the entire crystal. To obtain information about other regions as well, the multisection device is displaced and the procedure is repeated. With a multi-pinhole beam as we use ( $50\ \mu\text{m} \times 50\ \mu\text{m}$  beams spaced by 1 mm along the y- and along the z-axis) 20 integrated rocking curve images are needed to fill an entire row and 20 rows are needed to scan the crystal part that is illuminated by the incident beam, resulting in 400 integrated rocking curve images. The pure exposure time to record such a big amount of data can rise up to  $400 \times 20 \times 15\ \text{s} \approx 35\ \text{h}$ . Together with the step-scanning procedure the experiment would last too long. Therefore we only register integrated rocking curve images for 9 or 25 positions of the multisection device. As before the motor position is calibrated with the angular Bragg position at each position of the multisection device. The positions are ordered in a square of  $3 \times 3$  to  $5 \times 5$  as is shown in Fig. 3.13. The data allows to obtain the angular misorientation in a local region. The information in the remaining regions, where no data is recorded, might be obtained by interpolation methods.

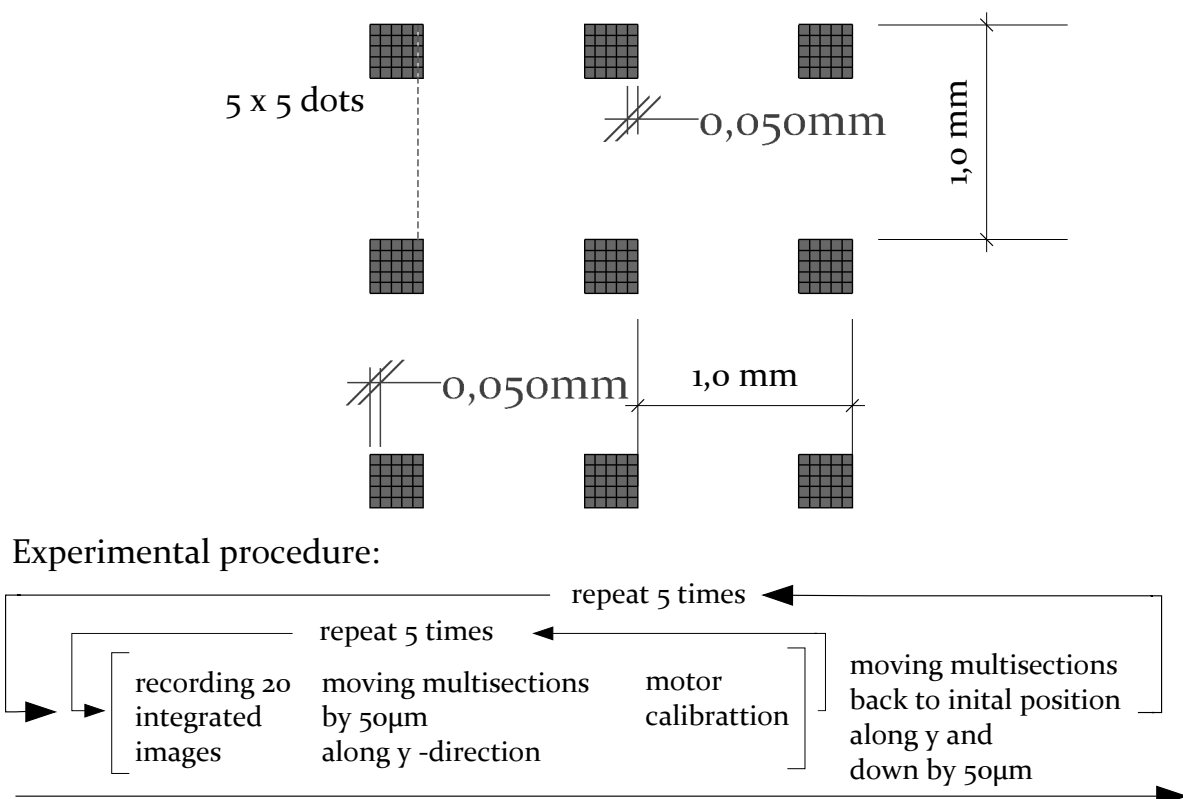


**Figure 3.13:** Arrangement of 25 positions of the multisection device to a  $5 \times 5$  square; experimental procedure in multi pinhole X-ray diffraction topography.

### 3.4.4 Deforming the crystal

After step-scanning the two Bragg diffracted images and registering multi-pinhole integrated rocking curve images on one of them, we have enough information gathered to

deduce the complete angular misorientation and all components of the curvature tensor (Chap. 1.15). In a next step the crystal is loaded by a pneumatic press (Fig. 3.8) in order to induce plastic deformation. We typically load the crystal by a pressure of 0.2 MPa for 15 to 45 minutes. The anisotropic deformation of crystalline ice (Chap. 1.3) leads to a very different evolution of the angular misorientations of the basal and the prismatic lattice plane families. The loading must not be too long because we wish to investigate the early stages of deformation.

Once the load is removed the elastic stresses in the crystal are relaxed instantaneously, however creep recovery may take a long time before it becomes negligible. We therefore wait for up to one hour before continuing the experiment. The plastic deformation remains after the loading, the crystalline structure has been transformed in a different state. The deformation of the sample environment normally implies a disorientation of the crystal and the loss of the Bragg diffracted image on the detector. They need to be found again by slightly moving the rotation motors by a few degrees. Once the reference orientation (Fig. 3.9) is retrieved the crystal is scanned again, in the same manner as is described above, Fig. 3.14. In such a way, depending on the incident beam intensity and the experimental difficulties two to four states of a crystal can be studied in a one week experiment.

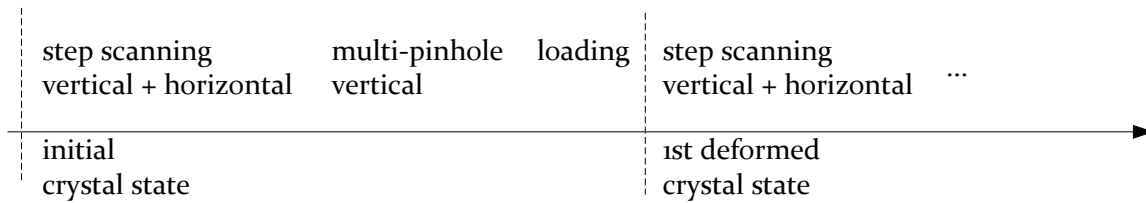


**Figure 3.14:** Experimental procedure

### 3.4.5 Data usage

We have described the procedure allowing to record the data required to access quantitative values for the sample distortion, in particular the curvature tensor. The data processing that is necessary to obtain those parameters is described in the following chapter.

# Data analysis

This chapter describes the data analysis that leads from the recorded raw data to quantitative results. An important part of the data analysis is computer-based and was carried out by using the proprietary software *Mathworks Matlab* (Matlab) that was running on a calculation machine connected to the ESRF network. These machines, internally called *Coral*, provide a 2.6 GHz AMD Opteron 64 bit processor and 8 GB of memory. Writing the Matlab scripts for the data analysis was a part of the thesis.

## 4.1 Recorded raw data

Only a small part of the recorded data is registered on films. They are mainly used for orienting the crystal in space and give a rough idea about the crystalline quality. The raw images recorded by our digital cameras are stored in an electronic form. The cameras used in our experiments, the FreLoN [Labiche 96] and the pco.2000, provide a dynamic range of 14 bit what results in  $2^{14} = 16384$  possible intensity values. Both cameras use CCD sensors composed of  $2048 \times 2048$  pixels. The images are saved in a *ESRF data file* (EDF) [Daly 96]. The EDF format supports 16 bit data so that  $2^{16} = 65536$  intensity values can be distinguished. This is much more than our cameras provide and the last two bits in our EDFs may be considered as empty. The maximal disk space taken by an image recorded with our cameras and stored in EDF is  $2048 \times 2048 \times 16 \text{ bit} = 67108864 \text{ bit} = 8388608 \text{ byte} = 8 \times (1024)^2 \text{ byte} = 8 \text{ MB}$ . The size of an EDF can be reduced by restricting the camera's field of view to a region of interest (ROI). By selecting a ROI the CCD read out process is sped up as well. Beside the image itself, additional information is stored in the header of an EDF. This information is acquisition time & date of the image, exposure duration, storage ring current, position of all motors and all detector values. The images need to be imported into Matlab for further processing. A script developed by the grain tracking team at the beamline ID19/ESRF allows easy importing of EDF files.

## 4.2 Step scanning data analysis

The step scanning procedure (Chap. 3.4.2) produces RCI image stacks where each stack corresponds to a defined position of the multisection device or otherwise said, to a well defined region in the crystal. That region is composed of  $50 \mu\text{m}$  thick sections spaced by 1 mm. Each RCI image stack is analysed independently. As shown in Fig. 4.1-LHS, an RCI image stack can be regarded as a discrete scalar function  $I(i, j, k)$  in 3D space, where  $i, j, k = 1, 2, 3, \dots$ . The two components  $(i, j)$  describe the detector plane  $(y, z)$ , whereas  $k$  describes the lattice plane orientation  $\omega$ . The discretisation of the components  $(y, z)$  is given by the pixelsize of the camera, whereas the  $\omega$  step corresponds to the angular stepsize in the RCI scan. By

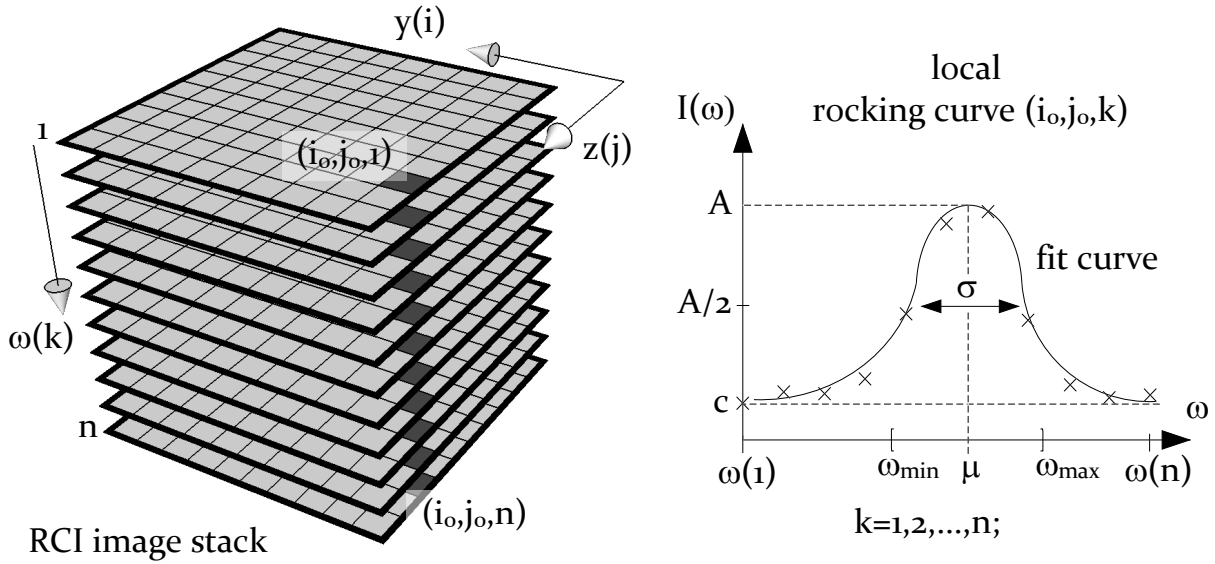


**Figure 4.1:** LHS: RCI image stack represented as a scalar function  $I(i, j, k)$  on a 3D space. The  $i, j$  represent the  $y$ - and the  $z$ -axis on the detector plane and  $k$  the angular orientation  $\omega$  of the crystal. RHS: the local rocking curve in the detector pixel  $(i_0, j_0)$  is extracted from the RCI image stack by fixing  $i = i_0$  and  $j = j_0$ :  $I(i_0, j_0, k)$ ,  $k = 1, \dots, n$ . Also shown is the fit function, including the angular peak position  $\mu$  on the  $\omega$ -axis and  $\sigma$ , associated to the FWHM of the rocking curve. The values  $\omega_{\min}$  and  $\omega_{\max}$  define the interval of confidence that characterises the angular resolution of the experiment.

fixing  $k$  to a value  $k_0$  we obtain the Bragg diffracted image  $I(i, j, k_0)$   $i, j = 1, 2, \dots$  at the given crystal orientation  $\omega(k_0)$ . By fixing the spatial components  $(i, j)$  to  $(i_0, j_0)$  we obtain a local rocking curve  $I(i_0, j_0, k)$   $k = 1, 2, \dots, n$ , shown in Fig. 4.1-RHS. That local rocking curve only contains information about the region of the crystal that was Bragg diffracting X-rays on the pixel  $(i_0, j_0)$  of the detector. Every local rocking curve in a RCI image stack is analysed independently and the results of all rocking curves in an RCI image stack are arranged in 2D maps that are associated to regions illuminated by the incident beam. In our experiment these regions are  $50 \mu\text{m}$ -thick sections that are spaced by  $1 \text{ mm}$  (Chap. 3.4.2).

### 4.2.1 Local rocking curve analysis

A local rocking curve is analysed by fitting a mathematical function that models its shape. That function must have parameters that describe the angular width, the position and the intensity of the rocking curve. Our fit model is a superposition of a constant value  $c$  and a 1D Gauss function:

$$f_{A,\mu,\sigma,c}(\omega) = A \exp \left[ -\frac{1}{2} \left( \frac{\omega - \mu}{\sigma} \right)^2 \right] + c. \quad (4.1)$$

Although rocking curves are mostly described by other functions, we approximate the Gaussian shape for simplicity. In our fit the parameter  $A = \max_k [I(i_0, j_0, k)]$  describes the maximally Bragg diffracted intensity. The parameter  $\mu$  describes the angular position where the crystal is diffracting the most. That angular position corresponds to the orientation of the lattice planes  $\omega = \theta_B$ , Eq. 2.9. The parameter  $\sigma$  describes the full width at half maximum (FWHM) of the rocking curve and is correlated with the inner mosaicity of the region emitting the local rocking curve. Last but not least the parameter  $c$  is added to take into account the background noise level of the digital camera.

The Matlab scripts written for the data analysis load an entire RCI image stack into the RAM and fit a Gaussian to each local rocking curve  $I(i_0, j_0, k)$ . Internal functionalities of the *Matlab Curve Fitting Toolbox* allow non-linear fits based on established numerical algorithms such as *non least square means*. Although fitting options (number of iterations, precision, etc.) can be set, the calculation time for a fit could not be reduced below 0.1 s with the given computational possibilities. This is by far too long for a reasonable duration of the data analysis. For example, if no ROI is chosen,  $2048 \times 2048$  rocking curves per RCI image stack need to be fitted, resulting in almost 120 h calculation time. In addition, at least 21 RCI image stacks are recorded per Bragg diffraction image, two Bragg diffraction images per deformation state are investigated and at least two deformation states of the sample are induced. The curve fitting would therefore last for months.

To reduce the calculation time, a different fitting approach is chosen. A local rocking curve  $I(i_0, j_0, k)$ ,  $k = 1, 2, \dots, n$  is considered as a sample of a *statistical population* which is assumed to be normally distributed on  $n$  different values of  $\omega$ . Here  $n$  is the number of angular steps in a RCI image stack, Fig. 4.1. The amount of single elements  $N$  in that sample is equal to the integrated intensity and is obtained by summing up the counts of the local rocking curve:

$$N(i_0, j_0) = \sum_{k=1}^n I(i_0, j_0, k). \quad (4.2)$$

Under these preconditions point estimations  $\hat{\mu}(i_0, j_0)$  and  $\hat{\sigma}(i_0, j_0)$  for the two Gaussian parameters  $\mu(i_0, j_0)$  and  $\sigma(i_0, j_0)$  can be constructed:

$$\hat{\mu}(i_0, j_0) = \frac{1}{N} \sum_{k=1}^n I(i_0, j_0, k) \quad (4.3)$$

$$\hat{\sigma}(i_0, j_0) = \frac{1}{\sqrt{N-1}} \sum_{k=1}^n [I(i_0, j_0, k) - \hat{\mu}]^2. \quad (4.4)$$

These point estimations are the “best unbiased” for a normally distributed statistical population [Georgii 02, Fisz 80]. The statistical approach allows a much faster fitting procedure and leads to precise results under the condition that the constant  $c(i_0, j_0)$  in Eq. 4.1 is subtracted from the rocking curve before the calculation. The value of  $c(i_0, j_0)$  is chosen by hand and most often corresponds to the minimal value of the rocking curve,  $\min_k [I(i_0, j_0, k)]$ . It is correlated with the background noise level of the digital camera and is the same for every local rocking curve in a RCI image stack and even in an entire step scanning data set:  $c(i_0, j_0) = c(i, j)$ . Logically only one value of  $c(i, j)$  for an entire step scanning data set is chosen.

The described procedure considerably reduces computing time. It is valid when applied to rocking curves characterised by a one peak shape. However it provides inaccurate results for more complex peak profiles. For instance multiple peaks in a rocking curve are not detected. A multi peak profile may occur when the associated voxel in the crystal exhibits several distinct crystalline orientations. This is possible in strongly distorted regions or during the polygonisation process. A superposition of two rocking curves from different regions of the crystal in one pixel of the detector due to misorientations around the direction of the direct beam wave vector is also possible when the deformation of the crystal increases (Fig. 3.12). In order to be able to neglect multiple peaks in one pixel of the camera due to lateral deviations of the Bragg diffracted beam, we reduce the distance between the sample and the camera as much as possible. Further on we have verified that complex, non one peak shape, rocking curve profiles do not occur frequently but are very rare in our high quality crystals and in the early stages of deformation.

The “statistical” curve fitting procedure is applied to every local rocking curve  $(i, j)$  in an RCI image stack. As a result we obtain the three parameters with a physical meaning,  $A(i, j)$ ,  $\mu(i, j)$  and  $\sigma(i, j)$ , that may be represented in 2D maps as for instance shown in Fig. 5.5.

**Integrated image** The curve fitting mentioned above extracts three parameters out of a RCI image stack. A fourth and very important parameter, the integrated intensity  $N$ , already introduced before and defined in Eq. 4.2, is obtained by summing up the counts of a local rocking curve. It can be considered as a projection of the RCI image stack on the  $(y, z)$ -plane.

**Angular resolution** As already mentioned the resolution of the angular misorientations we measure depend on the chosen angular stepsize during the step scanning experiment. The following paragraph wishes to go further and to quantify the resolution of our measurements. To do so, the model of the rocking curve as a sample of a normally distributed statistical population is consequently reused. Based on our assumptions we can construct a confidence interval [David 05] for the point estimation  $\hat{\mu}$ , Eq. 4.3. A confidence interval is surrounding the point estimation:  $\omega_{\min} < \hat{\mu} < \omega_{\max}$  as is shown in Fig. 4.1 and can be regarded as a resolution of the measurements. Its endpoints  $\omega_{\min}, \omega_{\max}$  are chosen in a way that the probability  $P$  to find the real parameter  $\mu$  in the interval is equal to the confidence level  $\gamma$  [Georgii 02, Fisz 80, David 05]:

$$P(\mu \in [\omega_{\min}; \omega_{\max}]) = \gamma = 1 - a \quad (4.5)$$

For a normally distributed statistical population with an unknown parameter  $\sigma$  the interval of confidence for  $\mu$  is symmetrical around the point estimation  $\hat{\mu}$ :

$$[\omega_{\min}; \omega_{\max}] = \left[ \hat{\mu} \pm \frac{\hat{\sigma}}{N} \cdot t_{N-1} \left( 1 - \frac{a}{2} \right) \right], \quad (4.6)$$

where  $t_{N-1}(1 - \frac{a}{2})$  is the Student’s t-distribution for  $N - 1$  degrees of freedom at the confidence level  $1 - \frac{a}{2}$  [David 05]. It should also be mentioned that according to Eq. 4.6, the confidence interval (and with it the resolution) depends on the integrated intensity  $N$  that is different for each local rocking curve. Theoretically this implies a different misorientation resolution for every local rocking curve in a RCI image stack. For simplicity reasons we choose a constant resolution factor that is equal to the biggest confidence interval of the RCI image stack. Generally the integrated intensity  $N(i_0, j_0)$  of a local rocking curve is high enough to approximate  $t_{N-1}(1 - \frac{a}{2})$  by  $t_{\infty}(1 - \frac{a}{2})$ . Values of the t-distribution can be found in statistical tables. The calculations prove that in general our resolution for angular misorientations in RCI is at least a fifth of an angular step in RCI:

$$\Delta\alpha_i \geq \frac{\Delta\omega}{5n} \quad i = y, z \quad (4.7)$$

## 4.2.2 Calculating misorientation

The procedure is applied to all RCI image stacks recorded for a Bragg diffraction. Typically at least 21 RCI image stacks are recorded for each Bragg diffraction and each crystalline deformation state. As a result we obtain 21  $\mu(i, j)$ -maps. These maps only contain the motor positions where local angle  $\omega(i, j)$  is equal to the Bragg angle. To transform these values into angular misorientation components  $\alpha(i, j)$  (Fig. 1.8) we refer them to an angle  $\phi$  that is associated to a reference orientation (Eq. 1.10):

$$\alpha(i, j) = \mu(i, j) - \phi \quad \forall i, j. \quad (4.8)$$

where  $\alpha$  is the angular misorientation around the z-axis:  $\alpha_z$ , when the beam is horizontally Bragg diffracted and  $\alpha_y$  if vertically.

The choice of a reference orientation is arbitrary. As shown in Chap. 1.4, relative angular misorientations between two regions  $(i_1, j_1)$  and  $(i_2, j_2)$  do not depend on  $\phi$ :

$$\alpha(i_1, j_1) - \alpha(i_2, j_2) = \mu(i_1, j_1) - \phi - \mu(i_2, j_2) - (-\phi) \quad (4.9)$$

$$= \mu(i_1, j_1) - \mu(i_2, j_2) = \quad \forall \phi. \quad (4.10)$$

A region that exhibits a lattice orientation  $\mu(i, j)$  equal to the reference orientation  $\phi$  is considered to have undeformed lattice planes:  $\alpha(i, j) = 0$ . As reference orientation we choose the value  $\phi$  where the sum of angular misorientations over all regions of the crystal (this includes all RCI image stacks) becomes zero:

$$\sum_i \sum_j \alpha(i, j) = \sum_i \sum_j \mu(i, j) - \phi = 0 \quad (4.11)$$

Since this is a linear equation system, the solution is unique and only one reference orientation  $\phi$  as defined by Eq. 4.11 exists. The physical interpretation of our choice is that under any deformation state the condition  $\omega = \theta_B$  is still fulfilled and the value of the Bragg angle remains constant. One could say that the loading of our crystal induce crystalline deformation but does not change the global lattice characteristics, for instance the shape of the unit cell.

### 4.3 Multi pinhole data analysis

The data collected with multi pinhole X-ray diffraction topography (Chap. 3.4.3) is generally more prone to noise because of the longer exposure times. The first step of the data analysis is to create corrected images out of the collected data. A corrected Bragg diffracted image  $I_{\text{corr.}}(y, z)$  is calculated by summing up the  $n$  individual exposures  $I_k(y, z)$ ,  $k = 1, 2, \dots, n$  and subtracting  $n$ -times the darkfield image  $I_{\text{dark}}(y, z)$ :

$$I_{\text{corr.}}(y, z) = \sum_{k=1}^n I_k(y, z) - nI_{\text{dark}}(y, z). \quad (4.12)$$

As a result we obtain corrected Bragg diffracted images that contain the integrated intensity values of the emitting regions of the crystal. The arrangement of the regions is shown in Fig. 3.13. Each corrected Bragg diffracted image is composed of several rods. The shape of a rod is associated to the radial misorientation around the x-axis (Fig. 1.8), by Eq. (3.3). Every rod image in a multi pinhole X-ray diffraction data set is analysed independently. The analysis is presented in the following part.

#### 4.3.1 Rod image analysis

Fig. 4.2 shows a theoretical example of a rod image on the detector plane. If there was no misorientation around the x-axis, the rod would be straight and parallel to the pixel columns of the detector and they would all be spaced by the same distance (1 mm in our case). The example shown in Fig. 4.2 indicates a negative (Fig. 3.1) misorientation of the Bragg diffracting lattice planes around the x-axis at the X-ray entrance crystal surface because the rod is bent to the left in the upper part. When propagating through the crystal thickness the Bragg diffracting lattice planes describe a positively oriented spiral as it occurs in a screw. For a better understanding please have a look at Fig. 3.12 as well.

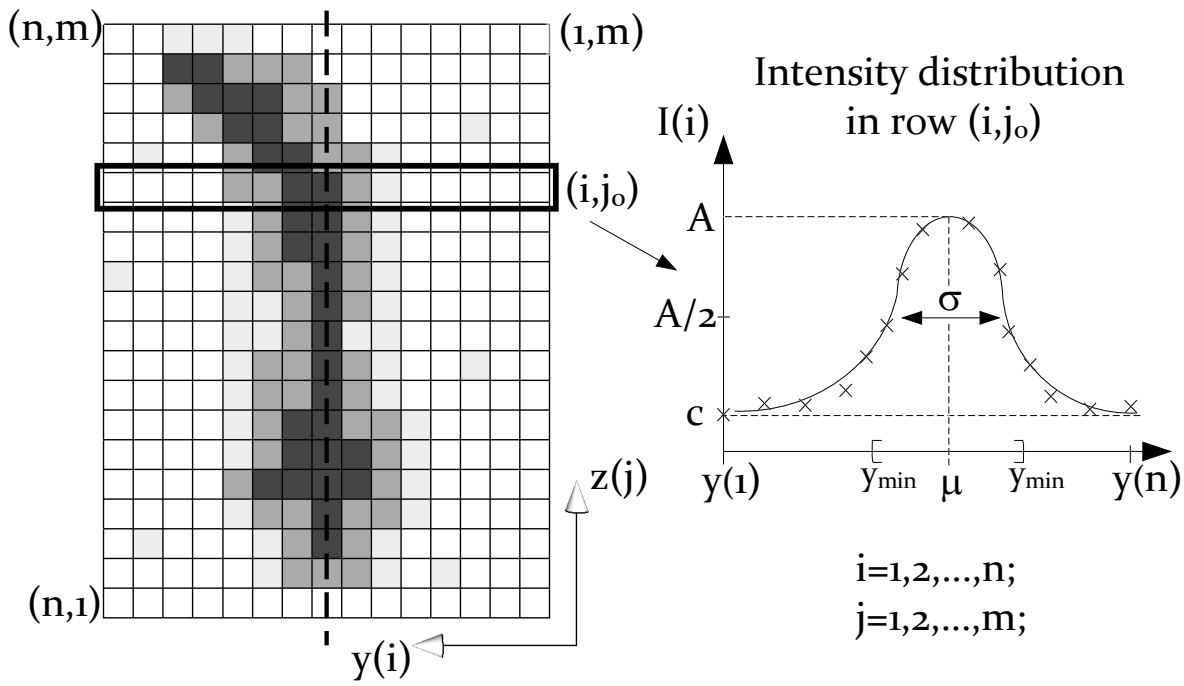


**Figure 4.2:** Pinhole X-ray diffraction topography - LHS: Intensity distribution on the detector in the shape of a rod; RHS: Intensity distribution in a row  $(i, j_0)$ ,  $i = 1, \dots, m$  of the rod image and a curve fit characterised by the parameters  $\mu, \sigma$ ; the interval  $[y_{\min}, y_{\max}]$  indicates the interval of confidence of the measurement.

The rod may also exhibit a varying thickness. Differences in thickness of the rod occur due to different inner mosaicities of the investigated voxels. High mosaicity means a high amount of differently oriented regions that Bragg diffract X-rays in different directions. As a result the shape of the rod is broadened.

To analyse a single rod image, a quantitative evaluation of the alignment and the thickness of a rod is needed. A rod image as shown in Fig. 4.2-LHS, can be considered as a  $n$  by  $m$  data matrix, where the components  $i = 1, 2, \dots, n$  and  $j = 1, 2, \dots, m$  represent pixel rows and columns on the detector plane. Please note that we maintain here our conventions about the experimental coordinate system (Fig. 3.1), so the origin is in the down right corner of the image and the positive direction of the y-axis shows to the left. To evaluate the shape of the rod, each row  $(i, j_0)$  of the data matrix is analysed independently. The intensity distribution in that row can be plotted in a graph, exemplary shown in Fig. 4.2-RHS. We consider the intensity to be normally distributed over the  $n$  pixels of the  $j_0$ -th row. Once again the two parameters  $\mu$  and  $\sigma$  describe the position and the FWHM of the Gaussian (Eq. 4.1). As before we do not use the numeric algorithms in Matlab to fit a curve to the data but consider the measurement as a sample of a normally distributed population, what allows us to use the point estimations in Eq. 4.3 and Eq. 4.4. Only the indices need to be adapted:

$$\hat{\mu}(j_0) = \frac{1}{N(j_0)} \sum_{i=1}^n I(i, j_0) \quad (4.13)$$

$$\hat{\sigma}(j_0) = \frac{1}{\sqrt{N(j_0) - 1}} \sum_{i=1}^n [I(i, j_0) - \hat{\mu}]^2, \quad (4.14)$$

where  $N(j_0)$  is the sum of the pixel count over all pixels in the row  $j_0$ :

$$N(j_0) = \sum_{i=1}^n I(i, j_0). \quad (4.15)$$

The parameter  $\hat{\mu}(j)$  describes the position and  $\hat{\sigma}(j)$  the FWHM of the rod in the row  $j$ . The procedure is repeated for each row  $j$  of the rod image,  $j = 1, 2, \dots, n$ , so that  $n$  values for the two parameters are obtained. They are arranged in a 1-by- $n$ -array.

### 4.3.2 Calculating misorientation

The procedure is repeated for every rod in a Bragg diffraction image (Fig. 5.25) and every of the recorded Bragg diffraction images. We obtain a quantity of  $\hat{\mu}$  and  $\hat{\sigma}$  vectors. Each of them contains information about a  $50 \mu\text{m} \times 50 \mu\text{m} \times 4 \text{mm}$  volume in the crystal. The  $\hat{\mu}$  arrays contain the pixel positions on the detector associated to the centre of mass of a the rod intensity. To deduce the angular misorientation of the diffracting lattice planes around the x-axis:  $\alpha_x(i, j)$ , the values need to be related to a reference position. A possible reference position for a rod is indicated in Fig. 4.2 as a dashed line. Each rod image on a Bragg diffraction image needs its own reference position, however the positions cannot be chosen independently from each other. They must respect the arrangement of the pinhole beams during the experiment. As shown in Fig. 3.13 the pinholes are horizontally spaced by 1 mm and are vertically in the same line. The reference positions for two rods that are vertically one over the other, must be on the same vertical line. For two rods that are horizontal neighbours, the reference position need to be displaced by 1 mm on the detector plane. We call the reference position  $\phi$  again. The reference is a position on the detector and is associated to a crystalline reference orientation  $\phi_0$  (Eq. 1.10). The lateral displacement of the Bragg diffracted beam on the detector  $\Delta y$  (Eq. 3.3) is calculated for each row of every rod by:

$$\Delta y(j) = \mu(j) - \phi. \quad (4.16)$$

As before the choice of a reference position is arbitrary and does not modify the relative lateral displacement of two rows of a multi pinhole X-ray diffraction data set. Again we choose a value  $\phi_0$  for the reference position so that the sum of all lateral displacements of a data set become zero:

$$\sum_j \Delta y(j) = 0, \quad (4.17)$$

The equation associated the positions of the rods on the detector  $\mu(j)$  to lateral displacements  $\Delta y(j)$ . Those are put into Eq. 3.3 that provides the angular misorientations around the x-axis:  $\alpha_x(j)$ .

## 4.4 Volume composition

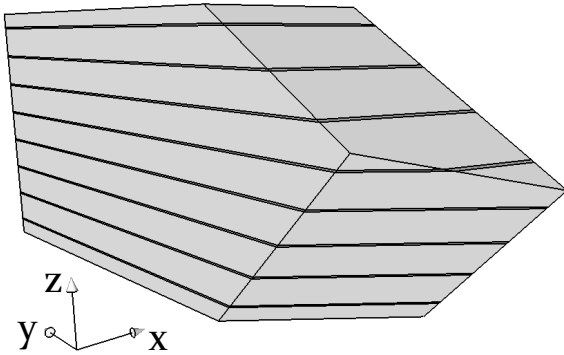
In order to calculate the components of the curvature tensor it is necessary to rearrange the obtained results into a 3D matrix that represents the illuminated volume of the crystal. Until now the results issued from the step scanning analysis are stored in 21 sets of four 2D-maps for each parameter  $A, \mu, \sigma, N$ . An example for such a map is shown in Fig. 5.4.

The pinhole X-ray diffraction topography results are stored in many 1-by- $n$  arrays, where each of them contains information about a the  $50 \mu\text{m} \times 50 \mu\text{m} \times 4 \text{mm}$  volume in the crystal (Fig. 4.5).

### 4.4.1 Composing step scanning maps to a crystal volume

Each set of four maps contains information coming from a region of the crystal that is composed of  $50\ \mu\text{m}$ -thick sections spaced by  $1\ \text{mm}$ . Depending on the experimental geometry (vertically or horizontally Bragg diffracted beam), the sections are horizontally or vertically aligned (Fig. 2.14). The two possible arrangements of the regions in the crystal volume are shown in Fig. 4.3. Due to size of the incident beam at BM05 (Chap. 3.2) there are typically six to nine horizontal sections or 13 to 15 vertical sections in per map.

horizontally aligned sections



vertically aligned sections

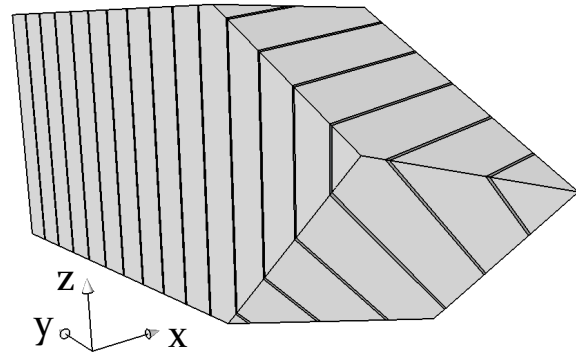


**Figure 4.3:** Distribution of the section images from one RCI image stack over the volume of the crystal; LHS: vertically Bragg diffracted spot, RHS: horizontally Bragg diffracted spot.

The crystal regions of two adjacent sets are displaced by  $50\ \mu\text{m}$  perpendicularly to the sections, so that the regions belonging to the first 20 sets entirely fill the crystal volume. For the 21st set the multisection device has been displaced by  $20 \times 50\ \mu\text{m} = 1\ \text{mm}$  so that the region correlated to the 21st set is the same as for the 1st one. The purpose of the 21st set is to verify if the defect arrangement of the sample was not evolving during the scan time.

In order to correctly rearrange the maps into a 3D matrix that represents the crystal volume, the first section image of the first set is put into an empty 3D matrix. Then the first section of the second set is put next to it, and so on until we arrive at the 20th set. Then the second image of the first set is put into the matrix. The filling procedure is continued until every section finds its place in the 3D matrix. The proper order is shown in Fig. 4.4 which is a zoom on the crystal already illustrated in Fig. 4.3.

A Matlab script has been written, that automatically recognises a section shape in a map and then puts it into the right place in the 3D matrix. It works for both experimental geometries (vertically and horizontally Bragg diffracted beam). As a result of the filling procedure we obtain a 3D crystal volume matrix for every of the four parameters  $A(i, j, k)$ ,  $\mu(i, j, k)$ ,  $\sigma(i, j, j)$  and  $N(i, j, k)$ . The indices  $(i, j, k)$  now represent the spatial dimensions  $(x, y, z)$ .

### 4.4.2 Composing pinhole vectors to a crystal volume

The data issued from pinhole X-ray diffraction topography is composed of many 1-by- $n$ -arrays, where each of them contains information about a  $50\ \mu\text{m} \times 50\ \mu\text{m} \times 4\ \text{mm}$  volume in the crystal. The regions that are associated to one Bragg diffraction image (Fig. 5.9) are distributed over the 3D crystal volume matrix (Fig. 4.5). A Matlab script that reorganises the 1D arrays in a 3D crystal volume matrix has been written as well. The sum of  $50\ \mu\text{m} \times 50\ \mu\text{m} \times 4\ \text{mm}$  volumes does not fill the entire crystal volume that would have been illuminated by the incident beam without the pinholes. As a result an important part of the

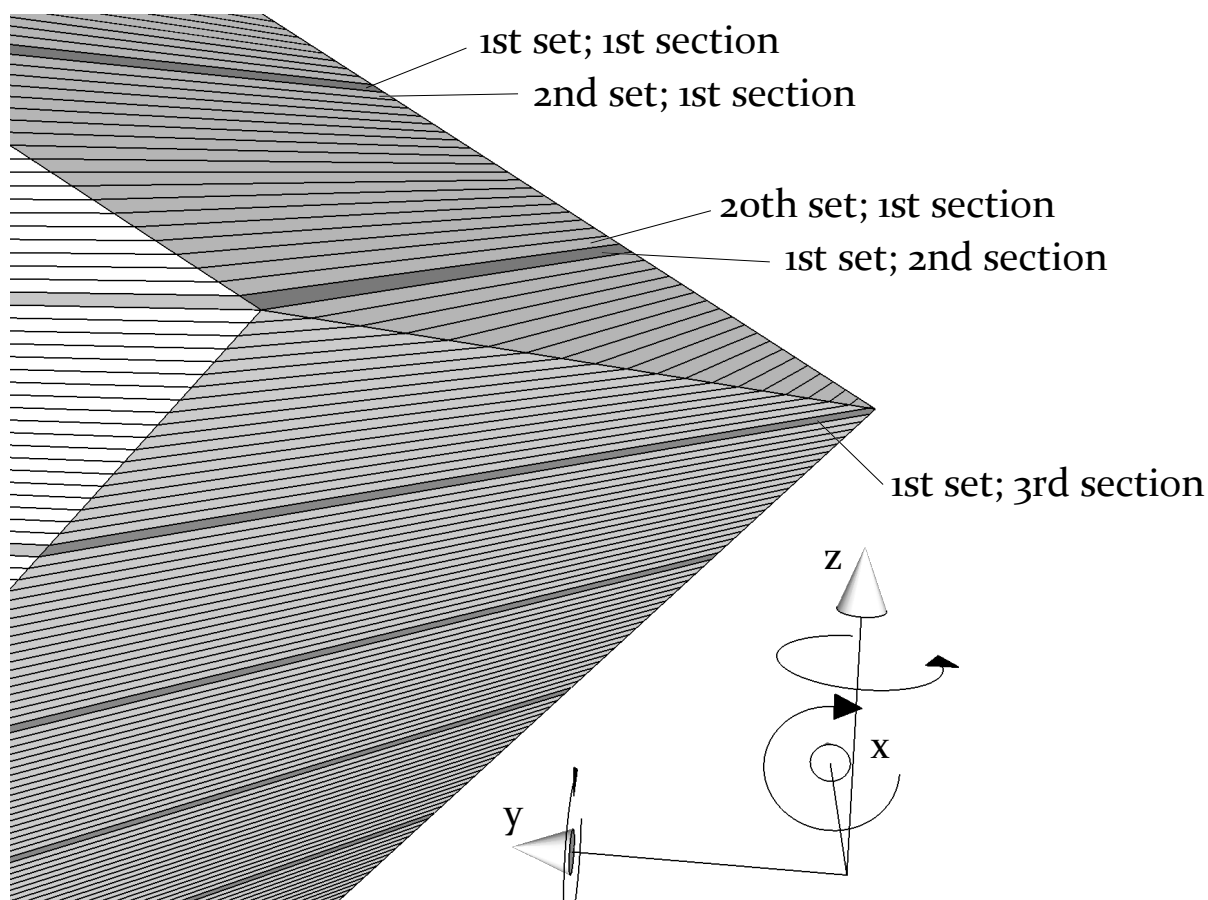


**Figure 4.4:** Section arrangement according to sets into a 3D crystal volume.

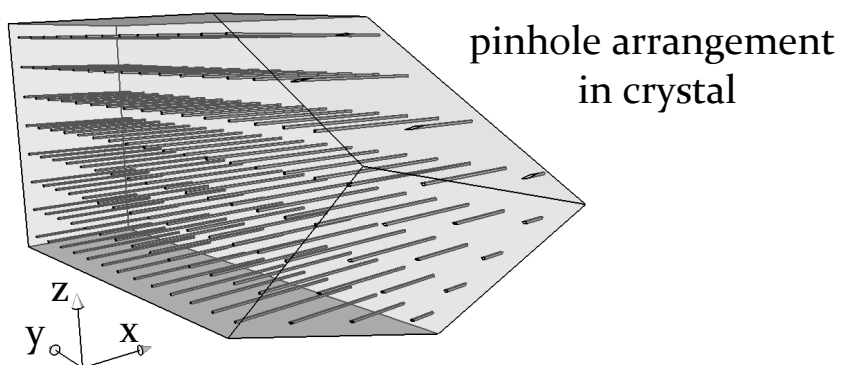


**Figure 4.5:** Arrangement of regions in the crystal correlated to rods in one pinhole Bragg diffraction image.

3D crystal volume matrix  $\mu(i, j, k)$  remains empty. Here again the indices  $(i, j, k)$  represent the spatial dimensions  $(x, y, z)$

### 4.4.3 Axis scaling in 3D crystal volume matrix

The assembly of 3D crystal volume as explained above rearranges the results in 3D matrices. These matrices exhibit different resolutions along the three spatial dimensions depending on the experimental procedure and the experimental geometry.

**x-scaling:** In step scanning as well as in multi pinhole X-ray diffraction topography, the sample dimension along the x-axis (the thickness) is projected on the detector plane. That projection shrinks the image as is shown in Fig. 4.6. Therefore the spatial resolution of our measurements along the x-axis not only depends on the pixelsize on the detector, but on the Bragg angle  $\theta_B$  as well. The variables of the following part can be found in Fig. 4.6. There is

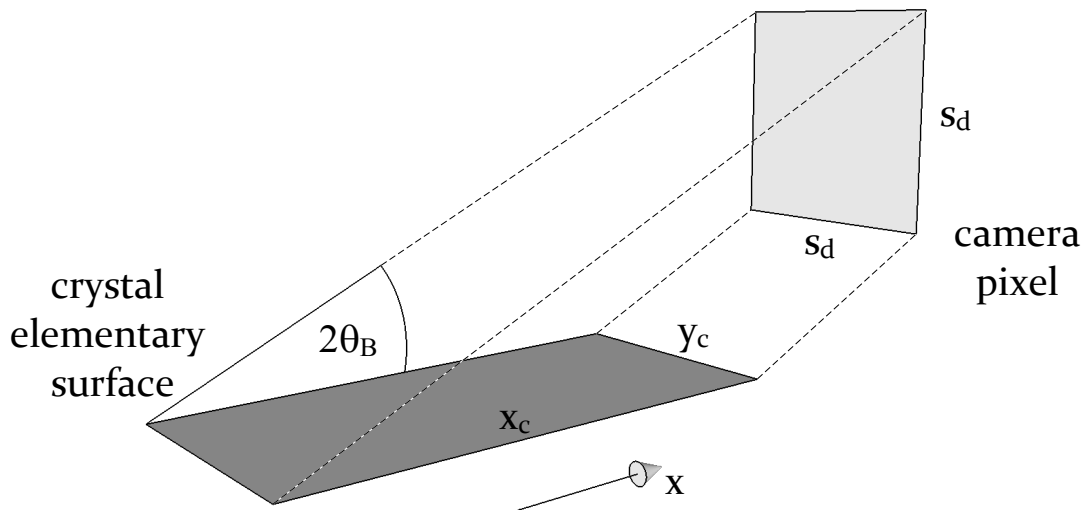


Figure 4.6: Shrinking of the Bragg diffraction image due to projection.

no shrinking along the y-axis and we get  $y_c = s_d$ , where  $s_d$  is the edge length of a pixel on the detector. The dimensions on the x-axis  $x_c$  are projected on  $s_d$  on the detector. We obtain  $x_c = s_d / \tan 2\theta_B$ .

Our cameras and their optical systems provide quadratic pixels with a pixelsize of approximately  $s_d = 10\mu m$  and our Bragg angle is approximately  $\theta_B = 5^\circ$  for both Bragg diffractions. The scaling of our crystal volume matrices along the x-axis therefore is approximately  $56\mu m$ .

**y- and z- scaling for step scanning:** In step scanning the remaining two axis of the crystal volume matrices have a different scaling as well. For a vertically Bragg diffracted image, the resolution along the z-axis is given by the slitsize of the multisections ( $50\mu m$  in our case) and along the y-axis by the detector resolution ( $10\mu m$ ), whereas in horizontal geometry, the scaling corresponds to the y-axis.

**y- and z- scaling for pinholes:** In multi pinhole X-ray diffraction topography, the scaling is the same for the y- and the z-axis because it is given by the size of the pinhole beams. The pinholes are quadratic and  $50\mu m \times 50\mu m$  big.

The crystal volume matrices that result from different experimental procedures therefore have different resolutions along a space axis. Actually the elementary region in the crystal that is represented by an entity of a crystal volume matrix is not even rectangular but a parallelepiped due to the projection effect. The shape of the elementary volumes in the crystal volume matrix entity are shown in Fig. 4.7.

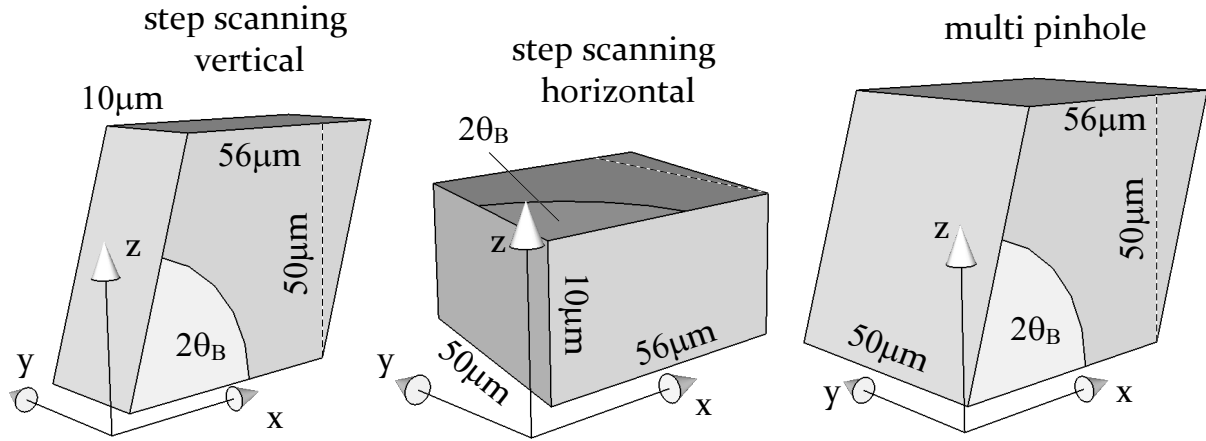


**Figure 4.7:** Size and shape of the elementary volumes represented by a crystal volume matrix entity.

## 4.5 Calculating curvature tensor

To make conclusions on the geometrically necessary dislocation density, the curvature tensor must be calculated from the angular misorientation matrices. There are three 3D volume matrices  $\alpha_i(l, m, n)$   $i = x, y, z$  that correspond to the angular misorientation components around the axis of the coordinate system (Fig. 1.8). The coordinates  $(l, m, n)$  describe a discretisation of the 3D crystal volume (Fig. 4.7). According to Eq. 1.16 misorientation components are directly associated to the curvature tensor. We calculate the curvature tensor components by:

$$K_{ij} = \alpha_{i,j} \quad i, j = x, y, z; \quad (4.18)$$

The formula is derived in Chap. D. Since we only have values in a discretised volume, the partial differentiations become a finite steps in 3D space. For example the curvature tensor components that describe the curvature around the x-axis are

$$\begin{aligned} K_{xx}(l_0, m, n) &= \frac{\alpha_x(l_0 + 1, m, n) - \alpha_x(l_0, m, n)}{\Delta x} \\ K_{xy}(l, m_0, n) &= \frac{\alpha_x(l, m_0 + 1, n) - \alpha_x(l, m_0, n)}{\Delta y} \\ K_{xz}(l, m, n_0) &= \frac{\alpha_x(l, m, n_0 + 1) - \alpha_x(l, m, n_0)}{\Delta z} \end{aligned} \quad (4.19)$$

where  $\Delta x, \Delta y, \Delta z$  correspond to the edge lengths of the elementary volumes (Fig. 4.7).

# Results

A main challenge of the project was to develop an experimental procedure that allows to measure quantitative values for the misorientations of the crystal with a 3D spatial resolution. The development was partially trial and error based and involved many experiments. There were twelve beamtimes, where different types of samples (LiF, Silicon, single- and 3-grain ice crystals) were used, for example to verify our equations to correct dispersive effects (Chap. A). Different digital cameras and camera manipulators were tested to find out that only the FReLoN provides integrated intensity images in pinhole X-ray diffraction topography with a high enough signal to noise ratio, and only the tomography camera manipulator exhibits motion ranges that are wide enough to catch the Bragg diffracted beams. Especially the motion along the z-axis by 47 cm in order to catch the pinhole Bragg diffracted beam at a distance 1.5 m should be mentioned. The multisection device was redesigned in order to have enough translation move and the tungsten multisection slits had to be replaced by new ones made of gold. The ESRF topography station was moved from the beamline ID19 to the beamline BM05 during the project and a part of the time was devoted to reinstall the apparatus. The long duration of our scans pushed the equipment to its limits and beyond. For example we discovered backlash motions in the tilt motors of the diffractometer tower (Fig. 3.3) that could spoil the measurements. Finally the whole diffractometer was exchanged by the newer one, situated at the beamline ID19 and additional rotation motors, for instance the motor *ome* and *rot2* were installed. Also mentioned could be the replacement of the goniometer head, that found out to be unstable when vertically mounted, by a very decent photographic tripod ball head. After all improvements, the last experiment in March 2011 provided the data to obtain quantitative results. The chapter therefore is mainly about that last experiment that was performed by the protocols described in Chap. 3. The data allows to compute complete 3D volume matrices for every fitting parameter and to access all nine components of the curvature tensor.

The sample was the three-grain-crystal II-5-123-3 and exhibits a very high crystalline quality at the beginning of the experiment. The investigated grain was larger than the largest possible beam at the BM05. The data was therefore gathered from a “cropped” region of interest containing the triple junction line (Fig. 5.1) and the two grain boundaries that separate the grain from its neighbours. Initially the crystal’s longest edge is aligned parallel to the y-axis and its largest surfaces are perpendicular to the x-axis (Fig. 3.7). From this orientation on the crystal was first inclined by  $-20^\circ$  around the y-axis and in a second step by  $-5^\circ$  around the x-axis in order to orient the grain in the multiple Bragg diffraction case (Fig. 3.10). Due to the second rotation of the sample around the x-axis by  $-5^\circ$ , its long edge (the load direction) is inclined by  $-5^\circ$  as seen in Fig. 5.1 and the angle opened by its surfaces and the z-axis is  $-20^\circ \cdot \cos 5^\circ$ . The chosen Bragg diffractions were the basal  $\vec{h}_{\text{basal}} = 0002$  and the first order prismatic  $\vec{h}_{\text{prism.}} = 1\bar{1}00$ . The prismatic one is perfectly vertically diffracted, so that its Bragg diffraction image is exactly above the direct beam image. As a consequence

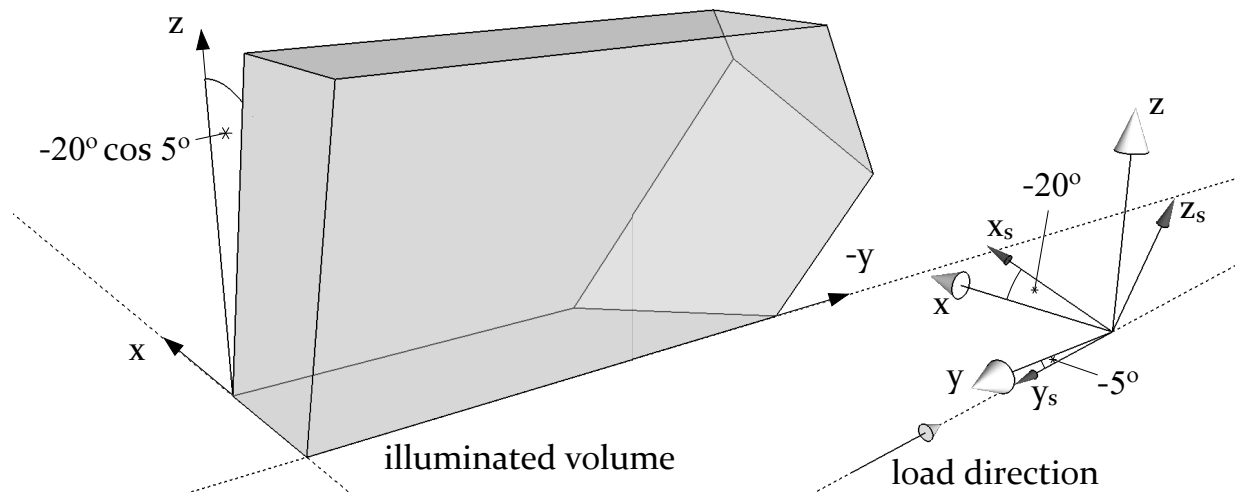


**Figure 5.1:** Illuminated part of the investigated grain. The crystal was inclined by  $-20^\circ$  around the  $y$ -axis and in a second step by  $-5^\circ$  around the  $x$ -axis in order to orient it to the multiple Bragg diffraction case. The big coordinate system with the white arrows represents the experimental hutch, the smaller one with darker arrows represents the crystal:  $x_s$  is along the sample thickness,  $y_s$  its long and  $z_s$  its short edge (Fig. 3.7).

the basal Bragg diffraction appears horizontally to the direct beam image but is situated slightly lower than the direct beam image. In the following, we refer to Bragg diffractions by “basal” and “prismatic” and the investigated grain is called “crystal”. For better reading, the figures containing results are chosen to be small. The interested reader may find these figures again, in a larger format and a higher resolution in the appendix (Chap. E).

The experiment contains data to characterise three different deformation states of the crystal. The first “initial” deformation state refers to the crystal as it was in the beginning of the experiment before any loading. An “intermediate” deformation state was achieved by loading the crystal by 1.1 MPa along its longitudinal direction during 40 minutes, and a “final” deformation state after a second loading of 1.1 MPa during 40 minutes.

## 5.1 Initial deformation state

The sample exhibits low distortions in its initial state of the experiment in March 2011. The integrated rocking curves were recorded in an angular interval  $\Delta\omega_{\text{basal}} = 0.03^\circ$  for the horizontally Bragg diffracting basal planes and  $\Delta\omega_{\text{prism.}} = 0.01^\circ$  for the vertically Bragg diffracting prismatic planes. The rocking curves are mainly broadened by dispersive effects (Chap. A) that are stronger in the horizontally diffracting geometry than in the vertically one.

Integrated intensity images (Eq. 4.2) of three exemplary sections are shown in Fig. 5.3 for the prismatic Bragg diffraction. The diffraction sense was vertically, the sections are therefore horizontally aligned. The third section in Fig. 5.3 contains the triple junction line. The white vertical lines that are periodically arranged in each section correspond to the absorption of the gold wires perpendicularly aligned in each slit of the multisection device (Chap. 3.2). The image exhibits an increased Bragg diffracted intensity around the column 950, due to a surface defect at the X-ray exit surface (see also Fig. 2.14): the induced strain expands into the crystal. The sections contain points that are mainly distributed on a virtual line in the centre of the crystal and parallel to the surfaces. Those points are associated to dislocations. They appear as a point because the dislocation line crosses the crystal volume

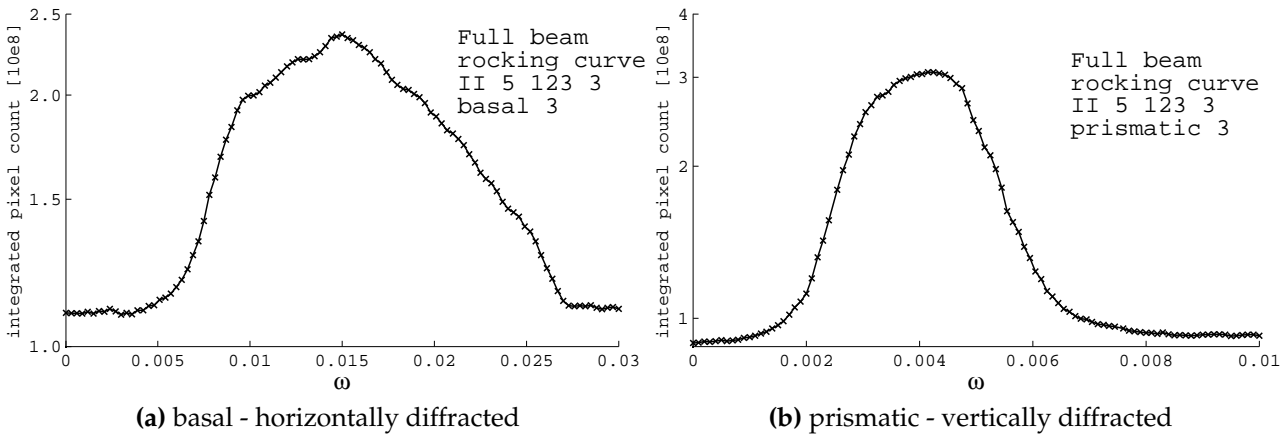


**Figure 5.2:** Rocking curves - initial state

that is illuminated by a section beam. The Bragg diffracted intensity in the dislocation region is about five times higher than in a region without dislocations or other crystal defects. A further feature is the interference pattern due to dynamical wavefield diffraction in the Borrmann triangle in the crystal (Chap. 2.2.1), clearly visible in the right part of the third section. The appearance of that pattern is an indicator for the high quality of the crystal: it preserves the wavefront of the X-ray beam and its coherence.

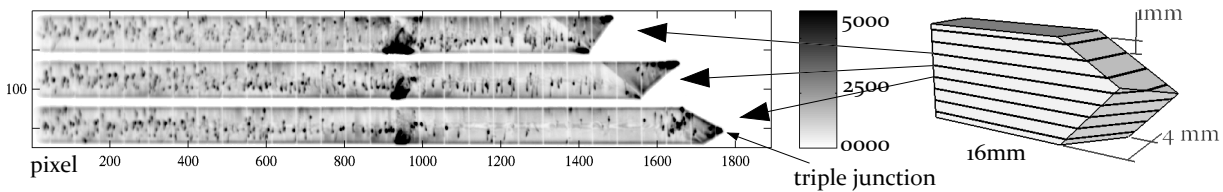


**Figure 5.3:** Integrated intensity - 3 sections - initial state- prismatic - vertically diffracted

The dislocations which are visible as dots on the integrated intensities of the prismatic image, are not visible on the integrated intensity map of the basal image (Fig. 5.4). The extinction rule,  $\vec{h} \cdot \vec{b} = 0$  (see also Eq. 1.4), allows to determine the direction of the Burgers vector to be parallel to the basal planes. Beside the surface defect that appears in the region around the column 1100 and the row 300 and some strain close to the crystal surfaces, the basal integrated intensity section image contains a few diagonal lines. Both integrated intensity images, the basal and the prismatic one, attest the crystal a high quality in its initial state.

The first of 21 2D maps, that result of the fitting procedure, are shown in Fig. 5.5 for the prismatic Bragg diffraction. The angular Bragg peak positions lie in a range of  $30''$ , mostly due to dispersive effects that are not corrected at this point of the data analysis. Beside a sharp misorientation around the already mentioned surface defect that appears in the prismatic Bragg diffraction (Fig. 5.5b), the crystal shows no major misorientations. The FWHM map (Fig. 5.5b) provides more features. The Bragg peaks are broader in regions that contain dislocations: whereas a perfect region exhibits values close to the Darwin width (Tab. 2.1) a region that contains one isolated dislocation reaches values of about  $5''$ . The surfaces of the crystal, the grain boundaries and the triple junction exhibit higher FWHM as well what attests lower surface quality and first strain incompatibilities at the grain boundaries. The left edges of the sections in Fig. 5.5b are defined by the border of the incident beam. The FWHM

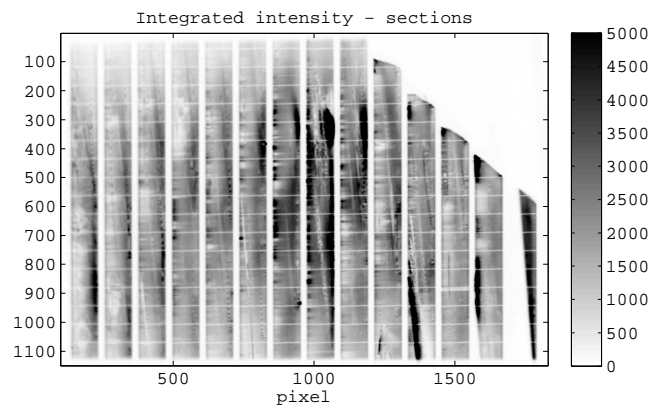


**Figure 5.4:** Integrated intensity - sections - initial state- basal - horizontally diffracted

values on those edges correspond to those of the bulk and not to those of the surface, indicating that the crystal is bigger than the beam. The surface defect mentioned before, is visible in the first five sections, it can therefore be identified as a surface scratch along the vertical direction.

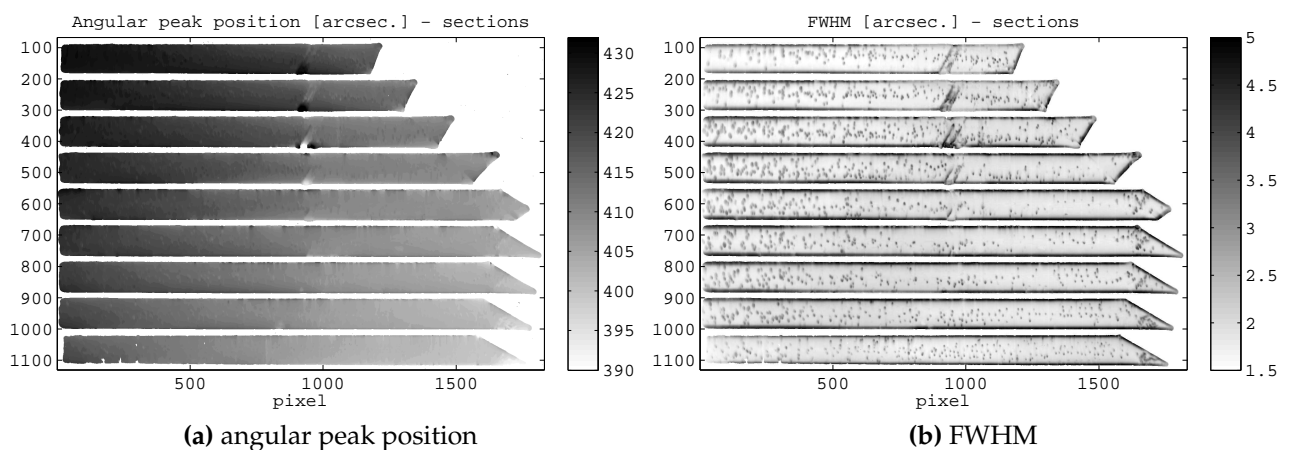


**Figure 5.5:** 2D maps showing the angular Bragg peak position (a) and the FWHM (b) - initial state - prismatic - vertically diffracted

The basal map (Fig. 5.6a) shows the angular Bragg peak positions that are characterised by dispersive effects as well. The dispersion spreads the values in an interval of 50". The FWHM of the Bragg peaks in the basal image (Fig. 5.6b) correspond in most of the pixels to the Darwin width (Tab. 2.1) except for the surface of the crystal. Finally the vertical lines that appeared in the integrated intensities are visible as well, for example in the first section from the left.

The assembling of the 2D maps into 3D volume matrices allows to visualise the integrated intensity, the angular positions, or the FWHM in other virtual slices then the section images presented until here. Fig. 5.7 exemplary shows virtual slices that are parallel to the crystal surfaces. They contain the integrated intensity values, Bragg diffracted by the prismatic lattice planes. Each image corresponds to a 56  $\mu\text{m}$  thick slice, Fig. 5.7a to the entrance surface, Fig. 5.7b to the slice located in the middle of the crystal and Fig. 5.7c to the exit surface. The surface defect seen in the section images (Fig. 5.5) appears white (lower intensity) at the entrance surface and black at the exit surface. The images mimic an integrated intensity topograph of a virtual slice without the constraints associated to the image con-

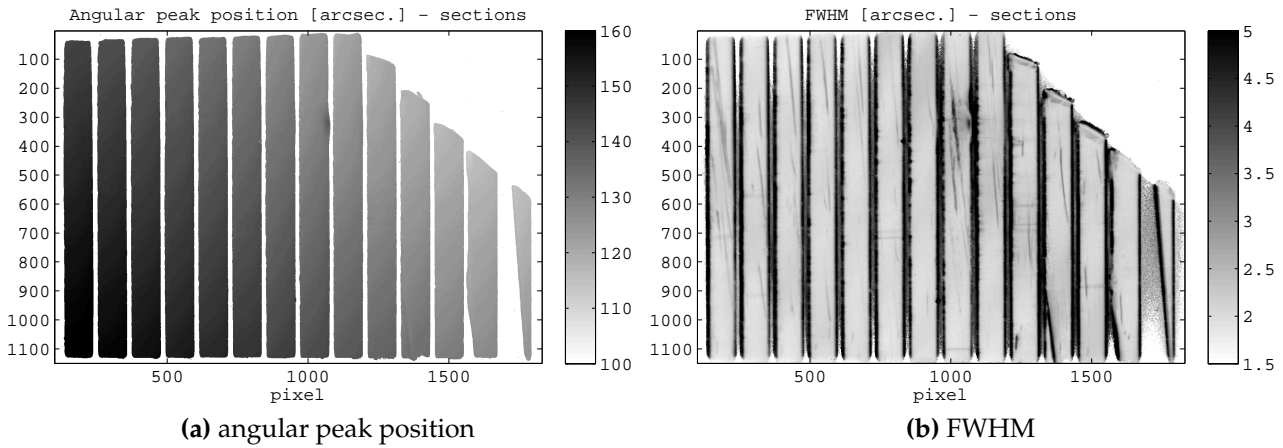


**Figure 5.6:** 2D maps showing the angular Bragg peak position (a) and the FWHM (b) - initial state - basal - horizontally diffracted

trast disappearing in “thin” crystals [Penning 68, Tanner 72]. Thin refers here to crystals thinner than the half of the Pendellösung length (Tab. 2.1). The dislocations associated to the points in Fig. 5.3, are clearly visible as vertical lines in the central slice of the prismatic Bragg diffraction (Fig. 5.7b), although in a crystal exhibiting a thickness of a virtual slice, the defects would be invisible. Our procedure to reconstruct the 2D maps into 3D volume provides significant advantages here compared to standard X-ray Bragg diffraction topography (Fig. 2.13). Finally the central slice (Fig. 5.7b) shows some intensity modulations, especially in the region a few millimetres to the left of the triple junction. These artefacts arise from the Borrmann triangle interference patterns that are observed on the section images (Fig. 5.3). The surface slices exhibiting lower crystalline quality, do not display those artefacts.

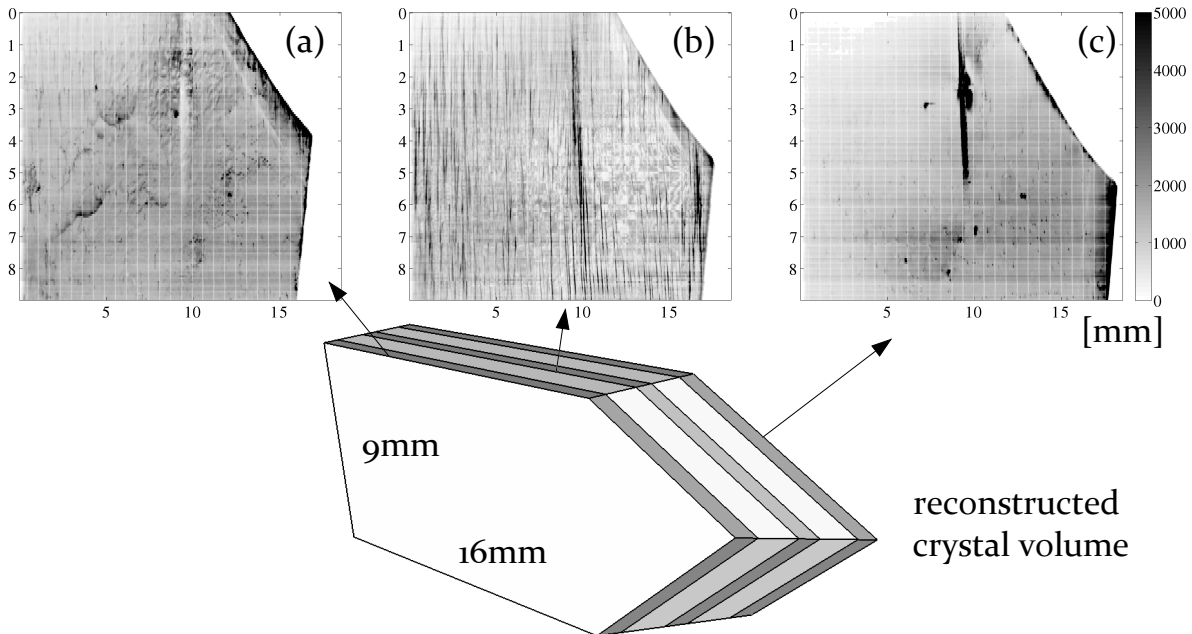


**Figure 5.7:** Integrated intensities in the X-ray entrance, central and X-ray exit virtual slice - prismatic image - initial state

A virtual slice from the middle of the crystal showing the angular Bragg peak positions

of the prismatic Bragg diffraction image is presented in Fig.(5.8). The grain exhibits a global misorientation of  $40''$  along the horizontal direction. This corresponds to a curvature Radius of about 200 m. The image contains vertical lines, associated to dislocation lines. They exhibit angular misorientations of around  $2''$  compared the surrounding area. The dislocations are visible in the Bragg peak position maps, although normal vector field of the prismatic planes surrounding a basal dislocation is circularly symmetric (Fig. 6.1). An interpretation is given in Chap. 6.1.

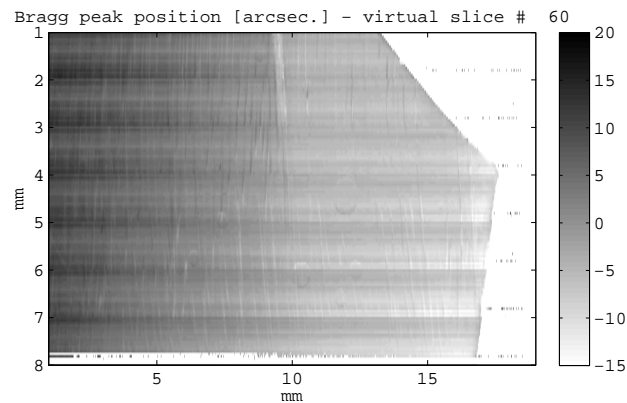


**Figure 5.8:** Angular Bragg peak positions - central virtual slice - prismatic image - vertically diffracted

**Misorientations around x-axis:** In the initial deformation state, 100 multi pinhole X-ray diffraction topographs were recorded on the vertically Bragg diffracting prismatic planes. They correspond to 100  $50\ \mu\text{m} \times 50\ \mu\text{m}$  dots, that are arranged in a  $10 \times 10$  square. The recorded images are all similar to the first one, presented in Fig. 5.9. There is no remarkable lateral deviation of the rod images, what indicates that no misorientations around the x-axis are present in the crystal. The data analysis was performed anyway, but the resolution of the method is lower than the distortions in the crystal. The sample therefore may considered as undistorted around the x-axis within the resolution of the experimental method.

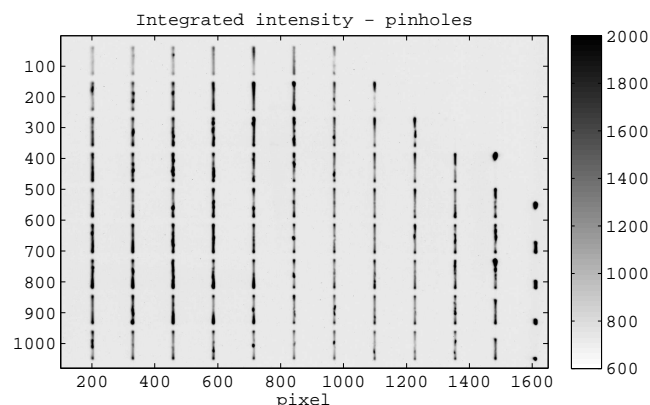


**Figure 5.9:** First integrated intensity image recorded by multi-pinhole X-ray diffraction topography. The rods all have the same shape and orientation. There is no considerable crystalline misorientation around the x-axis.

## 5.2 Intermediate deformation state

The intermediate deformation state of the crystal was achieved by applying an external stress of 1.1 MPa along its longitudinal edge (Fig. 5.1). It plastically deformed the crystal during 40 minutes. The plastic deformation induced a broadening of the global rocking curves (Fig. 5.10). The basal rocking curve was recorded in an angular interval  $\Delta\omega = 0.13^\circ$  and the prismatic one in  $\Delta\omega = 0.09^\circ$  which is approximately  $10\times$  bigger than in the initial state. At this point the dispersive effects are negligible, the broadening of the rocking curves arises from crystal lattice distortions. The basal rocking curve still has a one peak shape whereas the prismatic one reveals first polygonisation effects: it contains a main peak characterised by a FWHM of around  $0.005^\circ$  and a background where at least two broader peaks can be distinguished.

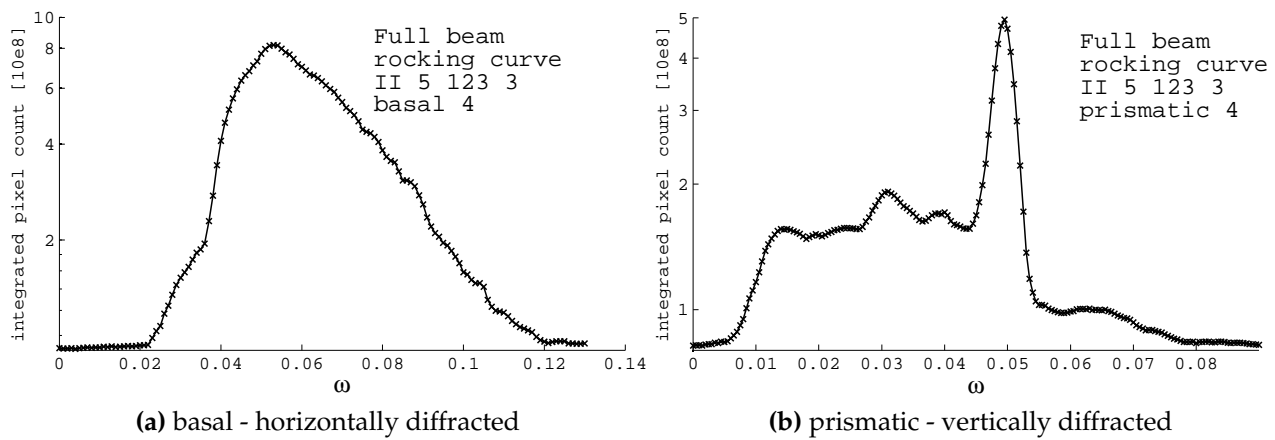
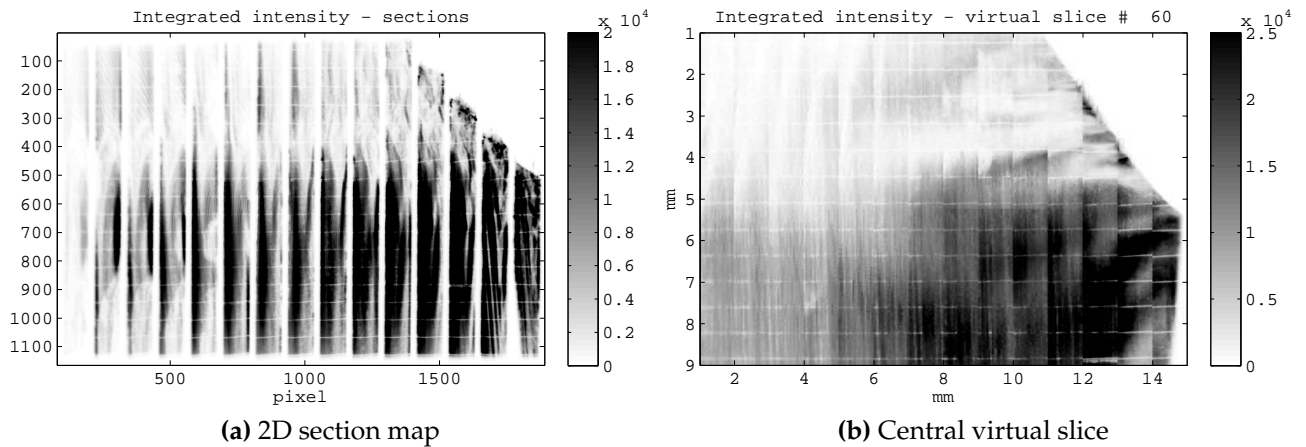


Figure 5.10: Rocking curves - intermediate deformation state

### 5.2.1 Basal Bragg diffraction

The basal Bragg diffraction image features inhomogeneities in integrated intensity due to the plastic deformation of the crystal (Fig. 5.11). The region close to the triple junction and to the X-ray entrance surface exhibits a  $10\times$  higher Bragg diffracted intensity than the upper left corner of the image, an indication for stronger lattice distortions. The upper parts of the integrated intensity section image still look homogeneous and suffered only minor distortions. Remarkable in these regions are the fine intensity modulations along the vertical direction, visible for example in the upper part of the third section from the left. They turn out to be experimental artefacts. Their appearance is explained in the following chapter (Chap. 6).

The repetitive shift at every millimetre along the horizontal direction in Fig. 5.12b are due to a continuation of the viscoplastic deformation during the eight hours scan time. The last section image that is generated by a slit of the multisection device is stitched to the first section image of the neighbouring slit. The two sections are based on data recorded at two different moments of the experiment, separated by eight hours. Therefore the evolution of the sample is visible. Obviously the sample continues to deform plastically many hours after the load is removed. To prevent that problem, the experiment could be interrupted after the loading of the sample until the dislocation movement and the crystal reaches a thermodynamic equilibrium.



**Figure 5.11:** Integrated intensity - basal Bragg diffracted image - intermediate state

The angular positions of the Bragg peak confirm the previous observations, and mainly the region closer to the triple junction is distorted compared to the rest of the crystal. A mutual misorientation of  $200''$ , especially along the horizontal direction and rather parallel to the load direction (Fig. 5.12b) is measured. A remarkable feature is a stronger misorientation along the upper grain boundary at an image height of around 3.5 mm, that propagates into the illuminated area. The modulation along the horizontal direction, repetitive at every 1 mm, is again an artefact from the fact that the crystal was evolving during the scan.

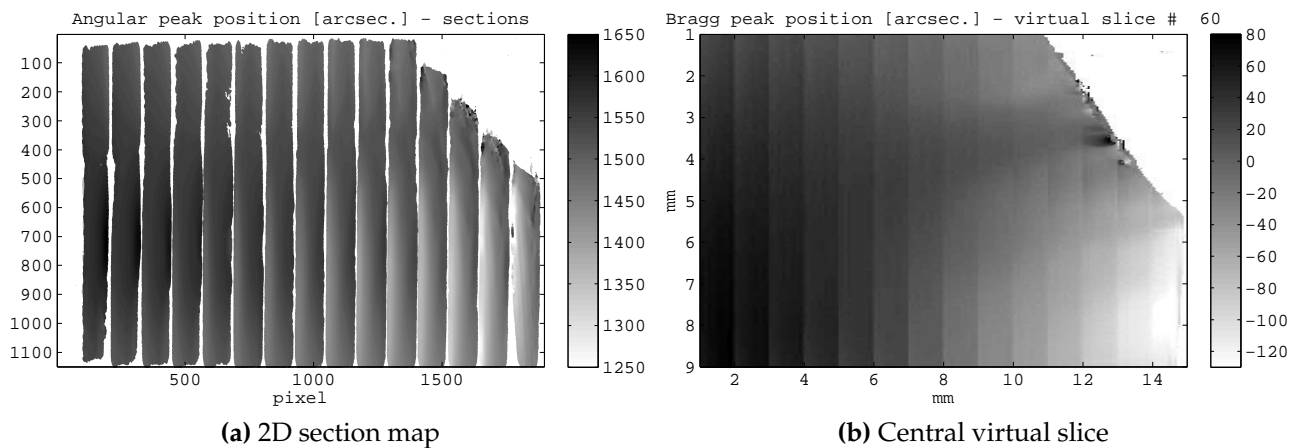


**Figure 5.12:** Bragg peak positions - basal Bragg diffracted image - intermediate state

The stronger lattice distortions closer to the triple junction result in higher FWHM as well. There is no distinct difference between the quality of the surfaces and the bulk of the crystal any more because the bulk quality has been diminished and is now at the same level as the surface quality. The FWHM maps exhibit similar modulations in the upper part of the image as were seen for the integrated intensity, but with a stronger contrast. Here again these are experimental artefacts that will be explained in the following chapter (Chap. 6). These zones exhibit FWHM values of around  $5''$ . Single dislocations are no longer observed because their density is now too high. The upper part of the illuminated volume (Fig. 5.11b) may be considered as very little distorted. The orientation of the described intensity modulation in a virtual slice could be determined on the Fig. 5.13b. However, the continuous sample evolution along the scan time has modified that pattern as well and it is charac-

terised by abrupt jumps at every 1 mm along the horizontal direction. The regions close to the triple junction exhibit the broadest Bragg diffraction peaks, the FWHM values reach up to 15'' what implies that plastic deformation of a high quality crystal mainly occurs in the surrounding area of the triple junction.

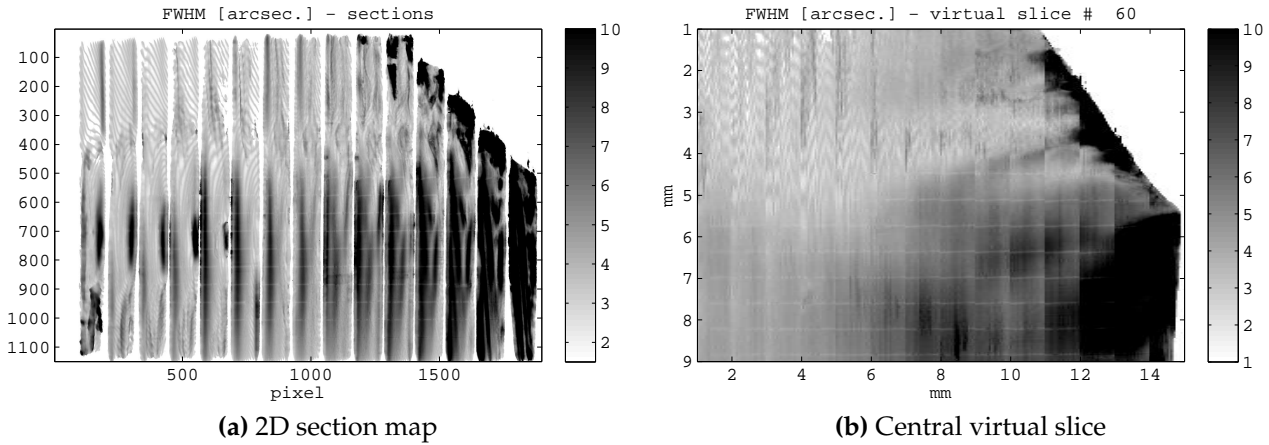


**Figure 5.13:** FWHM - basal Bragg diffracted image - intermediate state

## 5.2.2 Prismatic Bragg diffraction

The prismatic images are characterised by a strong dislocation multiplication. The integrated intensity section images (Fig. 5.14a) showing the scene along the thickness of the crystal contain many parallel lines that correspond to activated basal planes where dislocation glide occurred. The regions closer to the triple junction clearly exhibit an up to 10× higher integrated intensity than the rest of the crystal. The central virtual slice visualises the activated basal planes as vertical lines going through the entire illuminated area. Their concentration is stronger in the regions closer to the triple junction and the grain boundaries. The images also contain the left edge of the sample (Fig. 5.14b) where the integrated intensity is higher than in the rest of the crystal. This is because the crystal was unintentionally moved in the negative y-direction during the loading procedure, and the illuminated volume has grown by approximately by 1 mm along y. The edge of the crystal that is now visible is where the load was applied.

The activated planes are visible in maps representing the angular Bragg peak positions as well (Fig. 5.15) although in a lower contrast as in integrated intensity images (Fig. 5.14). The induced lattice misorientations lie in an interval of 200'' and are mainly along the loading direction (horizontal in the images). As seen in Fig. 5.15b there are strong lattice distortions closer to the triple junction whereas the first 5 mm from the left only exhibit minor misorientations. Generally the finer features that are visible in integrated intensity and in FWHM maps, are less visible in angular misorientation images. This allows the conclusion, that the induced crystal defects only weakly influence the major orientation of an elementary volume (voxel).

The FWHM maps (Fig. 5.16) contain the same features as the integrated intensities but with a stronger contrast: the shape of the activated basal lattice planes is sharper. The density of activated planes increases towards the triple junction. Their distribution is inhomogeneous. For example in Fig. 5.16b there is a region in form of a 1 mm thick vertical band, at around 6 mm where no activated lattice planes appear. That line has FWHM values around

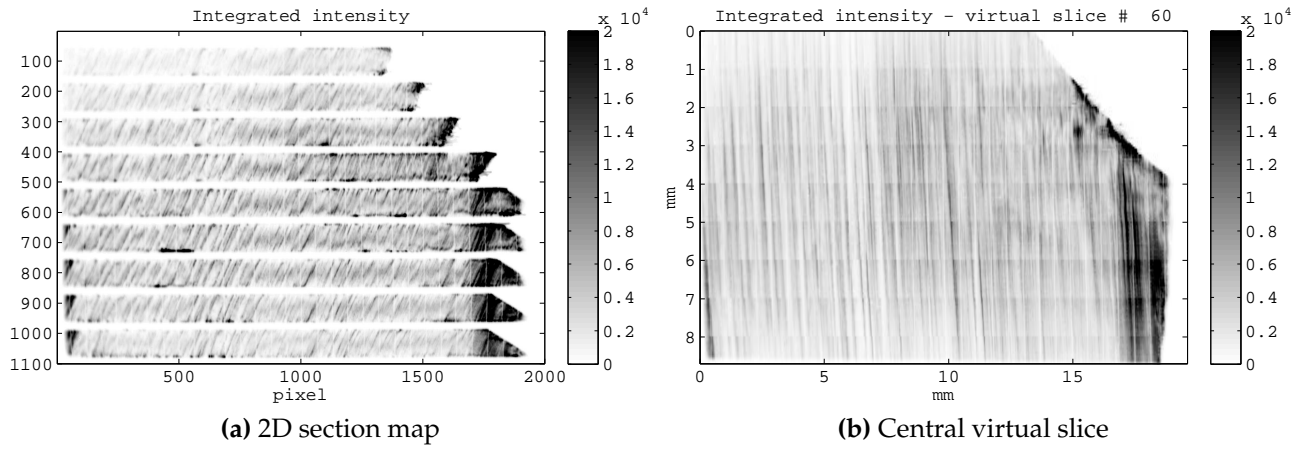


Figure 5.14: Integrated intensity of the prismatic Bragg diffracted image - intermediate state

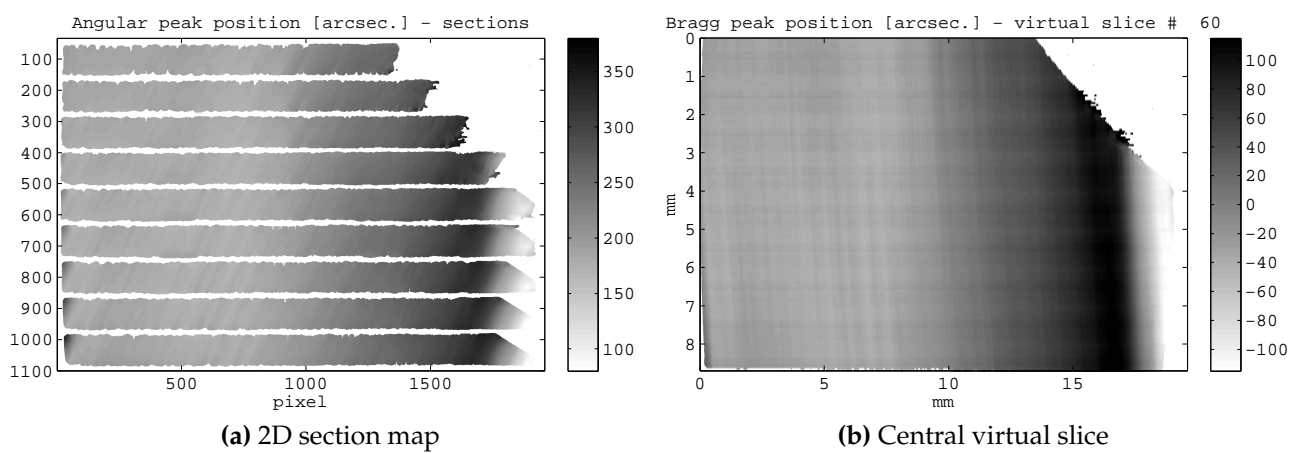
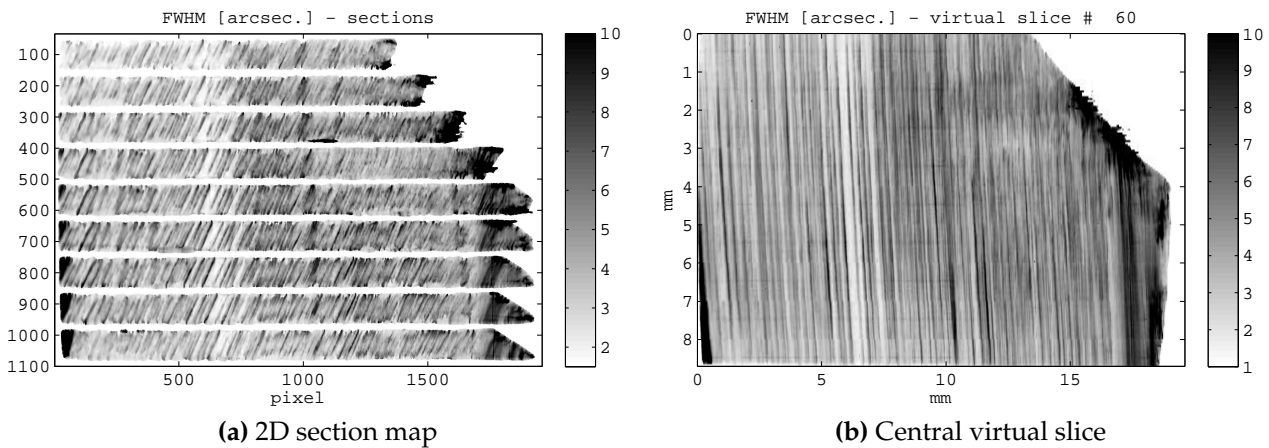


Figure 5.15: Bragg peak positions - prismatic Bragg diffracted image - intermediate state

the Darwin width. The activated basal planes are characterised by values in the range of  $[5'', 15'']$  depending on the concentration.



**Figure 5.16:** FWHM values - prismatic Bragg diffracted image - intermediate state

**Misorientations around x-axis:** In the intermediate deformation state 25 multi pinhole X-ray diffraction topographs, arranged to  $5 \times 5$  squares were recorded (Fig. 3.13). They show first lateral deviations of the rod images, especially in the regions closer to the crystal surface near the triple junction and, a little bit weaker, to the crystal boarder on the left. The data analysis provides angular Bragg peak position maps that are used to calculate the curvature tensor components  $K_{i1}$ ,  $i = 1, 2, 3$ . Despite to the effort to reduce the noise in those images (multiple expositions, Chap. 3.4.3) the signal to noise ratio is rather low. Even the varying sensitivity of the four channels of the FReLoN camera is visible: the left bottom quarter of the image exhibits the highest noise and corresponds to channel of the FReLoN with the highest sensitivity.

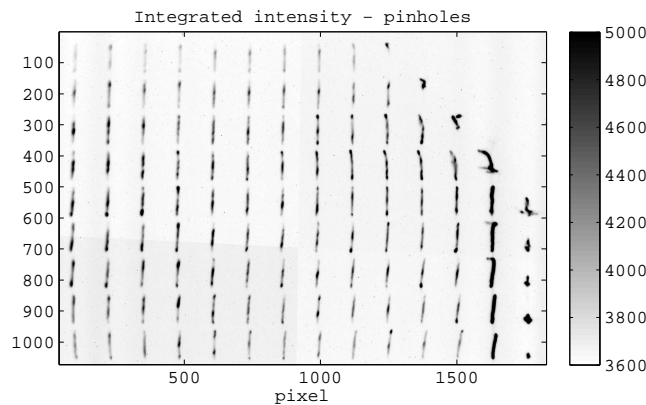


**Figure 5.17:** First integrated intensity image recorded by multi-pinhole X-ray diffraction topography. There is no visible feature indicating the already mentioned surface defect.

## 5.3 Final deformation state

The final deformation state was induced by a second loading at 1.1 MPa during 40 minutes. The plastic deformation leads to a further broadening of the global rocking curves (Fig. 5.18).

The basal rocking curve was recorded in an angular interval  $\Delta\omega = 0.5^\circ$  and the prismatic one in  $\Delta\omega = 0.8^\circ$ . That is five to ten times larger than the intervals in the intermediate state of the crystal. The interval sizes indicate that the crystal suffered big plastic deformations. The basal rocking curve has no longer a one peak shape but shows polygonisation effects as well. The prismatic Bragg diffraction is characterised by very large tails that diffract at lower intensity. They arise from regions close the triple junction and the borders of the sample and make it necessary to register the rocking curves in such a large interval  $\Delta\omega$ . The main peak in the prismatic rocking curve (Fig. 5.18b) is characterised by a FWHM of  $0.05^\circ$  and is almost as thick as the entire rocking curve interval in the intermediate state (Fig. 5.10b).

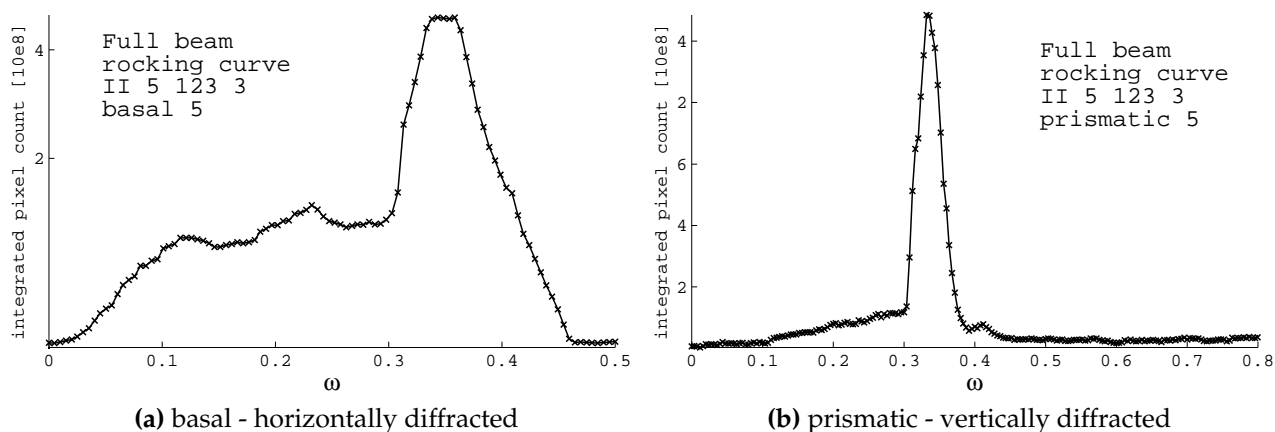
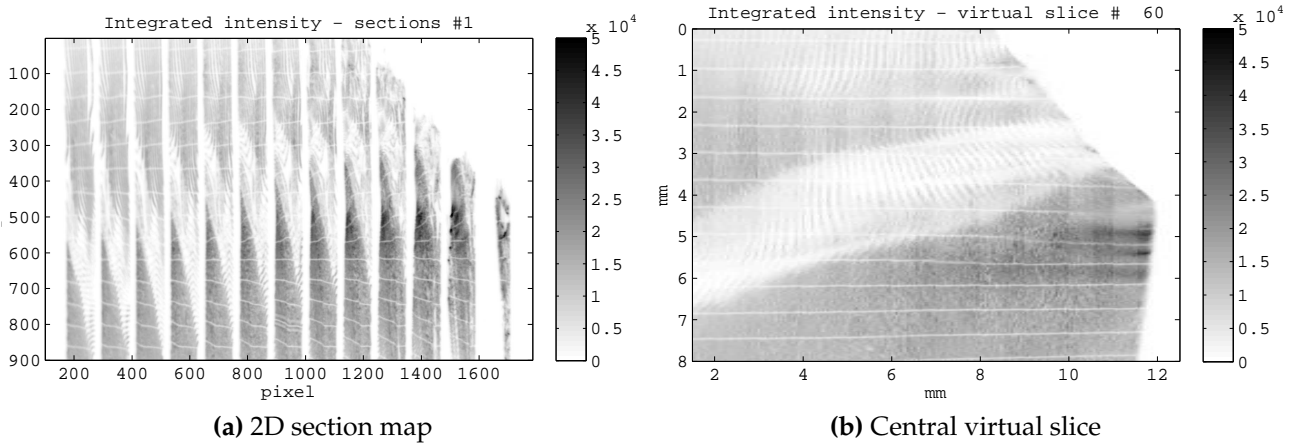


Figure 5.18: Rocking curves - final state

### 5.3.1 Basal Bragg diffraction

The integrated intensity maps and virtual slices on the basal image (Fig. 5.19) are characterised by three distinct regions: a first region in the lower part that exhibits an up to  $2\times$  higher diffracted intensity than the upper part, and a band in the centre of the crystal, where the integrated intensity is weak (a tenth of the intensity of the first region where the diffraction is the strongest). The region exhibiting the strongest intensity starts at the lower part of the X-ray entrance surface and decreases along the thickness of the crystal. The higher intensities appear to be associated with the formation of a subgrain in that region (polygonisation). The central virtual slice (Fig. 5.19b) shows the low diffracting band in the centre of the crystal. The band exhibits a relatively high crystalline quality, also visible from the FWHM values (Fig. 5.20b). Although it is very close to the distorted subgrain. The subgrain region has well defined borders in the neighbourhood of the triple junction. In the upper part of the crystal the quality is not substantially degraded, but a well pronounced intensity modulation is visible.

The lines of low intensity in each section (Fig. 5.19a) that are associated to the gold wires in the multisection device are no longer straight but appear distorted, especially in the region of the subgrain. They are an indication for lateral deviations of the Bragg diffracted beam that appear when the crystal exhibits angular misorientations around the x-axis (Fig. 3.12). In the subgrain region, those white lines are horizontal and straight when close to the X-ray exit surface. In a depth of around 1 mm in the crystal, they exhibit a distinct kink upwards and climb continuously until they reach the X-ray entrance surface. The sections to the right of Fig. 5.19a appear to have a second kink that is weaker pronounced. It is situated closer to the X-ray entrance surface.



**Figure 5.19:** Integrated intensity of the basal Bragg diffracted image - final state

The FWHM maps represent the inner mosaicity of the crystal and exhibit the highest contrast among all images. The values reach up to  $120''$ , whereas the broadening of the local peaks in the upper regions is comparably weak: values down to  $2''$ , i.e. just a bit larger than the Darwin width, have been measured. The modulation due to the experimental artefact, that appeared in the integrated intensity images is visible here as well. The modulation is shifted in phase, though. A point exhibiting maximal integrated intensity, is characterised by a minimal FWHM value. The average value of those modulations is approximately  $6''$ .

There is a darker band in the bottom part of each region in Fig. 5.20a indicating the passage from the subgrain regions to those belonging to the remaining crystal. This "transition" zone is characterised by the highest FWHM values of the image, up to  $120''$ . The subgrain itself, that showed no contrast in the integrated intensities, exhibits values around  $30''$ . Let us note a white line inside the transition zone, where the values only reach  $40''$ . The line is clearly visible in the last three sections to the right of Fig. 5.20a

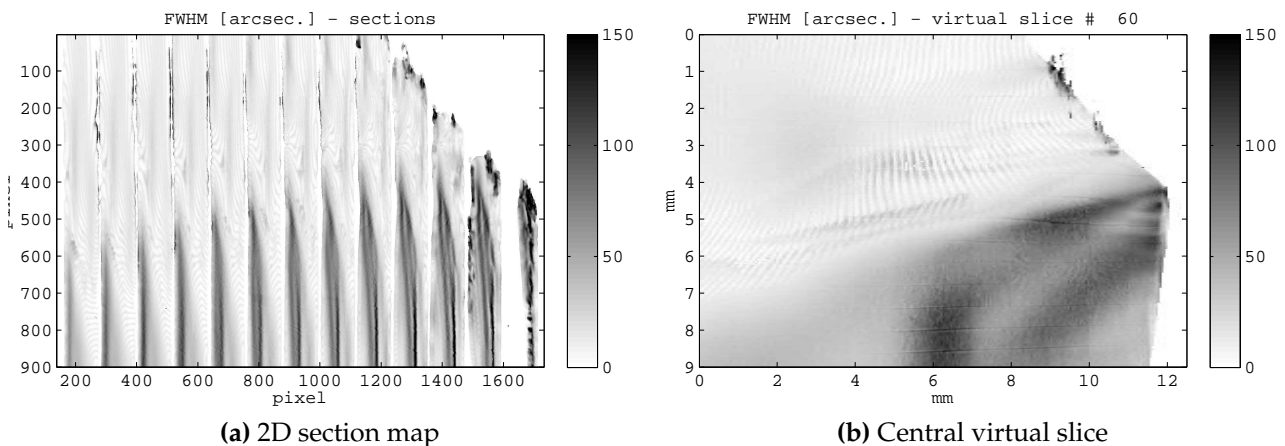


**Figure 5.20:** FWHM - basal Bragg diffracted image - final state

The angular positions of the Bragg peak (Fig. 5.21) do not exhibit the fine details as do integrated intensities and the FWHM: that implies that the contrast is generated by an inner mosaicity of the elementary volumes (voxels), their angular positions are centred around the average value. The overall orientation changes smoothly and there is a global lattice bending from the subgrain region in the bottom towards the upper part of the image. The

subgrain region is misoriented by approximately  $0.3^\circ$  compared to the better quality part of the crystal. The boarder between the subgrain and the remaining part of the crystal and contain the triple junction (Fig. 5.21b)

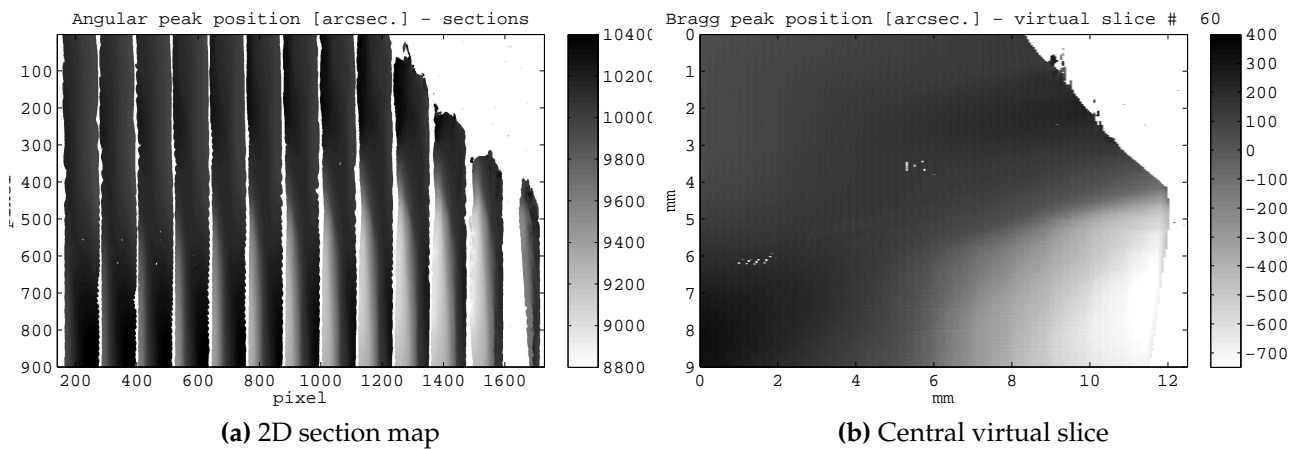


Figure 5.21: Bragg peak positions - basal Bragg diffracted image - final state

### 5.3.2 Prismatic Bragg diffraction

The central volume slice of the prismatic image (Fig. 5.22b), once again, is characterised by a continuous sample evolution during the scan time of nine hours. Although they appear to be strongly distorted, the individual activated basal lattice planes are still visible in the integrated intensity images (Fig. 5.22). They are straight and parallel to each other in the upper sections (Fig. 5.22a). In the lower sections they appear to be bent when going towards the X-ray entrance surface (that is the subgrain region in the basal image). The bending of the activated basal planes is an artefact that origins on lateral deviations of the Bragg diffracted beam (Fig. 3.12). Those deviations are visible in Fig. 5.25. They make a straight line in a section image to appear bent. The effect was not visible in the initial and the intermediate state because lateral deflections of the Bragg diffracted beam, that are associated to angular misorientations around the  $x$ -axis, were weaker than in the final deformation state. The section images as shown in Fig. 5.24a could be corrected on the basis of the shape of the rods in Fig. 5.25. Both images, the section map and the rod image must be undistorted in the same manner. The procedure is correct when the shape of the rods becomes straight and their spacing is 1 mm. In this case the activated basal planes in the section image become straight as well. Such an image manipulation would require advanced knowledge of image processing that could not be acquired in the time that was devoted to the project.

The fifth section from the top in Fig. 5.22a shows a linear alignment of dots that is connecting the triple junction with the X-ray entrance surface in the middle of the image. That lines is associated to the boundary of the subgrain that is visible in the basal image.

The section images of the angular Bragg peak positions (Fig. 5.23a) show a strong bending of the prismatic lattice planes in the closer regions of the triple junction, along the horizontal direction. The lines in the sections, associated to activated basal planes are also visible in the Bragg peak position maps, the contrast is weak though (Fig. 5.21a). The subgrain that was clearly misoriented in the basal image, is not visible in the angular Bragg peak position maps of the prismatic image. The prismatic Bragg diffraction image (Fig. 5.22a) shows strong intensity fluctuations in the final deformation state. There are regions in the crystal, especially the spaces between the activated glide planes in the upper section images that

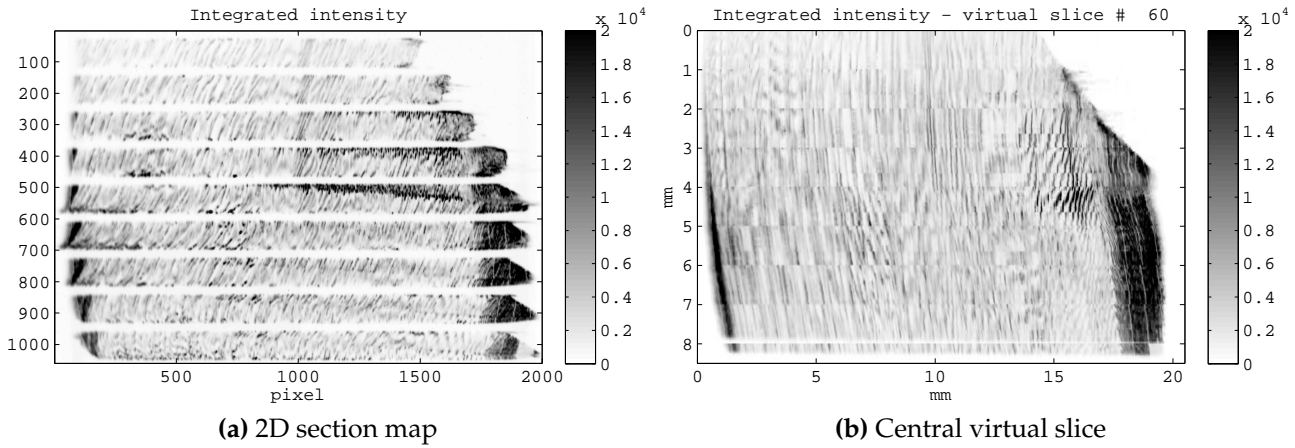


**Figure 5.22:** Integrated intensity - prismatic Bragg diffracted image - final state

exhibit weaker integrated intensity values than the surrounding area of the sections in the lower part. Here the diffracted intensity of a section is so high, that the diffusive light (on the fluorescent screen of the digital camera) generates intensity values around the section image that are higher than those inside a section in the upper part of the image. As a consequence there is no threshold value for the integrated intensity to distinguish between the diffraction image and its background. When the threshold value is chosen high, the shape of the sections is properly defined, but many pixels in the upper part of the image are set to zero. If the threshold value is low, then all pixels inside a section are recognised, but a lot of diffusive intensity around the sections is not eliminated. We have chosen the threshold value to be low. As a consequence the FWHM maps (Fig. 5.24a) and especially the angular Bragg peak positions (Fig. 5.23a) show a kind of blurring artefact around the section images. This does not affect the stitching of the sections to a 3D crystal volume since it is performed on the basis of the integrated intensity maps (Fig. 5.22a). Here the shape of the sections is clearly visible.

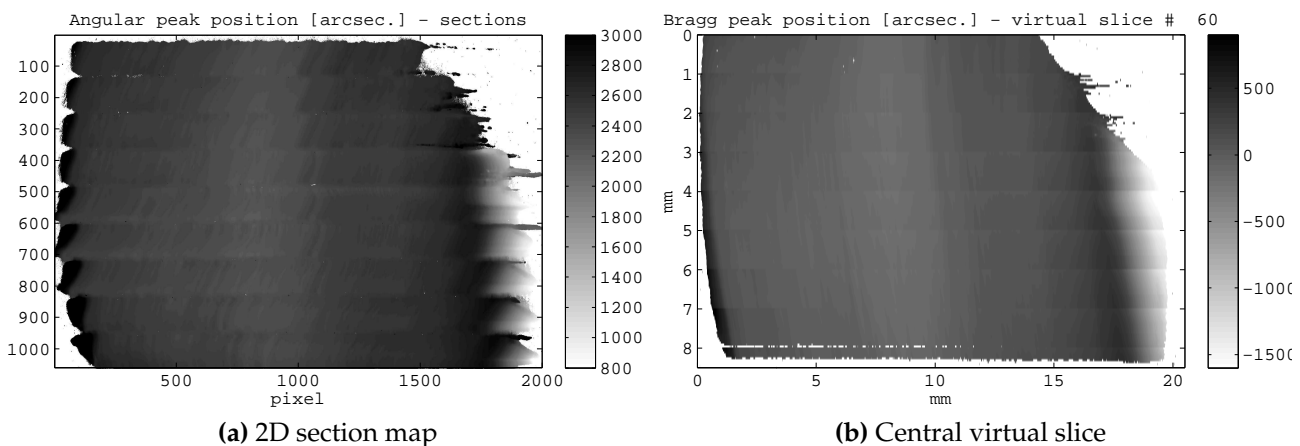


**Figure 5.23:** Bragg peak positions - prismatic Bragg diffracted image - final state

The FWHM maps have the strongest contrast, once again. We still may find weakly distorted regions that exhibit values of only 5". The regions closer to the triple junction and the sample edges on the left of Fig. 5.24b exhibit values up to 100". Whereas the subgrain region as seen on the basal image has clearly exhibits higher FWHM values, the subgrain is

practically invisible on the FWHM map of the prismatic image. The reconstruction of the central virtual section (Fig. 5.24) shows the continuous evolution of the sample during the scan time.

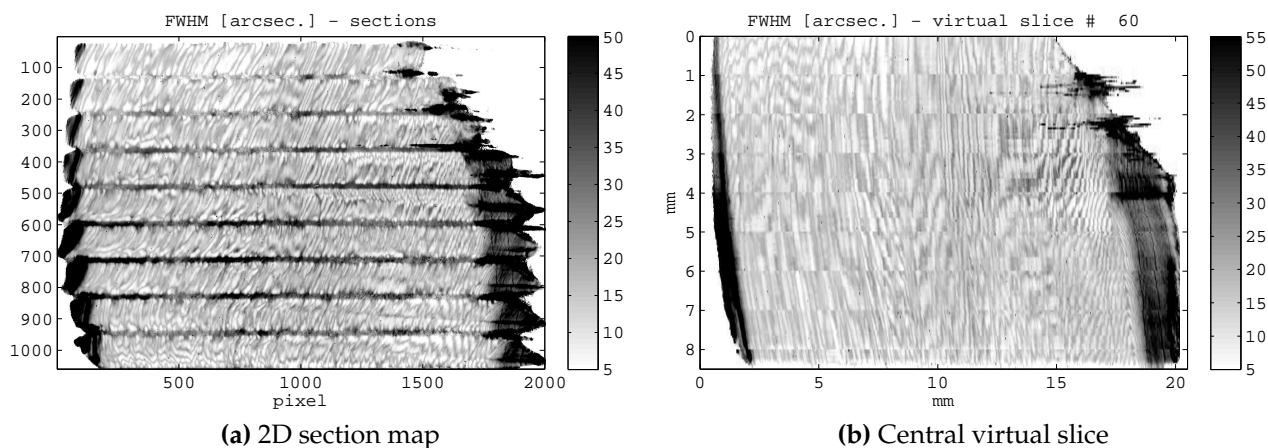


Figure 5.24: FWHM - prismatic Bragg diffracted image - final state

**Misorientations around the x-axis** The prismatic planes exhibit strong misorientations around the x-axis, visible in Fig. 5.25. The lateral deviations lead to a blurring of the entire image and even a change in the shape of the whole diffraction image. In the bottom region of the virtual slice images, where the subgrain is situated, the image has become wider and measures almost 20 mm. The images have even higher noise, due to the large rocking curves that increased the exposition time. The regions close to the triple junction exhibit the strongest lattice misorientations around the x-axis. Some of the rod images, especially in the lower part of Fig. 5.25 exhibit a kink as was observed in the gold wire lines in the basal image. The shape indicates that the subgrain exhibits angular misorientations around the x-axis. Together with the information from the prismatic Bragg peak position map (Fig. 5.23a) we conclude that the prismatic lattice planes in the subgrain are not misoriented around the y-axis but they are misoriented around the x-axis. This will be further discussed in the following chapter (Chap. 6).

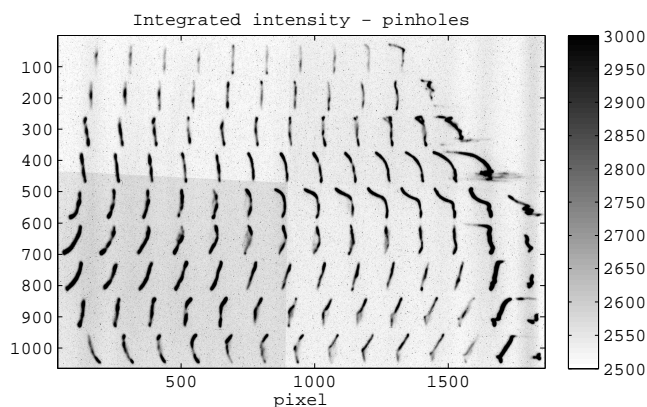
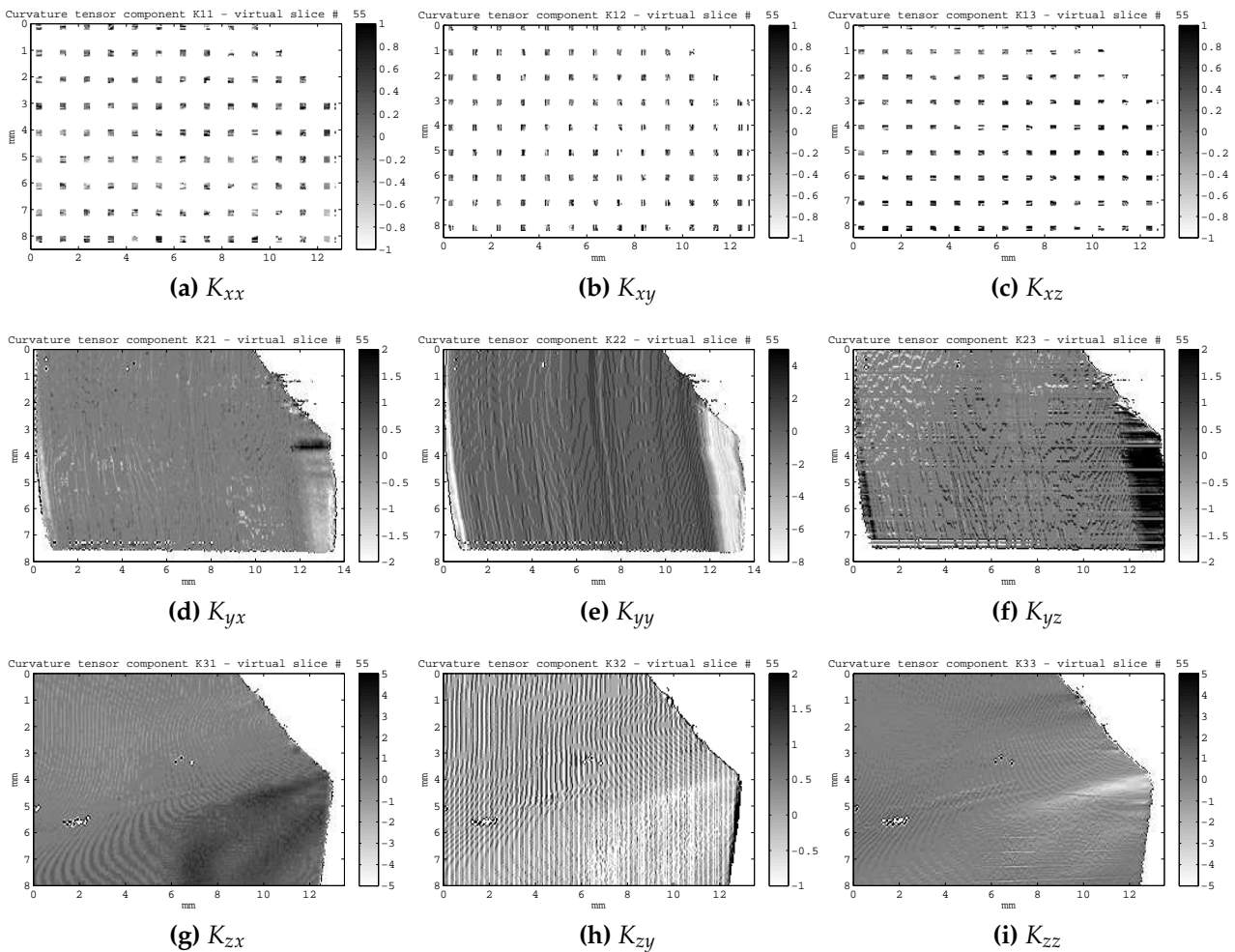


Figure 5.25: First integrated intensity image recorded by multi-pinhole X-ray diffraction topography.

## 5.4 Curvature tensor components

The angular orientation maps that were presented above allow to calculate all nine components of the curvature tensor as defined by Eq. 1.15 for every deformation state. Fig. 5.26 exemplarily shows the curvature tensor components for the final deformation state in the central slice of the crystal. The final state was chosen because the lattice curvatures supposed to be the strongest here and the images exhibit more features. The components  $K_{xx}$ ,  $K_{xy}$ ,  $K_{xz}$  are calculated from the multi-pinhole X-ray diffraction topography images and only show the investigated parts of the sample. The lateral deviations of the Bragg diffracted beam in this deformation state change the shape of the crystal in the images. This is especially visible on the components  $K_{yx}$ ,  $K_{yy}$ ,  $K_{yz}$  (Fig. 5.26d, 5.26e, 5.26f). Those curvature tensor component maps need to be corrected by the same image procedure as the section maps of the prismatic image (Chap. 5.3.2). Once those corrections are done, a pixel  $(i_0, j_0)$  in every curvature tensor component map would be associated to the same elementary volume (voxel) in the crystal. A simple coordinate transformation would finally allow to rotate the tensor and obtain the components along the crystalline axis of the sample.



**Figure 5.26:** Curvature tensor components of final deformation state in the central slice of the crystal.

## 5.5 Chapter conclusion

The amount of results that could be presented in Figures is very huge. There are two Bragg diffraction images investigated. For each of them, the four parameters integrated intensity, angular peak position and FWHM could be presented in 21 2D maps that contain the section images. The composition of 3D matrix volumes for each parameters contains around 100 different virtual slices. This is to demonstrate the impressive amount of data and results that are obtained in only one experiment. The results will be discussed in the following chapter.

# Discussion

The initial aim of the present work was to design and commission a technique, based on a combination of transmission diffraction section topography and rocking curve imaging, able to provide the three-dimensional local (at the level of a 50  $\mu\text{m}$  sized voxel) curvature tensor. In the process of recording the data needed to access to this curvature tensor, a series of original results were obtained. They include topographic results on the integrated intensity, peak position and width of the local rocking curves for virtual slices located in the bulk of the crystal, and allow to obtain quantitative results on the defect images, beyond what was measured up to now. The present chapter will mainly discuss some of these novel results, with emphasis on the mosaic spread of a voxel containing a dislocation, the peak position of the corresponding rocking curve, the way this evolve when glide planes are created, and the initial polygonisation state that appears when deforming the crystal.

## 6.1 Dislocation visibility

The initial state of the crystal is characterised by a very low dislocation density, so that individual dislocations are observed. The integrated intensity basal images (Fig. 5.6) contain no clear dislocations images, whereas the prismatic ones exhibit many dislocation images, visible as points in the sections (Fig. 5.3) and as lines parallel to the basal planes in the virtual slices (Fig. 5.3b). As they are not visible on basal image, the extinction law allows to conclude that their Burgers vector lies in the basal plane, ( $\vec{h}_{\text{prism}} \perp \vec{b}$ ). By following the movement of one “dislocation point” in the section images along the z-direction we can derive the orientation of the associated dislocation line: the angle opened by the dislocation line and the normal vector of the Bragg diffracting prismatic planes is approximately  $30^\circ$ , in other words, the orientation of the dislocation line is perpendicular to the  $\{11\bar{2}0\}$  prismatic planes. Based on those observations, these dislocations are very probably of  $\vec{b} = 1/3(11\bar{2}0)$  screw type, the most observed ones in ice.

Within this assumption we may calculate the width  $w$  of the associated dislocation image as seen on the prismatic lattice planes. The direct image of a dislocation (Chap. 2.2.2) is predominant in the low absorption case we are concerned with. It is issued by the distorted region around the defect, where the induced lattice distortions exceed  $q \cdot \omega_D$  where  $q \in [0.5; 1.5]$  [Authier 01, Miltat 75]. The theoretical dislocation image width results from the convolution of the intrinsic width of the dislocation  $w_i$ , the detector resolution  $R_d$  and the image widening associated to the angular divergence of the Bragg diffracted beam  $L$ .

$$w = \sqrt{w_i^2 + R_d^2 + L^2} \quad (6.1)$$

According to Klapper [Klapper 76], the intrinsic width is

$$w_i = \frac{V_c \cos \theta_B |\vec{h} \cdot \vec{b}|}{2r_e |F_{hkl}| \lambda P} \quad (6.2)$$

where  $P$  is the polarisation factor ( $P = 1$  for vertically Bragg diffracted beam at the ESRF). The values from Tab. 2.1 allow to calculate  $w_i = 5 \mu\text{m}$  for the mentioned basal screw dislocations, visible in the prismatic image. The detector resolution is  $20 \mu\text{m}$  in our case. The divergence of the Bragg diffracted beam is given by the FWHM of the Bragg peak in a dislocation region. We measure FWHM values in a dislocation region of around  $5 \mu\text{m}$  (see Fig. 5.5b) and the distance between the sample and the detector was  $1 \text{ m}$ . The broadening due to the divergence of the Bragg diffracted beam therefore is  $L = 1 \text{ m} \cdot 2 \cdot 2.5 \times 10^{-5} \text{ rad} = 5 \times 10^{-5} \text{ m}$ . As a result for the width  $w$  of a dislocation image, we obtain  $w \approx 54 \mu\text{m}$ . The dislocations that we observe exhibit  $w = 50 \mu\text{m}$  which is in keeping with the theoretical value.

The dislocations are also visible in the FWHM maps, Fig. 5.5, where they exhibit values around  $5''$  compared to  $1.5''$  for the “perfect crystal”. The global dislocation density is estimated by counting the points in one section. For example we count 30 points in the middle section of Fig. 5.3 to the right of the surface defect. Each point corresponds to a dislocation length of around  $50 \mu\text{m}$  because it intersects the section nearly perpendicularly. The volume represented by the section area is  $V_{\text{section}} = 50 \mu\text{m} \cdot 4 \text{ mm} \cdot 8 \text{ mm} = 1.6 \times 10^{-3} \text{ cm}^3$ , and the global dislocation density in the crystal is approximately  $100 \text{ cm}^{-2}$ . This is too low to broaden the rocking curve of the entire Bragg diffraction image. However when referred to an elementary volume  $50 \mu\text{m} \times 50 \mu\text{m} \times 10 \mu\text{m}$ , that contains a single dislocation with a length segment of  $50 \mu\text{m}$ , we obtain dislocation density of  $50 \mu\text{m} / 50 \mu\text{m} \times 50 \mu\text{m} \times 10 \mu\text{m} = 2 \times 10^5 \text{ cm}^{-2}$ . According to Kaganer [Kaganer 10] the value is high enough in order to broaden the local rocking curve. The presence of one dislocation in the otherwise perfect crystal increases the FWHM of the rocking curve of the associated voxel to a value of  $5''$ .

It is not unexpected that the basal screw dislocations are visible on the integrated intensity of the prismatic image (direct image contrast). Their appearance in the FWHM maps is explained by the broadening of the local rocking curve due to the “local dislocation density”. However they also appear in the angular Bragg peak positions (Fig. 5.8), where they shift the Bragg peak by  $2''$  in the negative or positive direction. This is astonishing because the average misorientation of the prismatic planes in a voxel containing a basal screw dislocation is zero as is shown in the following: the vector field of the normals to the prismatic planes in the surrounding area of a basal screw dislocation exhibits a circular symmetry (Fig. 6.1). When very far from the dislocation core, the normal vector to the prismatic lattice planes is parallel to the basal dislocation line. The closer we get to the dislocation core, the more the normal vector is inclined. Yet, in a circle around the dislocation core, the angle between the normal vector of the lattice planes and the dislocation line is constant. As a result the misorientation of the lattice planes on one side of the dislocation is cancelled out by those on the opposite side. The average orientation of the prismatic lattice planes in a voxel is therefore not affected by the presence of a basal screw dislocation. However if the dislocation line is not centred in the voxel, but closer to its edge, there may be a net contribution of the distortion field and a shift in the mean orientation of the voxel. In this case the distortion field on the outside of the concerned voxel results in a shift of the orientation of the adjacent voxel in the opposite sense. Indeed, some dislocation images in the misorientation maps exhibit a transition of the misorientation from the positive (darker) to the negative (brighter) sense, for instance in the right down corner of Fig. 5.8, but it is not completely clear if this corresponds to a single dislocation. On the other hand, this “mechanism” would lead to the visibility of very roughly about a half of the dislocations, i. e. the ones located near the “edges” of the voxel. The comparison of the integrated intensity map (Fig. 5.7) with

the FWHM shows that nearly all dislocations are visible on this last image, with a stronger contrast.

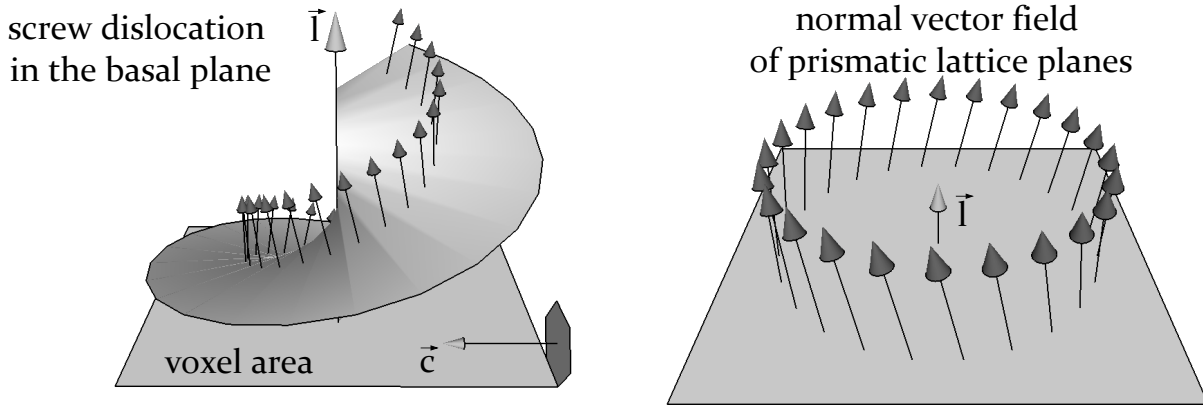


**Figure 6.1:** The normal vector field of the prismatic lattice planes, associated to a basal screw dislocation has a circular shape. The average misorientation of an elementary volume (voxel), which is much larger than the distortion field, is therefore zero.

Another feature could explain the shift of the Bragg peak in the dislocation region: an incident beam that propagates through a dislocation line, crosses one lattice plane less (or one lattice plane more, depending on the orientation of the Burgers vector of the screw dislocation). The thickness of a virtual slice is approximately  $50 \mu\text{m}$  while one lattice spacing distance is  $d \approx 5 \times 10^{-10} \text{m}$ . This leads to a variation in the effective lattice spacing  $\Delta d/d \approx 10^{-5}$ . For a monochromatic beam ( $\lambda = \text{const.}$ ) we obtain from the Bragg equation:  $\Delta d/d = \Delta\theta / \tan\theta = 10^{-5}$ . The difference in the Bragg angle is  $\alpha = \theta'_B - \theta_B = \Delta d / (d \tan\theta_B) \approx 2''$  which is in keeping with the values that we have measured (Fig. 5.7).

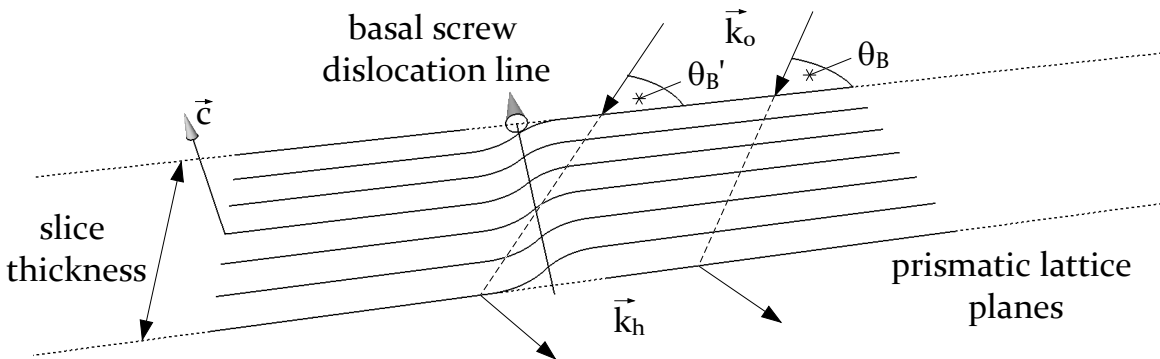


**Figure 6.2:** Variation in the effective lattice spacing  $d$  due to the presence of a screw dislocation. The beam that propagates through the dislocation line, has crossed on its path one lattice plane more than a beam in the perfect lattice. If the screw turned in the other direction, the beam going through the dislocation would cross one lattice plane less than a beam going through the perfect lattice. The variations in the effective lattice spacing are associated to a difference in the Bragg angle  $\theta'_B$  and an angular shift, visible on the Bragg position maps.

## 6.2 Crystal deformation

Already after the first loading of the crystal, the basal screw dislocation density seen on prismatic images is too high to resolve single dislocations (Fig. 5.14a). The dislocations are

arranged into basal glide planes which allow the plastic deformation of the crystal. The glide planes are visible as parallel line in the prismatic integrated intensity images of the intermediate and the final deformation state, but also on the FWHM maps (Fig. 5.16a and Fig. 5.24a) where glide plane exhibits values in the range  $[5'', 20'']$ . In the initial state the presence of one dislocation in the prismatic image is associated to an additional broadening of the local Bragg peak which goes from  $1.5''$  to  $5''$ . If we assume a “linear dependency” between the FWHM of the elementary volume rocking curve and the amount of basal dislocations in that elementary volume, we can associate a FWHM value of  $20''$  in a glide plane to the presence of five dislocations.

An interesting feature is visible in the prismatic integrated intensity section image of the final deformation state (Fig. 5.22a). In the fifth section, that contains the triple junction as well, the glide planes are stronger pronounced in the upper part of the section and downwards to a line in the centre of the section. When prolonged, this line crosses the triple junction. This is the only indication of the subgrain in the prismatic images.

The subgrain in the lower part of the crystal volume, visible on the left of the sections in Fig. 5.20a, exhibits a lower crystalline quality. The FWHM values on the basal image of that region reach values of  $30''$ . The subgrain boundary, visible as a dark line in the lower part of the sections, exhibits values up to  $120''$ . The dislocation density is higher here allows the different orientations of the two regions or in other words, the formation of the subgrain. The dark boundary line contains a white sharp line, where the FWHM values are particularly low and only reach values of about  $40''$ . A possible explanation of the white line is maybe the beginning of the formation of a second subgrain. Let us note that the remaining parts of the crystal show a higher crystalline quality than the subgrain itself. The formation process the two differently oriented zones is asymmetric what concerns the dislocation density in the two parts. Finally the white band, clearly visible on the integrated intensities (Fig. 5.19) is much less pronounced on the FWHM maps.

Last but not least the basal glide planes in the fifth section in Fig. 5.22a are slightly inclined compared to those in the rest of the image due to lateral deflection of the Bragg diffracted beam, associated to misorientations around the  $x$ -axis. The effect is visible on the dot image (Fig. 5.25). Angular misorientations by  $0.3^\circ$ , between the subgrain in the lower crystal and the remaining parts, are clearly visible on the basal image (Fig. 5.21). No such misorientations appear on the prismatic image. Though the shape of the lines associated to the gold wires in each section, as it appears in the basal image (Fig. 5.19a) and the rod images (Fig. 5.25) show strong misorientations around the  $x$ -axis. The information allows to determine the entire misorientation between the subgrain and the remaining parts of the crystal. The misorientation is shown in Fig. 6.3. This is remarkable, since the main deformation in ice occurs by basal dislocation glide.

### 6.3 Final deformation state characteristics

In the final deformation state, the initially perfect crystal is strongly distorted, the prismatic lattice planes exhibit angular misorientations of about  $0.3^\circ$  along the horizontal direction, the basal planes are characterised by two differently oriented regions and show the beginning of polygonisation (formation of a subgrain).

Further on finer features can be observed in the integrated intensities (Fig. 5.19a) and the FWHM (Fig. 5.20a). The images exhibit an oscillation of the values in regions close to the right up corner. These oscillations do not correspond to physical properties of the crystal: they are artefacts that occur in rocking curve imaging, when the angular steps that are made along the rocking curve, are chosen too big. In this case the number of points on a local

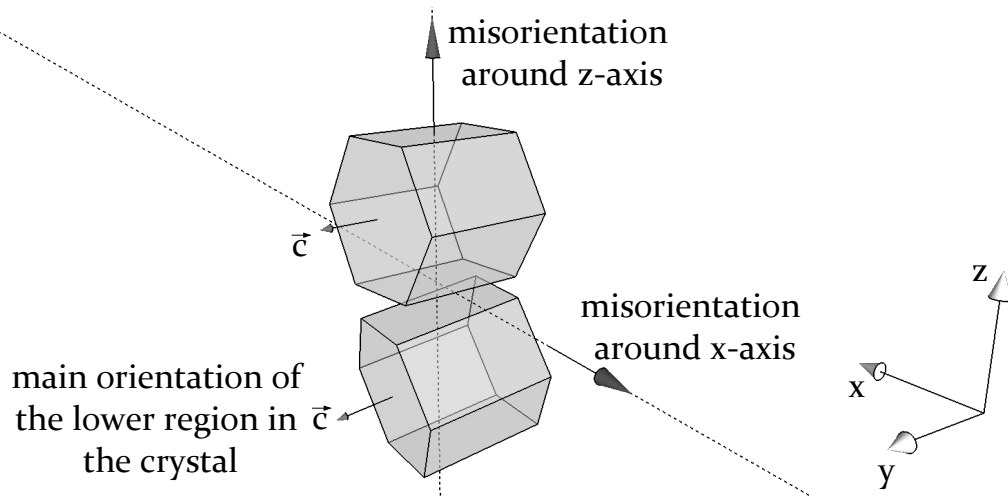


**Figure 6.3:** Misorientation of the subgrain compared to the remaining parts of the crystal. The two regions are misoriented by  $0.3^\circ$  around the z-axis and around the x-axis with the same amplitude. However there is no significant misorientation around the y-axis.

rocking curve can be very small (sometimes only one point) and the region might not be in full Bragg condition for any of the angular steps. Such a region appears darker. The artefact disappears when the step size is reduced. The overall deformation led us to scan over a big angular interval of  $0.5^\circ$ . The number of points per rocking curve should have been increased by at least a factor of three to eliminate the artefact. In this case the scan time would have been approximately three times longer and the step scanning of the basal Bragg diffraction in the final deformation state would have taken 24 hours instead of eight. This was not compatible with the allocated experimental time. The difficulty might be regarded as a technical limit of our experimental procedure in terms of the observable crystal quality. The technique is perfectly suited for the early stages of plastic deformation where the crystal distortions are small and a high angular resolution is needed. For a deformation as was reached after the second loading of the crystal, techniques with lower angular resolution that can measure over bigger angular intervals are surely a better solution. As example for a technique we mention topo-tomography [King 08]. The mentioned artefacts have only minor influence on the Bragg peak position. When the local Bragg peak is missed and is lying between two points, the measurements introduce an error that is maximally equal to the chosen stepsize. The induced error is therefore one step, in our case  $18''$ . Indeed, the oscillations do not appear on the Bragg peak position maps (Fig. 5.19a).

The stronger deformation at this state of the crystal reaches the limits of the statistical fitting procedure as described in Chap. 4.2.1. Here we assume a simple back projection of the Bragg diffracted beam from the detector to the sample no crossing of beams associated to different regions in the crystal. As mentioned the statistical method does not discriminate multiple peak profiles. A closer look at our data reveals that this assumption is not valid for a few local rocking curves in our data. As shown in Fig. 6.4, some regions of the subgrain feature a non one peak local rocking curve. Either the lateral deviations of the Bragg diffracted beam are too big, or the inner mosaicity of the voxel features several distinct orientations. We repeat here that our data contains very few of such local rocking curves. The general case is characterised by a one peak behaviour where our fitting protocol works perfectly. Better results could be achieved with more calculation power and a classic fitting procedure as *least square means* that detects multiple peaks. The FWHM maps of the basal image in the final deformation state are still an indicator for the inner mosaicity of a voxel, however they have to be analysed with caution.

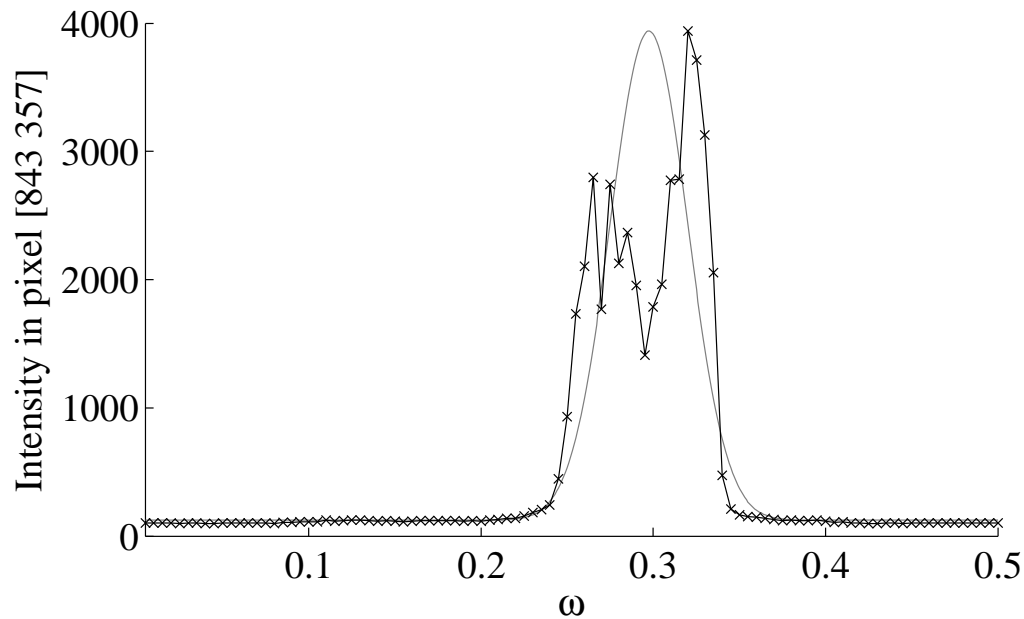


**Figure 6.4:** Selected local rocking curve on the basal diffraction image, issued from the subgrain region in the final deformation state, including the result of the statistical fitting procedure. Several peaks can be distinguished.

**Image smearing:** The lateral deviations of the Bragg diffracted beam, associated with crystalline misorientations around the  $x$ -axis (Fig: 3.12) result in a change of the shape of the Bragg diffracted images. When comparing the dot image, presented in Fig 5.25 with a virtual slice of the same Bragg diffraction, for instance Fig. 5.22b, we observe basically the same modifications of the Bragg diffraction. Calculations in the appendix (App. B) show that there is practically no influence of misorientations around the  $x$ -axis on the misorientation measurements around the other axis of the coordinate system. However the lateral deviations lower the spatial resolution when measuring the misorientations around the  $y$ - and around the  $z$ -axis because the intensity in a pixel of the camera can no longer be associated to a well defined voxel in the crystal. The lateral deviations add contributions of surrounding voxels and reduce also its own one. A way to handle the problem is to increase the size of a voxel. The result is a lower spatial resolution. This could be disturbing when correlating the curvature tensor components to each other: the nine components must refer to the same elementary volume. The effect of lateral deviation on the 3D volumes could be reduced by image processing: the section images could be distorted back by tacking reference to the pinhole images. This, whereas possible, appeared to be a time consuming task which is left for a future work. Let us finally note that the effect of lateral deflections may be reduced by a smaller sample to camera distance. We were aware of that effect, but the experimental apparatus design does not allow to approach the FReLoN closer to the sample.

## 6.4 3D versus 2D

The main feature of our experimental procedure is the access to all three spatial dimensions of the sample, whereas usual diffraction topography generates projection images (Fig. 2.13). The gain of spatial resolution stands against a strongly increased experimental time: registering the images on various angular orientations of the crystal (RCI) the multisection device takes around 20 min, the step scanning procedure may last up to 10 h. This inevitably

awakes the question about benefits of the technique. We wish to show that the technique reveals many additional information that unless would not be accessible to the scientist. As an example Fig. 6.5 shows the prismatic (a) and the basal (b) Bragg diffraction image in the final deformation state as it would appear in RCI without any sections. Compared to that

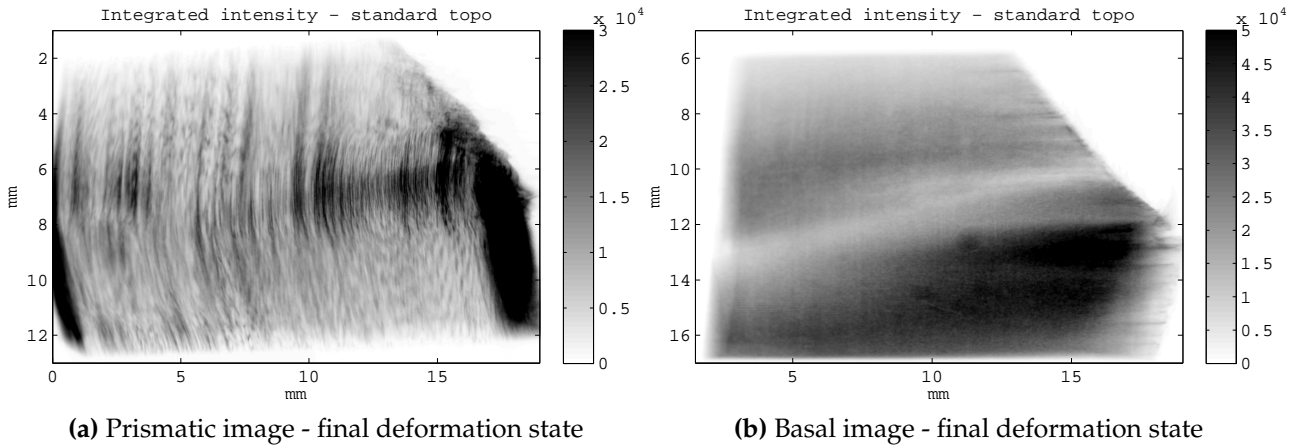


**Figure 6.5:** The Bragg diffraction images, as they appear in standard X-ray Bragg diffraction topography (Fig. 2.13). The shape of the subgrain along the thickness of the crystal cannot be determined. The orientation and the density of the activated basal glide planes is not accessible from the prismatic Bragg diffraction image without the three dimensional spatial resolution.

we show three different virtual slices of the same Bragg diffraction but recorded with the step scanning technique (Fig. 6.6). We can deduce the shape of the subgrain, as it begins at the entrance surface. We see how the subgrain boundary starts at the triple junction and propagates into the crystal. This shows that the deformation mechanism of ice and crystals in general is an actual 3D phenomenon and its understanding requires 3D data. The 3D feature is in addition the key to all nine components of the curvature tensor. The simple RCI would only provide six components, the components where differentiation is along the x-axis ( $K_{xx}$ ,  $K_{yx}$  and  $K_{zx}$ ) could not be determined.

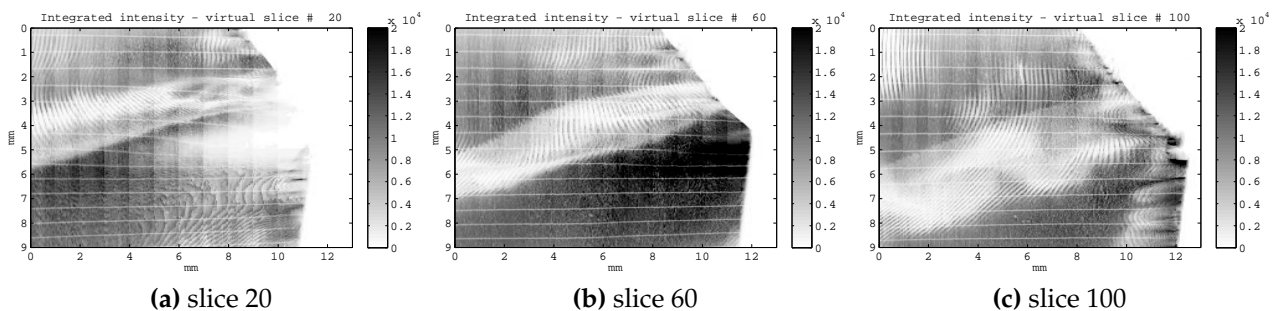


**Figure 6.6:** Orientation of the basal and prismatic lattice planes in the illuminated area.

## 6.5 Sample stability

The long scan times allow to observe the continuous sample evolution after the loading. As mentioned in Chap. 3, where our experimental procedure is described, after loading the

experiment is interrupted to give the crystal time to find its thermodynamic equilibrium. We assumed that after one hour the defect structure is stationary and there is no dislocation movement any more. Our results reveal that this assumption turned out to be a first approximation. When comparing the 2D maps issued from the 1st RCI image stack compared to the 21st for instance the integrated intensities presented in Fig. 6.7, we see rather different images: the density of activated basal glide planes is higher in the 21st maps than in the 1st, the pre-existing glide planes are more pronounced and some of them seem to be larger as well. The images differ, although the associated regions in the crystal are the same. The images are normalised to the incident beam intensity so the difference does not origin from variations of the X-ray beam. The only explanation is a continuous evolution of the crystal

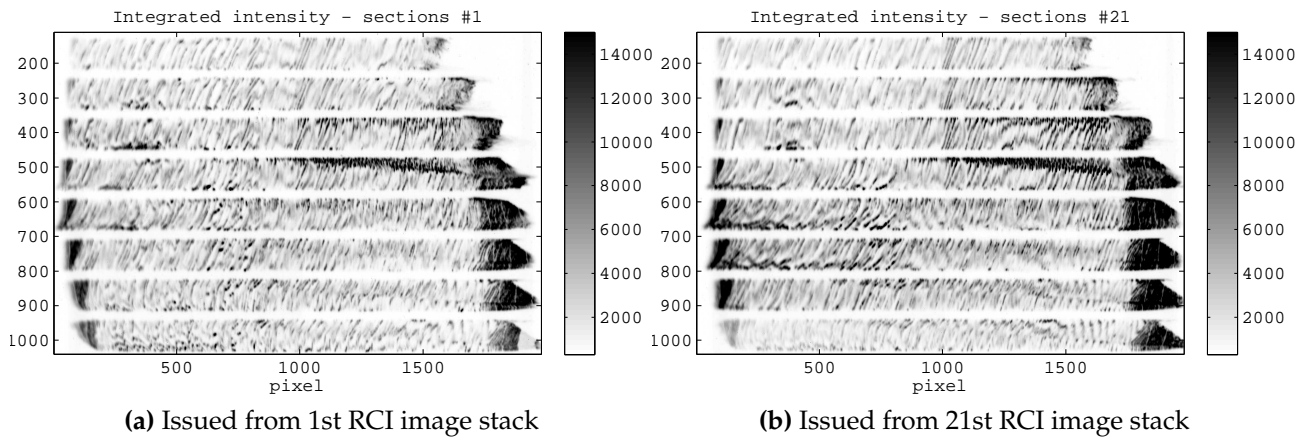


**Figure 6.7:** Integrated intensity section maps of the 1st and the 21st RCI image stack. The associated region in the crystal is the same, but the maps are different, revealing continuous sample evolution during the step scanning procedure.

many hours after the loading. Although not foreseen like that, the long scan time provides information about the relaxation of the crystal after the loading. It must be mentioned as well, that the evolution implies an error when the 2D maps are stitched to a 3D volume. Those contain artefacts that are especially visible when passing from the 20th image of a section to the first one of a neighbouring one.

## 6.6 Curvature tensor components

All nine components of the curvature tensor have been experimentally determined for the first time. They are shown in Fig. 5.26 for the central slice of the crystal. They contain the entire curvature information of the crystal in the measured points. We observe the highest values for the components  $K_{yy}$ , where strong heterogeneities appear in the regions close to the triple junction and the grain boundaries. That component is associated to a torsion of the crystal around the y-axis, that is nearly parallel (Fig. 5.1) to the  $\vec{c}$ -axis of the crystal. The component  $K_{zx}$  corresponds to a flexion of the basal plane around the  $[1\bar{1}00]$  direction.  $K_{zz}$  is associated to a torsion around the z-axis and exhibits a high curvatures in the regions close to the triple junction. It corresponds to polygonisation observed on the angular peak position maps. The information obtained from the curvature tensor is in keeping with those issued from the Bragg diffraction images. Those images provide the data to calculate the curvature tensor components.

The curvature tensor components provide the data required to extract the geometrically

geometrical meaning of  
curvature tensor components

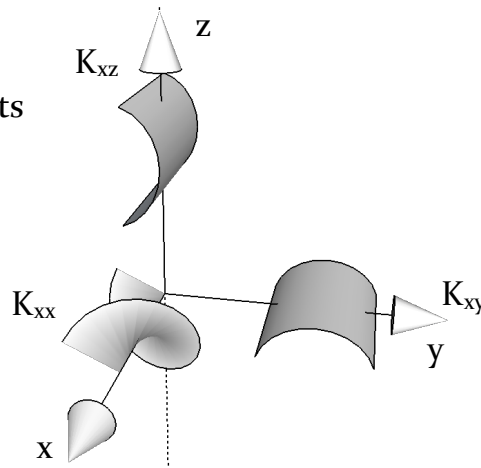


**Figure 6.8:** Geometrical explanation of the curvature components  $K_{xx}$ ,  $K_{xy}$ ,  $K_{xz}$ . The component  $K_{xx}$  corresponds to a torsion around the x-axis,  $K_{xz}$  to a flexion of a plane perpendicular to the y-axis around the x-axis and  $K_{xy}$  to a flexion of a plane perpendicular to the z-axis around the x-axis.

necessary dislocation density tensor. The dislocation density at this point cannot be determined by simple counting on the topographs: they are too close to each other and their images superpose into a glide plane. The curvature tensor will allow to determine the dislocation density anyway. First of all the curvature tensor component images must be corrected from lateral deviations of the Bragg diffracted beam (Chap. 6.3). In the following a data interpolation for the components  $K_{xx}$ ,  $K_{xy}$  and  $K_{xz}$  is needed to fill the gaps that occur in multi pinhole Bragg diffraction topography. In a final step a coordinate transformation to crystalline axes of the crystal has to be applied. The resulting geometrically necessary dislocation density tensor will be associated to the different types and orientations of dislocations.

# Conclusion

The main goal of the project was to develop an experimental method that allows to measure the complete crystalline misorientation in an ice polycrystal in order to then access the geometrically necessary dislocation density tensor along all three spatial dimensions of a crystal. This involved designing and commissioning a new experimental procedure and writing the scripts for the computer based data analysis. In the end the substantial part of the time was devoted to this main challenge. The last experiment indeed demonstrated that the capabilities of the new procedure fulfilled our demands.

Beside the curvature tensor measurements that should be compared with the results of numerical simulations of the deformation [Robertson 99], we also had access to other quantitative or semi-quantitative aspects (Chap. 6) of the deformation process that were not observed before. The three dimensional characteristics of our experiments play an important role here and has helped to reveal a variety of interesting features of the deformation process. This includes the observation of the distortion in a voxel containing a single dislocation in the initial state and to the estimation of the number of dislocations per voxel in a glide plane in the final deformation state. The technique provided detailed results of the polygonisation process on the basal lattice planes of the crystal and the misorientations around the  $x$ -axis, allowed us to determine the global misorientation of the crystal in three dimensions. The insight into the bulk revealed the subgrain boundary and shows a characteristic transition layer of low dislocation density (white line in Fig. 5.20a). The observed features in the three grain crystal turn out to be complex. The grain boundaries as well as the triple junction introduce complicated, initial conditions of the problem, and more investigations should be performed in the future for a deeper understanding. The oscillations as they appear on the FWHM maps and the integrated intensities when the crystal is strongly deformed, might show up the technical limits of the technique. It is perfectly suited for the measurements of small lattice distortions and the study of the early stages of deformation of initially high quality crystals. It reaches its limits when the interval of the global rocking curves exceed values of  $0.5^\circ$ . Here other methods like diffraction contrast tomography [King 08] might do a better work.

To the best of our knowledge this is the first time, that RCI is combined with section topography in order to observe the deformation process in the bulk. The possibilities of the new experimental method are not fully exploited yet. For example, beside the application to deformation of ice, the method could find its application in other materials. Those are not only hexagonal lattice metals but any type of polycrystals that allow Bragg diffraction topography experiments in Laue geometry. As seen from now, the method is a useful complement to other distortion measurement techniques such as RCI on layers [Mikulik 06] or topo-tomography [King 08]. There might be an exchange of new experimental aspects in all the techniques and the methods could benefit from their different advantages.

In terms of an outlook for the future work, of course the described experimental method could be further improved. First of all, the working energy could be reduced to 10 keV in order to obtain bigger Bragg angles and a lower shrinking factor of the image (Fig. 4.6). The sample shape could then be changed to a cylindrical form and allow measuring misorienta-

tions around the  $x$ -axis by sample rotations by  $90^\circ$  and not by the lateral deviations of the Bragg diffracted beam. The advantage would be to have the same spatial resolution along the  $x$ -axis of the crystal as for other axes and a complete misorientation around the  $x$ -axis map. However changing the Bragg angle to lower values implies a camera manipulator that allows even more different positions of the camera.

On the beamline BM05 changing the working energy leads to lower incident beam intensities due to the characteristic energy value of a bending magnet at the ESRF (Eq. 2.3) and the higher X-ray absorption of air. Lower working energies make it necessary to use even more vacuum or He-filled beamguides. At a lower working energy the experiment would last even longer. Reducing the experimental time would be a key improvement, since it is a main drawback of the method: it implies continuous sample evolution and slight backlash motions in the motorisation of the diffractometer tower. The best way to reduce the experimental time is by changing the X-ray source to an insertion device. The question if an ID beamline should devote experimental time to such a type of experiment will mainly depend on its success, especially in terms of scientific output. Further improvements would be a diffractometer tower with larger motion range that allows studying crystals with a wider range of crystalline orientations.

But even without any further improvements the experimental procedure is ready to be used, the protocols allowing the data analysis are written and accessible. Further ice crystals with different crystalline orientations, different quality and defects could be investigated to hopefully find theoretical explications for the features we observed and, in this way, to generally progress in the understanding of crystalline deformation. Other materials with smaller lattice spacing do not even need a lower working energy: the Bragg angles are bigger.

The main task to develop the experimental procedure and the data analysis, is fulfilled. We believe that the work will benefit from that work and surely produce further unexpected results!

## Dispersive effects

The X-ray beam generated by a synchrotron exhibits the opening angles  $\gamma_z$  and  $\gamma_y$  along the z- and the y-axis. (Fig. A.1). The beam divergence allows to illuminate bigger samples, a fact that is used in X-ray imaging. It is the origin of dispersive artefacts in misorientation maps: even perfectly oriented lattice planes may appear distorted along the y- and the z-direction of the coordinate system. Especially for high quality crystals the dispersive effects may overlay an actual lattice distortion [Serrano 08, Matsouli 00]. In some publications the dispersive effects are quantified by the help of DuMond diagrams, [Servidori 01a, Servidori 01b, Shunsheng 88]. Pure geometrical considerations allowed us to derive theoretical correction formulas. In addition rocking curves on perfect Si single crystals were recorded and the derived formulas were verified.

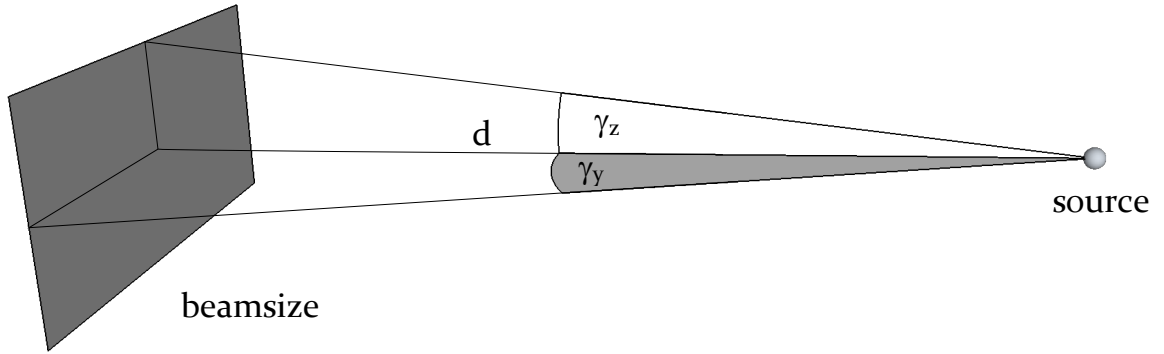


**Figure A.1:** Angular divergence of a synchrotron beam. The angles  $\gamma_z$  and  $\gamma_y$  are the opening angles along the z- and the y-axis.

The beam divergence is associated with variations of the angle  $\omega$ , opened by the crystal lattice planes and the incident beam wave vector.  $\omega$  depends on the position  $(y, z)$  in the incident beam:

$$\omega = \omega(y, z) \quad (\text{A.1})$$

The variations in  $\omega$  can be calculated by purely geometric considerations. Fig. A.2 shows a lattice plane that is illuminated by a divergent source. The centre of origin is the centre of the crystal surface, so that  $\omega_{B_0}(0, 0) = \omega_{B_0}$ . In Fig.( A.2)-LHS a 1D section of the problem is shown ( $y = 0$ ). The distance  $d$  between the source and the crystal is known. We calculate  $x_B = d \cdot \cos \omega_{B_0}$  and  $e = d \cdot \sin \omega_{B_0}$ . We also know that  $\tan \omega_B(x) = e / (x_B + x)$ . Inverting this equation gives  $\omega_B(x) = \arctan(e / (x_B + x))$ . These expressions are used to get  $e$  and  $x_B$ . Finally we express the variable  $x$  by  $z$ , the height in our experimental coordinate system

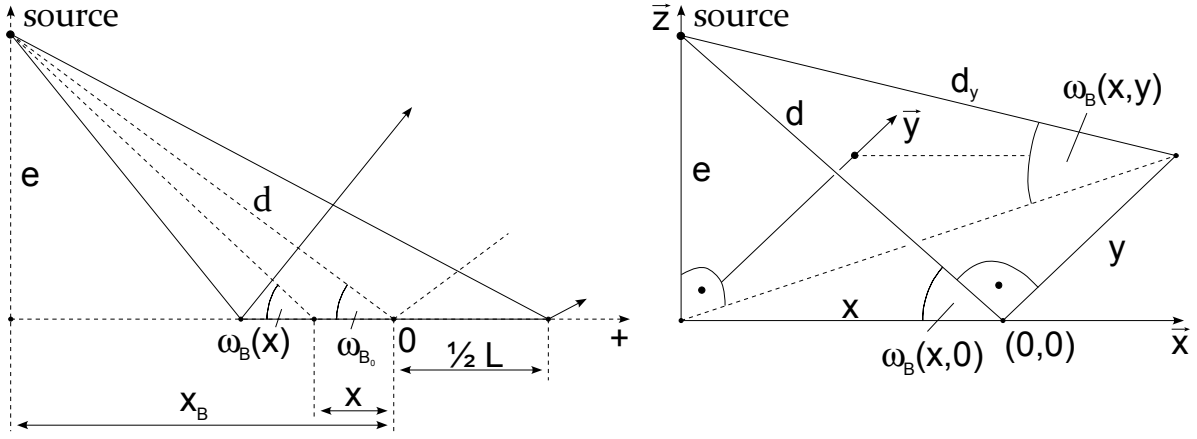


Figure A.2: Geometrical sketch to calculate the local  $\omega$ .

(Fig. 3.1),  $x = z \sin \omega_{B_0}$  and get a formula for  $\omega_{B_0}(z)$  in the 1D case ( $y = 0$ ):

$$\omega_B(\theta_{B_0}, z, 0) = \arctan \left[ \frac{d \cdot \sin \omega_{B_0}}{d \cdot \cos \omega_{B_0} + z \sin \omega_{B_0}} \right]. \quad (\text{A.2})$$

Fig. A.2-RHS allows to deduce  $\omega_B(x, y)$  by using  $\sin \omega_B(x, y) = e/d_y$ . We get  $e$  in the same manner as in the 1D case:  $e = d \cdot \sin \omega_B(x, 0)$ . Using Pythagorean theorem we get  $d_y = \sqrt{d^2 + y^2}$ . These two expressions allow to replace all unknown parameters in the equation for  $\omega_B(y, z)$  and we obtain:

$$\omega_B(\theta_{B_0}, y, z) = \arcsin \left[ \frac{d \cdot \sin (\omega_B(\theta_{B_0}, z, 0))}{\sqrt{d^2 + y^2}} \right] \quad (\text{A.3})$$

**Wavelength dispersion:** The beam divergence affects the wavelength  $\lambda$  of the monochromatic beam, that is generated by a Si-monochromator. The first Si-crystal is inclined by the Bragg angle  $\theta_B$  so that its centre position Bragg diffracts the wavelength part of the white beam that corresponds to the chosen working energy. The wavelength diffracted by any other position on the crystal is different. This “local” wavelength is expressed as:

$$\lambda(y, z) = 2d_{111}^{\text{Si}} \sin [\omega_B(\theta_B, y, z)] \quad (\text{A.4})$$

Eq. (A.4) shows that wavelength dispersion is directional: the main variations in wavelength occur along the  $z$ -axis.

**Angular dispersion:** The angle  $\omega$  on the sample position may also be expressed by Eq. A.3. The Bragg diffracting lattice planes are inclined to the incident beam, by the Bragg angle. Depending on the experimental geometry (horizontally or vertically Bragg diffracted image) the effect is directional. The main direction of angular dispersion is along the  $y$ -axis for horizontally diffracting lattice planes and along the  $x$ -axis for vertically diffracting lattice planes. Therefore the angular dispersion may not be distinguished from wavelength dispersion when the Bragg diffracting sense is vertical. The local  $\omega$  at the sample position is

expressed by

$$\omega_B^{\text{vert.}}(\theta_{\text{sample-lattice}}, y, z) = \arcsin \left[ \frac{d \cdot \sin \omega_B(z, 0)}{\sqrt{d^2 + y^2}} \right] \quad (\text{A.5})$$

$$\omega_B^{\text{hor.}}(\theta_{\text{sample-lattice}}, y, z) = \arcsin \left[ \frac{d \cdot \sin \omega_B(y, 0)}{\sqrt{d^2 + z^2}} \right] \quad (\text{A.6})$$

**Application to a perfect Si crystal:** The corrections were verified on a RCI data set that was recorded on the (111) planes of a 5 mm thick silicon crystal. The crystal was cut out from a single crystal ingot and polished by the crystal lab at the ESRF. Those crystals are usually produced for X-ray optical applications and exhibit no dislocations at all, the surface are polished to high perfection as well. The crystal may be considered as perfect and its thickness prevents elastic strains that might be induced by the sample holder. As a consequence, any measured lattice distortions must be artefacts that occur due to dispersive effects. Such a sample is very suitable to verify if the derived equations properly remove dispersive artefacts: once they are applied, the distortion map must be homogeneous.

The crystal has the Si (111) planes perpendicular to its surfaces, those were chosen as Bragg diffracting lattice planes due to the high structure factor (Eq. 2.8). As already mentioned, wavelength dispersive effects mainly occur along the vertical direction of the Bragg diffraction image, whereas angular dispersion is mainly parallel to the direction of the Bragg diffraction. The direction of the Bragg diffraction chosen horizontally in order to distinguish angular dispersion from wavelength dispersion. It is then easier to see, which part is wrongly corrected. The experimental was performed in Laue geometry (Chap. 2.2) in order to match with our ice experiments and at the BM05 beamline (Chap. 3.2) at the ESRF, where our experiments generally take place. Here, the distance between the X-ray source and the sample is 55 m, the Si monochromator is situated at 27 m after the source. The working energy was 30 keV which is higher than in our ice experiments but assures the penetration of the X-ray beam through the thick Si sample. The initial Bragg position map, including all dispersive effects, is shown in Fig. A.3. The detector was the pco.2000 that provides a pix-

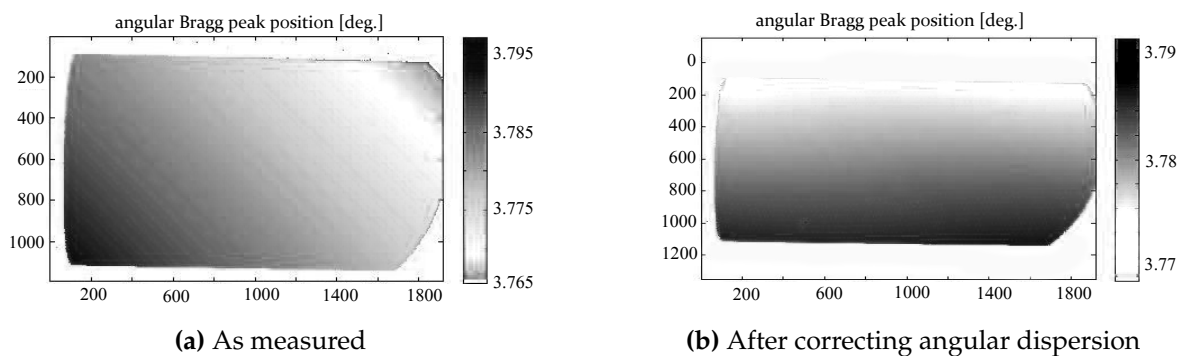


**Figure A.3:** Angular position of the Bragg peaks - Si 111-Bragg diffraction - Laue geometry - E=30 keV.

elsize of  $10 \mu\text{m}$  so the size of the Bragg diffraction image is approximately  $18 \text{ mm} \times 9 \text{ mm}$ . Both components, angular- and wavelength dispersion occur in the image: the wavelength part mainly exerts along the vertical direction, whereas the angular one along the horizontal. As the two effects superpose, the result is a nearly linear evolution of the Bragg peak position along the diagonal from the left bottom corner to the right upper corner of the map.

In a first step the angular component is removed from the Bragg peak position map by applying the angular shift calculated by Eq. A.6. The result is shown in Fig. A.3b. The angular component of the dispersion, that was mainly present along the horizontal direction of the map, has disappeared. The angular positions along a horizontal line are now constant what confirms the correctness of our angular dispersion calculations.

Finally the wavelength dispersion component is removed as well by taking into account the position dependent wavelength (Eq. A.4). The result is presented in Fig. A.4. The an-

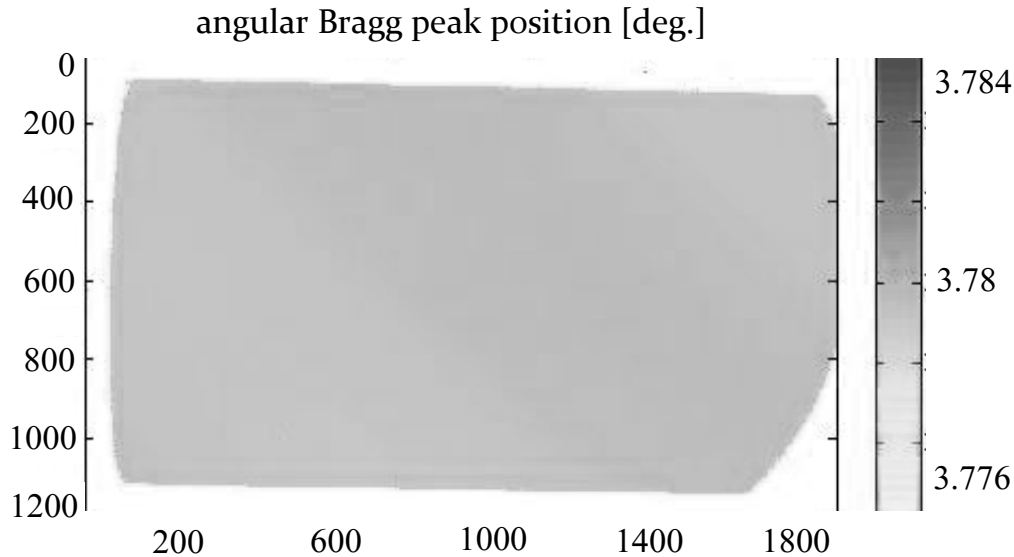


**Figure A.4:** Angular position of the Bragg peaks on the dataset shown in Fig. A.3, after removing both dispersive effects.

gular position map now appears homogeneous also along the vertical direction and attests a correct handling of wavelength dispersion as well. There are no distortions visible on the map what is in perfect accordance with the investigation of a practically perfect Si crystal. Let us note the small width of the rocking curve. Whereas the graytones in Fig. A.3 represent an angular interval of  $0.03^\circ$ , the final “corrected” position map is presented in a range of  $0.008^\circ$  and there are still no inhomogeneities observable. Our equations are experimentally confirmed on a perfect crystal and may be applied to distorted ones.

**Application to ice** In the following an application of our dispersion corrections to a distorted crystal is shown. The following experiment was performed on a pyramidal Bragg diffraction of an ice single crystal. The working energy was chosen to be 18 keV, as usual. This time, the rocking sense is vertical (horizontal rocking axis). Fig. A.5 shows a map of angular positions of the Bragg peaks. The Bragg diffracting basal planes seem to be distorted along the vertical direction.

After removing the dispersive artefacts, the angular interval that contains all Bragg peak positions is diminished, the contrast of the map may therefore be enhanced (Fig. A.6) what reveals more details about crystalline defects. Dislocations that were hardly visible before, appear now very strong and in higher quantity. The Bragg diffracting lattice planes, that appeared to be distorted along the vertical direction, are actually horizontally distorted. The example shows how dispersive effects may falsify the results, especially on weakly distorted crystals, and underlines the importance of a correction.

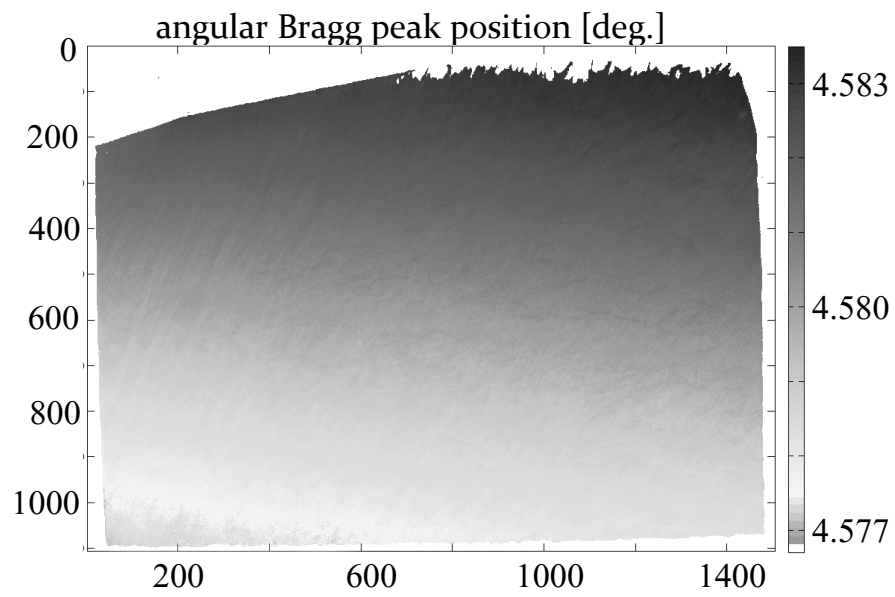


**Figure A.5:** Angular position of the Bragg peaks on a pyramidal Bragg diffraction, vertically diffracted, before applying dispersion corrections.

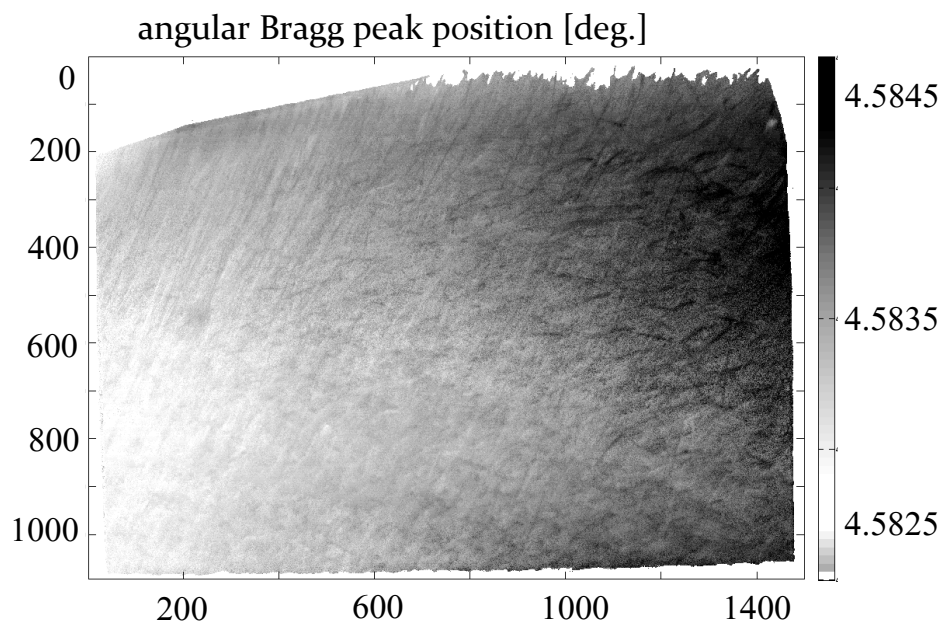


**Figure A.6:** Angular position of the Bragg peaks on a pyramidal Bragg diffraction, vertically diffracted, before applying dispersion corrections.

# Lateral deviations of the Bragg diffracted beam

The present appendix deals with misorientations around the x-axis. In our experimental coordinate system (Fig. 3.1) they correspond to misorientations around the x-axis (Fig. 1.8). The effect of such misorientations needs to be quantified, first to know their influence on the measurement of other misorientation components, and second to measure themselves, because, as already mentioned, we cannot measure them by a  $90^\circ$  rotation of the sample. In the following, a misorientation component around an axis of the coordinate system is expressed as a rotation matrix. For example  $R_{\alpha_x}^{\vec{x}}$  is a misorientation around the x-axis by the angle  $\alpha_x$ . The incident X-ray beam has per definition a wave vector oriented along the x-axis:  $\vec{k}_0 = k(1/0/0)$ . Please note that according to our coordinate system the value of  $\theta_B$  is negative because the region is rotated clockwise along the y-axis direction in order to bring it into diffraction. Eq. (B.11) correlates misorientations around the x-axis with lateral deviations of the Bragg diffracted beam. The formula is used in our data analysis (Chap. 4.3.2).

A region, that is perfectly oriented along the z-axis, exhibits a diffraction vector  $\vec{h} = h(0/0/1)$ . The angular misorientation  $\alpha_x$  around the x-axis is generated by applying its associated rotation matrix  $R_{\alpha_x}^{\vec{x}}$  to the diffraction vector of a perfectly oriented region  $\vec{h}$ . As a result we obtain the diffraction vector of the misoriented region  $\vec{h}'(\alpha_x)$ :

$$\vec{h}'(\alpha_x) = R_{\alpha_x}^{\vec{x}} \vec{h} = \begin{pmatrix} 1 & 0 & 0 \\ 0 & \cos \alpha_x & -\sin \alpha_x \\ 0 & \sin \alpha_x & \cos \alpha_x \end{pmatrix} \cdot h \begin{pmatrix} 0 \\ 0 \\ 1 \end{pmatrix} = h \begin{pmatrix} 0 \\ -\sin \alpha_x \\ \cos \alpha_x \end{pmatrix} \quad (\text{B.1})$$

In order to have a general case, we apply a misorientation around the y-axis by  $\alpha_y$  as well and obtain  $\vec{h}''_{\alpha_x, \alpha_y}$ :

$$\vec{h}''(\alpha_x, \alpha_y) = R_{\alpha_y}^{\vec{y}} \vec{h}' = \begin{pmatrix} \cos \alpha_y & 0 & \sin \alpha_y \\ 0 & 1 & 0 \\ -\sin \alpha_y & 0 & \cos \alpha_y \end{pmatrix} \cdot h \begin{pmatrix} 0 \\ -\sin \alpha_x \\ \cos \alpha_x \end{pmatrix} = h \begin{pmatrix} \sin \alpha_y \cos \alpha_x \\ -\sin \alpha_x \\ \cos \alpha_x \cos \alpha_y \end{pmatrix} \quad (\text{B.2})$$

As mentioned in Chap. 1.4, the rotations associated to small misorientations we are concerned with ( $\alpha < 1^\circ$ ), are commutative. It makes therefore no difference if we misorient the region first around the x-axis and then around the y-axis, or the other way around. Further on, a rotation around the z-axis does not significantly misorient lattice planes that exhibit a mean orientation around the z-axis. We therefore may regard the obtained diffraction vector  $\vec{h}''$  as a general case.

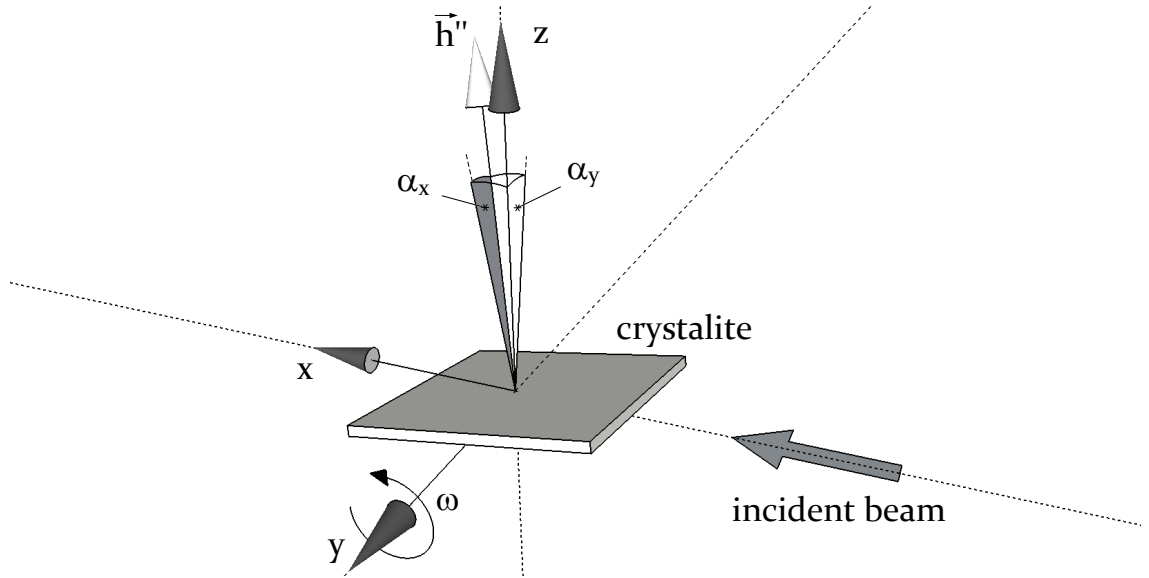


**Figure B.1:** A generally misoriented region is rotated by an angle  $\omega$  around the y-axis.

In the following, the lattice planes associated to  $\vec{h}''$  are oriented in a way, that they vertically Bragg diffract the incident beam. For this, the region needs to be turned around the y-axis by an angle that we call  $\omega$ . The resulting Bragg diffraction vector is called  $\vec{h}^*$ :

$$\begin{aligned}
 \vec{h}^*(\alpha_x, \alpha_y, \omega) &= R_{\omega}^y \vec{h}'' = \begin{pmatrix} \cos \omega & 0 & \sin \omega \\ 0 & 1 & 0 \\ -\sin \omega & 0 & \cos \omega \end{pmatrix} h \begin{pmatrix} \sin \alpha_y \cos \alpha_x \\ -\sin \alpha_x \\ \cos \alpha_x \cos \alpha_y \end{pmatrix} \\
 &= h \begin{pmatrix} \cos \omega \sin \alpha_y \cos \alpha_x + \sin \omega \cos \alpha_x \cos \alpha_y \\ -\sin \alpha_x \\ -\sin \omega \sin \alpha_y \cos \alpha_x + \cos \omega \cos \alpha_x \cos \alpha_y \end{pmatrix} \\
 &= h \begin{pmatrix} \cos \alpha_x \sin(\omega + \alpha_y) \\ -\sin \alpha_x \\ \cos \alpha_x \cos(\omega + \alpha_y) \end{pmatrix} \tag{B.3}
 \end{aligned}$$

The vector  $\vec{h}^*$  represents a Bragg diffraction vector associated to lattice planes that are misoriented by  $\alpha_x$  around the x-axis, by  $\alpha_y$  around the y-axis and turned by an angle  $\omega$  around the y-axis. The two misorientation angles  $\alpha_x, \alpha_y$  are smaller than  $1^\circ$  whereas the  $\omega$  represents a macroscopic rotation.

The beam is Bragg diffracted when the angle opened by the lattice planes and incident beam wavevector  $\vec{k}_0$  is equal to the Bragg angle  $\theta_B$ . In other words, the angle opened by  $\vec{k}_0$  and the diffraction vector  $\vec{h}^*$  must be equal to  $90^\circ - \theta_B$ . This is mathematically expressed by:

$$\frac{\vec{k}_0 \circ \vec{h}^*}{|\vec{k}_0| |\vec{h}^*|} = \cos(90^\circ - \theta_B) = \sin \theta_B \tag{B.4}$$

The only variable in that equation is the angle  $\omega$  that changes the orientation of  $\vec{h}^*$ . We use the expression Eq. (B.3) for  $\vec{h}^*$  and  $\vec{k}_0 = k(1/0/0)$  to obtain an expression that allows to

resolve  $\omega$ :

$$\begin{aligned}\cos \alpha_x \sin (\omega + \alpha_y) &= \sin \theta_B \\ \omega &= \arcsin \left[ \frac{\sin \theta_B}{\cos \alpha_x} \right] - \alpha_y \\ \omega &\approx \theta_B - \alpha_y\end{aligned}\tag{B.5}$$

In the last step there was approximated  $\cos \alpha_x \approx 1$ . Eq. (B.5) allows a first and very important stating: small misorientations around the x-axis do not modify the angle  $\omega$  within a first approximation. That angle must be set to achieve the orientation of the lattice planes where Bragg diffraction occurs. This ensures that rocking curve imaging only measures one component of angular misorientations: the z-component for a horizontally Bragg diffracted beam and the y-component for a vertically Bragg diffracted beam. These misorientations simply shift the angle  $\omega$  (Eq. B.5). By using  $\omega = \theta_B - \alpha_y$  in Eq. (B.3), we obtain the diffraction vector  $\vec{h}^*$  as it is when the lattice planes Bragg diffract the monochromatic beam:

$$\vec{h}^*(\alpha_x, \alpha_y) = h \begin{pmatrix} \sin \theta_B \\ -\sin \alpha_x \\ \cos \theta_B \end{pmatrix}\tag{B.6}$$

Once again it was approximated  $\cos \alpha_x \approx 1$ . The direction of the Bragg diffracted beam is characterised by its wavevector  $\vec{k}_h$  that may be calculated by the Laue equation (Eq. 2.5):

$$\vec{k}_h = \vec{h} - \vec{k}_0 = \begin{pmatrix} h \sin \theta_B - k \\ -h \sin \alpha_x \\ h \cos \theta_B \end{pmatrix}\tag{B.7}$$

The Bragg diffracted beam propagates on a line  $\vec{l}$  that is defined by  $\vec{l} = a \cdot \vec{k}_h$ ;  $a \in \mathbb{R}$ . We want to know where the Bragg diffracted beam intersects the detector plane. The detector plane, situated in a distance  $D$  behind the crystal, is characterised by  $x = D$ . We resolve  $a$ :

$$a \cdot k_{hx} = D \Leftrightarrow a = \frac{D}{h \sin \theta_B - k}\tag{B.8}$$

The lateral deviation of the Bragg diffracted beam, that means along the y-direction, is

$$\begin{aligned}\Delta y &= a \cdot k_{hy} \\ &= \frac{D}{h \sin \theta_B - k} \cdot (-h \sin \alpha_x) \\ &= \frac{D}{k/h - \sin \theta_B} \cdot \sin \alpha_x\end{aligned}\tag{B.9}$$

By using  $k = 1/2d \sin \theta_B$  and  $h = 1/d$  we may express  $\Delta y$  in terms of the Bragg angle  $\theta_B$

$$\Delta y = \frac{D}{\frac{1}{2 \sin \theta_B} - \sin \theta_B} \sin \alpha_x\tag{B.10}$$

Finally we approximate  $\sin \alpha_x \approx \alpha_x$  and simplify the equation to:

$$\Delta y = 2D \frac{\sin \theta_B}{\cos 2\theta_B} \cdot \alpha_x\tag{B.11}$$



## APPENDIX C

# Permuting rotations

A misorientation component  $\alpha_i$ ,  $i = x, y, z$  may be represented by a rotation matrix:

$$R_{\alpha_x}^{\vec{x}} = \begin{pmatrix} 1 & 0 & 0 \\ 0 & \cos \alpha_x & -\sin \alpha_x \\ 0 & \sin \alpha_x & \cos \alpha_x \end{pmatrix} \quad R_{\alpha_y}^{\vec{y}} = \begin{pmatrix} \cos \alpha_y & 0 & \sin \alpha_y \\ 0 & 1 & 0 \\ -\sin \alpha_y & 0 & \cos \alpha_y \end{pmatrix} \quad (\text{C.1})$$

where the misorientations that we measure in our experiments do not exceed values of  $0.5^\circ$ :  $\alpha_i < 0.5^\circ \approx 0.01$  rad. That allows to approximate:  $\sin \alpha_i \approx \alpha_i$  and  $\cos \alpha_i \approx 1$ .

As mentioned in Chap. 1.4, the application of two rotation matrices is generally not commutative:

$$\mathcal{R}_{\alpha_1}^{\vec{q}_1} \mathcal{R}_{\alpha_2}^{\vec{q}_2} \neq \mathcal{R}_{\alpha_2}^{\vec{q}_2} \mathcal{R}_{\alpha_1}^{\vec{q}_1} \quad (\text{C.2})$$

We show here that the error, that occurs by permuting the rotation matrices representing the measured misorientations, is negligible. We do this by using the mentioned approximations and then calculating  $R_{\alpha_x}^{\vec{x}} R_{\alpha_y}^{\vec{y}}$  and  $R_{\alpha_y}^{\vec{y}} R_{\alpha_x}^{\vec{x}}$

$$R_{\alpha_x}^{\vec{x}} R_{\alpha_y}^{\vec{y}} = \begin{pmatrix} 1 & 0 & 0 \\ 0 & 1 & -\alpha_x \\ 0 & \alpha_x & 1 \end{pmatrix} \cdot \begin{pmatrix} 1 & 0 & \alpha_y \\ 0 & 1 & 0 \\ -\alpha_y & 0 & 1 \end{pmatrix} = \begin{pmatrix} 1 & 0 & \alpha_y \\ \alpha_x \alpha_y & 1 & -\alpha_x \\ -\alpha_y & \alpha_x & 1 \end{pmatrix} \quad (\text{C.3})$$

$$R_{\alpha_y}^{\vec{y}} R_{\alpha_x}^{\vec{x}} = \begin{pmatrix} 1 & 0 & \alpha_y \\ 0 & 1 & 0 \\ -\alpha_y & 0 & 1 \end{pmatrix} \cdot \begin{pmatrix} 1 & 0 & 0 \\ 0 & 1 & -\alpha_x \\ 0 & \alpha_x & 1 \end{pmatrix} = \begin{pmatrix} 1 & -\alpha_x \alpha_y & \alpha_y \\ 0 & 1 & -\alpha_x \\ -\alpha_y & \alpha_x & 1 \end{pmatrix} \quad (\text{C.4})$$

The small misorientation values make the product of misorientations negligible compared a misorientation itself:  $\alpha_x \cdot \alpha_y = 10^{-4} \ll \alpha_i$  and we approximate  $\alpha_x \cdot \alpha_y \approx 0$ . As a result we obtain:

$$R_{\alpha_x}^{\vec{x}} R_{\alpha_y}^{\vec{y}} \approx R_{\alpha_y}^{\vec{y}} R_{\alpha_x}^{\vec{x}} = \begin{pmatrix} 1 & 0 & \alpha_y \\ 0 & 1 & -\alpha_x \\ -\alpha_y & \alpha_x & 1 \end{pmatrix} \quad (\text{C.5})$$

Very similar calculations can be done for other misorientation components around the axis of the coordinate system. The error in the misorientation measurements, that is induced by permuting misorientation components is maximally  $\alpha_x \cdot \alpha_y / \alpha_i \sim 1\%$ .

## Curvature tensor calculations

This chapter sets up a mathematical correlation between the three misorientation angles around the axis of the coordinate system and the components of the curvature tensor. We assume here the same approximations as before: the misorientation angles are small enough to allow permuting the rotation components (Chap. C) and we may express  $\cos \alpha_i \approx 1$  and  $\sin \alpha_i \approx \alpha_i \forall i$ . We calculate the general misorientation matrix  $\mathcal{R}_\alpha^{\vec{q}}$  by applying a rotation around the z-axis to the result in Eq. C.5:

$$\mathcal{R}_\alpha^{\vec{q}} = \mathcal{R}_{\alpha_z}^z \begin{pmatrix} 1 & 0 & \alpha_y \\ 0 & 1 & -\alpha_x \\ -\alpha_y & -\alpha_x & 1 \end{pmatrix} = \begin{pmatrix} 1 & -\alpha_z & \alpha_y \\ \alpha_z & 1 & -\alpha_x \\ -\alpha_y & \alpha_x & 1 \end{pmatrix} \quad (\text{D.1})$$

The rotation matrix  $\mathcal{R}_\alpha^{\vec{q}}$  describes the misorientation between two regions in the crystal, situated in  $\vec{r}_1$  and  $\vec{r}_2$ . The crystalline orientation in  $\vec{r}_2$  can be retrieved from the orientation in  $\vec{r}_1$  by:

$$\phi(\vec{r}_2) = \mathcal{R}_\alpha^{\vec{q}}(\vec{r}_1, \vec{r}_2)\phi(\vec{r}_1) \quad (\text{D.2})$$

In the next step, the rotation vector  $\theta_\alpha^{\vec{q}}$  is retrieved from the rotation matrix  $\mathcal{R}_\alpha^{\vec{q}}$ . The direction of the rotation vector corresponds to the rotation axis  $\vec{q}$ , its length to the rotation angle  $\alpha$ .

According to Pantleon [Pantleon 08] the rotation vector is associated to the rotation matrix by

$$\theta_i = -\epsilon_{ijk} \frac{\mathcal{R}_{jk}}{2} \quad (\text{D.3})$$

and the rotation vector is

$$\vec{\theta} = \begin{pmatrix} \alpha_x \\ \alpha_y \\ \alpha_z \end{pmatrix} \quad (\text{D.4})$$

The curvature tensor is the tensor taken on the vector field  $\vec{\theta}(\vec{r})$  and is calculated by:

$$K_{ij} = \theta_{i,j} = \alpha_{i,j} \quad (\text{D.5})$$

APPENDIX E

# Figures in large format

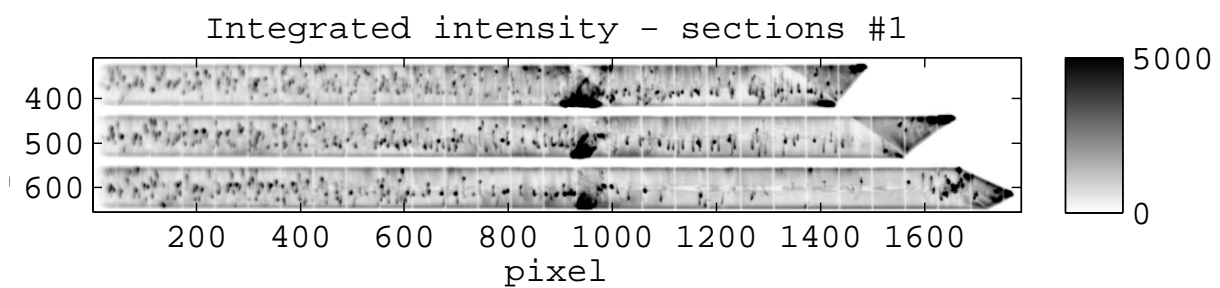


Figure E.1: In text: Fig. 5.3

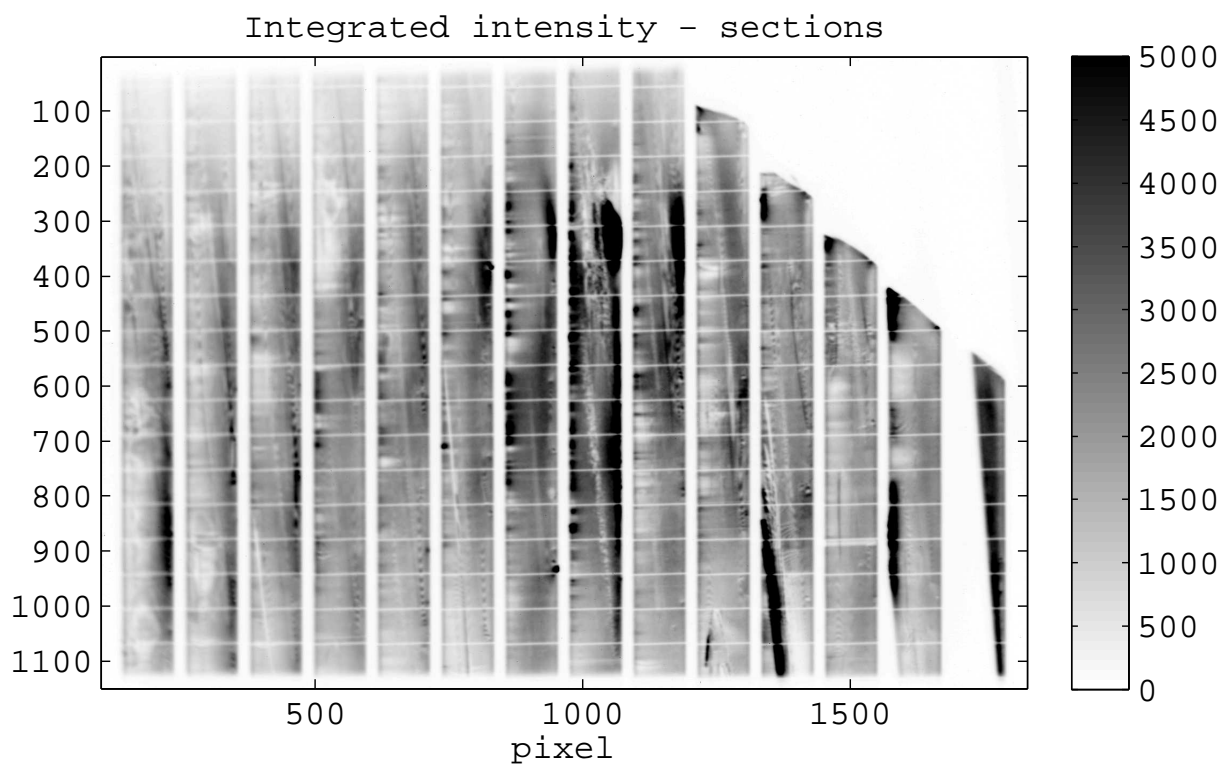


Figure E.2: In text: Fig. 5.4

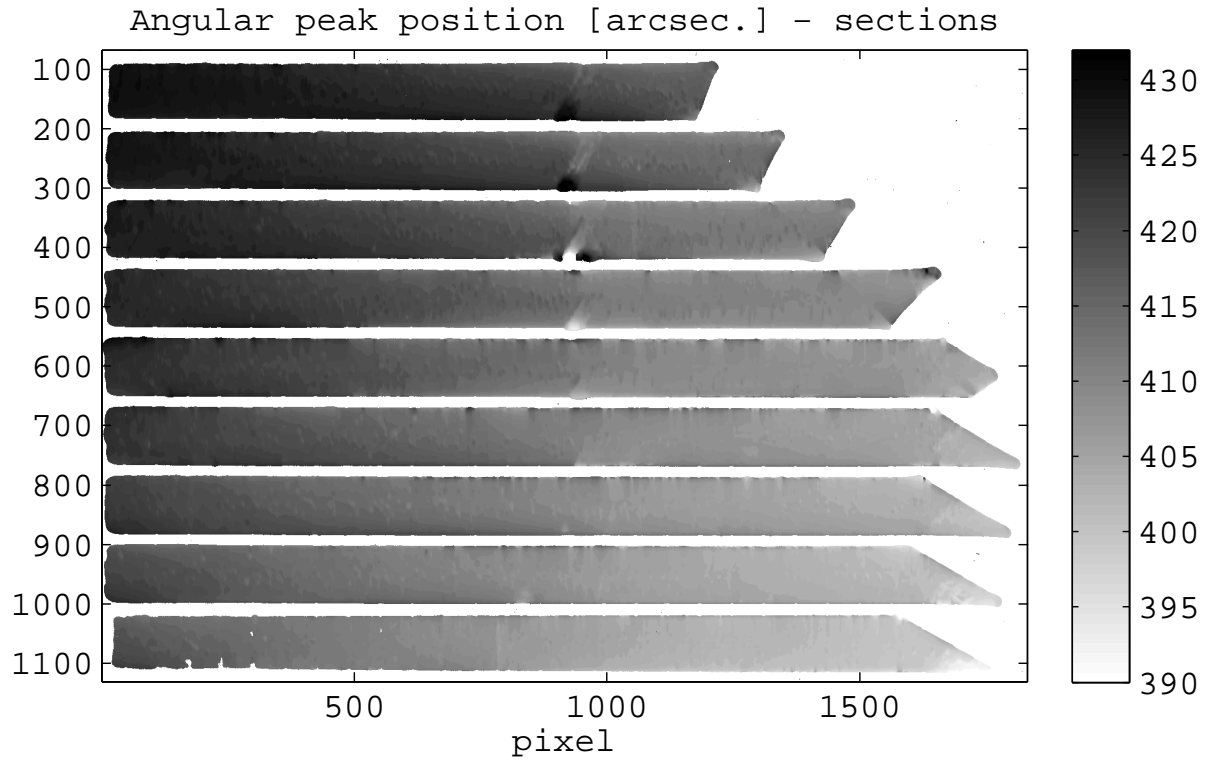


Figure E.3: In text: Fig. 5.5a

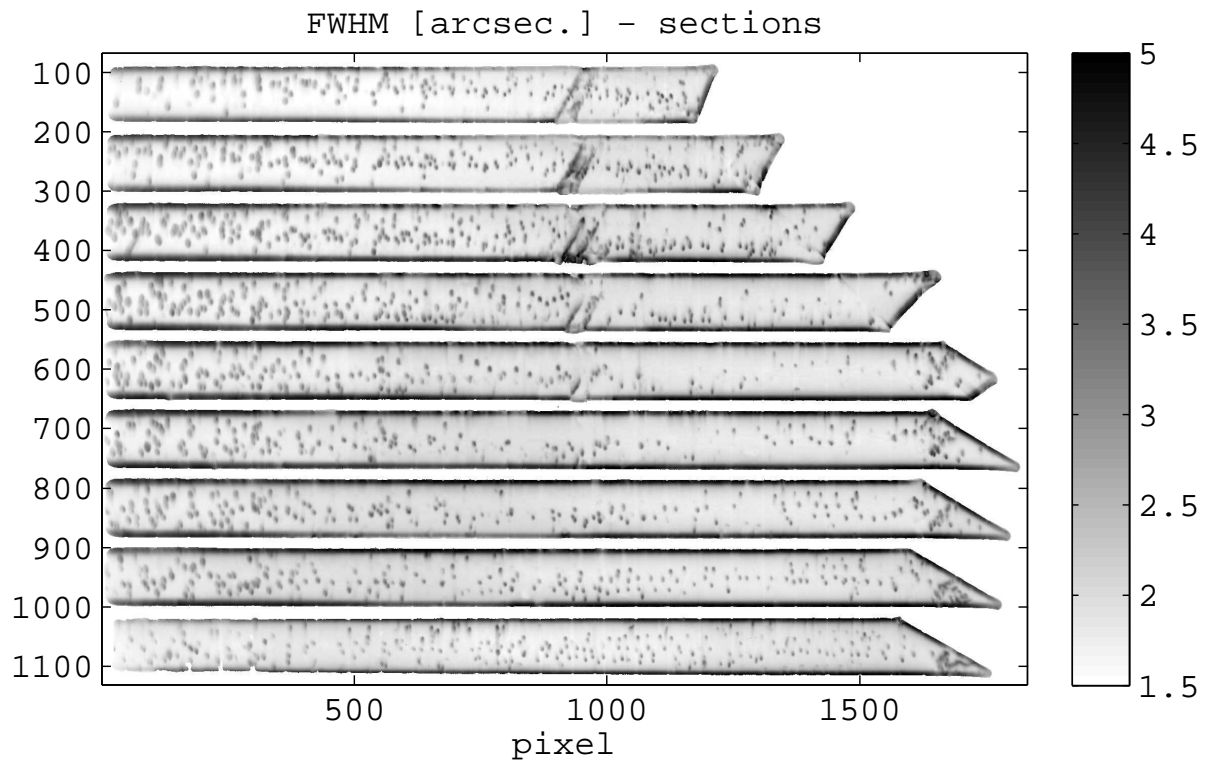


Figure E.4: In text: Fig. 5.5b

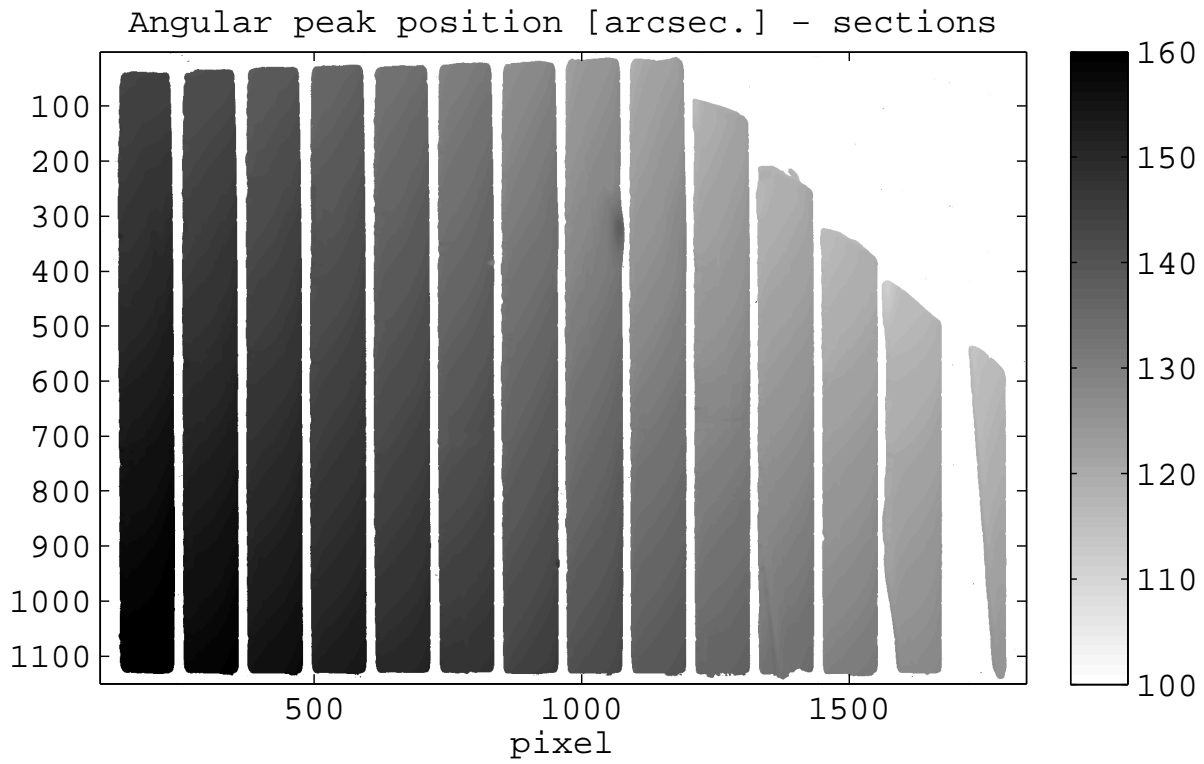


Figure E.5: In text: Fig. 5.6a

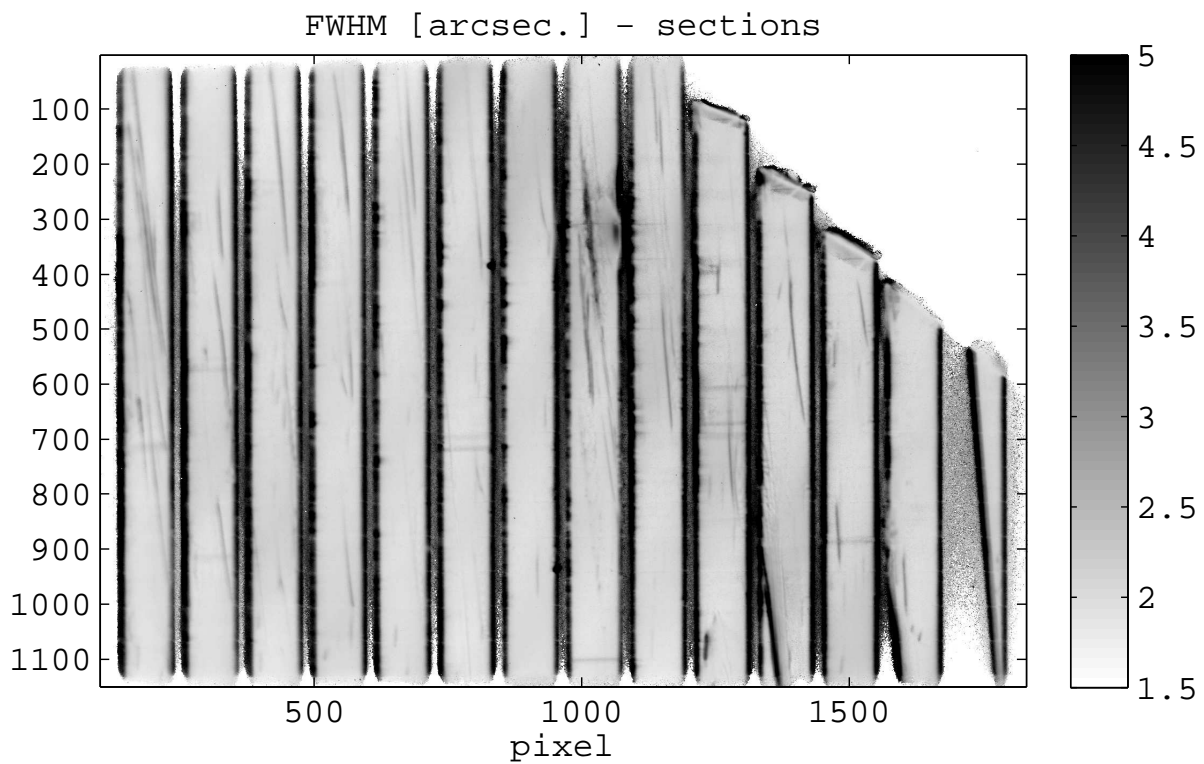


Figure E.6: In text: Fig. 5.6b

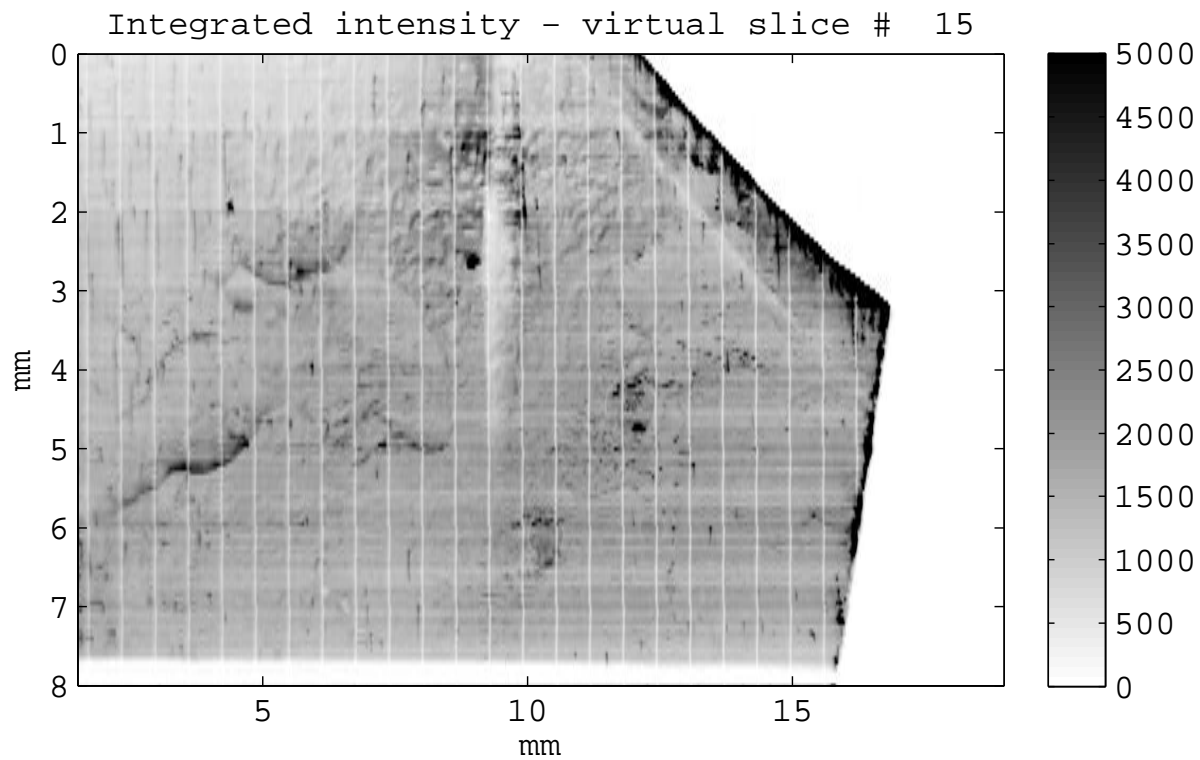


Figure E.7: In text: Fig. 5.7a

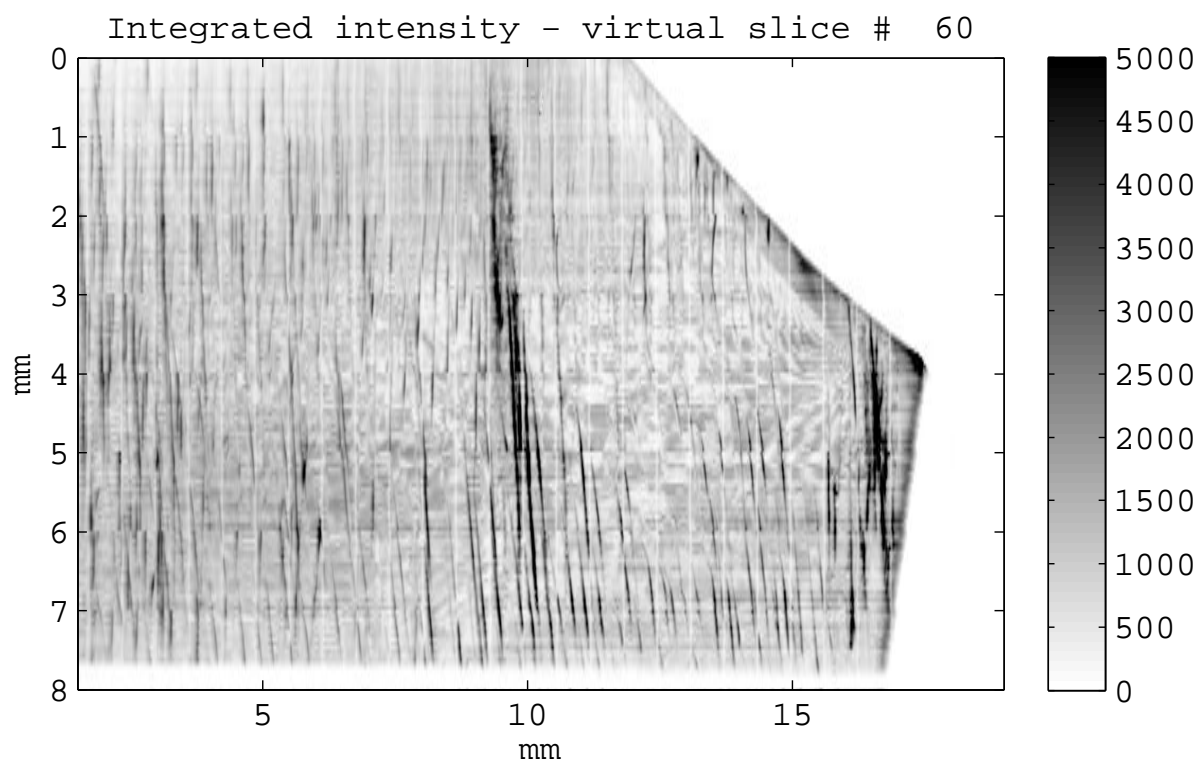


Figure E.8: In text: Fig. 5.7b

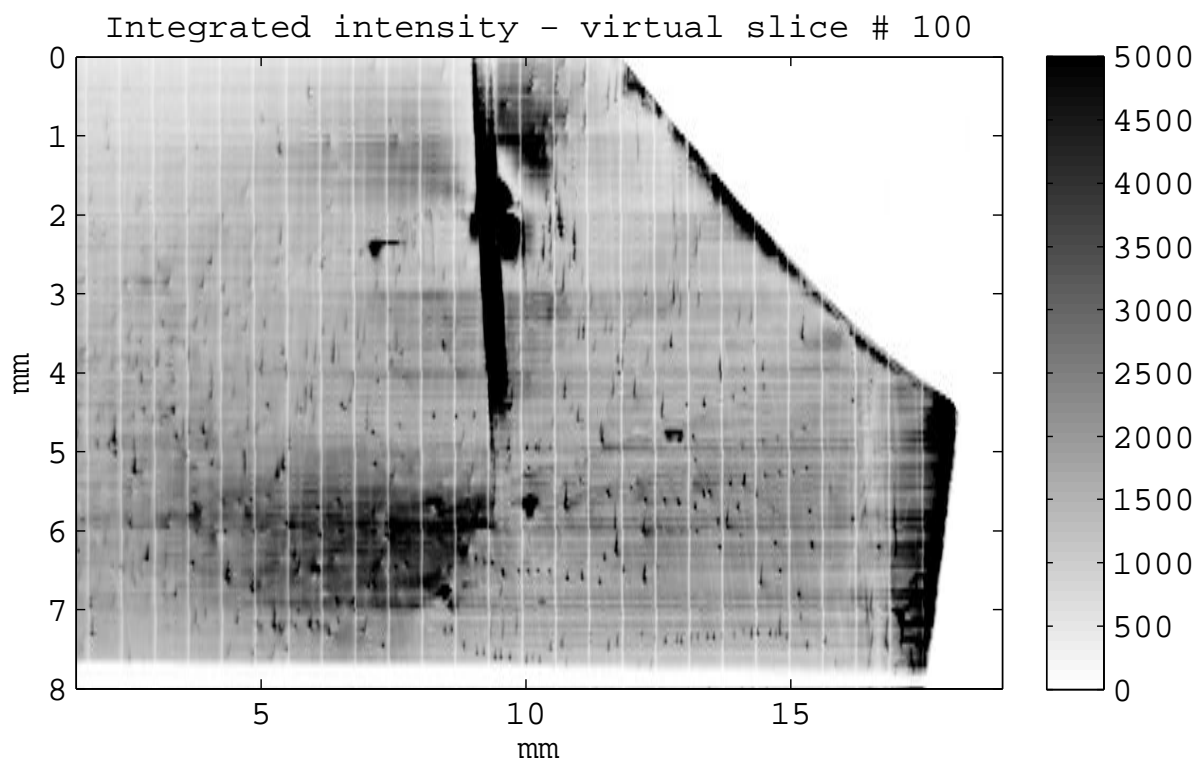


Figure E.9: In text: Fig. 5.7c

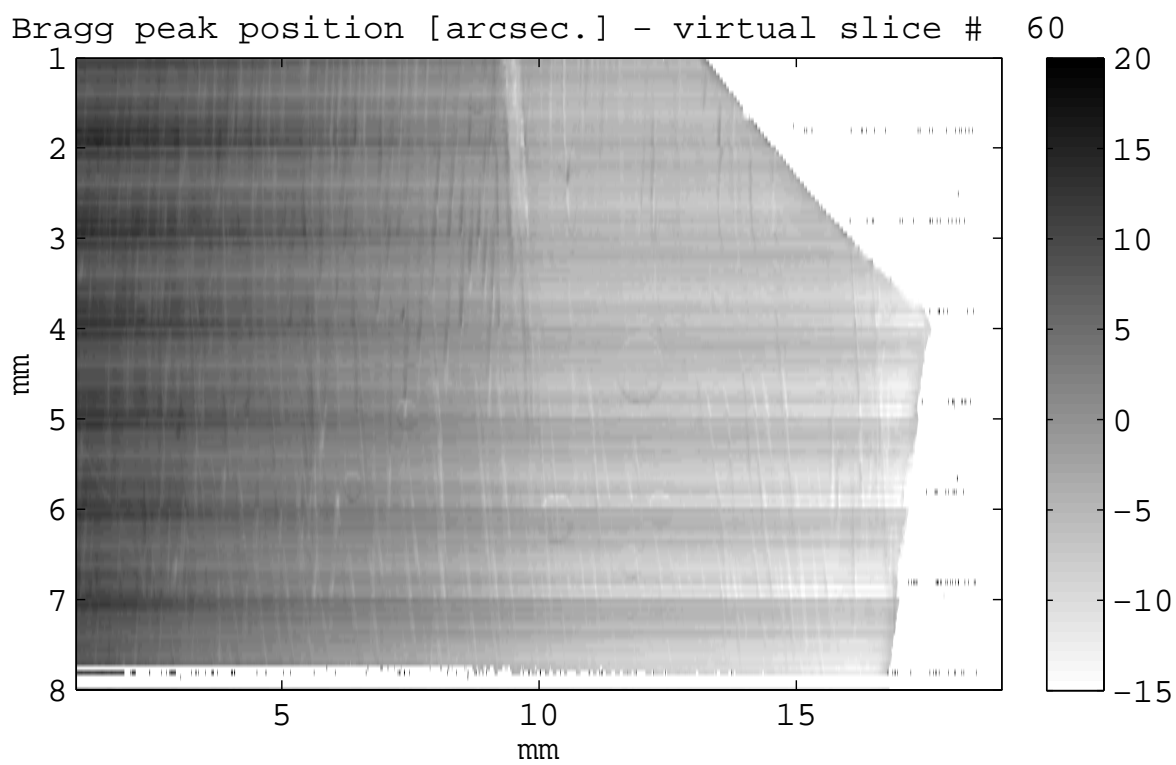


Figure E.10: In text: Fig. 5.8

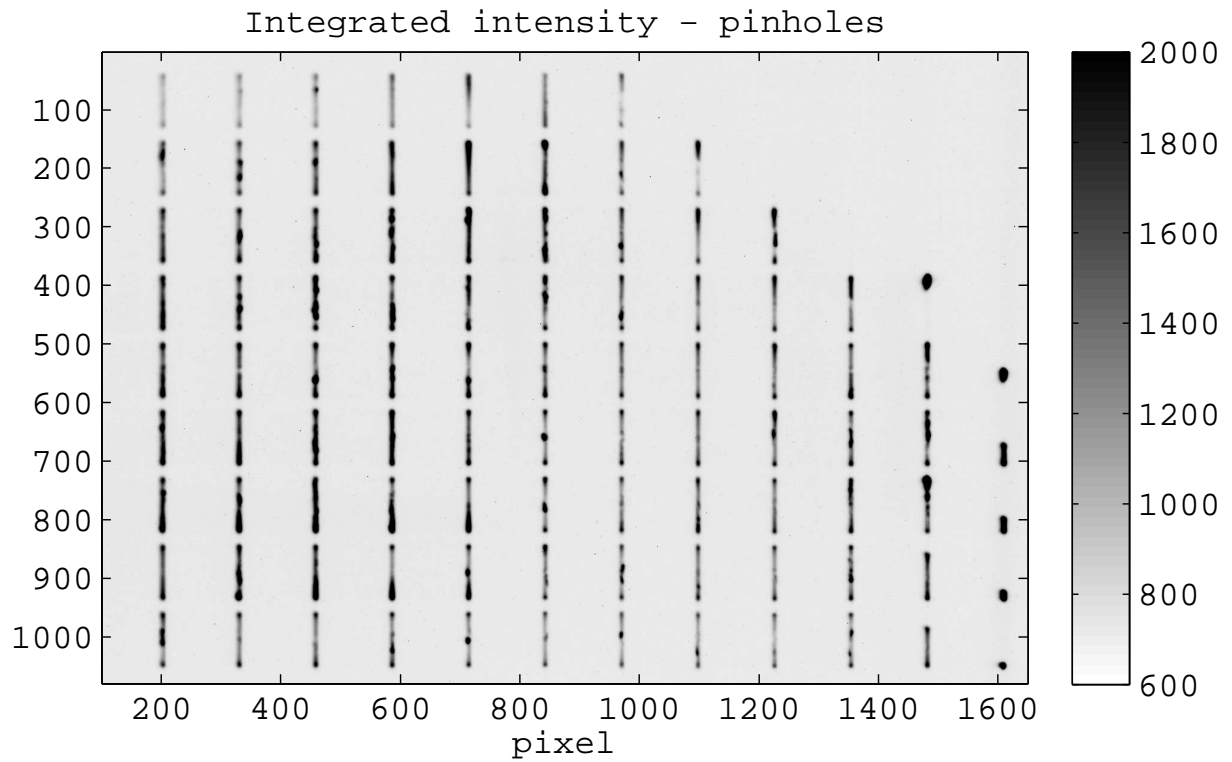


Figure E.11: In text: Fig. 5.9

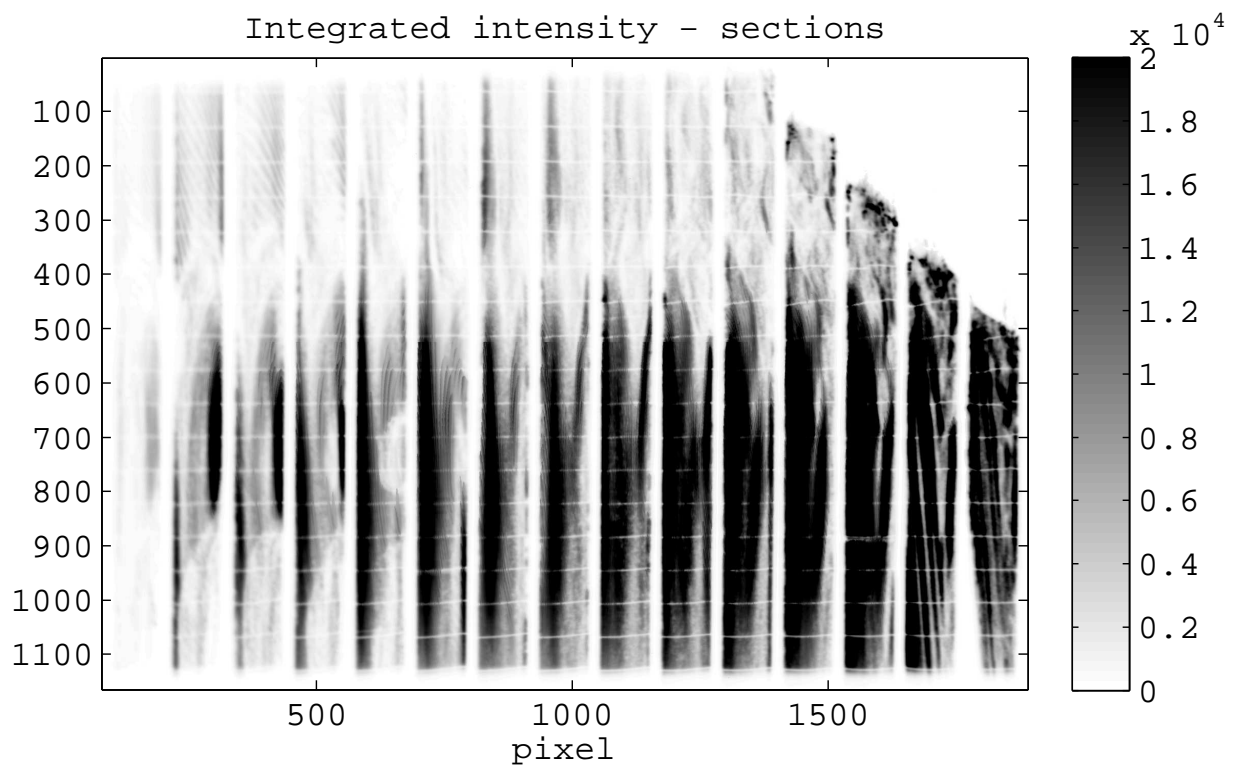


Figure E.12: In text: Fig. 5.11a

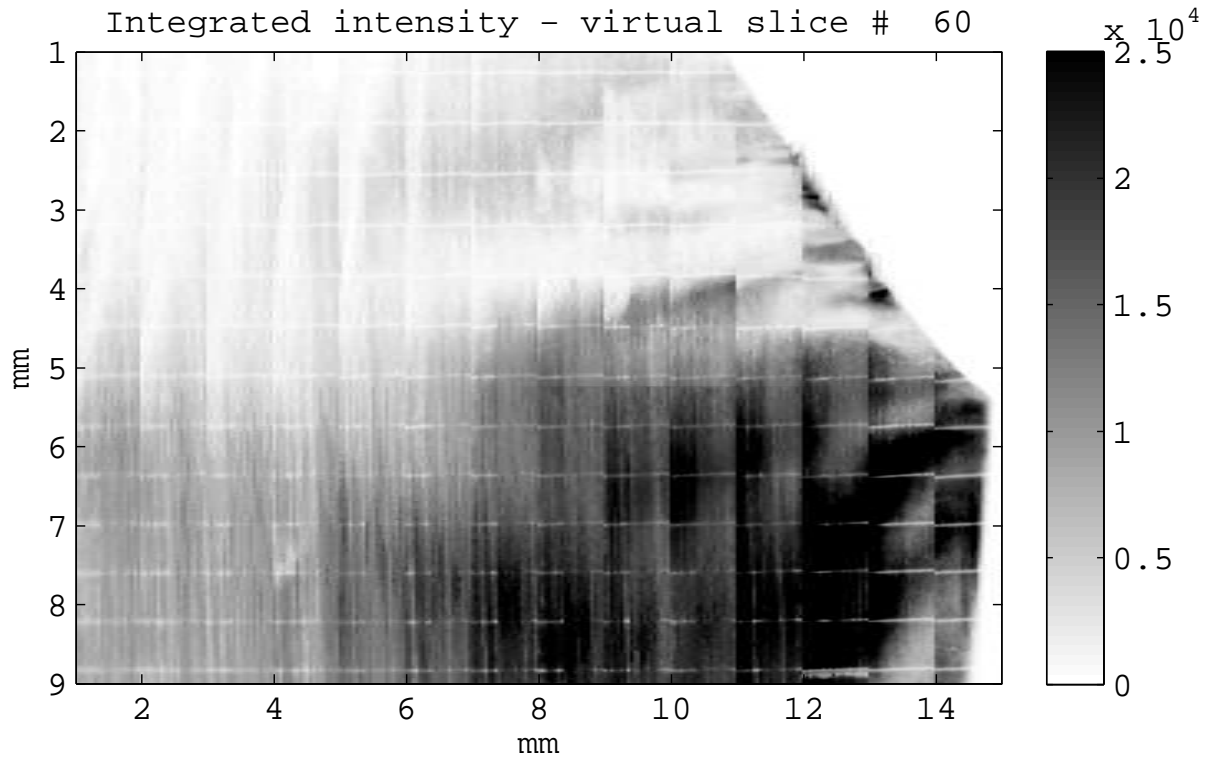


Figure E.13: In text: Fig. 5.11b

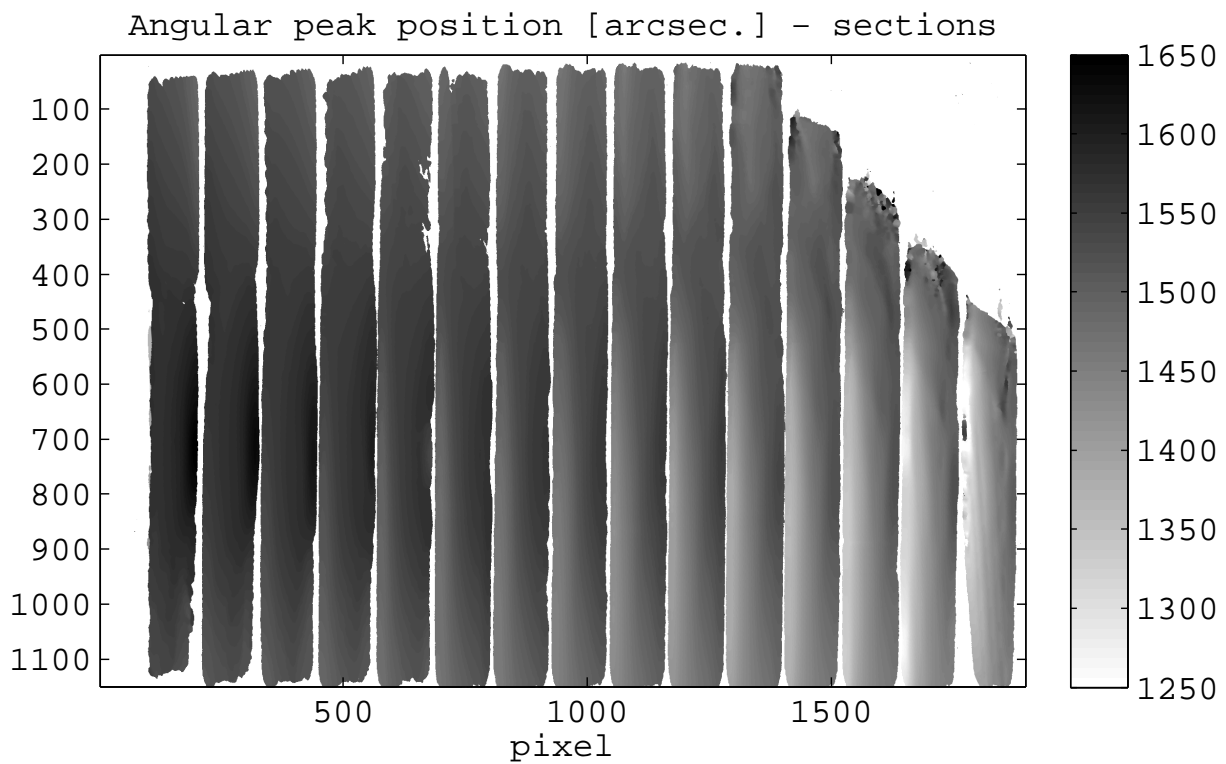


Figure E.14: In text: Fig. 5.12a

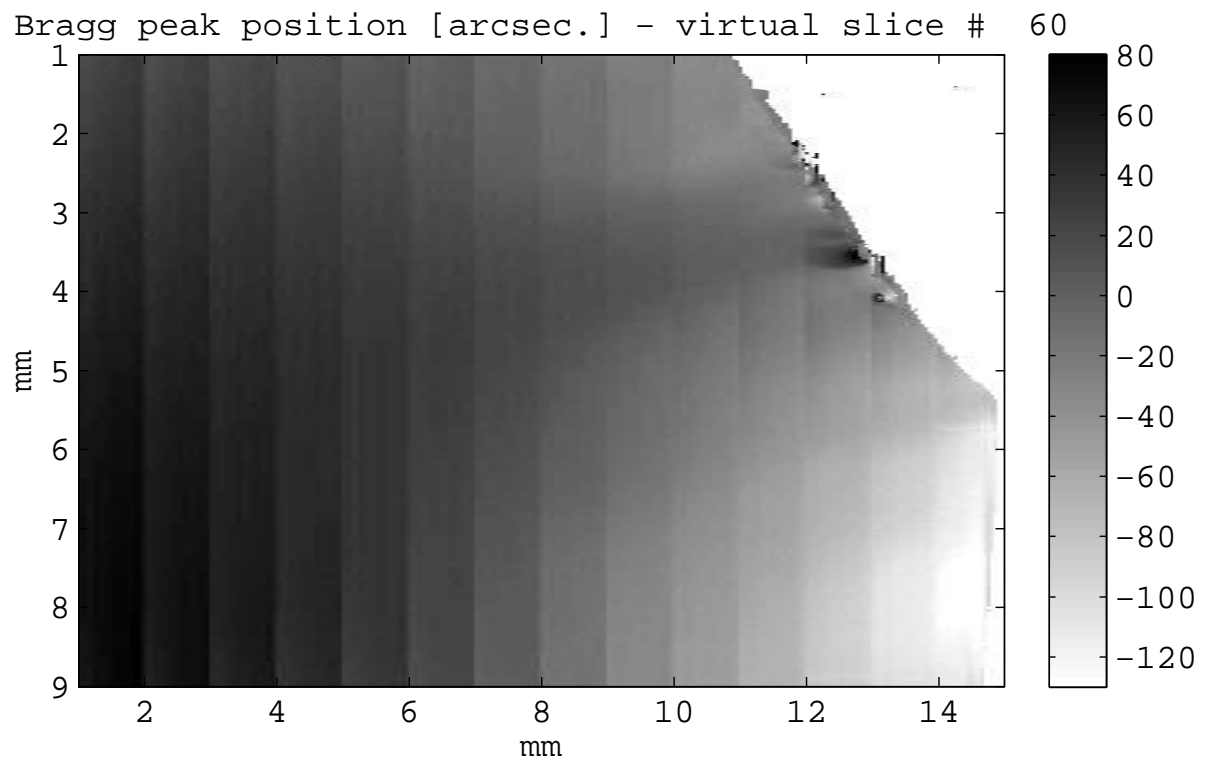


Figure E.15: In text: Fig. [5.12b](#)

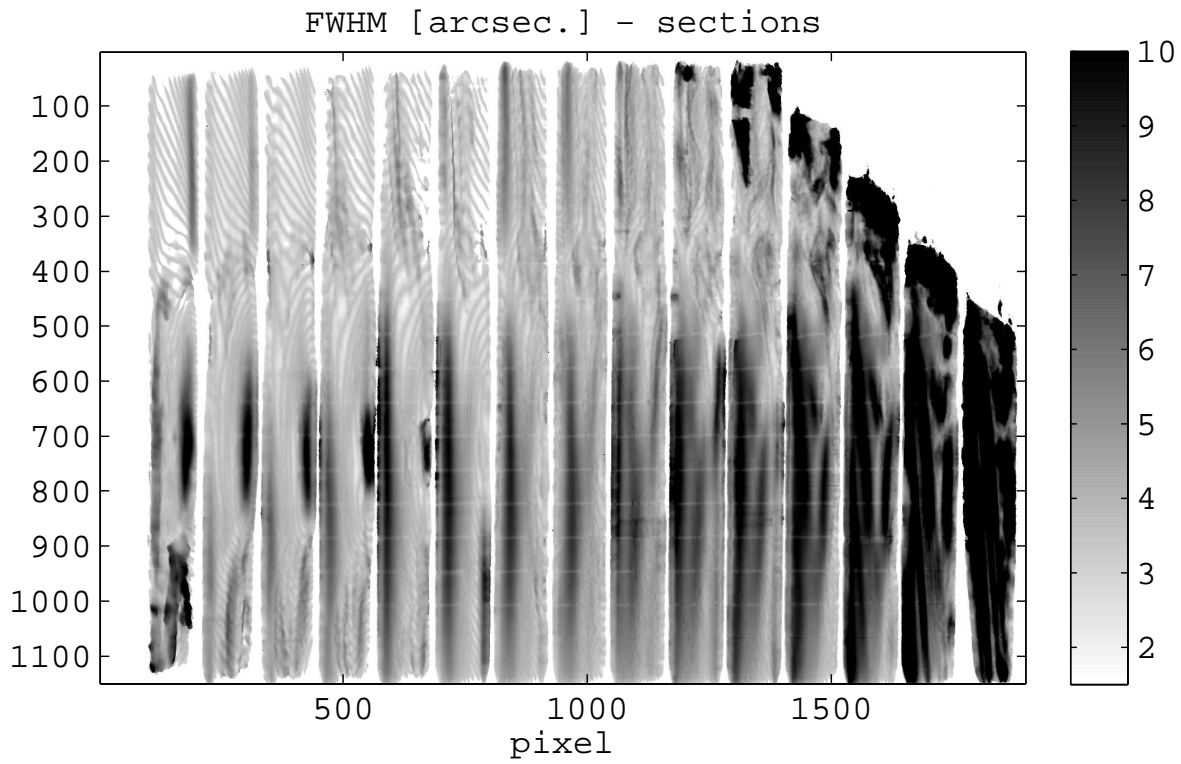


Figure E.16: In text: Fig. 5.13a

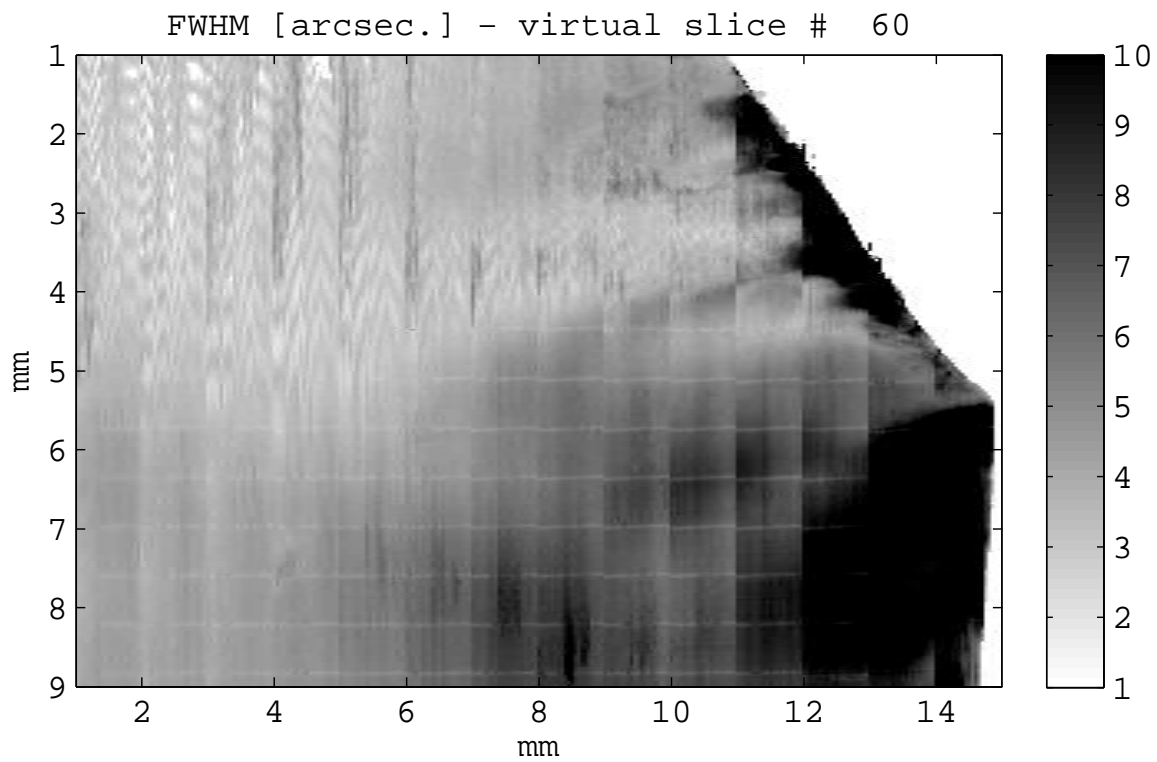


Figure E.17: In text: Fig. 5.13b

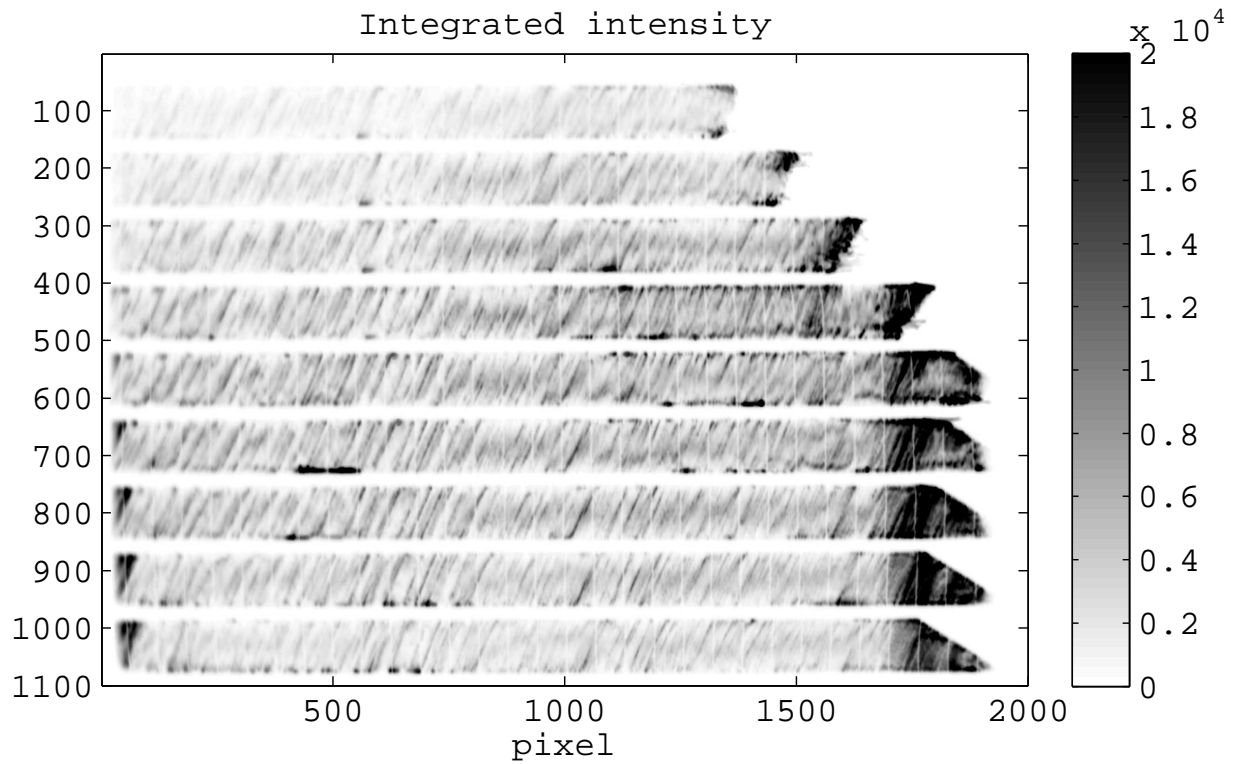


Figure E.18: In text: Fig. 5.14a

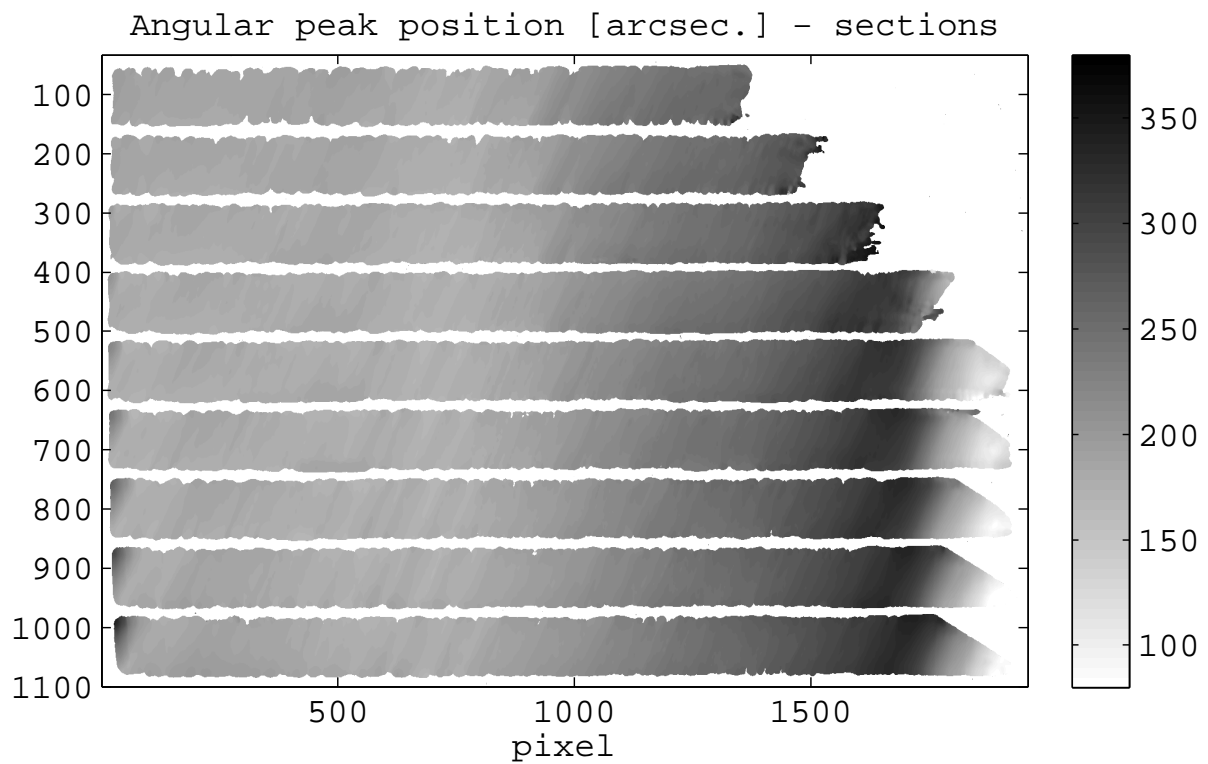


Figure E.19: In text: Fig. 5.15a

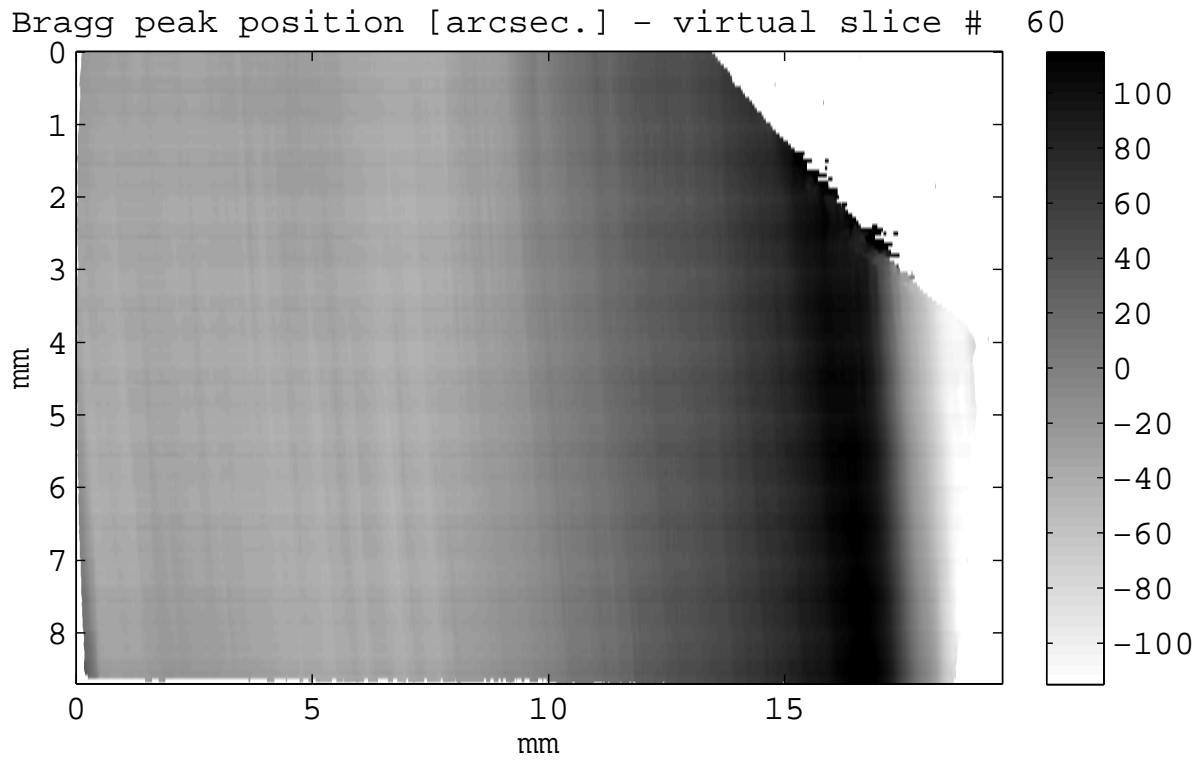


Figure E.20: In text: Fig. 5.15b

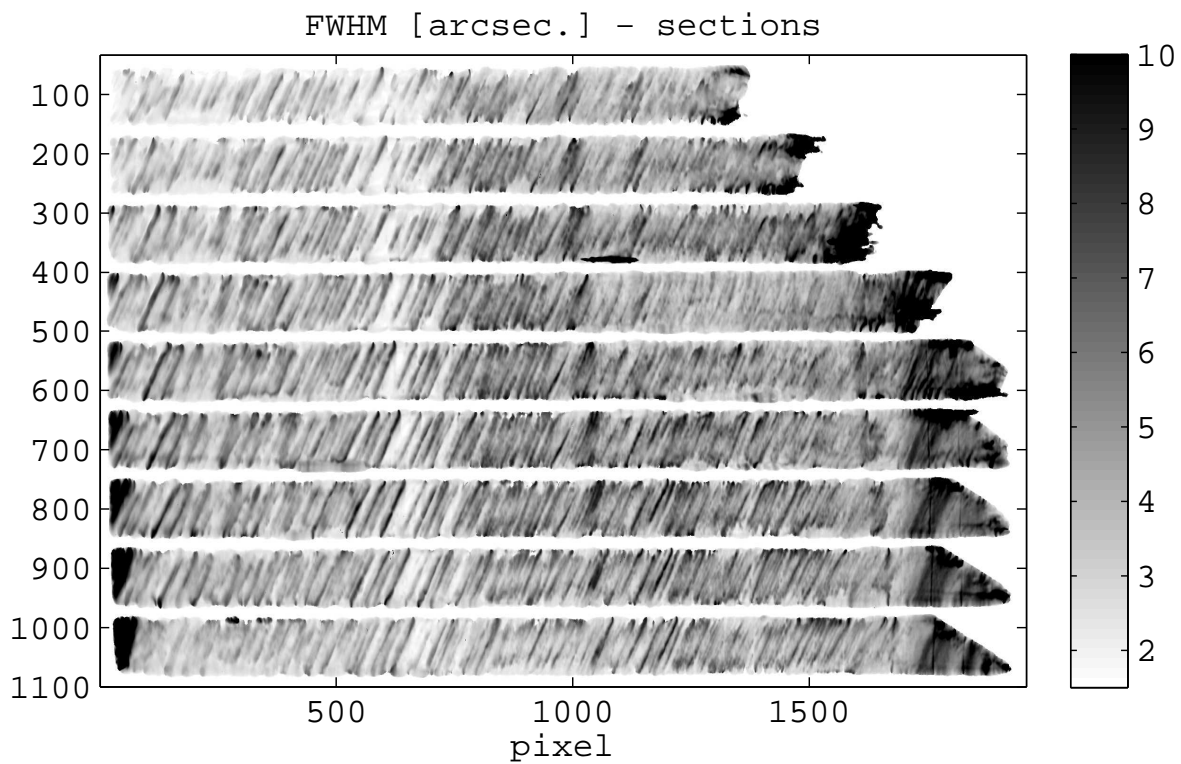


Figure E.21: In text: Fig. 5.16a

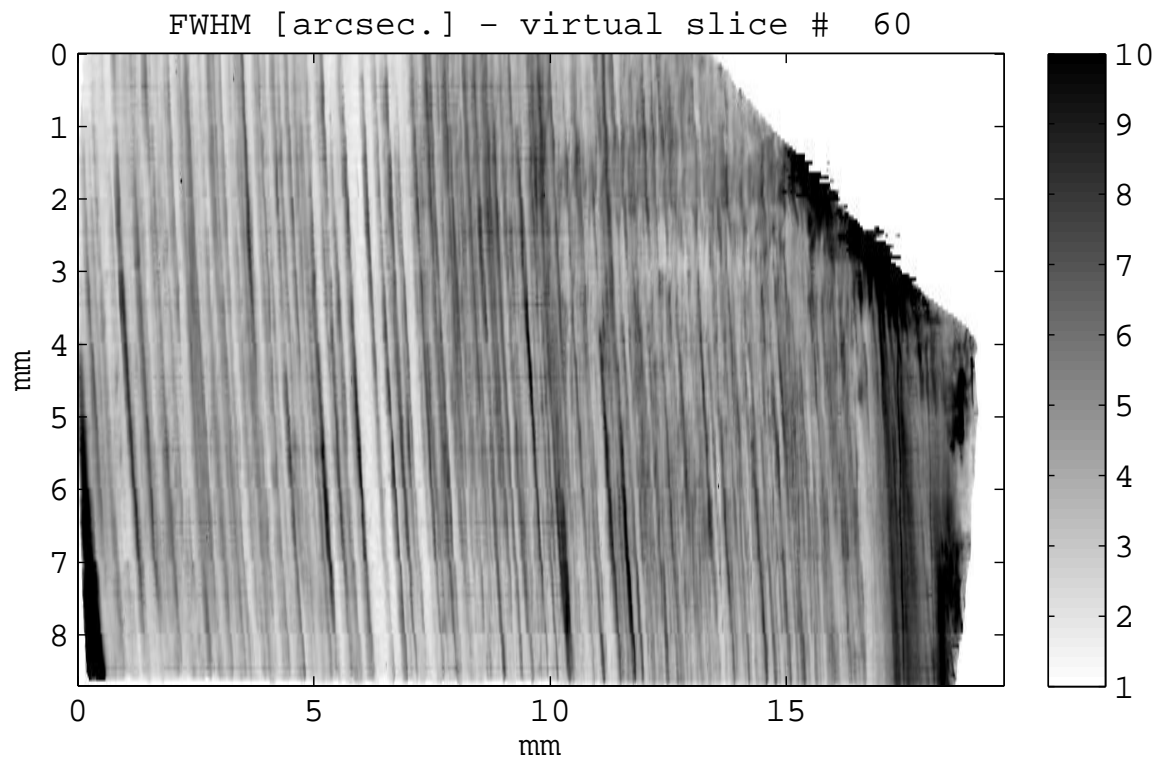


Figure E.22: In text: Fig. 5.16b

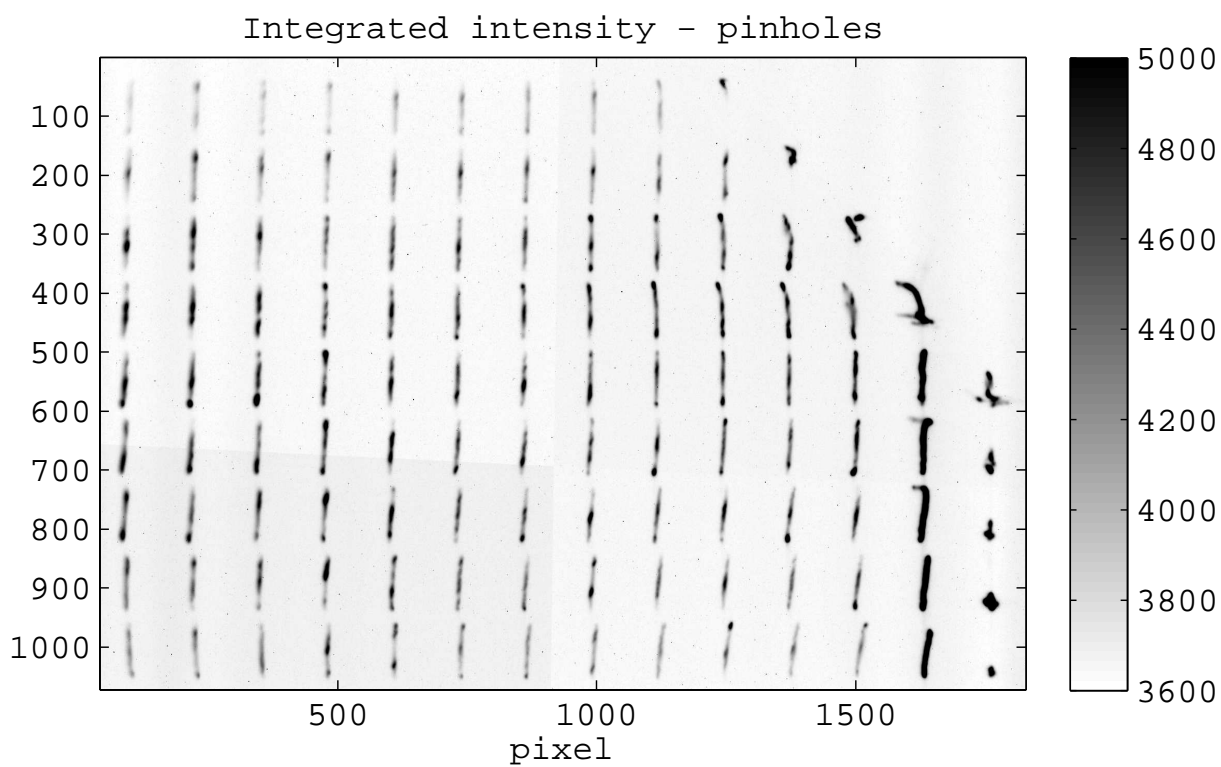


Figure E.23: In text: Fig. 5.17

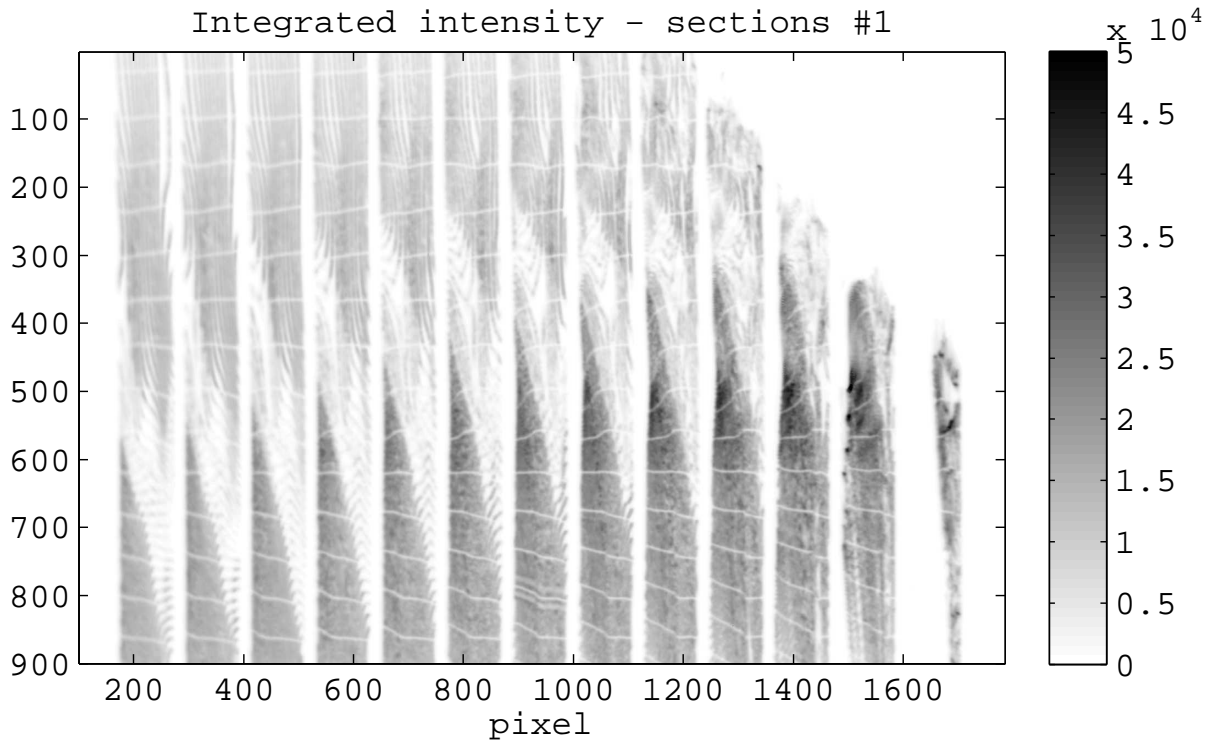


Figure E.24: In text: Fig. 5.19a

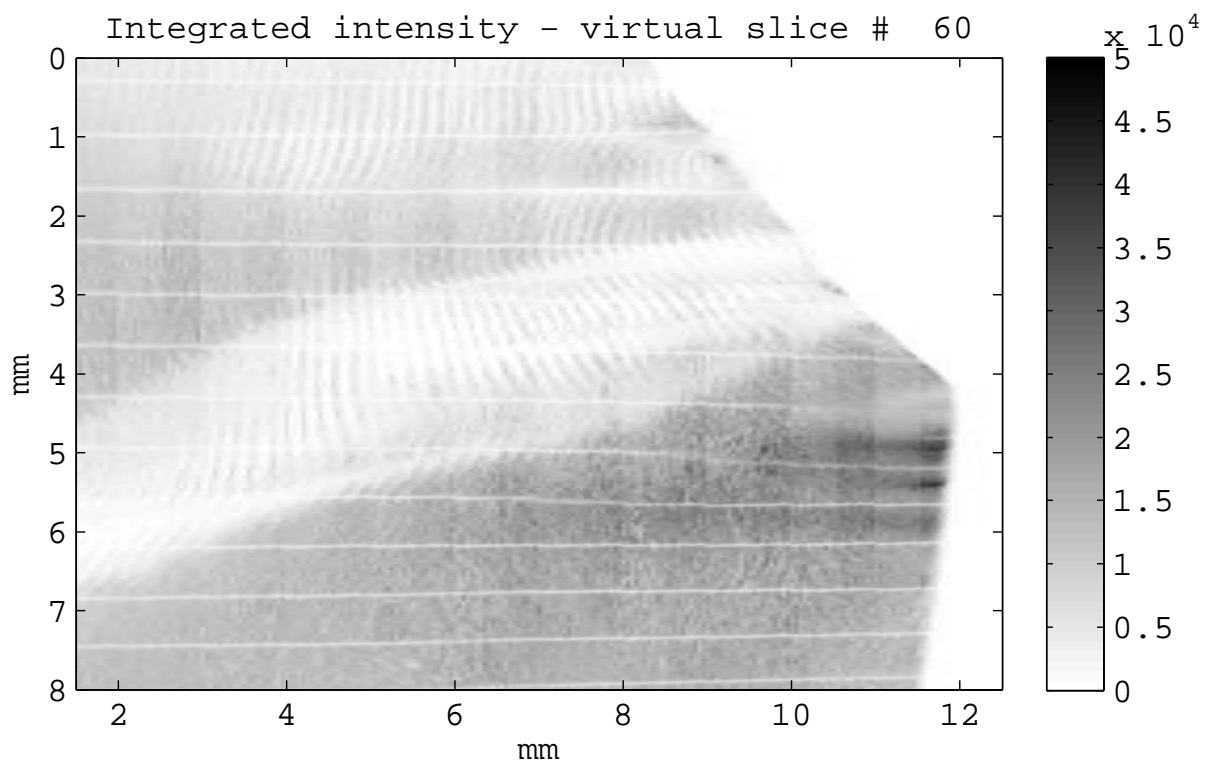


Figure E.25: In text: Fig. 5.19b

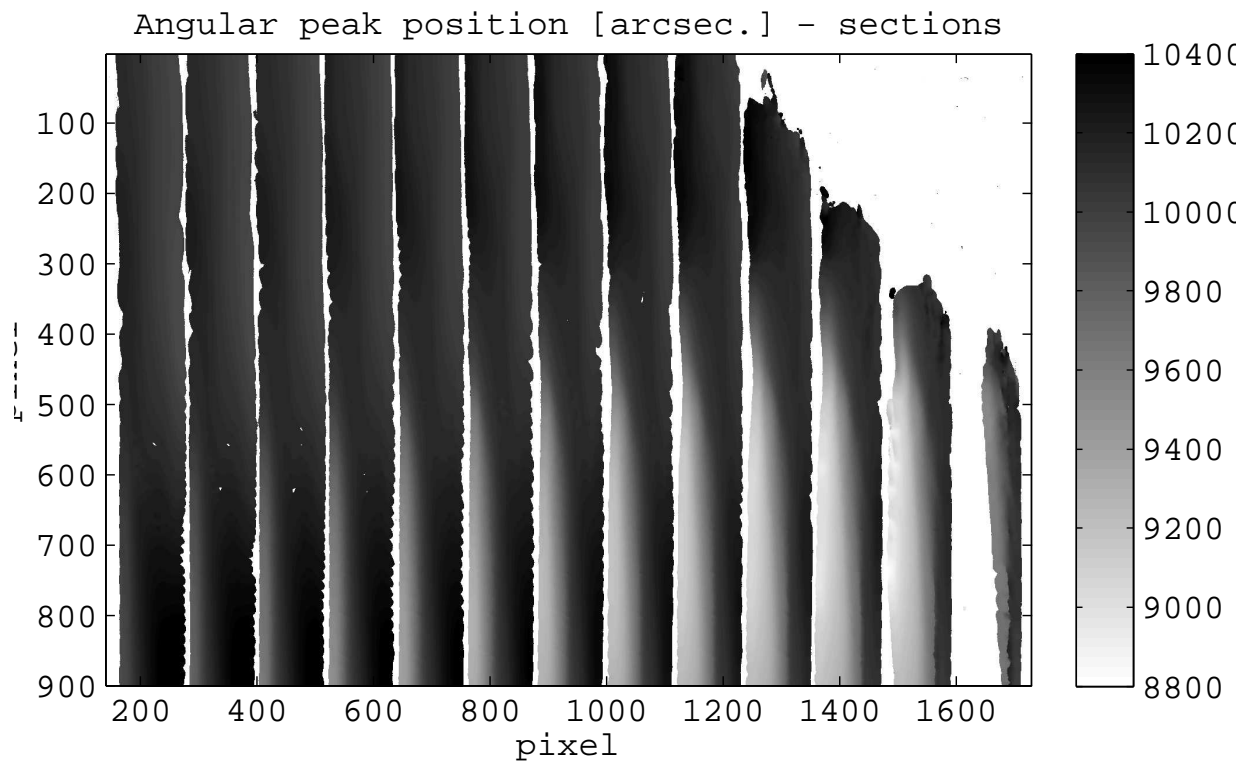


Figure E.26: In text: Fig. 5.21a

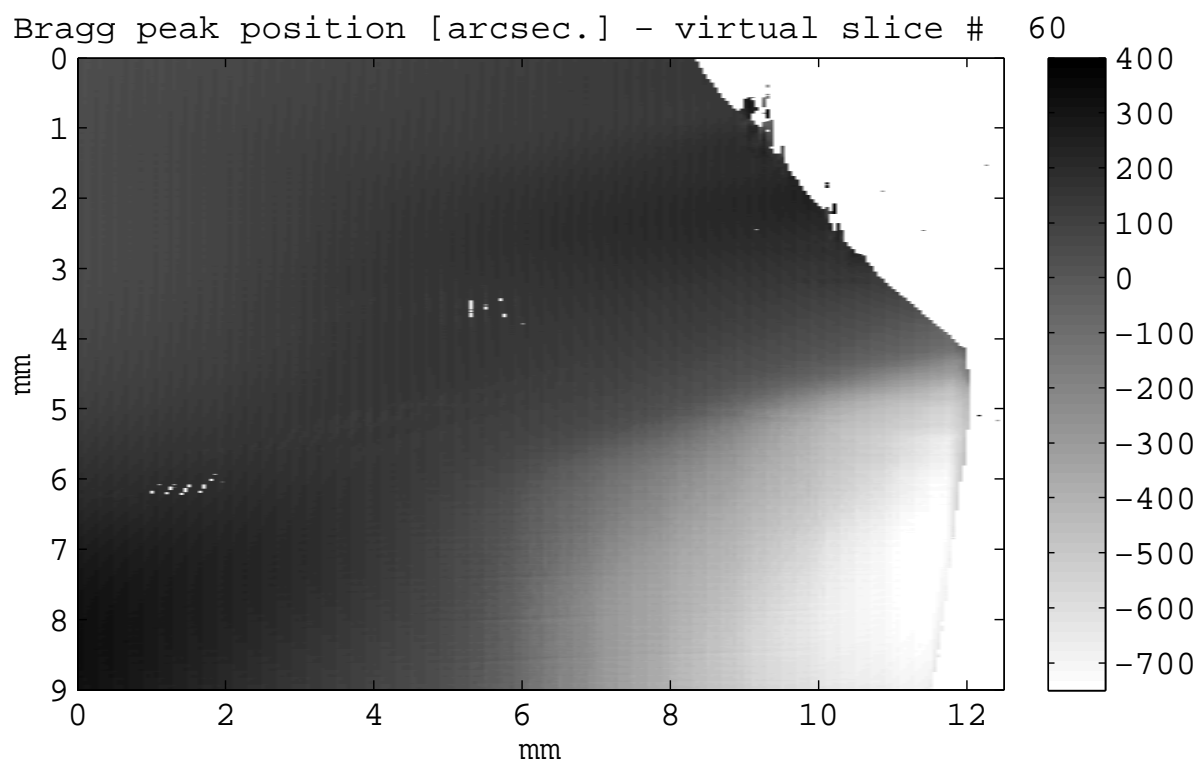


Figure E.27: In text: Fig. 5.21b

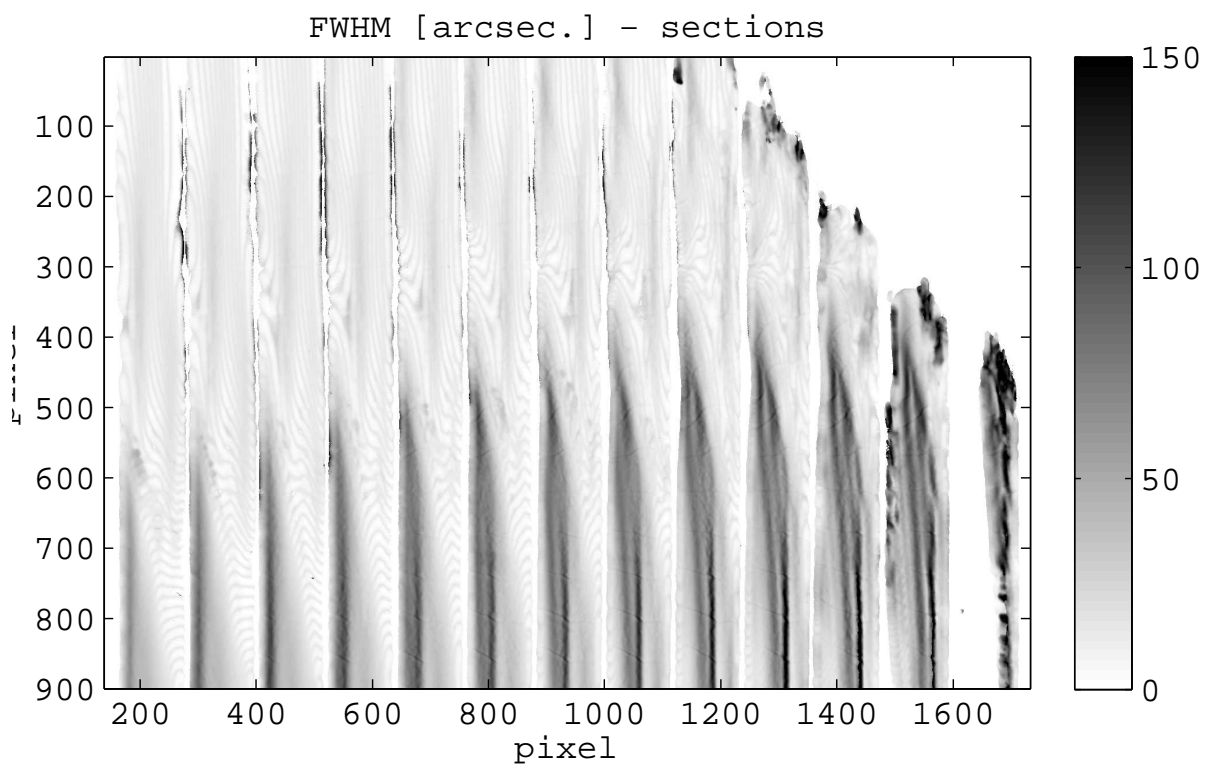


Figure E.28: In text: Fig. 5.20a

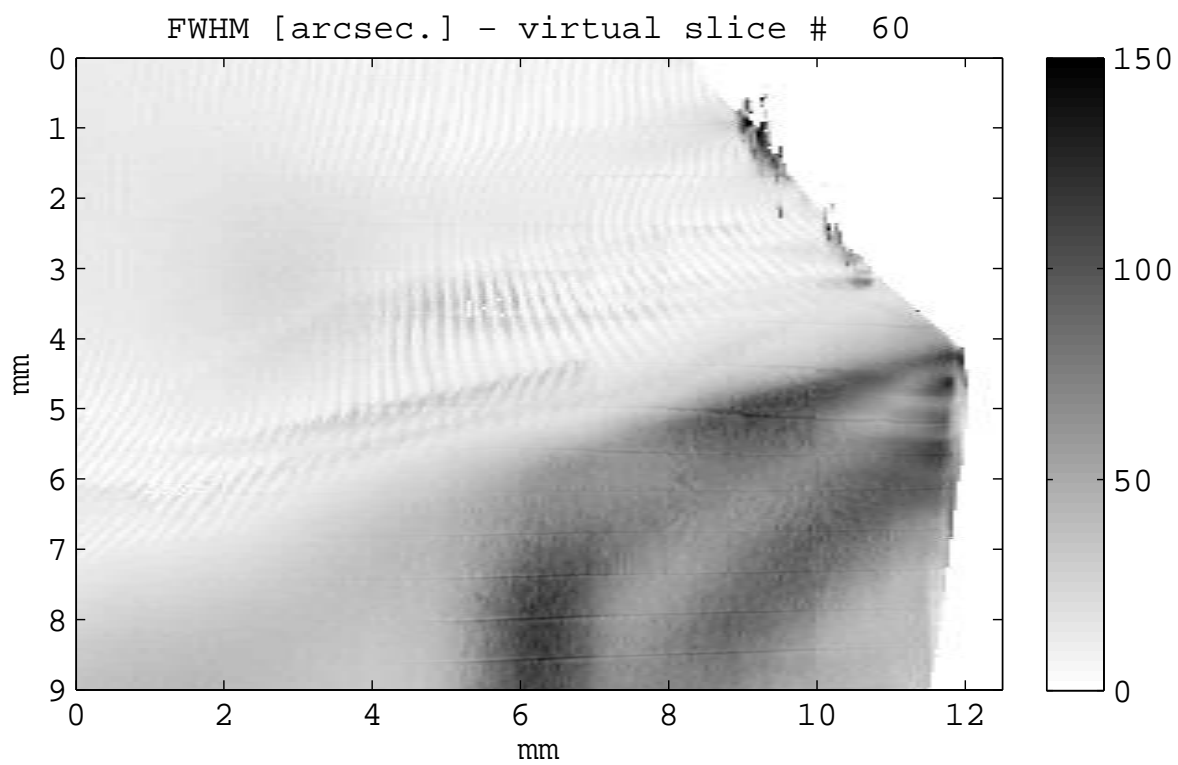


Figure E.29: In text: Fig. 5.20b

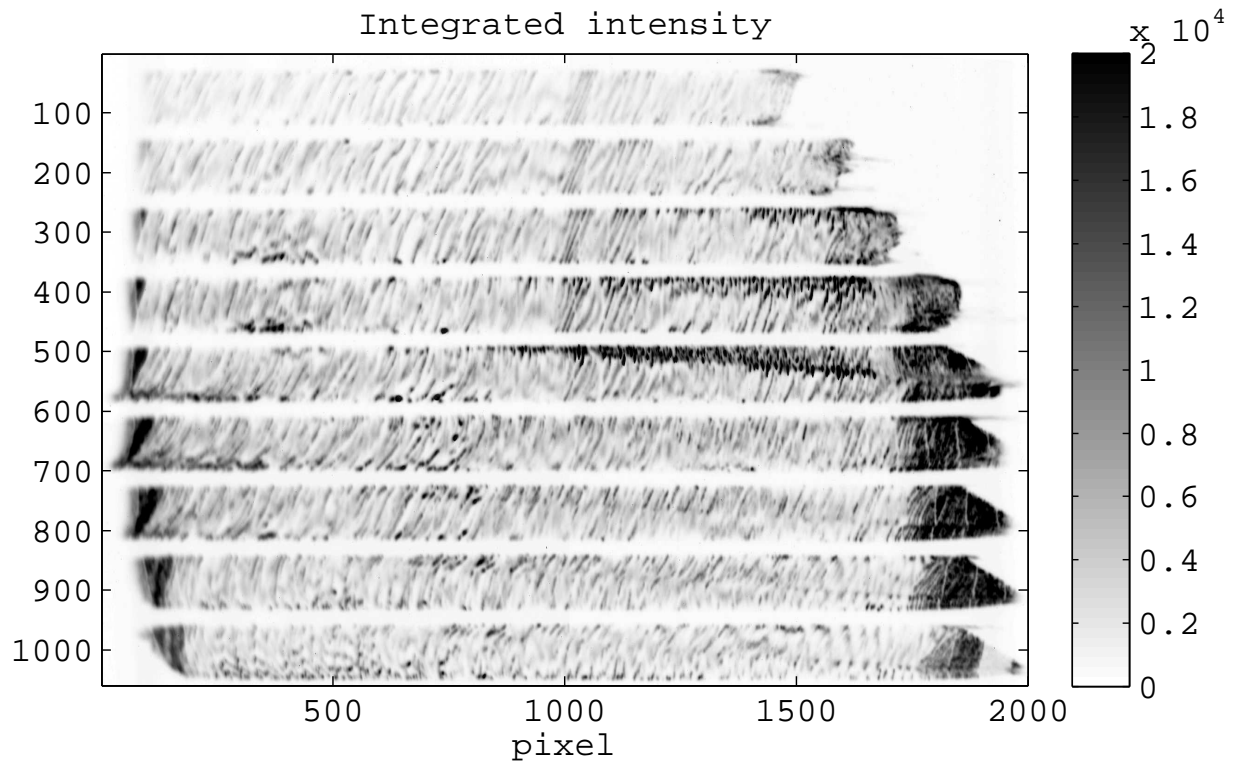


Figure E.30: In text: Fig. 5.22a

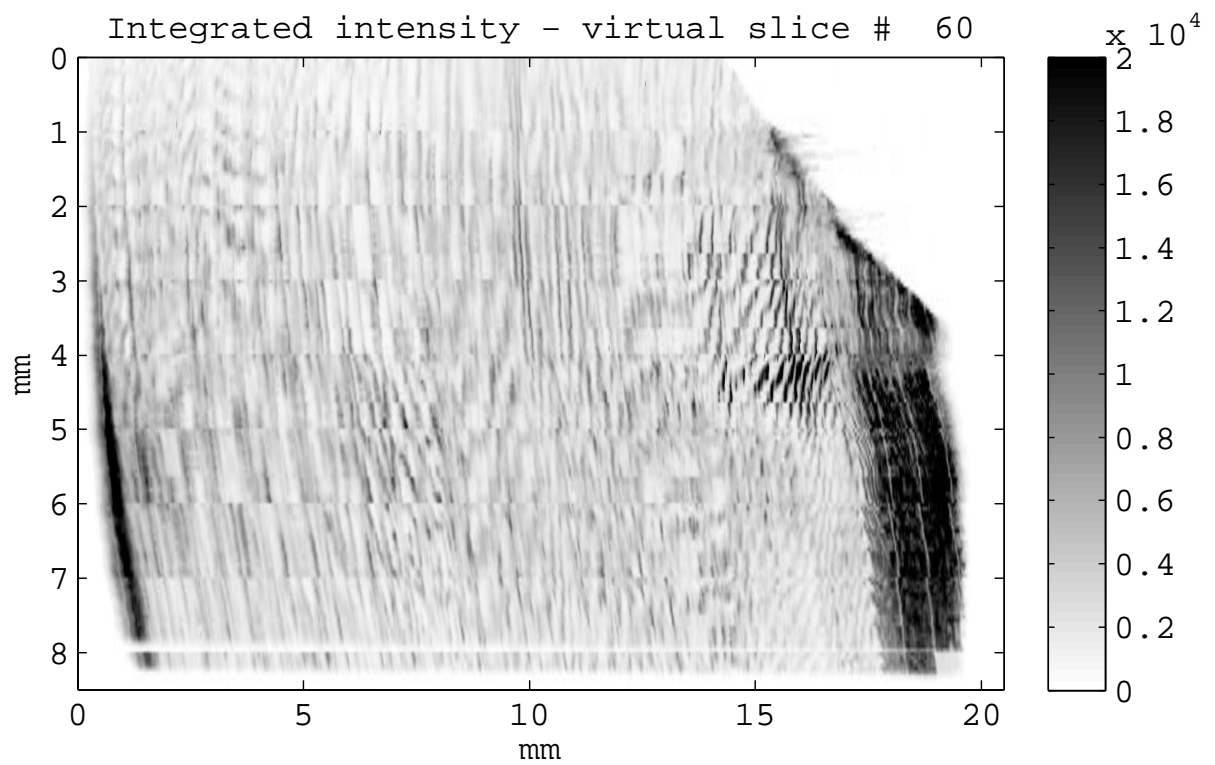


Figure E.31: In text: Fig. 5.22b

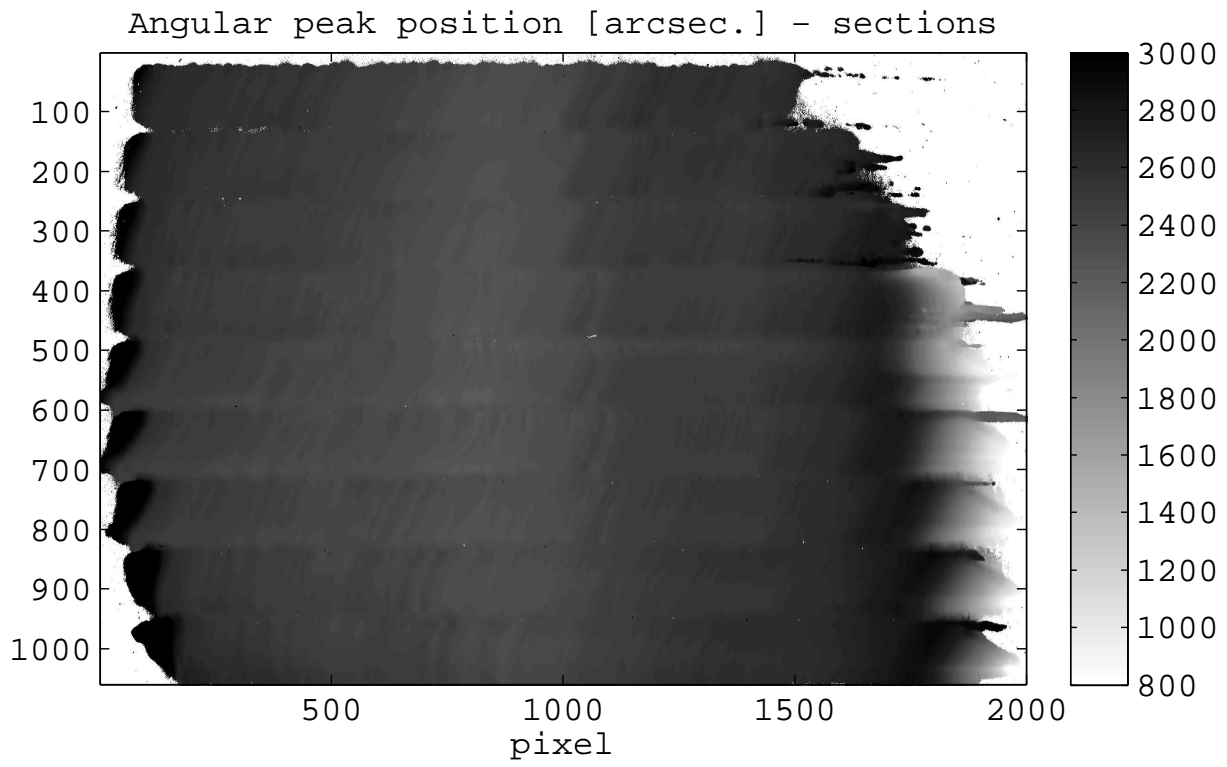


Figure E.32: In text: Fig. 5.23a

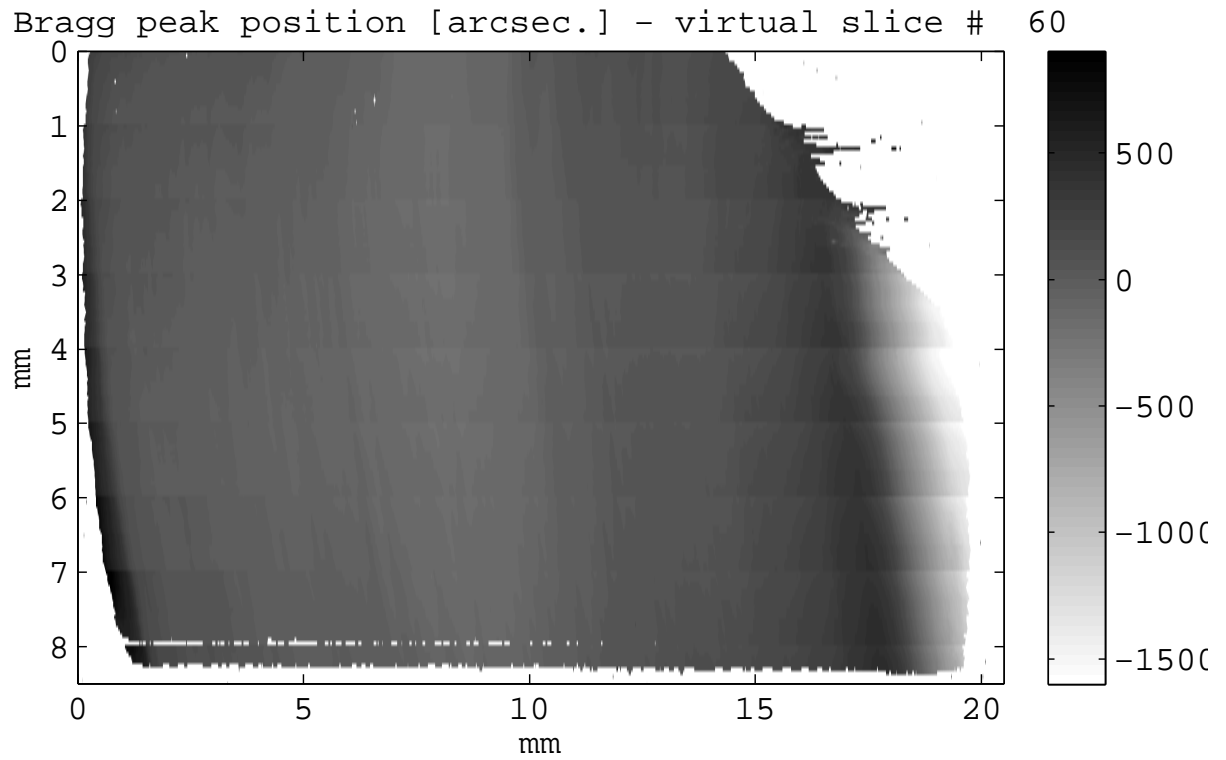


Figure E.33: In text: Fig. 5.23b

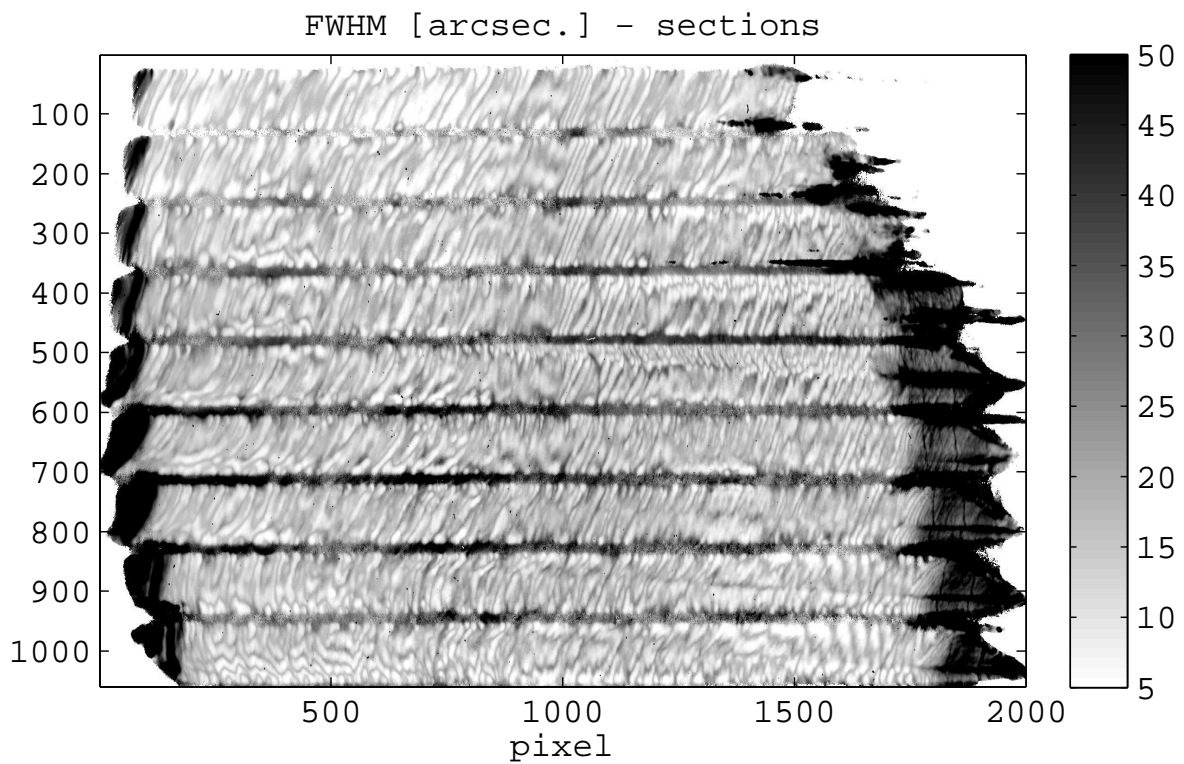


Figure E.34: In text: Fig. 5.24a

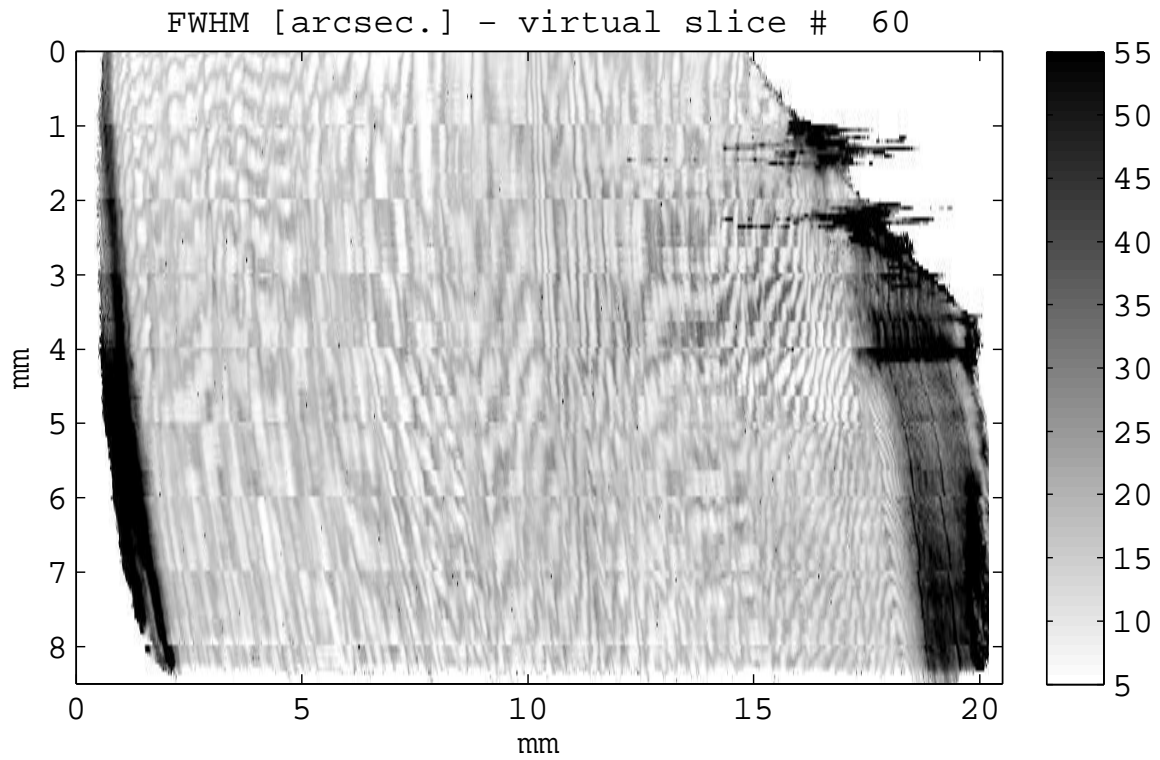


Figure E.35: In text: Fig. 5.24b

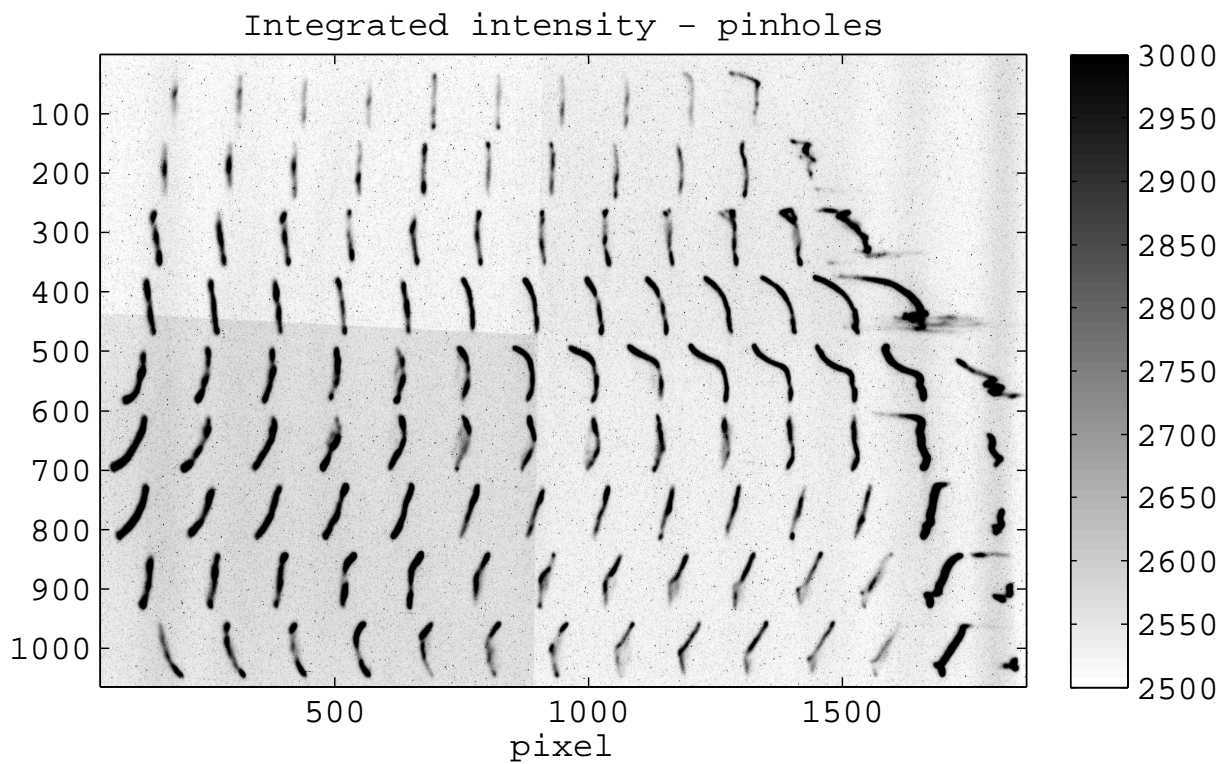


Figure E.36: In text: Fig. 5.25

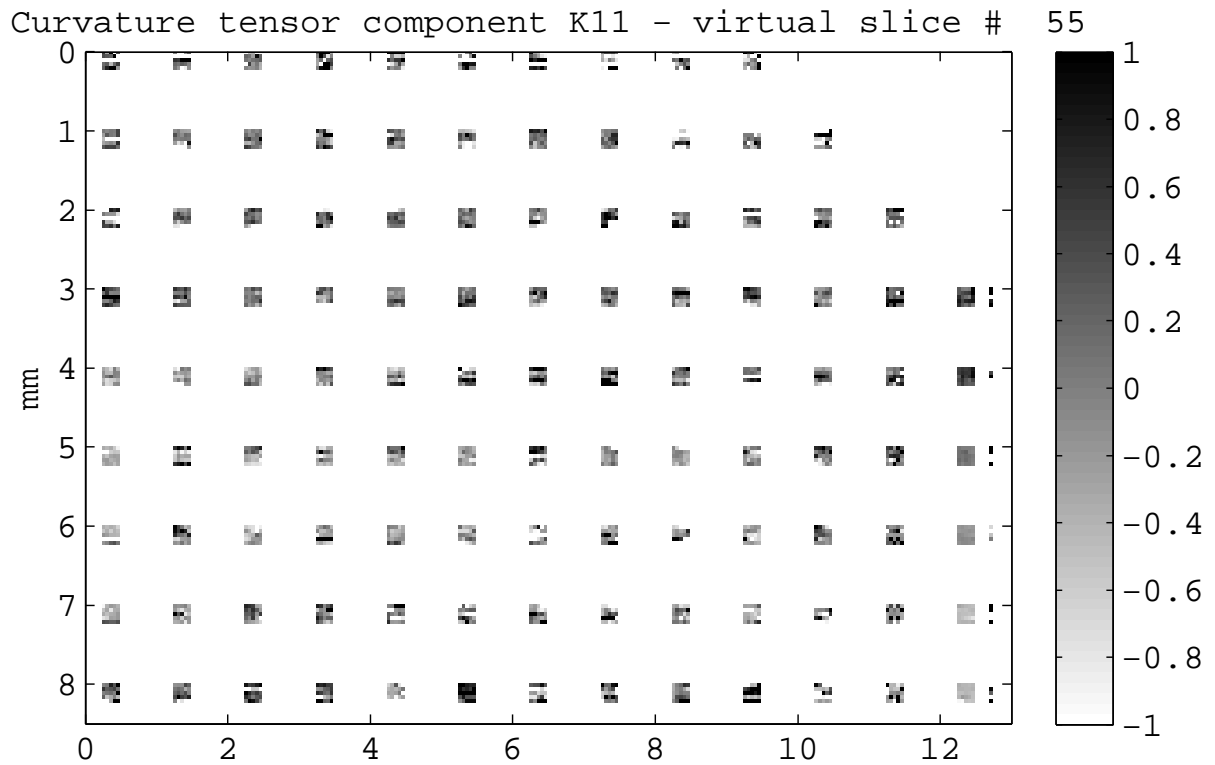


Figure E.37: In text: Fig. 5.26a

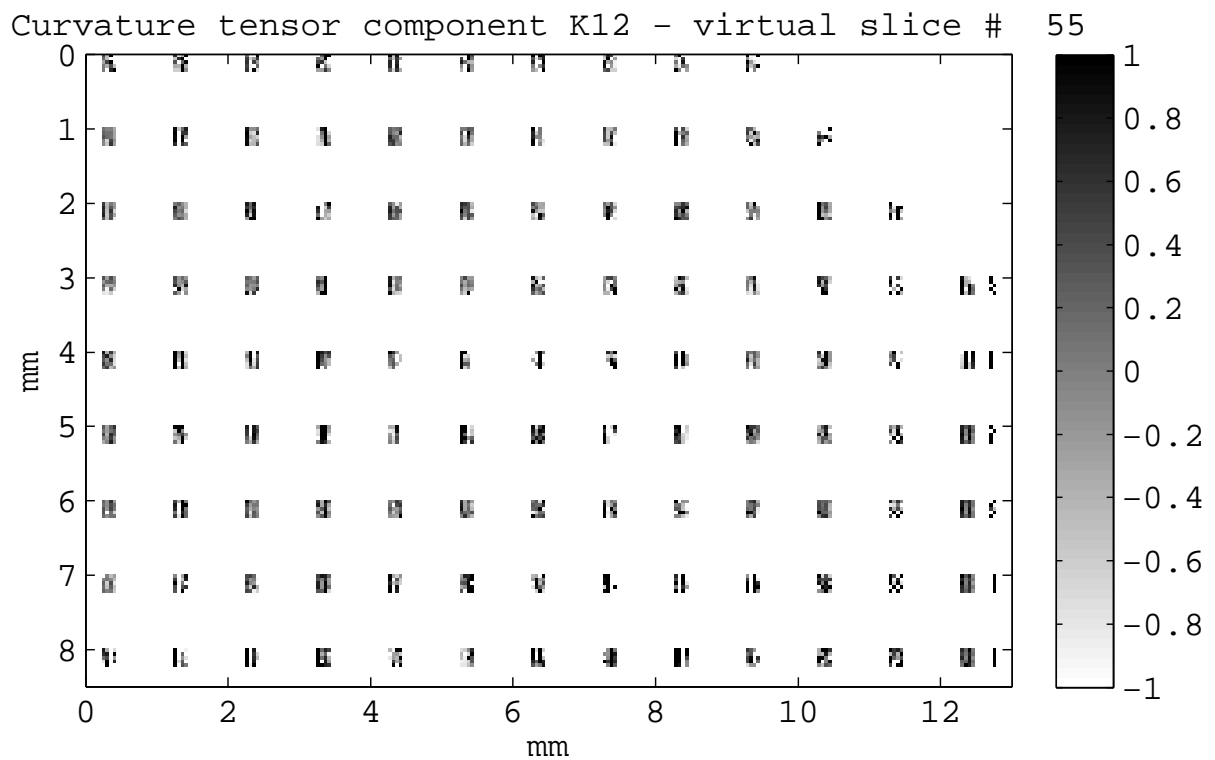


Figure E.38: In text: Fig. 5.26b

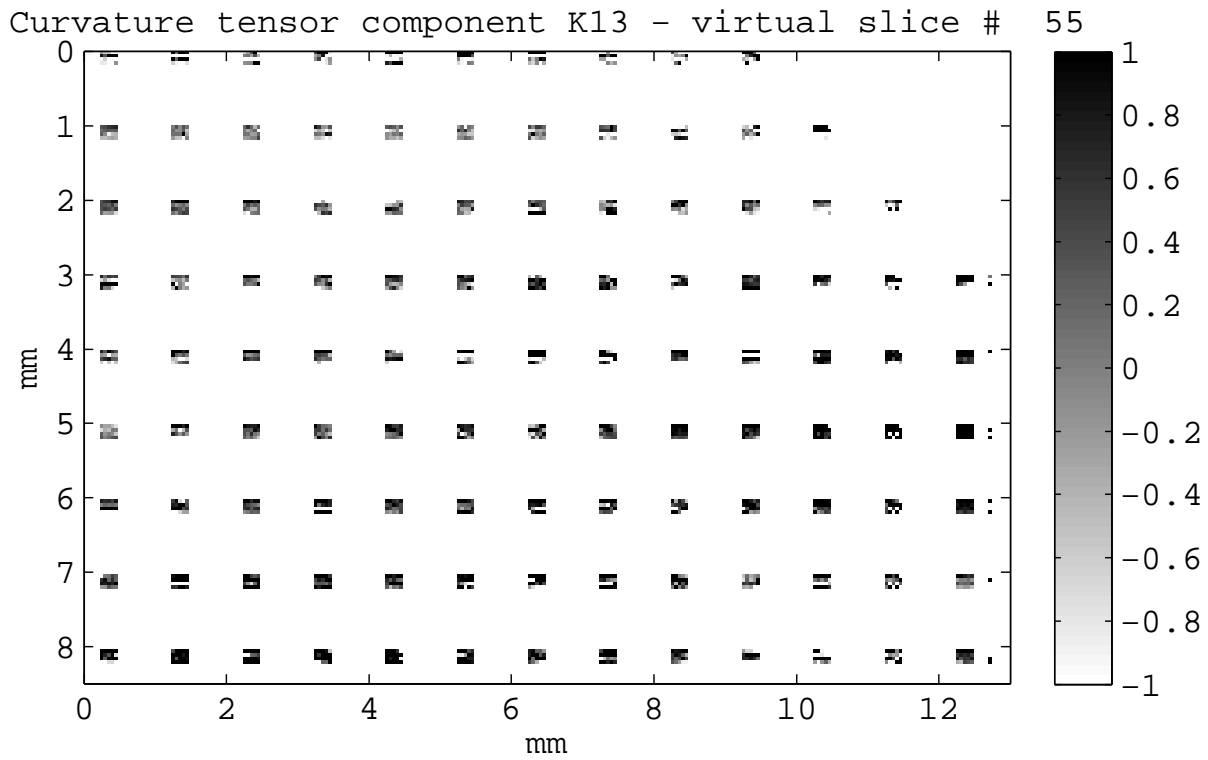


Figure E.39: In text: Fig. 5.26c

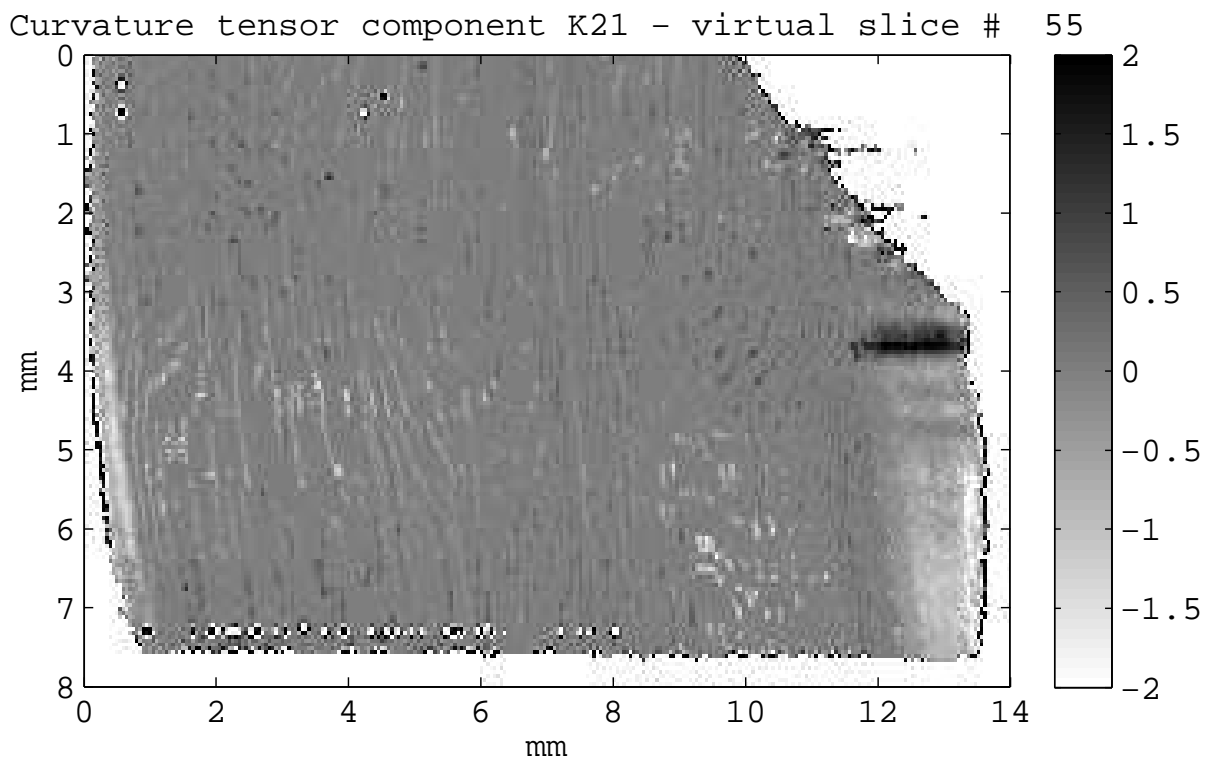


Figure E.40: In text: Fig. 5.26d

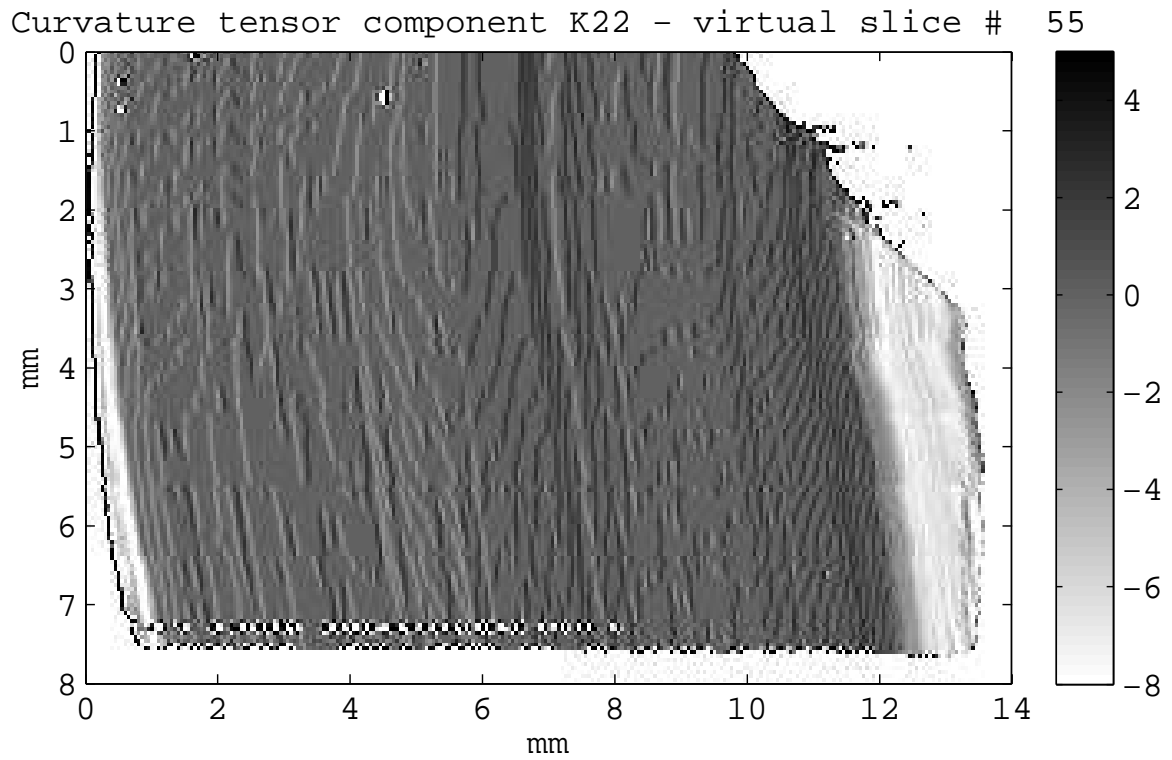


Figure E.41: In text: Fig. 5.26e

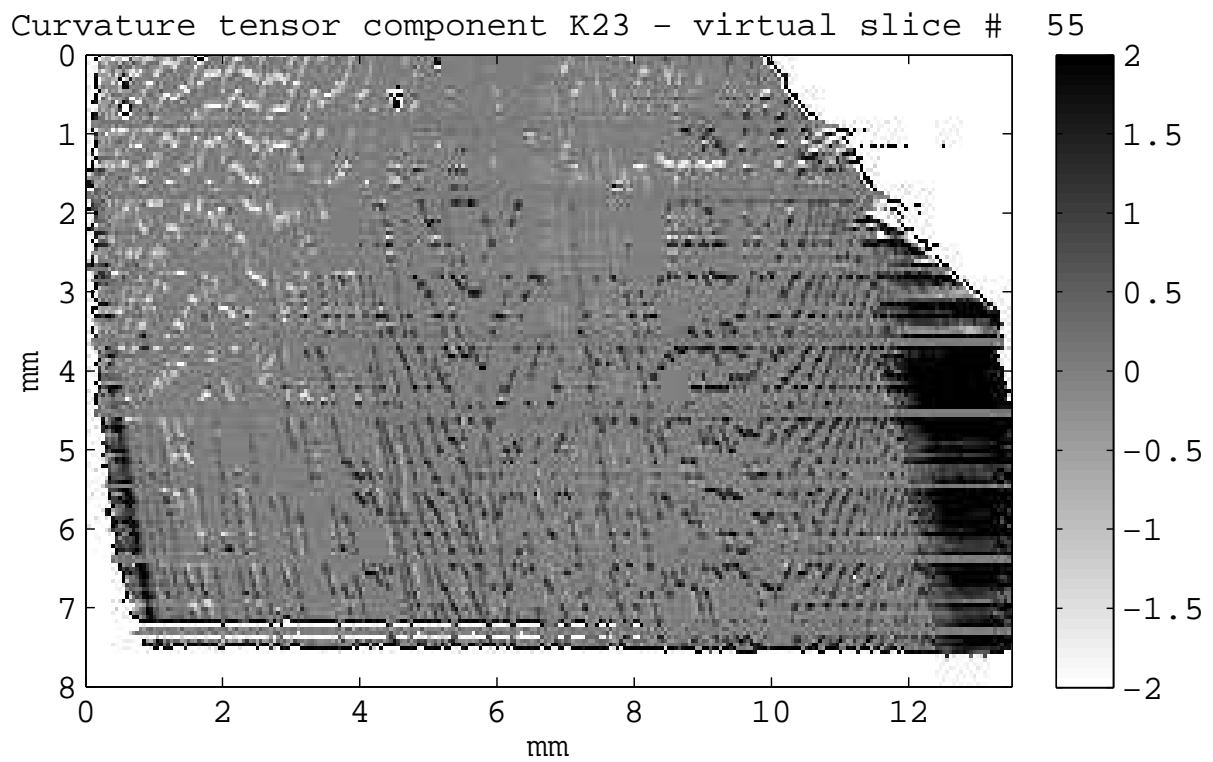


Figure E.42: In text: Fig. 5.26f

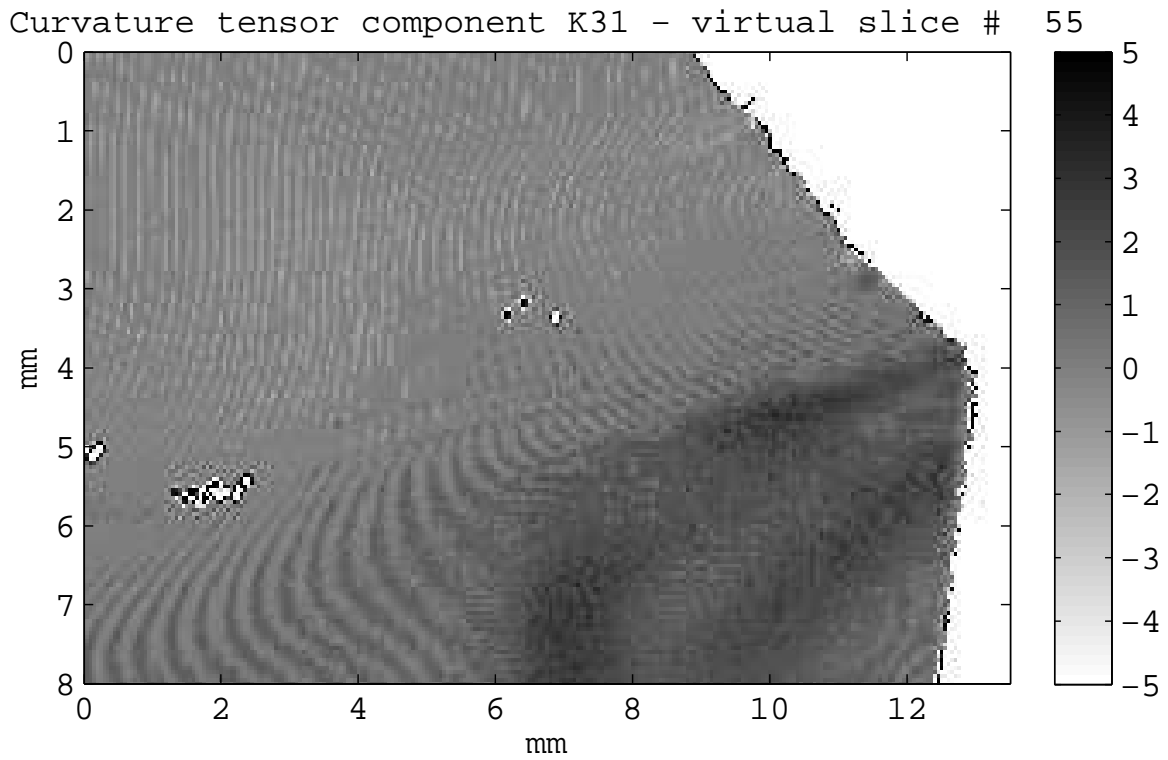


Figure E.43: In text: Fig. 5.26g

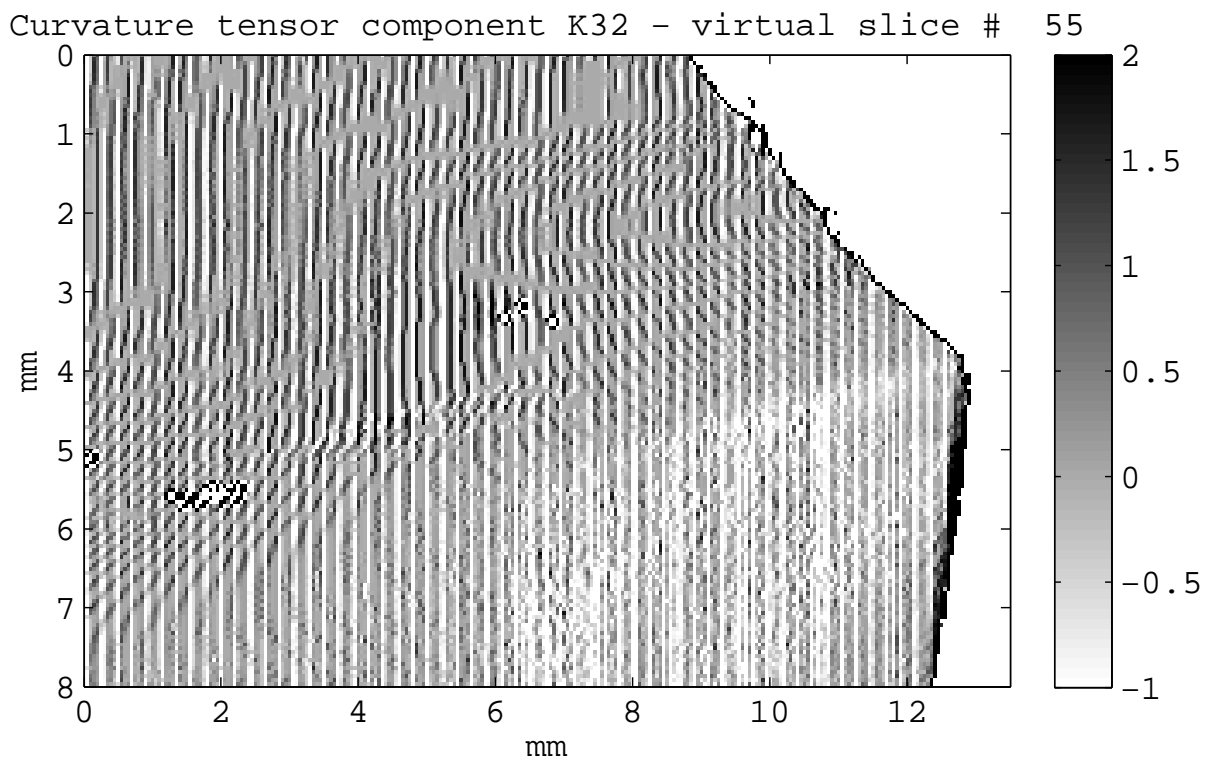


Figure E.44: In text: Fig. 5.26h

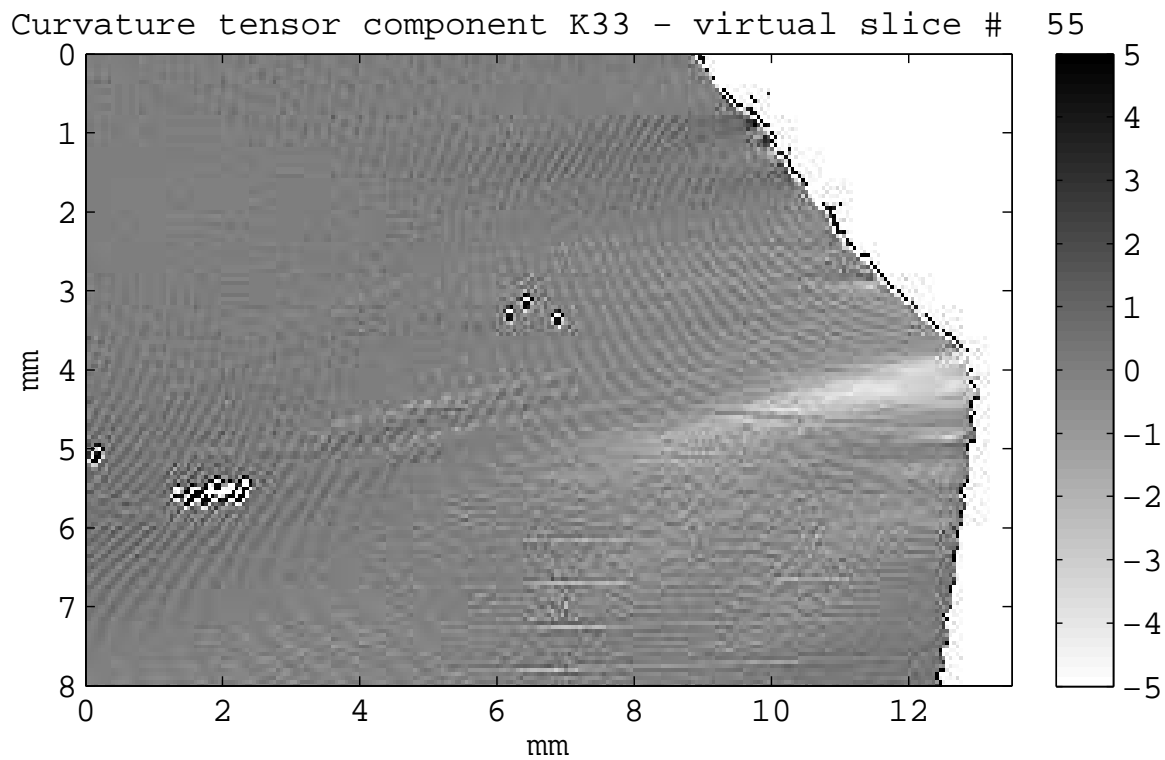


Figure E.45: In text: Fig. 5.26i

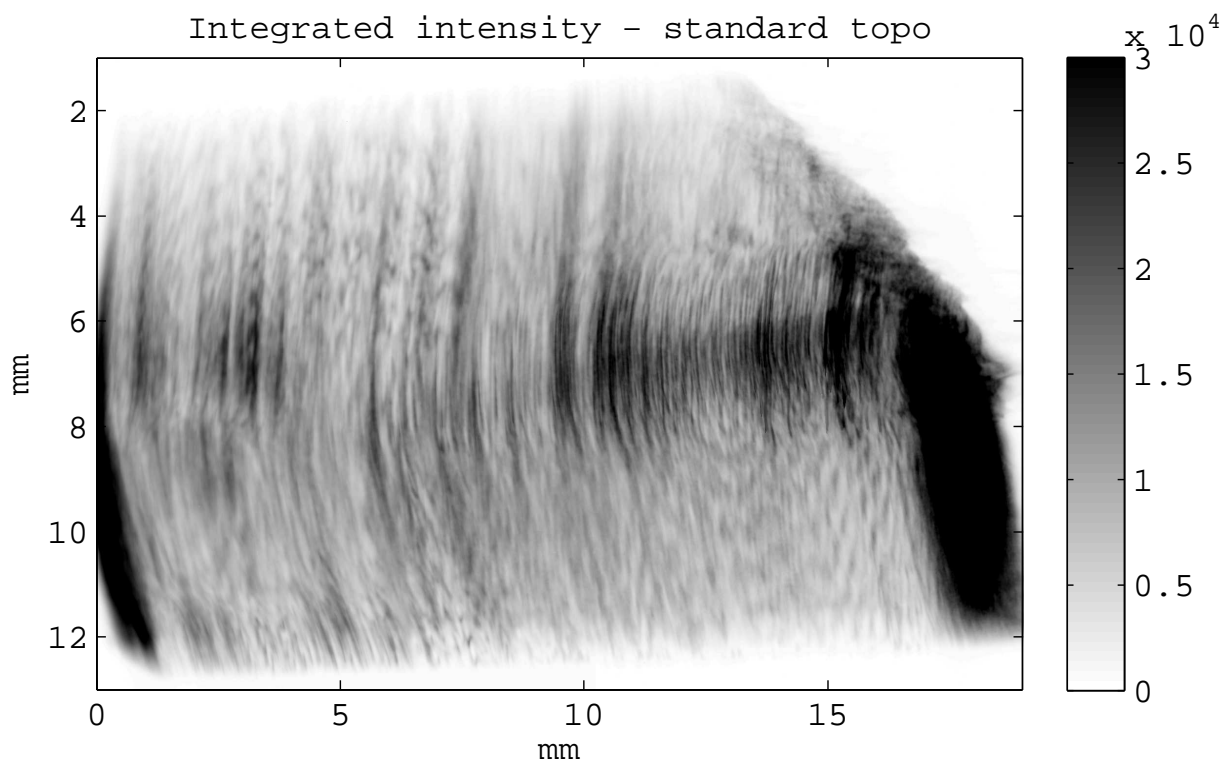


Figure E.46: In text: Fig. 6.5a

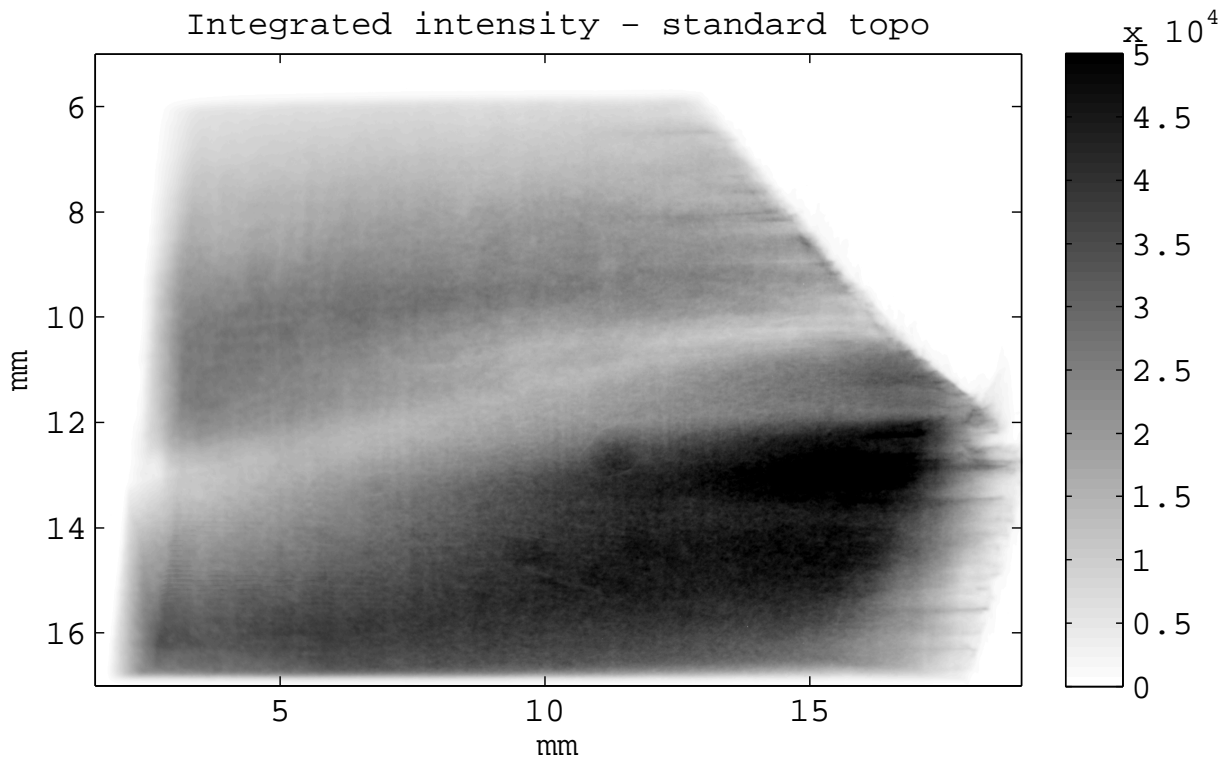


Figure E.47: In text: Fig. 6.5b

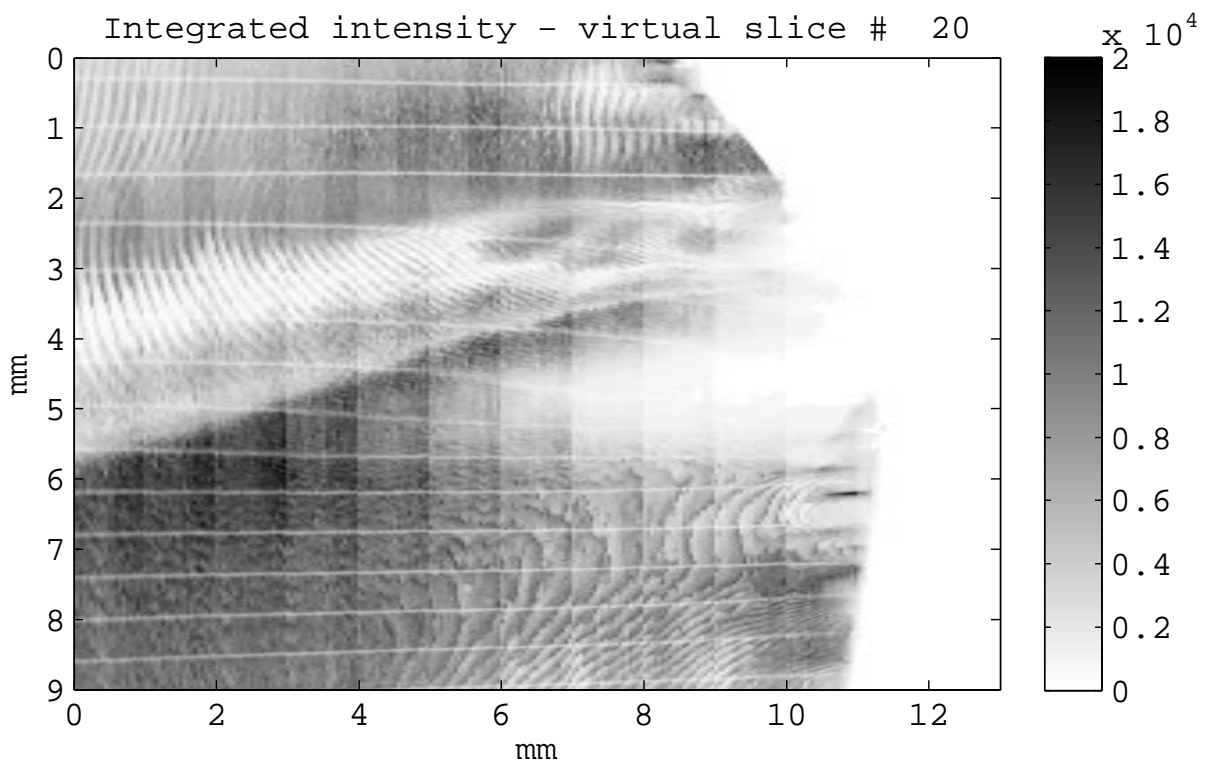


Figure E.48: In text: Fig. 6.6a

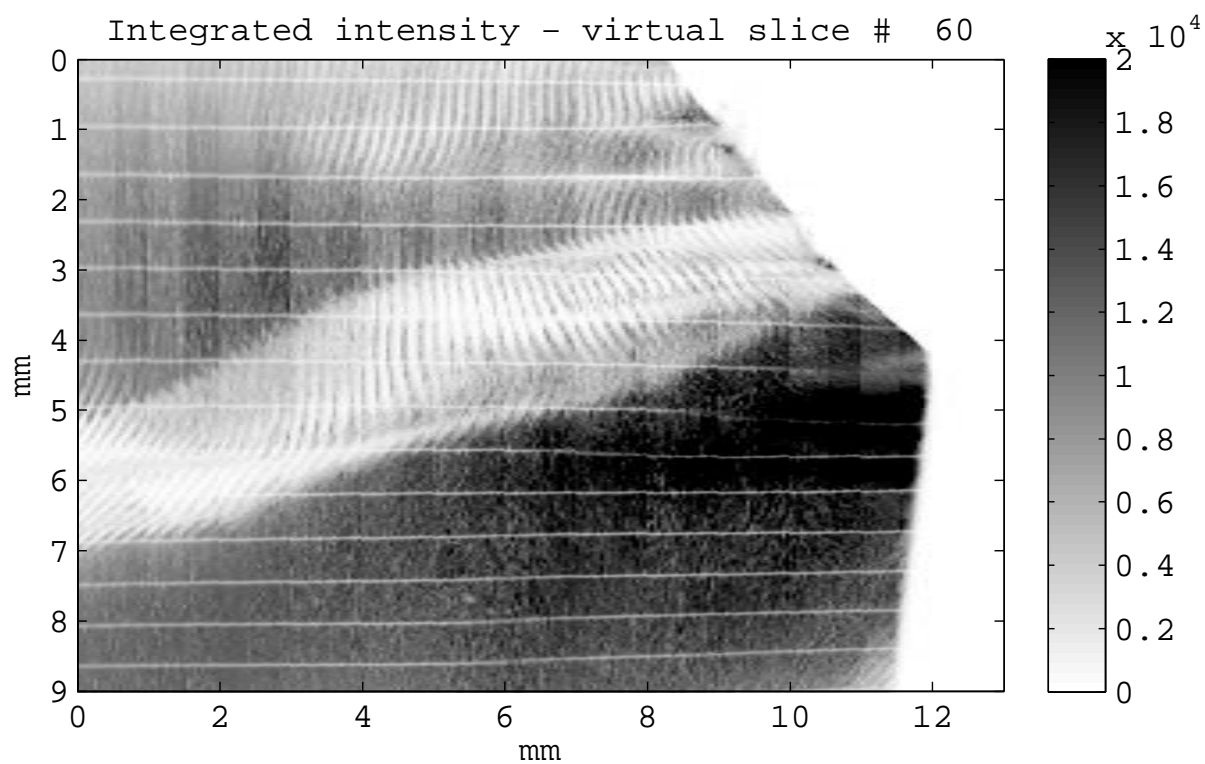


Figure E.49: In text: Fig. 6.6b

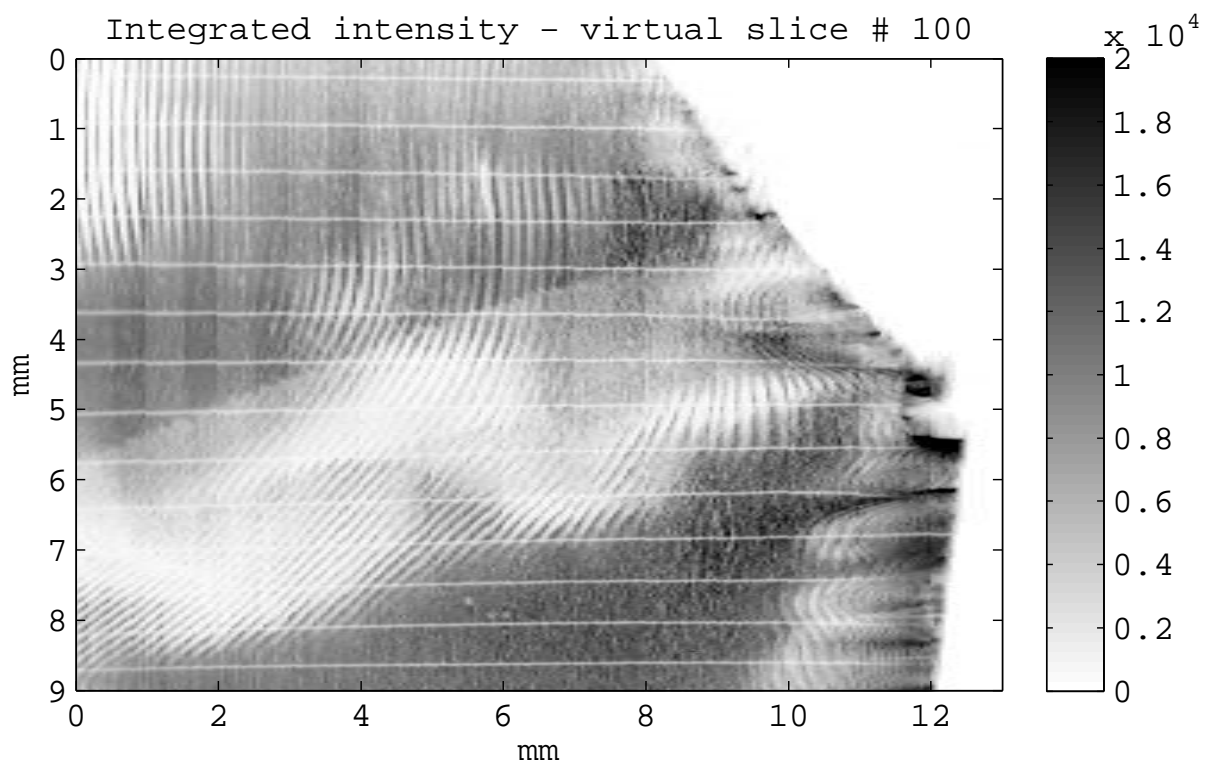


Figure E.50: In text: Fig. 6.6c

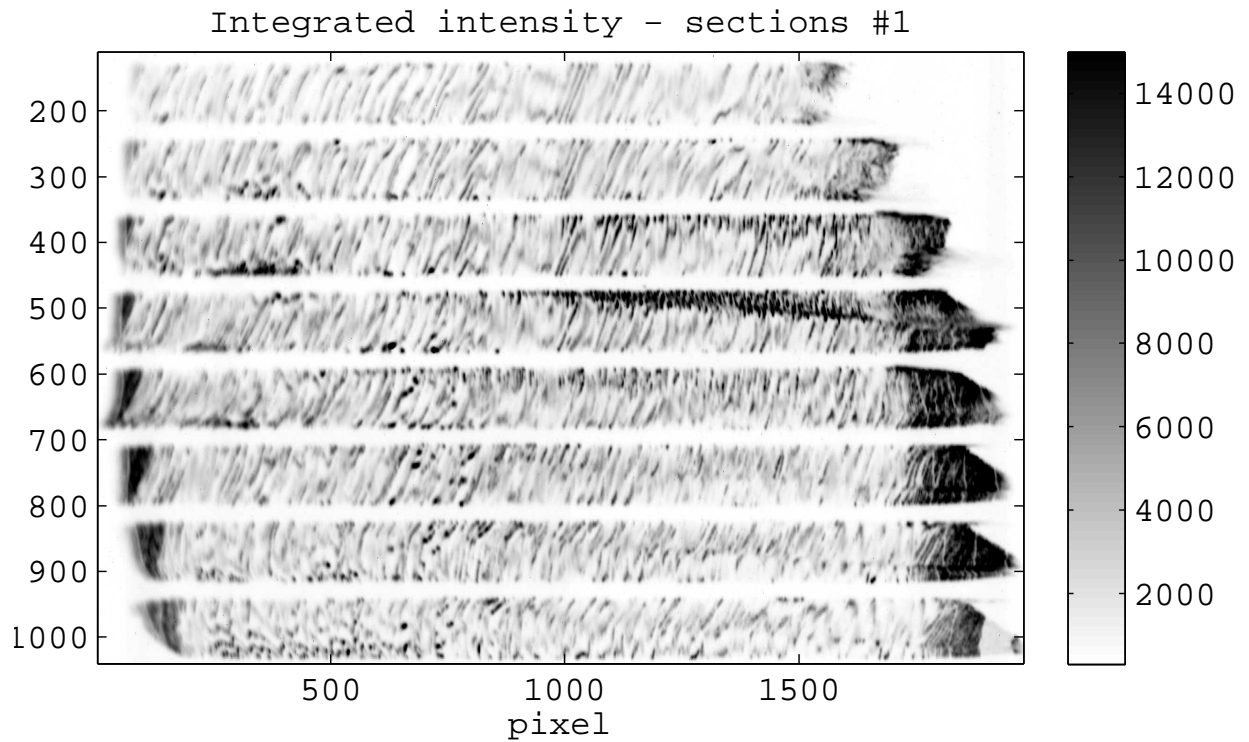


Figure E.51: In text: Fig. 6.7a

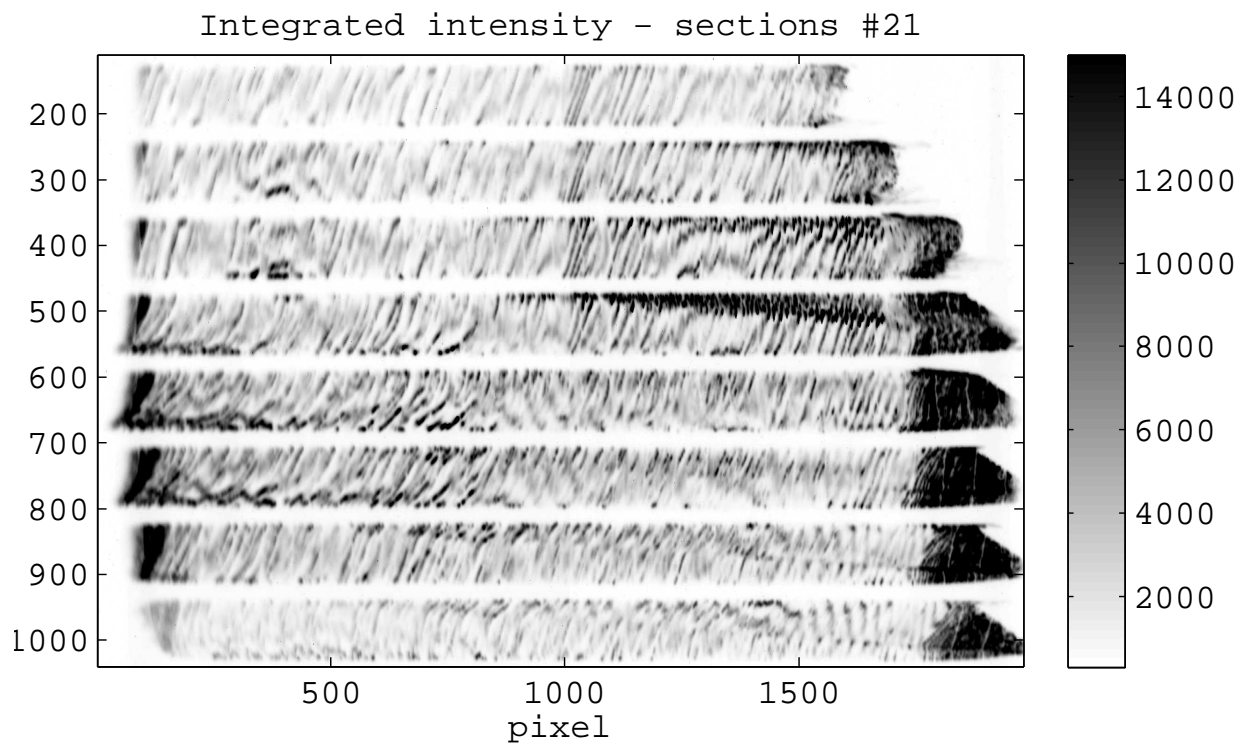


Figure E.52: In text: Fig. 6.7b

# Bibliography

- [Ahmad 88] S. Ahmad & R. W. Whitworth. *Philosophical Magazine A*, vol. 57, pages 749–766, 1988.
- [Allen 11] D. Allen, J. Wittge, J. Stopford, A. Danilewski & P McNolly. *Journal of applied Crystallography*, vol. 44-3, pages 526–531, 2011.
- [Als-Nielsen 01] J. Als-Nielsen & McMorrow. D. *Modern x-ray physics*. John Wiley & Sons, 2001.
- [Andersen 74] A. L. Andersen & L. Gerward. *Physica Status Solidi (a)*, vol. 23, page 537, 1974.
- [Ando 66] Y. Ando & N. Kato. *X-ray diffraction topographs of an elastically distorted crystal*. *Acta Crystallographica*, vol. 21, pages 282–285, 1966.
- [Ashby 70] M. F. Ashby. *The deformation of plastically non homogeneous material*. *Philosophical Magazine*, vol. 21, pages 399–424, 1970.
- [Authier 01] A. Authier. *Dynamical theory of x-ray diffraction*. Oxford University Press Inc., New York, 2001.
- [Baruchel 93] J. Baruchel, J.L. Hodeau, M.S. Lehmann, J.R. Regnard & C. Schlenker, editeurs. *Neutron and synchrotron radiation for condensed matter studies*. Springer, Berlin, 1993.
- [Batterman 64] Boris W. Batterman. *Dynamical Diffraction of X Rays by Perfect Crystals*. *Reviews of modern physics*, vol. 36, pages 681–717, 1964.
- [Calamiotou 07] M. Calamiotou, N. Chrysanthakopoulos, G. Papaioannou & J. Baruchel. *Journal of Physics D: Applied Physics*, vol. 102, page 352, 2007.
- [Capolo 07] L. Capolo. *Contribution à l'étude des hétérogénéités de déformation viscoplastique de la glace Ih mono et multi cristalline: essais de compression in-situ sous rayonnement X*. PhD thesis, Université Joseph Fourier Grenoble, 2007.
- [Daly 96] Peter Daly. *ESRF Data Format*. [http://wikiserv.esrf.fr/bliss/index.php/ESRF\\_Data\\_Format](http://wikiserv.esrf.fr/bliss/index.php/ESRF_Data_Format), 1996.
- [David 05] Freedman David. *Statistical models: theory and practice*. Cambridge University Press, 2005.

- [Duval 91] P. Duval, P. Kalifa & J. Meyssonier. *Creep constitutive equations for polycrystalline ice and effect of microcracking*. In Ice-structure Interaction. IUTAM-IAHR Symposium St. John's Newfoundland, Canada, 1991.
- [Fisz 80] M. Fisz. *Wahrscheinlichkeitsberechnung und mathematische statistik*. Dt. Verlag d. Wissenschaften, 1980.
- [Fletcher 70] N. H. Fletcher. *The chemical physics of ice*. Cambridge University Press, 1970.
- [Georgii 02] H.-O. Georgii. *Einführung in die wahrscheinlichkeitstheorie und statistik*. Walter de Gruyter - Berlin - New York, 2002.
- [Glen 54] J. W. Glen & M. F. Perutz. *The growth and deformation of ice crystals*. *Journal of Glaciology* 2, vol. 10, page 397, 1954.
- [Hahn 95] Theo Hahn, editeur. *International tables for crystallography*. Kluwer academic publishers, 1995.
- [Hart 66] Michael Hart. *Pendellösung Fringes in Elastically Deformed Silicon*. *Zeitschrift für Physik*, vol. 189, pages 269–291, 1966.
- [Härtwig 01] J. Härtwig. *Hierarchy of dynamical theories of X-ray diffraction for deformed and perfect crystals*. *Journal of Physics*, vol. 33, pages 70–77, 2001.
- [Higashi 88] A. Higashi. *Lattice defects in ice crystals*. Hokkaido University Press, Sapporo, Japan, 1988.
- [Hondoh 92] T. Hondoh. *Glide and climb processes of dislocations in ice*. *Physics and Chemistry of Ice*, 1992.
- [Hondoh 00] T. Hondoh. *Nature and behavior of dislocations in ice*. *Physics of ice core records*, pages 3–23, 2000.
- [Hoszowska 01] J. Hoszowska, A. K. Freund, E. Boller, J. P. F. Sellschop, G. Level, J. Härtwig, R. C. Burns, M. Reba & J. Baruchel. *Journal of Physics D: Applied Physics*, vol. 34, page A47, 2001.
- [Huber 09] Isabella Huber, Petr Mikulik & Tilo Baumbach. *Correctness of a particular solution of inverse problem in rocking curve imaging*. *Physica Status Solidi(a)*, vol. 206, pages 1860–1864, 2009.
- [Hull 84] D. Hull & D. J. Bacon. *Introduction to dislocations*. Pergamon, 1984.
- [ipp 01] *IPCC Third assessment report*. <http://www.grida.no/publications>, 2001.
- [Jackson 98] J. D. Jackson. *Classical electrodynamics*. John Wiley & Sons, 3 edition, 1998.
- [Jones 70] S.J. Jones. *X-ray topographic evidence for prismatic dislocations in ice*. *Journal of Applied Physics*, vol. 41, pages 2738–2739, 1970.

- [Kaganer 10] V. M. Kaganer & K. K. Sabelfeld. *X-ray diffraction peaks from correlated dislocations: Monte Carlo study of dislocation screening*. *Acta Crystallographica A*, vol. 66, page 703, 2010.
- [Kajiwara 07] K. Kajiwara, S. Kawado, S. Iida, Y. Suzuki & Y. Chikaura. *Features of dislocation images reconstructed from step-scanned white X-ray section topographs*. *Physica Status Solidi (a)*, vol. 204, pages 2682–2687, 2007.
- [Kato 66] Nario Kato & Yoshinori Ando. *Contraction of Pendellösung Fringes in Distorted Crystals*. *Journal of the Physical Society of Japan*, vol. 21, pages 964–968, 1966.
- [Kawado 79] S. Kawado & J. Aoyama. *Applied Physical Letters*, vol. 34, page 428, 1979.
- [Kawado 04] S. Kawado, T. Taishi, S. Iida, Y. Suzuki, Y. Chikaura & K. Kajiwara. *Journal of Synchrotron Radiation*, vol. 11, pages 304–308, 2004.
- [Kawado 05] S. Kawado, T. Taishi, S. Iida, Y. Chikaura & K. Kajiwara. *Journal of Physics D: Applied Physics*, vol. 38, pages A17–A22, 2005.
- [King 08] A. King, G. Johnson, D. Engelberg, W. Ludwig & J. Marrow. *Science*, vol. 321, page 382, 2008.
- [Klapper 76] H. Klapper. *The influence of Elastic Anisotropy on the X-ray Topographic Image Width of Pure Screw Dislocations*. *Journal of Applied Crystallography*, vol. 9, pages 310–317, 1976.
- [Kobayashi 96] S. Kobayashi & K. Nomizu. *Foundations of differential geometry*, volume 1. Wiley, John & Sons, Incorporated, 1996.
- [Kröner 55] Kröner. *Zeitschrift Physik*, vol. 142, pages 463–475, 1955.
- [Kvardakov 07] V. V. Kvardakov, K. M. Podurets, S. A. Schetinkin, J. Baruchel, J. Härtwig & M. Schlenker. *Nuclear Instrumental Methods*, vol. 575, page 140, 2007.
- [Labiche 96] J.C. Labiche, J. Segura-Puchades, D. van Brussel & J.P. Moy. *Frelon camera: Fast readout low noise*. *ESRF Newsletter* 25, p. 41-43, 1996.
- [Lang 57] A. R. Lang. *A method for the examination of crystal sections using penetrating characteristic X radiation*. *Acta Metallurgica*, vol. 5, pages 358–364, 1957.
- [Liu 92] F. Liu, I. Baker, G. Yao & M. Dudley. *Dislocations and grain boundaries in polycrystalline ice: a preliminary study by synchrotron X-ray topography*. *Journal of Material Sciences*, vol. 27, pages 2719–2725, 1992.
- [Lübbert 00] D. Lübbert, T. Baumbach, J. Härtwig, E. Boller & E. Pernot. *Nuclear Instrumental Methods B*, vol. 160, page 521, 2000.

- [Lübbert 05] D. Lübbert, C. Ferrari, P. Mikulik, P. Pernot, L. Helfen, N. Verdi, D. Korytar & T. Baumbach. *Journal of Applied Crystallography*, vol. 38, page 91, 2005.
- [Ludwig 01] W. Ludwig, P. Cloetens, J. Haertwig, J. Baruchel, B. Hamelin & P. Bastie. *Journal of Applied Crystallography*, vol. 34, pages 602–607, 2001.
- [Matsouli 00] I. Matsouli, V. V. Kvardakov & J. Baruchel. *Double-crystal diffraction imaging with a small effective divergence source: application to the magneto-acoustic vibrations in FeBO<sub>3</sub>*. *Journal of Applied Crystallography*, vol. 33, pages 1051–1058, 2000.
- [Mikulik 06] P. Mikulik, D. Lübbert, P. Pernot, L. Helfen & T. Baumbach. *Applied Surface Science*, vol. 253, page 188, 2006.
- [Mikulik 08] P. Mikulik. *Absorption and Diffraction imaging by synchrotron laminography, diffractometry and crystal optics*. PhD thesis, Masaryk University, Brno, 2008.
- [Miltat 75] J. Miltat & D.K. Bowen. *On the widths of Dislocation images in X-ray Topography under Low-Absorption Conditions*. *Journal of Applied Crystallography*, vol. 8, pages 657–669, 1975.
- [Nye 53] J. F. Nye. *Some geometrical relations in dislocated crystals*. *Acta Metallurgica* 1, vol. 2, page 153, 1953.
- [Pantleon 08] W. Pantleon. *Resolving the geometrically necessary dislocation content by conventional electron backscattering diffraction*. *Scripta Materialia*, vol. 58, pages 994–997, 2008.
- [Penning 68] P. Penning & A.H. Goemans. *Philosophical Magazine*, vol. 18, page 297, 1968.
- [Petrenko 99] V. F. Petrenko & R. W. Whitworth. *Physics of ice*. Oxford University Press Inc., New York, 1999.
- [Polcarova 98] M. Polcarova, J. Gemperlova, J. Bradler, A. Jacques, A. George & L. Priester. *Philosophical Magazine A*, vol. 78, pages 105–130, 1998.
- [Polcarova 06] M. Polcarova, J. Gemperlova, A. Jacques, J. Bradler & A. George. *Synchrotron radiation topographic study of slip transfer across grain boundaries in Fe-Si bicrystals*. *Journal of Physics D: Applied Physics*, vol. 39, pages 4440–4449, 2006.
- [Poulsen 04] H. F. Poulsen. *Three dimensional x-ray diffraction microscopy*. Springer, Berlin, 2004.
- [Rejmánková-Pernot 98] P. Rejmánková-Pernot, P. Cloetens, J. Baruchel & J.-P. Guigay. *Phase Retrieval by Combined Bragg and Fresnel X-ray Diffraction Imaging*. *Physical Review Letters*, vol. 16, pages 3435–3438, 1998.
- [Robach 11] O. Robach, J.-S. Micha, O. Ulrich & P. Gergaud. *Full local elastic strain tensor from Laue microdiffraction: simultaneous Laue pattern and spot energy measurement*. *Journal of applied Crystallography*, vol. 44, pages 688–696, 2011.

- [Robertson 99] C.F. Robertson & M.C. Fivel. *A study of the submicron indent-induced plastic deformation*. Journal of Material Research, vol. 14, pages 2251–2258, 1999.
- [Röttger 94] H. Röttger, A. Endriss, H. Ihringer, S. Doyle & W.F. Kuhs. *Lattice constant and thermal expansion of H<sub>2</sub>O and D<sub>2</sub>O ice Ih between 10 and 265 K*. Acta Crystallographica B, vol. 50, pages 644–648, 1994.
- [Serrano 08] Jorge Serrano, Claudio Ferrero, Marco Servidor, Jürgen Härtwig & Michael Krisch. *DuMond analysis of bending in single crystals by Laue diffraction using  $\sigma - \pi$  polarization geometry*. Journal of Applied Crystallography, vol. 41, pages 1053–1056, 2008.
- [Servidori 01a] M. Servidori, S. Cembali & S. Milita. *3D DuMond diagrams of mult-crystal Bragg-case synchrotron topography. I Flat sample*. Applied Physics A, vol. 73, pages 78–82, 2001.
- [Servidori 01b] M. Servidori, S. Cembali & S. Milita. *3D DuMond diagrams of mult-crystal Bragg-case synchrotron topography. II. Curved sample*. Applied Physics A, vol. 73, pages 83–90, 2001.
- [Shearwood 89] C. Shearwood & R. W. Whitworth. *X-ray topographic observations of edge dislocations glide on non-basal planes in ice*. Journal of Glaciology, vol. 35, pages 281–283, 1989.
- [Shunsheng 88] X. Shunsheng & L. Runshen. *The Three-Dimensional Dynamic Du-Mond Diagram for X-ray Diffraction analysis of Nearly Perfect Crystals*. Journal of Applied Crystallography, vol. 21, pages 213–217, 1988.
- [Sinha 89] N. K. Sinha. *Experiments on anisotropic and rate-sensitive strain ratio and modulus of columnar-grained ice*. Journal of Offshore Mech. Arct. Eng., vol. 111, pages 354–360, 1989.
- [spe ] *Certified Scientific Software*. <http://www.certif.com/>.
- [Stephani 95] H. Stephani & G. Kluge. *Theoretische mechanik - punkt- und kontinuumsmechanik*. 1995.
- [Tanner 72] B. K. Tanner. *Dislocation contrast in x-ray topographs of very thin crystals*. Physica Status Solidi (a), vol. 10, page 381, 1972.
- [Weertman 70] J. Weertman & J. R. Weertman. *Theorie elementaire des dislocations*. 1970.
- [Winick 81] H. Winick, G. Brown, K. Halbach & J. Harris. *Wiggler and undulator magnets*. Physics Today, vol. 34:5, page 50, 1981.